POLITECNICO DI MILANO

PhD School of Politecnico di Milano
Doctoral Program in Environmental and Infrastructure Engineering - XXVII CYCLE
Department of Civil and Environmental Engineering – Environmental Area

HETEROGENEOUS PHOTOCATALYSIS AND ELECTROPHOTOCATALYSIS ON NANOSTRUCTURED TITANIUM DIOXIDE FOR WATER AND WASTEWATER TREATMENT: PROCESS ASSESSMENT, MODELLING AND OPTIMIZATION

Doctoral Dissertation of
Andrea TUROLLA

PhD Advisor: Ing. Manuela *ANTONELLI*
PhD Tutor: Prof. Roberto CANZIANI
PhD Coordinator: Prof. Alberto GUADAGNINI

December 2014

CONTENTS

ABSTRACT

Titanium dioxide (TiO_2) photocatalysis is a chemical-physical process which attracted great research interest for water and wastewater treatment. Its potential for advanced oxidation and disinfection of refractory pollutants and resistant pathogens has been highlighted in many works published over the last 30 years. In fact, thanks to TiO_2 photoelectrochemical properties, reactive oxygen species are produced when it is irradiated by photons having wavelengths below 390 nm. TiO_2 displays numerous benefits, such as low cost, durability, photostability and non-toxicity, but a scarce development of competitive technological solutions has been achieved so far, due to the complexity of the phenomena involved and in turn to the relevant difficulties posed by a comprehensive modelling. The most challenging issues to be faced are represented by (i) the heterogeneous phase of the photocatalyst which makes difficult the description of the involved chemical-physical processes, and (ii) the low process yield with respect to other established advanced oxidation processes, such as ozone or hydrogen peroxide combined to UV radiation. Actually, further research is needed aimed at the development of sustainable technological applications at full-scale. Among the directions in which research efforts should be addressed to, there are a deeper understanding of the fundamental mechanistic phenomena and the process optimization and scale-up.

The present PhD thesis is focused on the assessment, modelling and optimization of both photocatalysis and electrophotocatalysis processes on nanostructured titanium dioxide. Specifically, TiO_2 nanoparticle suspensions and self-ordered nanotubular TiO_2 were used. Concerning the understanding of mechanistic phenomena, three main interrelated subjects, namely radiation transfer, reactive species generation and process modelling, have been investigated. A brief description is reported in the following.

(i) Radiation transfer is the driving force of the process, but its accurate description is challenging, asking for the characterization of the optical properties of TiO_2. Besides, a valuable description of radiation field in the reactor volume is needed, especially when TiO_2 nanoparticle suspensions are used. An innovative methodology for the characterization of the optical properties of TiO_2 suspensions has been proposed, based on experimental measurements and on modelling the reaction volume by means of a multi-purpose CFD code. The effectiveness of the proposed methodology has been demonstrated by integrating optics, fluid dynamics and chemical reactions in a CFD model, capable to reproduce the degradation of oxalic acid in a semi-batch annular photoreactor.

(ii) Reactive species are compounds characterized by high reactivity, scarce selectivity and short lifetime. Their efficient and massive generation is a key step for the applicability of advance oxidation processes. Actually, their monitoring is fundamental for assessing the influence of operating conditions on overall process yield, but they are particularly difficult to quantify. Two experimental protocols for the measurement of reactive species, namely photogenerated holes and hydroxyl radicals, were implemented. Then, these protocols were applied for investigating the influence of inorganic anions on the generation of reactive species. In detail, the detrimental effect of inorganic anions has been discussed and a kinetic model has been proposed for describing the influence of inorganic anions on TiO_2 reactivity. This assessment was performed both on commercial TiO_2 nanoparticles in suspension and on an innovative engineered nanomaterial, self-ordered nanotubular TiO_2, which was manufactured and characterized. As for TiO_2 nanoparticles, the occurrence of aggregation phenomena has been studied, since aggregate size can significantly affect TiO_2 reactivity. As for self-ordered nanotubular TiO_2, surface fouling and regeneration protocols were evaluated.

(iii) TiO_2 photocatalysis modelling asks for the comprehensive integration of the physics involved in the process, usually optics, fluid dynamics and chemical reactions. Considering a photocatalysis process based on TiO_2 nanoparticle suspensions, a simplified model for reactive species quenching has been developed, with reference to photogenerated holes and hydroxyl radicals. The model accounts for radiation transfer, TiO_2 nanoparticle aggregation and kinetic reactions. It was calibrated based on experimental data, and then successfully validated by measurements carried out in a different experimental setup. Radiation transfer and fluid dynamics were subsequently described by a more complex CFD model, reproducing an unbaffled stirred tank reactor. The effectiveness of CFD code in describing fluid dynamics was proved. As for radiation transfer, CFD model was calibrated by radiometric measures, Radiation intensity and local volumetric rate of photon adsorption in the reactor volume were satisfactory predicted.

Finally, process optimization and scale-up were investigated with reference to an electrophotocatalytic process based on self-ordered nanotubular TiO_2. In detail, an optimal design methodology was proposed based on generated photocurrent as an indicator of TiO_2 photoactivation. First, generated photocurrent was experimentally monitored as a function of two operating conditions, namely reactor geometrical configuration and solution transmittance. Then, experimental data was modelled to define a prediction model accounting for both TiO_2 photoactivation and efficient energy use. The model was effectively validated in a number of reactor configurations, and guidelines for the design of an optimized reactor were indicated.

CHAPTER 1
STATE OF THE ART

The present chapter is devoted to define a reference frame about the research topic, based on the recent advances reported in literature. In detail, the first part of the discussion (paragraph 1.1) refers to titanium dioxide photocatalysis and electrophotocatalysis, aimed at briefly summarizing the process fundamentals, the currently available photocatalytic materials and the application scenarios for water and wastewater treatment. Subsequently, some topics of major relevance for the PhD thesis work have been addressed with the aim of exploring these themes and providing useful and comprehensive elements for their correct understanding and effective integration in the research. Detailed insights concern reactivity in advanced oxidation processes (paragraph 1.2), nanoparticle aggregation (paragraph 1.3) and computational fluid dynamics (paragraph 1.4).

1.1 TITANIUM DIOXIDE (ELECTRO)PHOTOCATALYSIS

Titanium dioxide (TiO_2) photocatalysis is a widely investigated and promising process for water and wastewater treatment based on photoelectrochemical properties of this semiconductor [1]. To the best of the author's knowledge, TiO_2 photoreactivity was reported for the first time by Renz in 1921 [2], who observed the reduction of titania under sunlight illumination in the presence of organic compounds. Although many other papers were published in the following years concerning TiO_2 peculiar properties, the turning point in determining a considerable rise in scientific and technological interest is represented by the research published by Fujishima and Honda in 1972 [3], reporting the photoelectrochemical water splitting at a TiO_2 electrode surface. Afterwards, an increasing number of papers has been published, focused on the application of TiO_2 in several fields, including solar energy conversion, i.e. hydrogen generation from water splitting and new generation photovoltaic solar panels production, photocatalytic depolluting and photo-induced superhydrophilicity [4].

In addition to its photoelectrochemical properties, the interest toward this material was also due to some other characteristics making it an excellent photocatalyst, such as low cost, durability, photostability and non-toxicity when it is not used in form of nanoparticles. Therefore, TiO_2 is nowadays employed in many technological applications, ranging from dye-sensitized solar cells to self-cleaning surface coatings [5]. Moreover, TiO_2 non-photoreactive forms, mostly as nanoparticles, are currently widespread and used in a multitude of commercial products, including food, personal care products, paints, coatings, papers and fibers, because of brightness, high refractive index and UV resistance [6–8]. About 40,000 t of nanostructured TiO_2 are estimated to be produced every year only in the United States and this quantity is expected to grow in the future [6].

1.1.1 Process fundamentals

TiO_2 photoactivation occurs when the photocatalytic surface is hit by photons of energy equal or greater than the band gap energy, usually 3.2 eV for anatase and 3.0 eV for rutile, which corresponds to radiation wavelength approximately lower than 390 nm [9]. When such photons are absorbed by TiO_2 surface, electrons are promoted from the valence band to the conduction band in femtoseconds, originating the so-called electron-hole pair separation. A significant part of separated charges recombines immediately, while residual photogenerated holes and promoted electrons initiate reductive and oxidative pathways. Photogenerated holes and promoted electrons mainly react with hydroxyl ions and oxygen molecules, respectively determining the production of hydroxyl radicals ($OH^{\bullet}$) and superoxide ions ($O_2^{\bullet -}$). Nevertheless, other reaction pathways are possible. The produced reactive species, such as photogenerated holes, hydroxyl radicals and superoxide ions, are characterized by high reactivity, scarce selectivity and short lifetime, so that they can promote redox reactions leading to contaminant decomposition, potentially up to their complete mineralization. In figure 1.1 a scheme of TiO_2 photocatalysis process is shown, while the main reactions involved in TiO_2 photoactivation and generated reactive species generation are reported in equations e1.1 to e1.6 [9,10].

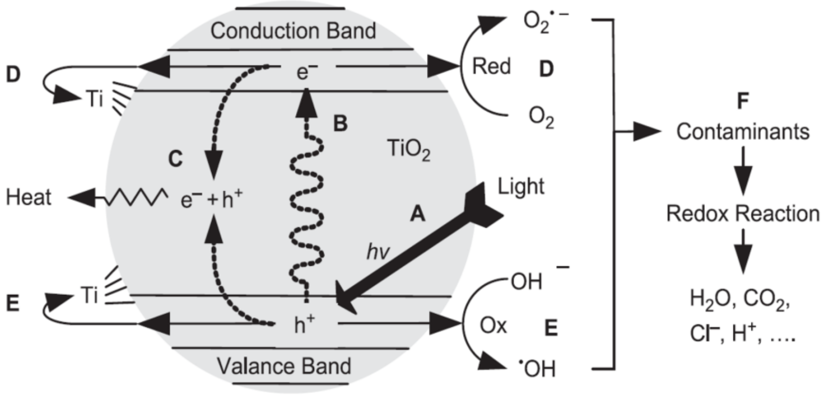

Figure 1.1 Scheme of the TiO_2 photocatalysis process: (A) surface irradiation, (B) electron-hole pair separation, (C) electron-hole pair recombination, (D,E) reductive and oxidative pathways, (F) redox reaction for the decomposition of contaminants in solution. Adapted from Choi et al. [11].

- Electron-hole pair separation: $TiO_2 \xrightarrow{hv} {h^+}_{VB} + {e^-}_{CB}$ (e1.1)
- Trapping of photogenerated holes: ${h^+}_{VB} \to {h^+}_{TR}$ (e1.2)
- Trapping of promoted electrons: ${e^-}_{CB} \to {e^-}_{TR}$ (e1.3)
- Electron-hole pair recombination: ${h^+}_{VB} + {e^-}_{CB} \to heat$ (e1.4)
- Oxidation of hydroxyls: ${h_{VB}}^+ + OH^- \to OH^{\bullet}$ (e1.5)

- Scavenging of promoted electrons: $e^{-} + (O_2)_{ADS} \rightarrow O_2^{\bullet -}$ (e1.6)

Equations (e1.2) and (e1.3) describe the surface trapping of photogenerated holes and promoted electrons: the charge carriers are bound on TiO_2 surface and do not undergo recombination immediately after photon excitation [12]. Such mechanism, together with the presence of electron scavengers as molecular oxygen, is fundamental in limiting the extent of electron-hole recombination and for promoting the production of reactive species. As an example, the positive effect of hydrogen peroxide (H_2O_2) as a scavenger of promoted electrons has been observed [13]. A viable alternative for the effective scavenging of promoted electrons consists in the application of an anodic polarization to immobilized TiO_2, that is used as photo-anode in a photoelectrochemical cell [14]. In detail, as a consequence of the electrical circuit created between the electrodes, a part of the promoted electrons can be effectively removed from the conduction band of the material, thus determining a reduction in the electron-hole pair recombination and promoting reactive species generation. On the other hand, electrophotocatalysis, as it is usually defined, requires the fabrication of conductive TiO_2 electrodes, such in case of nanotubular TiO_2 grown by anodic oxidation on Ti substrate. This photocatalyst has attracted considerable interest in recent years due to its great engineering potential [15].

In addition to the electron-hole pair recombination, another drawback for the development of TiO_2 photocatalytic technologies is related to the low quantum yield, indicating the fraction of absorbed photons leading to the generation of reactive species; as an example, TiO_2 quantum yield has been estimated to be 2% for hydroxyl radical [16]. Therefore, a thorough assessment of photocatalytic reactivity mechanisms, both in terms of measuring and modelling, is fundamental for process design and engineering, since operating conditions must be optimized to ensure process sustainability with respect to other established oxidation processes, such as H_2O_2/UV. Accordingly, reactivity in advanced oxidation processes is detailed in paragraph 1.2.

1.1.2 Photocatalytic materials

Several types of photoreactive TiO_2 have been synthetized. They can be roughly divided into two groups: TiO_2 particles and immobilized TiO_2. The main difference is related to their structure and, thus, to their mode of use. In fact, in the former case, TiO_2 particles are suspended in slurry phase and used in well-mixed reactors; while, in the latter case, TiO_2 is immobilized on solid substrates housed inside reactors. As a matter of fact, the maximization of both absorbed radiation and photocatalyst surface are common goals, but the issues related to the two groups are significantly different, being physical and photocatalytic properties affected by TiO_2 structure [17,18].

Concerning TiO_2 particles, the manufacturing of a large variety of TiO_2 particles is reported: some of these are distributed as commercial products (see table 1.1), while in most cases they are still prototypes in the research of advanced photocatalytic materials. Especially in case of nanometric structures, the key benefits of TiO_2 particles are the high area-to-volume ratios, the high specific production of reactive species and the scarce influence of mass transport limitations [19]. So far TiO_2 nanoparticles are the most widespread form of TiO_2 used in water and wastewater research. Actually, P25 Aeroxide, formerly P25 Degussa, is currently considered a benchmark in TiO_2 photocatalysis [20]. It should be mentioned that aggregation size and structure influence the extent of TiO_2 particle photoactivation. As an example, TiO_2 particles located in the core of an aggregate are effectively shielded from irradiation, since radiation penetration decreases as aggregate density increases and only exposed nanoparticles can generate electron-hole pairs. Moreover, aggregate size affects also the number of active sites and the mass transport phenomena [21].

Table 1.1 Most widespread commercial TiO_2 particles and main physical properties.

Type	Manufacturer	Specific surface area (m^2/g)	Primary particle size (nm)
P25 Aeroxide	Evonik Industries (Germany)	50±15	21
Aldrich	Sigma-Aldrich (USA)	45-55	< 25
Hombikat UV100	Sachtleben Chemie (Germany)	> 300	< 10

Nevertheless, the separation of TiO_2 particles from the liquid phase is required in water and wastewater treatment, especially in case of nanoparticles, in order to avoid the contamination of the effluent, since the impact of nanoparticle dispersion in the aquatic environment is causing noticeable concern [22,23]. TiO_2 post-separation determines the need for complex and expensive stages, consisting in filtration [24] or coagulation [25], whose effectiveness depends on the aggregate size [26]. Hence TiO_2 nanoparticle aggregation phenomena are particularly relevant, both for the proper understanding of photocatalytic reactivity and for the suitable design of an efficient separation process. Consequently, nanoparticle aggregation is discussed in detail in paragraph 1.3.

Otherwise, TiO_2 immobilization determines a simplification in the treatment scheme, but a number of drawbacks have to be considered, such as the reduction in the amount of active sites and the occurrence of mass transfer limitations [27]. Moreover, process engineering involves completely different criteria for reactor design, being the related research currently underdeveloped [11,28]. As a matter of fact, up to now the most of the research has been focused on the manufacturing of materials characterized by good mechanical and photocatalytic properties, rather than on the process engineering and technological development. In detail, immobilized TiO_2 can be prepared by several deposition or synthesis techniques, being the most diffused summarized in table 1.2. The removal of contaminants by immobilized TiO_2 was mostly studied at proof-of-concept scale, while further research is required for process optimization and scale-up.

Table 1.2 Some of the manufacturing techniques for immobilized TiO_2 preparation. Adapted from Fujishima et al. [4].

Method	Year	Reference
Thermal oxidation	1975	[29]
Sol-gel	1995	[30]
Electrophoretic deposition	1995	[31]
Spray pyrolysis	1998	[32]
CVD	1998	[33]
Silica gel substrate	1998	[34]
RF Magnetron sputtering	2002	[35]
Inorganic-organic graded film	2002	[36]
Chemical bath deposition	2003	[37]
Plasma spray	2003	[38]
Electron-beam evaporation	2004	[39]
Vacuum evaporation	2006	[40]
Anodic oxidation	2006	[41]

1.1.3 Application for water and wastewater treatment

The advanced oxidation and disinfection of refractory pollutants and resistant pathogens by TiO_2 photocatalysis has been reported in many published works over the last 30 years [26,42,43].

Regarding the advanced oxidation mechanisms, various degradation pathways can occur, whose relative relevance is usually related to the characteristics of the target pollutant and to the specific operating conditions [43]. Some contaminants can be directly oxidized or reduced by photogenerated holes or promoted electrons, respectively. In detail, photogenerated holes are powerful oxidants (+1.0 to +3.5 V vs. NHE) and promoted electrons are good reductants (+0.5 to -1.5 V vs. NHE), since the oxidizing or reducing power depends on the type of photocatalyst and the operating conditions. However, pollutants are mainly degraded by reactive species generated at TiO_2 surface ($OH^•$, $O_2^{•-}$) or by secondary reactive species, whose formation is due to radical propagation reactions (H_2O_2, perhydroxyl radical $HO_2^•$). In addition to this, several research works reported that the degradation of many pollutants asks for the pollutant preliminary adsorption on TiO_2 surface. The degradation rate is therefore effectively described by a Langmuir-Hinshelwood model, in which the reaction rate is proportional to surface coverage [26].

Concerning advanced disinfection, it has been observed that the oxidation of basic structures constituting the cell wall, such as the lipopolysaccharide layer, the peptidoglycan layer, the lipid membrane and the protein membrane, occur first; oxidation reactions proceed till the loss of potassium ions and the oxidation of phospholipids in the cell membrane, causing cell death [44].

Likewise the other UV-based advanced oxidation processes, TiO_2 photocatalysis is an energy intensive process, whose application is usually aimed at the removal of organic refractory compounds from water and wastewater. Good optical properties of the liquid phase are required for the proper radiation transfer, making TiO_2 photocatalysis poorly applicable to primary wastewater without any preliminary treatment stage. Such requirement is also important to protect the photocatalyst, that could be poisoned, covered or fouled by compounds in wastewater.

Therefore, TiO_2 photocatalysis is conventionally intended for water and wastewater polishing, rather than for the improvement of wastewater biodegradability upstream of a biological treatment, as Fenton process is sometimes applied [9]. Because of its high energetic requirements, a possible applicative scenario for TiO_2 photocatalysis is within complex treatment train intended for a stringent water and wastewater treatment, downstream of activated carbon or nanofiltration, being this stages eventually aimed at the removal of those contaminants that can be easily adsorbed or separated by filtration at a lower cost [11].

On the other hand, scarce information is available nowadays on the application of TiO_2 photocatalysis at the real scale, so that an estimation of process sustainability is not possible at this stage of research. In particular, being the energetic consumption typically decisive in defining process applicability, the assessment should be performed on optimized reactors under real operating conditions. Up to date most of the research works have been carried out at the laboratory scale in non-optimized photocatalytic reactors using a multitude of pollutants spiked in synthetic media, under significantly different operating conditions. In addition, a relevant part of these works do not approach photocatalysis under a modelling point of view, also due to the intrinsic difficulties in describing a multi-physics system in which optics, fluid dynamics and chemical reactions must be taken into account. Consequently, despite the evidence for the broad range of applicability of TiO_2 photocatalysis, significant advances in modelling are still required for scientific-technological literature generalization.

Several papers have been published on TiO_2 photocatalysis modelling so far, giving a more or less complex and comprehensive description of involved phenomena, for the most dedicated to TiO_2 nanoparticles in slurry phase, *inter alia* [1,45]. A current trend concerns the use of advanced numerical simulation tools, such as computational fluid dynamics (CFD) codes, able to integrate the various physics of the system [46]. Therefore, paragraph 1.4 is addressed to CFD techniques.

1.2 REACTIVITY IN ADVANCED OXIDATION PROCESSES

Radical species are atoms, molecules or ions characterized by unpaired valence electrons or an open electron shell. This peculiar feature determines the high reactivity of these species, that are highly electrophiles, so that they combine rapidly and non-selectively with nearly electron-rich compounds [47]. Because of their strong reactivity, radical species have short lifetime, usually in the order of nanoseconds, and high oxidizing power with respect to conventional oxidants, as reported in table 1.3 [48]. The strong reactivity results also in a complex process chemistry, since a significant number of reaction pathways are initiated, promoted and terminated simultaneously, so that the assessment of process intermediates and by-products is usually extremely difficult and expensive [26].

Table 1.3 Oxidation potential of common species used in environmental remediation. Adapted from Parsons [48].

Species	Oxidation potential (V)
Hydrogen radical	2.80
Superoxide ion	2.42
Ozone	2.07
Hydrogen peroxide	1.78
Perhydroxyl radical	1.70
Permanganate	1.68
Hypobromous acid	1.59
Chlorine dioxide	1.57
Hypochlorous acid	1.49
Chlorine	1.36

Advanced oxidation processes are based on significantly different chemical-physical phenomena aimed at generating reactive species as efficiently and massively as possible inside the reactor volume. As a consequence, radical reaction chains are displayed to ‘attack’ target pollutants and to determine their degradation into lower molecular weight compounds [48]. Therefore, there are the two fundamental features for the real-scale application of an advanced oxidation process: (i) the maximization of local concentration of generated reactive species, and (ii) the fast diffusion of target pollutants in proximity of reaction zones [18]. As for the former, it depends on the fundamentals of the single process, such as radiation transfer throughout reactor volume in case of UV-based processes. Concerning the latter, it is related to the locally-generated turbulent diffusion, since molecular diffusion is typically insufficient to ensure adequate mixing.

The degradation of model pollutants as reference variable for assessing process performance is often poorly reliable and representative, since no insight into the primary reactions is usually possible. For instance, the photocatalytic degradation of a simple compound, as oxalic acid, takes place through two different reaction mechanisms, both mediated by the adsorption on TiO_2 surface, but two types of active sites and reactive specie are involved, namely photogenerated holes and hydroxyl radicals [49].

1.2.1 Measurement protocols

Because of their nature, radical species are difficult to detect [50]; anyway, their accurate measurement may support the assessment of both process mechanisms and the influence of operating conditions on degradation yields. Several measurement techniques have been proposed in literature so far [51,52]. Many of these methods are based on the use of probe compounds reacting selectively with one or more reactive species, that generate products having measureable properties and that can be related to the concentration of reactive species using reaction stoichiometry. Probe compounds should: (i) not interfere with the advance oxidation process, (ii) be highly selective and sensitive with respect to the target reactive species, as well as (iii) form stable products. The main measurement techniques are reported in table 1.4.

Table 1.4 Measurement techniques for reactive species.

Reactive species	Measurement technique	Reference
Photogenerated hole (h^+)	Absorbance measures	[53]
	ESR measures	[54,55]
Hydroxyl radicals ($OH^\bullet$)	Absorbance measures	[56]
	Fluorescence measures	[57]
	ESR measures	[54,58,59]
Superoxide ion ($O_2^{\bullet -}$)	Chemiluminescence measures	[13,60]
Perhydroxyl radical ($HO_2^\bullet$)	Absorbance measures	[57]
Singlet oxygen ($^1O_2$)	Fluorescence measures	[50]
	Phosphorescence measures	[61]

Other techniques for the measurement of reactive species have been developed, such as those based on high performance liquid chromatography (HPLC) or diffuse reflectance laser flash photolysis [62]. In the following the most common techniques and the recent advances in the measurement of radical species in TiO_2 photocatalysis are briefly discussed:

- **ESR measures**

The presence of unpaired electrons results in paramagnetic properties, i.e. in electronic paramagnetic resonance (EPR). The EPR can be assessed by means of electron spin resonance (ESR) technique, based on the interaction between the electromagnetic radiation and the angular momentum of electrons, or the electron spin. In fact, when radicals are exposed to an external electromagnetic radiation at constant frequency, the electron spin resonance, as microwaves, can be measured by varying the intensity of the imposed magnetic field [63]. In detail, this method is based on a compound, called the spin trap, selectively reacting with reactive species and generating a product, the spin adduct, whose resonance can be measured.

The ESR technique was applied for the first time to TiO_2 photocatalysis by Jaeger and Bard [64]. In the past the efficiency in charge separation was measured by monitoring the trapping of promoted electrons on conduction band and the reaction of photogenerated holes with adsorbed oxygen in the valence band, since both reactions determine a measurable resonance [55]. Otherwise, the generation of photogenerated holes and hydroxyl radicals can be evaluated by dosing acetic acid as spin trap and, thus, generating $CH_3^\bullet$ and $CH_3COOH^\bullet$, respectively [58,63]. It is interesting to note that a single spin trap, acetic acid, produces two different and measurable spin adducts, so that solution pH must be controlled in order to determine their distribution [59].

Another procedure for using ESR technique consists in measuring the disappearance of a chemical compound characterized by a paramagnetic resonance response after its degradation due to the reaction with radical species. As an example, the reaction of several nitroxide radicals, such as CTPO (3-carboxy-2,2,5,5-tetramethyl-1-pyrrolidine-1-oxyl) nitroxide radical, with photogenerated holes and hydroxyl radicals causes a measurable decrease in ESR signal [54].

Although ESR technique provides precise and reliable results, it involves very high costs for instrumentation as well as high complexity and poor flexibility in trial execution [65].

- **Absorbance measures**

There is only one effective method reported in literature for the determination of photogenerated holes by absorbance measures. The probe compound is iodide, provided as potassium iodide; iodide is selectively oxidized to iodine by photogenerated holes, according to the reaction:

$$2I^- + 2h^+ \rightarrow I_2 \qquad \text{(e1.7)}$$

The measurement of iodine is then performed indirectly by monitoring the absorbance at 585 nm when starch is dosed, since it determines a turning of color to blue in the presence of iodine. Iodide selectivity towards photogenerated holes has been reported by various authors [13,66], while the same reaction has already been exploited to evaluate TiO_2 reactivity in the past [67]. It should be mentioned that generated iodine strongly absorbs UV radiation, so that a significant change in radiation transfer and, thus, in operating conditions is determined by this method.

Another method, denominated Fricke dosimetry, has been developed but it is not usually adopted. $FeSO_4$, $CuSO_4$ and H_2SO_4 are dosed during TiO_2 photocatalysis: ferrous ion is oxidized by hydroxyl radicals and hydrogen peroxide to ferric ion, being the oxidation rate related to amount of reactive species in solution. The generation of ferric ion can be evaluated by absorbance measures at 304 nm. Although this technique is effective in quantifying reactive species, the main limitation is related to the difficulty in distinguishing between the different reactive species. Moreover, there are two further drawbacks: (i) metallic species in solution absorb part of the UV radiation, reducing the available radiation for TiO_2 photoactivation, and (ii) the occurrence of ferrous ion oxidation by Fenton-type reactions, requiring that pH is maintained at high values.

Finally, a technique called Oxidation Extraction Photometry (OEP) has been efficiently applied to several research areas [68], including TiO_2 nanoparticle photocatalysis [65]. This method is based on the oxidation of DPCI (1,5-diphenylcarbohydrazine) to DPCO (diphenylcarbazone) by reactive species; DPCO can be extracted from aqueous solution and then quantified by an absorbance measurement at 563 nm. The main drawback is related to the impossibility to directly distinguish among reactive species, unless selective scavengers are used to isolate a specific reactive species.

- **Fluorescence and phosphorescence measures**

These methods are based on the generation of fluorescent probes from the reaction between probe compounds and reactive species. Some specific properties for fluorescence probes has been highlighted, in addition to the already-reported general characteristics [52]: (i) absence of photosensitivity, so as to produce fluorescence only in the presence of reactive species, (ii) high quantum yield of the generated product, (iii) broad spectrum of radiation excitation and emission.

In case of TiO_2 photocatalysis terephthalic acid is a widely used probe for hydroxyl radicals, thanks to its selectively and to the stability of the generated product, 2-hydroxyterephthalic acid [56]. In particular, terephthalic acid is hydroxylated to 2-hydroxyterephthalic acid, a fluorescent compound, having excitation and emission radiation wavelengths at 315 and 425 nm, respectively. The selectivity of terephthalic acid in reacting only with free hydroxyl radicals and not with hydroxyl radicals bound to TiO_2 surface as well as the 80% trapping efficiency were demonstrated [13,56,69]. A method for the measurement of singlet oxygen in TiO_2 photocatalysis was proposed, exploiting the phosphorescent properties of this reactive species [54,61]. As a matter of fact, singlet oxygen emits radiation at wavelength corresponding to the near infrared spectrum (~1270 nm). Phosphorescent response is due to the energy emitted during the decay of singlet oxygen ($^1O_2$) to a more stable state ($^3O_2$), linearly decreasing over a few microseconds.

A number of other techniques based on fluorescent probes have been developed for measuring reactive species generated in gas phase [50,70,71] or for other types of applications [52].

- **Chemiluminescence measures**

Chemiluminescence is the property of some reactions to emit electromagnetic radiation. The intensity of chemiluminescence is usually measured as the number of photons emitted by the solution in a given time interval (usually 20 seconds) at a certain wavelength [13]. Luminol is among the most studies compounds generating chemiluminescence, having its interaction with reactive species in TiO_2 photocatalysis been observed in 1984 [60]. Luminol is sensitive to oxidation reactions and to the presence of hydrogen peroxide; hence, it is used primarily for monitoring superoxide ion [72]. In detail, chemiluminescence is due to the production of luminol hydroperoxide, which decomposes rapidly in a more stable state, while emitting radiation at a wavelength of 425 nm.

In addition to luminol, MCLA (2-Methyl-6-(p-methoxyphenil)-[1,2-a]pyrazin-3(7H)-one) can be used for the measurement of superoxide ion, since it selectively reacts with this reactive species producing radiation at a wavelength of 465 nm [73]. Moreover, the use of TFF (4,4'(5')-Bis[2-(9-anthryloxy)ethylthio]tetrathiafulvalene) as probe for superoxide ion has been proposed, because of its high selectivity, giving a measurable chemiluminescent product [52].

1.2.2 Quantum yield

The efficiency of incident radiation in photoactivating the photocatalytic material can be expressed by several parameters, which correlate the number of delivered photons to the system and the number of molecules undergoing the studied reactions. The most widely used indicator is the quantum yield, defined as the ratio between the number of molecules produced in the process and the number of photons absorbed by TiO_2 surface [20]. Particularly referring to reactive species, the quantum yield is the ratio between the amount of generated reactive species and the number of absorbed photons, being some published results reported in table 1.5.

The assessment of quantum yield requires the quantification of the absorbed photons, which is usually considerably lower than the amount of photons delivered at TiO_2 surface. This difference is due to several side phenomena, including surface reflection and wavelength-selective absorption.

Therefore, the number of absorbed photons, which is strictly correlated to the amount of absorbed radiation, is generally difficult to quantify. For this reason, a number of published works refer to apparent quantum yield, which is calculated considering the photons delivered to TiO_2 surface. Apparent quantum yield is typically lower than quantum yield, since it considers the efficiency in photon delivery, in addition to the efficiency of electron-hole pair separation [74].

Table 1.5 Reactive species quantum yield and details about measurement procedure.

Reactive species	Quantum yield	TiO_2 photocatalyst	Measurement technique	Reference
Photogenerated hole (h^+)	0.02	TiO_2 film	Absorbance measures (iodide)	[16]
Hydroxyl radicals ($OH^•$)	$7·10^{-5}$	TiO_2 film	Fluorescence measures (terephthalic acid)	[16]
Superoxide ion ($O2^{•-}$)	0.8	TiO_2 film	Chemiluminescence measures (luminol)	[13]
Singlet oxygen ($^1O_2$)	0.31	P25 Aeroxide	Phosphorescence measures	[61]
$OH^•$, $HO_2^•$, H_2O_2 (indistinctly)	0.011-0.122	P25 Aeroxide	HCOOH degradation	[57]

Based on the literature that have been published on this topic, the following steps can be pointed out to estimate the amount of photons absorbed by TiO_2 surface:

1. Estimation of the amount of photons emitted by the source and entering the reactor.

2. Modelling of radiation transmission from the reactor boundaries to TiO_2 surface, analytically described by radiative transfer equation. Several methods have been developed for modelling the radiation transfer through the volume of the reactor, involving the development numerical or stochastic techniques [46,75]. In case of TiO_2 photocatalysis on nanoparticle suspensions, this step is particularly complicated by the occurrence of radiation scattering. Actually, some empirical-based methods, as the two-flux model or the six-flux model, have been proposed so far, instead of computational-intensive techniques for radiative transfer solution, described *inter alia* by [1,76,77].

3. Determination of the amount of photons absorbed by TiO_2 surface (R), according to [21]:

$$R = \int_{\lambda} \frac{I_\lambda \sigma_\lambda}{h\nu_\lambda} d\lambda \tag{e1.8}$$

   where I_λ is the radiation intensity, κ_λ is the absorption coefficient and ν_λ is the radiation frequency, being these variable function of radiation wavelength. h is the Plank constant. For the determination of the absorption coefficient several methods have been proposed, depending on TiO_2 morphology [78,79]. When the evaluation is complicated, as for different types of immobilized TiO_2, the apparent quantum yield has to be used. In case of suspended TiO_2 R can be referred to as local volumetric rate of photon absorption (LVRPA).

1.2.3 Reaction kinetics

Advanced oxidation processes are typically capable of generating reactive species in concentrations of the order of 10^{-11} to 10^{-9} mol/L [48]. The reaction of these compounds with target pollutants has been generally modeled in the past by a second-order reaction, according to:

$$\frac{d[Pollutant]}{dt} = -k_{P,R}[Pollutant][Reactive\ species] \tag{e1.9}$$

in which $k_{P,R}$ is the degradation rate of a certain pollutant by a given reactive species.

This equation permits an acceptable mathematical approximation for describing pollutant degradation, whose driving force is the number of interaction between the involved species, in turn proportionally related to the effective species concentrations [47]. In this framework, the low concentration of reactive species is usually compensated by the high reaction rate of pollutants in combining with reactive species, typically three to four orders of magnitude greater than the second-rate constants reported for other common oxidants. A short list of second-order rate constants for the reaction between several pollutants and hydroxyl radical, that is the main oxidizing agent involved in advanced oxidation processes, is reported in table 1.6.

Table 1.6 Second-order rate constants for the reaction between several pollutants and hydroxyl radical. Adapted from Buxton et al. [80]

Pollutant	Rate constant (L mol^{-1} s)
Atrazine	$2.6 \cdot 10^{9}$
Chlorobenzene	$4.5 \cdot 10^{9}$
2-Chlorophenol	$1.2 \cdot 10^{10}$
Geosmin	$1.4 \cdot 10^{10}$
Methyl tert-butyl ether	$1.6 \cdot 10^{9}$
MIB	$8.2 \cdot 10^{9}$
Phenol	$6.6 \cdot 10^{9}$
1,1,2-Trichloroethane	$1.1 \cdot 10^{8}$
Trichloroethylene	$4.2 \cdot 10^{9}$

The same structure of equation (e1.9) can be used for modelling the consumption rate of reactive species. As an example, the following general formulation for the consumption rate of hydroxyl radicals in TiO_2 photocatalysis is reported, developed in several previous works, *inter alia* [21,81]:

$$\frac{d[OH^{\bullet}]}{dt} = k_{OH^{\bullet}}[h^{+}][OH^{-}] - \sum_{i} k_i\,[OH^{\bullet}][i] \tag{e1.10}$$

in which $k_{OH^{\bullet}}$ is the rate constant for the reaction between photogenerated holes and hydroxyl ions and k_i is the rate constant for the reaction between the generic species i, having concentration [i] in the system, and hydroxyl radicals. In detail, the first term on the right side of the equation represents hydroxyl radical production, while the second term stands for all the reactions determining hydroxyl radical consumption. A major issue in this modelling procedure is the inclusion of all the reactions involved, each of them characterized by its own rate constant.

In order to provide a mechanistic description of radical reactions, the estimation of reactive species concentration is based on a modelling approach usually defined as pseudo-steady state [47]. In fact, times characterizing the generation and the disappearance of reactive species are very short, being those reaction rates several orders of magnitude faster than the macroscopic reaction rate of contaminant degradation. In detail, the equation (e1.10) is considered to be equal to zero, allowing to determine an equilibrium concentration for each reactive species in the reactor and, thus, to evaluate the overall degradation rate of a pollutant. It should be noticed that such equilibrium concentration increases with the extent of phenomena contributing to reactive species generation and decreases as a function of the mechanisms determining reactive species consumption.

1.2.4 Factors affecting reactivity

As already discussed, the efficiency of advanced oxidation processes is strictly related to the amount of reactive species which are generated and react with target pollutants. Both these aspects are influenced by several factors, some of them affecting the TiO_2 photoactivation and others the radical reactions chain development. In fact, on the one hand, TiO_2 photoactivation descends directly from electron-hole separation, which kicks off the generation of primary reactive species; on the other hand, some specific compounds can interfere with radical reactions chain progress, leading to a parasite consumption of reactive species [9]. TiO_2 photocatalyst loading or reactor design are usually determinant for the generation of reactive species, as well as chemical-physical water and wastewater characteristics, as solution pH and the presence of other compounds than target pollutant. The assessment of the influence of water and wastewater composition on TiO_2 photocatalysis is still critical, since most of published works are carried out using synthetic media. Nevertheless characteristics of the solution to be treated represent a great issue for process engineering and scale-up as. In the following, the most important factors affecting TiO_2 reactivity referring to the research work reported in the present PhD thesis are discussed, namely the solution pH and the presence of inorganic ions.

- **pH**

Solution pH has a multiple role in affecting TiO_2 reactivity. First, it determines the superficial charge of TiO_2 photocatalyst, in turn having strong consequences on the adsorption of compounds on TiO_2 surface [26]. Then, solution pH directly influences the production of hydroxyl radicals, since a higher concentration of hydroxyl ions results in a higher hydroxyl radical production, as introduced in equation (e1.10) [5]. Finally, some other minor phenomena have been observed, such as the direct influence of solution pH on the degradation of some pollutants or the modifications induced by solution pH to the characteristics of valence and conduction bands [26].

Point zero charge (PZC) is an useful parameter for describing the influence of solution pH on TiO_2 superficial charge. PZC is the pH value corresponding to the neutral charge of TiO_2 surface, and generally of a metal oxide, when no other ionic species are dissolved in solution [9]. In particular, hydroxyl groups on TiO_2 surface participate in defining the following acid-base equilibrium:

$$TiOH_2^+ \overset{pK_{a1}}{\longleftrightarrow} TiOH \overset{pK_{a2}}{\longleftrightarrow} TiO^- \tag{e1.11}$$

in which pKa_1 and pKa_2 are the co-logarithms of the acid dissociation constants, allowing the determination of PZC of TiO_2 surface by means of the following relation:

$$pH_{PZC} = \frac{1}{2}(pK_{a1} + pK_{a2}) \tag{e1.12}$$

As for TiO_2 photocatalyst, PZC depends on the photocatalyst morphological characteristics or on the fabrication technique. As an example, PZC for P25 Aeroxide is equal to about 6.25, since pKa_1 and pKa_2 are 4.5 and 8, respectively. As a function of solution pH, lower or higher than PZC, TiO_2 surface changes its charge, according to the following mechanisms:

$$pH < PZC \qquad TiOH + H^+ \leftrightarrow TiOH_2^+ \tag{e1.13}$$

$$pH > PZC \qquad TiOH + OH^- \leftrightarrow TiO^- + H_2O \tag{e1.14}$$

Hence, TiO_2 surface is positively charged when a photocatalytic system works at pH<PZC: in such conditions the electrostatic attraction among negative charges in solution and TiO_2 surface is enhanced. Contrarily, an opposite mechanism occurs for pH>PZC [26].

Furthermore, solution pH affects the adsorption of molecules on TiO_2 surface, and the partitioning between dissolved and adsorbed phases. For instance, the presence of free hydroxyl radicals is favored at high pH values, as suggested by the equilibrium described by the equation e1.15; otherwise, superoxide ion behaves inversely as a function of pH [82].

$$Ti^{4+} - OH^{\bullet} \leftrightarrow Ti^{4+} + OH^{\bullet} \tag{e1.15}$$

- **Inorganic ions**

Photocatalytic performances have been observed to drastically worsen when target pollutants are present in surface water instead of deionized water, at the same operating condition, due to the presence of compounds in solution [9]. In particular, inorganic ions are commonly present in real water and wastewater, negatively affecting TiO_2 reactivity by interfering with chemical-physical reactions. Several research works have already been published on the topic, *inter alia* [83–85], evidencing that inorganic ions can depress TiO_2 reactivity by potentially interfering with three process mechanisms: photon absorption, surface adsorption and photocatalytic degradation.

In the past the detrimental effect of inorganic ions has been observed with reference to the degradation of model pollutants, while Jassby et al. [21] reported a decrease in hydroxyl radical generation in the presence of chloride. In detail, 15% reduction in the hydroxylation of terephthalic acid was detected when 0.2 M chloride was dosed in a 40 mg/L P25 Aeroxide TiO_2 suspension.

In general, although UV screening has been reported for nitrate [86], surface adsorption and scavenging of reactive species are by far the most relevant phenomena involved in TiO_2 reactivity reduction by inorganic ions. On the one hand, inorganic ions compete for active sites on TiO_2 surface, having two detrimental effects: (i) inhibition of the reaction of those pollutants which have to be necessarily adsorbed before degradation, (ii) reduction of the amount of hydroxide ions bonded to TiO_2 surface, which are the precursors of radical species. On the other hand, the photocatalytic degradation is inhibited when reactive species are directly quenched by anions. However the extent of reactive species quenching is related to the specific reactivity of each anion with the reactive species [9].

As for the adsorption on TiO_2 surface, the competition for active sites among inorganic ions and other compounds has been described in the past by applying the Langmuir model [84]. In addition, the influence of adsorbed inorganic ions in determining a change in the electrostatic properties of TiO_2 surface has to be considered [26].

As for the scavenging effect of reactive species, the presence of inorganic ions can be modeled by introducing the reactions between reactive species and inorganic ions in the relations describing the consumption rate of reactive species. Therefore, the detrimental effect is more relevant the bigger inorganic ion concentrations are and as a function of the rate constants between inorganic ions and single reactive species. Some reaction rates for hydroxyl radical are reported in table 1.7 [85]. A proper modelling should account also for the production of other radical species from the reaction among inorganic ions and reactive species, usually characterized by a lower oxidation potential. As an example, the oxidation potential of carbonate radical, generated by the reaction of carbonate and bicarbonate ion with hydroxyl radical, is 1.85 V [87].

Table 1.7 Second-order rate constants for several inorganic ions with hydroxyl radical.
Adapted from Guillard et al. [85].

Inorganic ion	Rate constant ($L\ mol^{-1}\ s$)
Bicarbonate	$8.5 \cdot 10^6$
Carbonate	$3.9 \cdot 10^8$
Chloride	$4.3 \cdot 10^9$
Nitrate	$1.4 \cdot 10^8$
Phosphate	$< 10^6$
Sulfate	$1 \cdot 10^{10}$

Furthermore, some metal cations, such as Fe^{3+} and Cu^{2+}, were observed to have different influence on the overall process efficiency, depending on the metal type and concentration [9]. The effect of these ions is essentially related to their direct reaction with separated charges, causing a reduction in electron-hole recombination and, thus, a positive effect on TiO_2 reactivity. Otherwise, the effect is negative if the separated charges are subtracted to the generation of radicals [5].

Finally, in case of TiO_2 suspension, the presence of inorganic ions can determine modification on the aggregation state of nanoparticles, subsequently resulting in a change in TiO_2 reactivity [21], as described in more details later on in paragraph 1.3.

1.3 NANOPARTICLE AGGREGATION

As already introduced, the suspension of nanoparticles in slurry phase is widespread in TiO_2 photocatalysis for water and wastewater treatment [9]. Nowadays materials at nanometric scale are receiving more and more attention due to their peculiar properties, but concurrently they are creating great concern for the negative implications on environment and human health [22]. For this reason the understanding of chemical and physical behaviour of TiO_2 suspensions in photocatalytic reactors is crucial, since it affects both process yield and the removal downstream the process, preventing TiO_2 nanoparticles dispersion into the environment. In the following some interesting topics for the present PhD thesis, namely nanomaterial characterization (paragraph 1.3.1), DLVO theory and aggregation kinetics (paragraph 1.3.2) as well as TiO_2 nanoparticle aggregation (paragraph 1.3.3), are briefly discussed.

1.3.1 Nanomaterial characterization

The assessment of photocatalyst properties can be performed by several techniques, some of them developed for the characterization of nanomaterials in past years. The techniques used in the present research work are described in the following.

- **Light scattering**

Light scattering methods are a group of widely used techniques, capable of determining several average properties of nanoparticle suspensions, including aggregate size distribution and fractal dimension [88]. In particular, the measurement of aggregate size is derived from the angular distribution of scattered light intensity, which is monitored simultaneously by an array of detectors located at different angles around the sample. For particles smaller than 15 μm, light scattering is analytically described by the Mie theory, and computations are usually carried out directly by the measurement instrument, provided the refractive index of investigated material. Differently, aggregate size quantification is more complicated in case of fractal aggregates in which primary particles are very small, as in case of TiO_2 nanoparticle suspensions. The density of fractal aggregates can be very low, below 1%, so that the effective aggregate refractive index (RI_a) can only be approximately predicted, starting from the refractive index of primary particles (Ri_p) and their volume fraction (Φ) [89]. Consequently, the application of the Maxwell-Garnett medium theory is required obtaining equation e1.16 to be used for experimental data processing [90]:

$$\frac{m_a^2 - 1}{m_a^2 + 2} = \Phi \frac{m_a^2 - 1}{m_a^2 + 2} \qquad \text{(e1.16)}$$

A relatively recent technique for the measurement of aggregate size is the dynamic light scattering, which is based on the assumption that light scattered from a moving particle has a slightly different frequency with respect to the incident light. Experimental data processing involves the determination of the autocorrelation of scattered light intensity, so that the diffusion coefficient of nanoparticles and the effective nanoparticle size are derived [88].

Concerning the fractal dimension of aggregates, many studies reported that there is a region of linear dependence between the logarithm of the scattering light intensity, I(q), and the logarithm of the scattering vector, q, as predicted by the Rayleigh-Gans-Debye (RGD) theory [91]:

$$I(q) \propto q^{-D} \tag{e1.17}$$

As shown in figure 1.2, this dependence is function of aggregate fractal dimension, D, while the linearity region corresponds to the length scale over which the fractal behaviour holds [88].

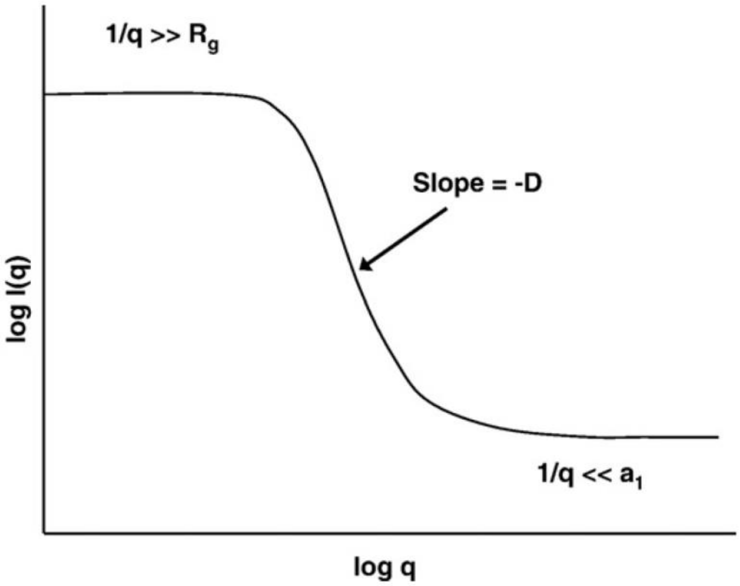

Figure 1.2 Logarithm of the scattering light intensity I(q) vs. logarithm of the scattering vector q for aggregates of particles, based on the RGD approximation. Image adapted from Gregory [88]

Although the application of RGD theory for fractal aggregates raised concern, it seems that it can be effectively applied in case of TiO_2 nanoparticles. In fact, the comparison of experimental results with theoretical predictions and other measurement methods indicated a fairly good agreement.

- **Environmental scanning electron microscope (ESEM)**

Scanning electron microscopy is a technique based on the exposure of a solid sample to a high energy focused beam of electrons to scan its surface. In detail, the response associated to electron interaction with the sample provides information about surface morphology, as size, shape, structure and aggregation. A report concerning the use of scanning electron microscopy for nanomaterial characterization has been compiled by Fukui [92]. A relevant issue with scanning electron microscope consists in complex sample preparation, asking for dehydratation, cryofixation and embedding. On the other hand, sample preparation is facilitated by using environmental scanning electron microscope (ESEM), allowing the analysis of hydrated samples.

- **X-ray diffractometry (XRD)**

X-ray diffraction (XRD) permits the determination of the crystalline structure and the chemical composition of the investigated material. It is a non-destructive technique based on the principle that every crystalline solid determines a unique characteristic X-ray pattern. In particular, the sample is irradiated by X-rays which display a peculiar scattering because of the interaction with the atomic structures. It has been effectively used for the characterization of bulk, nanometric and thin-film materials, providing information for the assessment of the crystalline phase content and changes in phase structure of the samples, as discussed by Jenkins and Snyder [93].

1.3.2 DLVO theory and aggregation kinetics

The stability of nanoparticles in water, whose behaviour is similar to colloidal particles, is essentially governed by solution pH and ionic strength, in agreement with the theory developed by Derjaguin, Landau, Verwey and Overbeek, also known as DLVO theory [47]. DLVO theory describes the aggregation of particles dispersed in water as a function of the attractive and repulsive forces between particles. In particular, aggregation occurs when particles are destabilized and collide with other particles, depending on binary collisions and, hence, according to a second-order rate.
A diagram qualitatively explaining DLVO theory is shown in figure 1.3, reporting the potential energy as a function of the distance between particles, modelled as flat plates with similar charge, in which κ^{-1} is the thickness of electrical double-layer surrounding the nanoparticles [47].

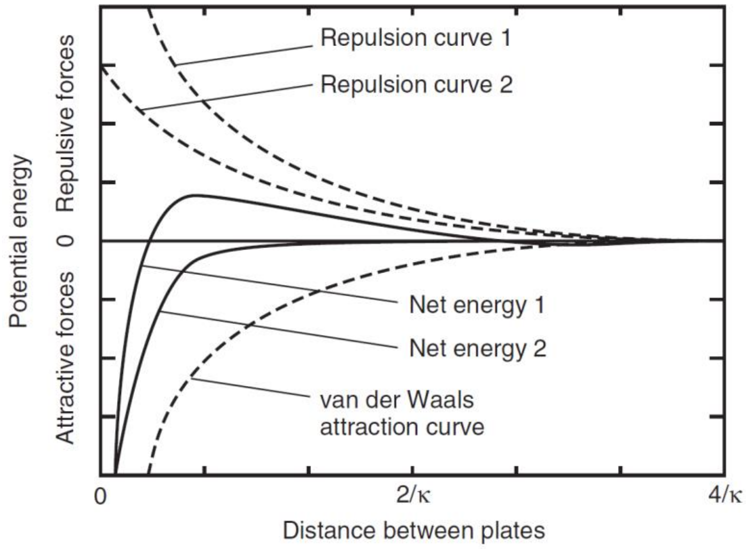

Figure 1.3 Qualitative representation of DLVO theory: potential energy as a function of the distance between plates. κ^{-1} is the thickness of electrical double-layer surrounding the particles. Adapted from [47].

In figure 1.3 two cases are illustrated, differing in the extent of repulsion between nanoparticles, that is determined by electrostatic forces. In case 1, repulsion is more intense and affects zones far away from nanoparticle surface while, in case 2, repulsion is significantly reduced. As attraction between nanoparticles is due to van der Waals force, the net energy is given by the difference between repulsive and attractive forces. In case 1, the attractive forces are prevailing in close vicinity and far away from nanoparticle surface, so that nanoparticles tend to repel and are stable in water. On the other hand, in case 2, attractive forces prevail over repulsive ones irrespectively of distance between nanoparticles, thus promoting the approach and aggregation of nanoparticles.

A damping in repulsive forces is determined when the electrical double layer is compressed, due to the partial neutralization of the surface charge. This can be achieved increasing both the ionic strength of the solution and the charge of counter-ions in solution. The minimum concentration of counter-ions resulting in a destabilization in nanoparticle suspensions is defined as critical coagulation concentration (CCC) and it depends on the type of ions that are dissolved in water. According to the Schultz-Hardy empirical rule, CCC is inversely proportional to the sixth power of the counter-ion charge, so that that the higher is the valence, the lower is the salt concentration necessary for nanoparticle destabilization.

The collision between nanoparticles may occur through two main mechanisms, namely Brownian diffusion and fluid motion, in turn leading to perikinetic or orthokinetic aggregation, respectively. Brownian motion, which is a random and disoriented motion of particles with diameter smaller than 1 μm, is particularly important in favouring aggregation. Aggregation rate depends on the collision frequency and the collision efficiency factor, determined by the degree of particle destabilization. Two behaviours have been observed for the two different mechanisms, as reported in figure 1.4: the total nanoparticle concentration decreases exponentially with time in case of orthokinetic aggregation, while the phenomenon is linear over time for perikinetic aggregation. Clearly, Brownian diffusion, unlike fluid motion, always occurs in any nanoparticle systems and in case both mechanisms are active these have to be treated as approximately additive [88].

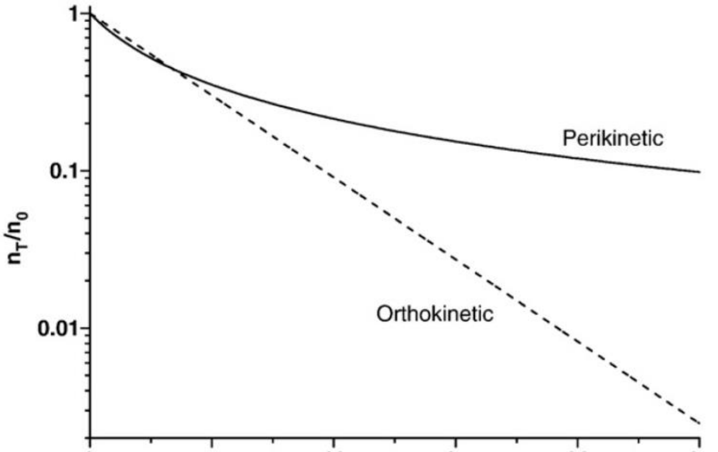

Figure 1.4 Relative decrease in total particle concentration for perikinetic and orthokinetic aggregation. Adapted from Gregory [88].

Aggregation mechanism affects fractal dimension, which usually varies from 1.7 to 2.5. When diffusion-limited (perikinetic) aggregates are forming, fractal dimension tends to the lower limit, whereas orthokinetic aggregation results in the opposite situation. Therefore, perikinetic aggregation determines the formation of loose aggregates, while aggregates are compact in case of orthokinetic mechanism [88].

1.3.3 TiO_2 nanoparticle aggregation

Aggregation involving TiO_2 nanoparticles does not differ from the mechanisms already described in paragraph 1.3.2. As for reactivity, discussed in paragraph 1.2, only the relevant parameters for the PhD thesis are argued in the following.

First, solution pH is fundamental for the stability of TiO_2 suspensions: the farther its value is from PZC, the more stable TiO_2 nanoparticles are and the smaller TiO_2 aggregates form. As a matter of fact, the electrostatic repulsion between two TiO_2 nanoparticles decreases concurrently with the difference between pH and PZC and, thus, with the surface charge of TiO_2 nanoparticles [94].

Then, accordingly to what reported in paragraph 1.3.2, an increase in ionic strength of the solution in which TiO_2 nanoparticles are suspended involves a lowering of nanoparticle electrostatic repulsion and, hence, favours the predominance of attractive forces. Moreover, it was demonstrated that the higher the ionic strength and the valence of the ions are, the greater the extent of aggregation is for TiO_2 nanoparticles, both as aggregate size and aggregation rate [95].

In the following the three most relevant and recent published research works on TiO_2 nanoparticle aggregation are discussed in order to highlight the influence of pH and ionic strength.

French et al. [96] prepared a 42 mg/L solution of TiO_2 nanoparticles synthetized via sol-gel method (PZC=6.8), having composition 63.3% anatase and 36.7% brookite. Experimental results are reported in figure 1.5. When sodium chloride (0.0045 M) was dosed at pH 4.5, TiO_2 aggregates were stable and measured 50-60 nm (figure 1.5a). TiO_2 aggregate size increased as sodium chloride concentration was increased as well as the dispersion of size distribution. For an ionic strength equal to 0.0165 M the size of TiO_2 aggregates ranged between 20 and 1000 nm, having an average value of about 150 nm (figure 1.5b). In case of pH higher than PZC, irrespectively that sodium chloride or calcium chloride were added, TiO_2 aggregates reached larger dimensions, in the scale of microns (figure 1.5c and 1.5d). A comparison between ionic species, sodium chloride and calcium chloride, at constant pH (4.8) showed a similar aggregation extent, although ionic strength was higher in the former case (figure 1.5b and 1.5d). This is due to the effect of valence in aggregation promotion. In figure 1.5d pH is lower than PZC, so that TiO_2 aggregates have positive charge. Therefore, it is unlikely that calcium ions could promote aggregation by acting as electrostatic bridges.

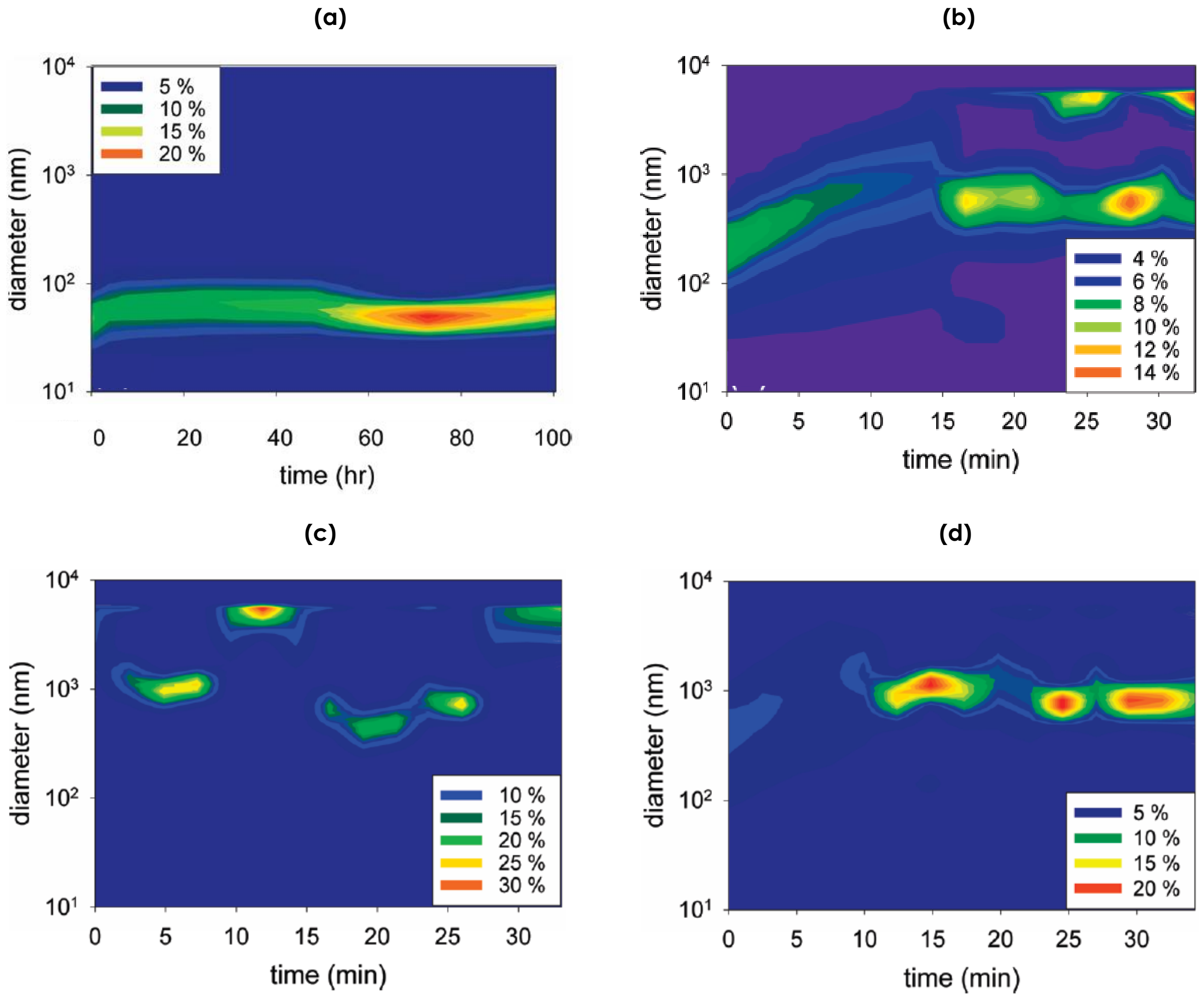

Figure 1.5 Aggregation over time of TiO_2 nanoparticles: (a) pH 4.5, ionic strength 0.0045 adjusted with NaCl, (b) pH 4.5, ionic strength 0.0165 adjusted with NaCl, (c) pH 8.2, ionic strength 0.0099 adjusted with NaCl, (d) pH 4.8, ionic strength 0.0128 adjusted with $CaCl_2$. Adapted from French et al. [96].

Shih et al. [97] focused their interest on aggregation kinetics. In this case a widespread commercial type of TiO_2 nanoparticles, produced by Sigma-Aldrich, were used, having PZC equal to 5.9. TiO_2 suspensions were prepared at pH around 7-7.5, so that TiO_2 nanoparticles were negatively charged. Various amounts of sodium, calcium and potassium chloride were added to TiO_2 suspensions, which were preliminary sonicated, obtaining TiO_2 nanoparticles having an average size of 200 nm. As for aggregation kinetics, a first-order pseudo-model was hypothesized, so that the aggregation constants for each combination of electrolyte and ionic strength were estimated. Then, the aggregation efficiency (α) was determined by normalizing the aggregation constants with respect to the value of the highest aggregation constant (k_{fast}), which represents the fastest aggregation kinetics:

$$\alpha = \frac{k}{k_{fast}} \tag{e1.18}$$

The aggregation efficiency was then plotted against salt concentration, as reported in figure 1.6, showing the existence of a discontinuity, corresponding to CCC, which represents the passage from an aggregation kinetic regime depending on salt concentration (α<1) to another which is independent.

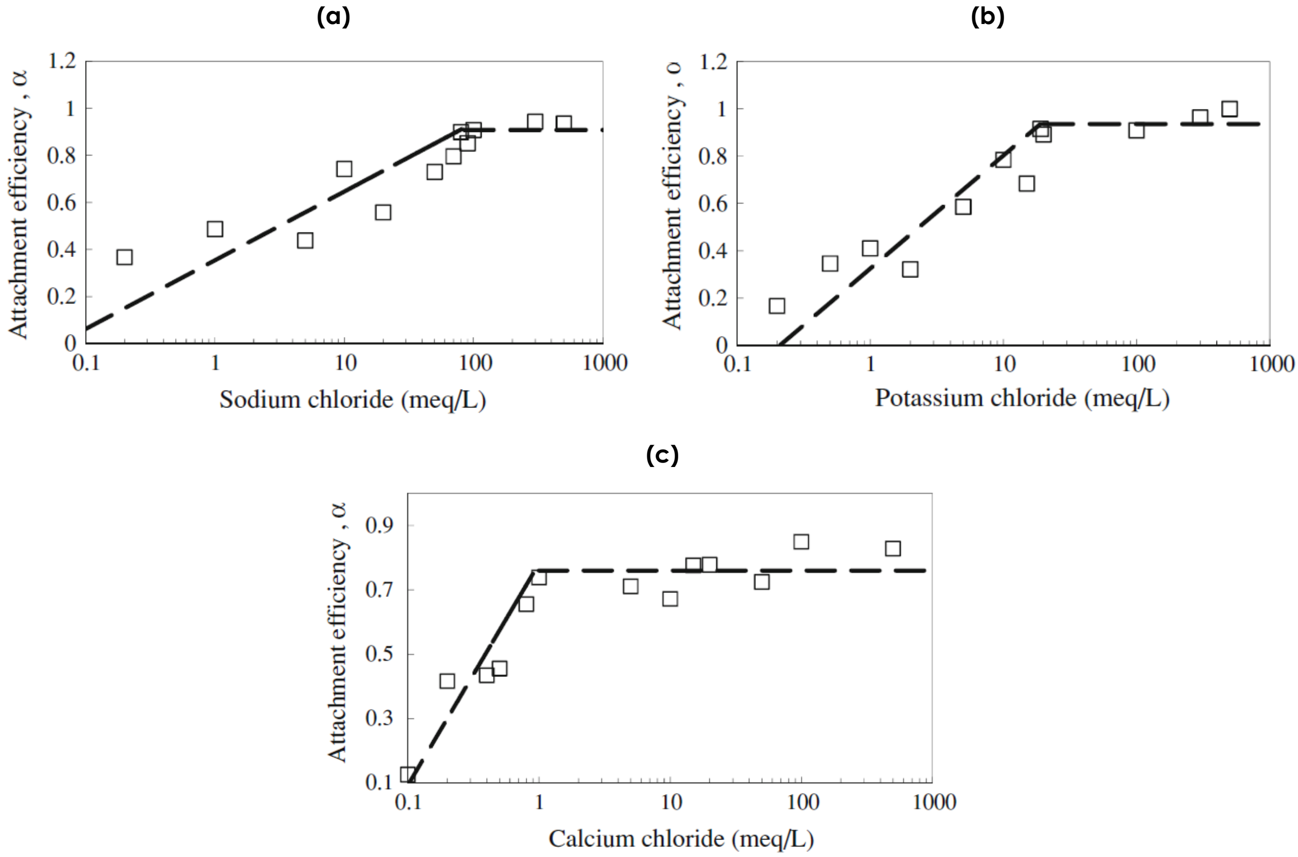

Figure 1.6 Attachment efficiencies of TiO_2 nanoparticles aggregates at different salt concentrations: (a) sodium chloride, (b) potassium chloride and (c) calcium chloride. Adapted from Shih et al. [97]

The estimated value of CCC were 80, 19 and 1 meq/L respectively for sodium, potassium and calcium. The growth of aggregate size over time, as a function of the added cation and the ionic strength, is shown in figure 1.7. An increase in ionic strength corresponded to an increase in aggregation rate, more consistently for calcium. In particular, when ion concentration was equal to CCC a peak in aggregation was observed.

Experimental results reported by Shih et al. [97] indicated that aggregation kinetics were slower than in [96]. In fact, the same aggregation extent under similar dosage of sodium chloride was obtained after 50 and 15 minutes in the two cases. This was probably due to the fact that TiO_2 nanoparticles were negatively charged in the former case and positively in the latter. Therefore, the faster aggregation in [96] was determined by the electrostatic influence exerted by cations.

The stability of TiO_2 nanoparticles positively charged in the presence of inorganic anions was studied by Shih et al. [98]. Sodium chloride and sodium sulfate were added at various concentrations. In the absence of electrolytes TiO_2 nanoparticle aggregates were stable in water.

Aggregation occurred in presence of both anions, but for higher chloride concentrations with respect to sulfate, in agreement with the greater influence of bivalent ions in promoting aggregation. Furthermore, acting chloride and sulfate as counter-ions for positively charged TiO_2 nanoparticles, the neutralization of superficial charge was observed simultaneously.

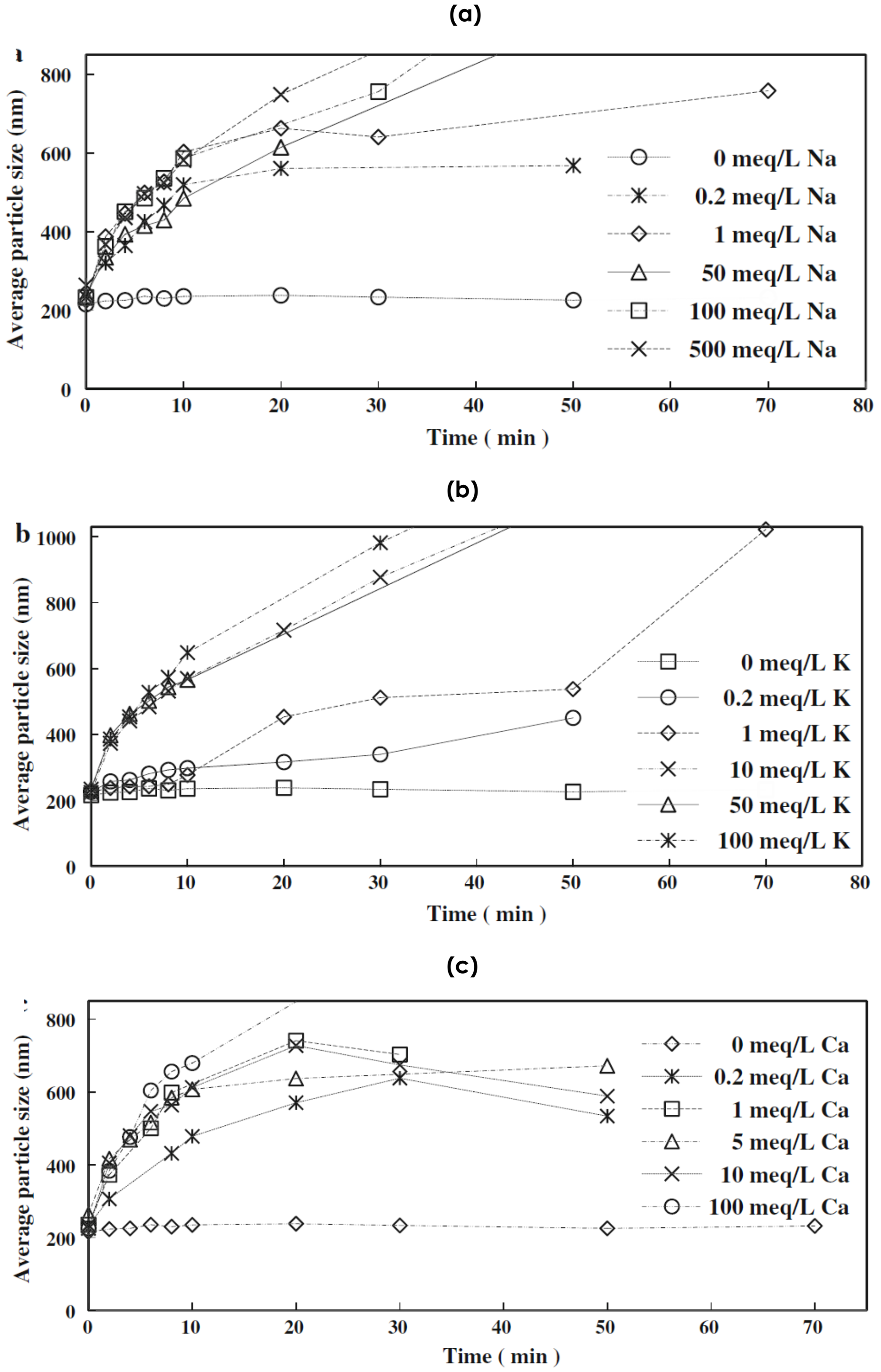

Figure 1.7 Aggregation over time of TiO_2 nanoparticles at different concentrations of salts: (a) sodium chloride, (b) potassium chloride, (c) calcium chloride. Adapted from Shih et al. [97].

1.4 COMPUTATIONAL FLUID DYNAMICS

Computational fluid dynamics (CFD) is an emerging field of fluid mechanics involving the use of computational methods and numerical algorithms for the analysis of chemical-physical phenomena taking place in real systems, such as fluid flow, heat and radiation transfer as well as chemical reactions. CFD codes have been greatly developed in recent years and applied to a wide range of areas, including also water and wastewater treatment [99]. In the following these techniques are briefly introduced, then the recent advances in their application to water and wastewater treatment as well as to TiO_2 photocatalysis are synthetically discussed.

1.4.1 CFD fundamentals

CFD codes are modelling tools capable of solving the governing equations within a defined geometric domain and of producing an accurate and reliable simulation of the behaviour of a multi-physics system. Several codes have been produced so far, including a number of widespread multi-purpose software such as ANSYS CFX, ANSYS Fluent, COMSOL, PHOENICS and STAR-CD [100]. Despite the important peculiar features, all codes are based on a same structure, characterized by three common elements: the pre-processor, the solver and the post-processor [100].

The pre-processor consists in the problem definition, so as it could be interpreted by the solver, comprising:

- the creation of the system geometry, also called computational domain,
- the mesh generation, namely the sub-division of the computational domain into small, non-overlapping, sub-domains, at which centroids, or nodes, governing equations are solved by the code,
- the definition of chemical and physical phenomena to be assessed,
- the specification of the appropriate boundary conditions for problem solving.

In this phase the most delicate issue concerns the mesh generation, since it is basically the key element in determining solution accuracy and computational efforts. In fact, solution accuracy is generally better the larger is the number of meshes, but the number of meshes directly affects the calculation time. It is therefore fundamental to identify the case-specific optimal mesh that could guarantee the grid-independence of results as well as sustainable computational requirements.

As for the solver, it is the numerical algorithm dealing with the governing equation solutions by:

- integrating the governing equations over the computational domain,
- discretising the integral governing equation into a system of algebraic equations,
- solving the algebraic equations by iterative methods till the solution convergence.

The most relevant aspect of this phase is the achievement of a converged solution. Universal criteria do not exist and the evaluation is usually related to the so-called residues, namely variables quantifying the error in prediction, whose extent is however related to the case-specific situation.

Finally, the post-processor is the part of the CFD code deputed to the graphical visualization of results and to the export of simulation outputs.

CFD codes are powerful tools that can support two relevant activities in engineering, i.e. process modelling and optimization. As for the former, the major benefits consist in (i) the integration of different chemical and physical phenomena in a multi-physics framework and in (ii) the description of involved variables at the local scale. Regarding the latter, CFD codes allow performing virtual experiments, avoiding the production of prototypes and, thus, reducing sensibly R&D costs.

Anyway, CFD codes have to be used carefully and in combination with other experimental techniques that could support their effectiveness. As a matter of fact, given the peculiarity of each domain, rarely the results of a CFD simulation can be extended to other cases or can be considered valid without a proper validation step. In detail, validation usually consists in the execution of experimental measurements for comparing real and simulated variables.

1.4.2 CFD for water and wastewater treatment

A relevant interest in CFD codes for water and wastewater treatment has grown over the past 15 years. This is mainly due to the development of software and hardware technologies that allowed the effective modelling of reactors by non-professional CFD users, with accessible computing resources. While the first efforts have been devoted to optimizing hydraulics, CFD codes have subsequently been applied to investigate the physical, chemical and microbiological processes taking place in reactors. However, although CFD codes are currently applied to an increasing number of situations, their use should be evaluated according to the real potential offered by these techniques. For example, CFD codes can be completely useless in the case of well-mixed reactors in which fluid dynamics do not affect the process significantly. On the other hand, since CFD codes are computationally-intensive numerical techniques with respect to other widespread modelling techniques, their application is convenient when modelling outputs are significantly improved with respect to the results obtained by means of established techniques [101].

In the past CFD has been applied to simulate various water treatment processes, such as flocculation [102], sedimentation [103], desalination [104] and disinfection [101]. Among these, most of published research works concern the modelling and optimization of disinfection reactors, since the efficiency of this process is strongly influenced by hydraulics. In particular, three main disinfection processes have been assessed so far, based on chlorine, ozone and UV radiation.

As for chlorine-based disinfection, contact tanks are aimed at ensuring a uniform contact time to the entire flow, so that the reactor design is usually based on chicane contact tanks behaving as similarly as possible to an ideal plug flow reactor [105]. Therefore, the goal of related research works is to identify and to limit non-ideality, as short-circuiting or dead zones, which results in detrimental effects on disinfection efficiency [106]. CFD codes are highly effective in evaluating the hydraulic efficiency of these reactors [107–109], although the combined application with reactions and inactivation kinetics is still a great challenge [101]. Concerning ozone contactors, the aim of providing a uniform contact time to the flow remains, but a different reactor scheme with respect to chlorine-based disinfection is needed, considering the dosage of the disinfectant by gas bubbling . Ozone contactors are usually defined as axial dispersion reactors [47]. The modelling of fluid dynamics of such configuration has been reported, together with the combination with reaction and inactivation kinetics. However, given the complexity of flow conditions, far from ideal, CFD codes represent a valuable tool, especially in case of ozone contactors characterized by an intricate geometry, as reported in several papers [110–112]. In both disinfection types, the most challenging part of CFD simulations is the proper prediction of turbulence in the geometrical domain, whose determination can be performed by various methods. Turbulence is resolved at all scales by direct numerical simulation (DNS), which is a method not always appropriate in engineering applications, given the long simulation times and the huge demand for computational resource. A simpler method is the large eddy simulation (LES), solving only the larger turbulent eddies, thus reducing the accuracy of the simulation but also the computational requirements. Therefore, this method is rarely used when the turbulence flow has to be accurately studied. Commonly turbulence models are based on the Reynolds-averaged Navier-Stokes (RANS) equations: averaged velocity fields are used and the concept of eddy viscosity is introduced, by which the fluctuating turbulent motions are modelled as an averaged viscosity coefficient. Therefore, flow fields are predicted with less accuracy by acceptable efforts [100].

Disinfection performance in UV reactors was largely assessed by CFD techniques, permitting to evaluate the distribution of UV radiation inside the reactor and to predict locally the UV intensity. In addition, particle tracking in CFD codes has been successfully used for determining the UV dose which particles crossing the reactor are subjected to [113,114]. The radiation fields inside the reactor are determined by solving the radiative transfer equation, which is a numerical problem commonly asking for relevant computational resources, especially in case of aqueous matrices whose particulate content is not negligible and, thus, in which it is necessary to account for the occurrence of scattering phenomena [101].

More recently CFD codes have been applied to advanced oxidation processes in a number of published works, *inter alia* [115,116]. The delay in the assessment of these processes by CFD codes is essentially due to the innovative nature of these technologies, whose development significantly increased in recent years. However, CFD codes are particularly useful for the modelling and optimization, since advanced oxidation technologies are usually based on closed-vessel reactors, whose fluid dynamic behaviour is more complex. Besides, UV-based advanced oxidation processes ask for further optimization for becoming sustainable with respect to other established technologies. In detail, CFD codes are particularly interesting because they allow determining the local concentration of reactive species inside reactor volume. Up to date only for H_2O_2/UV a consistent research work has been performed, including [117–119], in which the degradation of model pollutants has been described by integrating optics, fluid dynamics and chemical reactions.

1.4.3 CFD for TiO_2 photocatalysis

Although some research works have been published [120–123], CFD for TiO_2 photocatalysis is still a poorly studied topic. In particular, a major challenge with respect to other advance oxidation processes is represented by the heterogeneous phase of the photocatalyst, mostly resulting in great difficulties in the description of optical phenomena. The modelling of TiO_2 photocatalysis requires the integration of optics, fluid dynamics and chemical reactions, as detailed in the following.

- **Optics**

Radiation fields are determinant for reaction kinetics and photocatalytic reactor performance. As introduced, radiation fields can be described by solving the radiative transfer equation [124]:

$$\frac{dI_\lambda}{ds} = -\kappa_\lambda I_\lambda(s,\Omega) - \sigma_\lambda I_\lambda(s,\Omega) + \frac{1}{4\pi}\sigma_\lambda \int_0^{4\pi} p(\Omega' \rightarrow \Omega) I_\lambda(s,\Omega') I_\lambda(s,\Omega') d\Omega' \qquad \text{(e1.19)}$$

in which I_λ, κ_λ, σ_λ are the radiation intensity, the absorption and the scattering coefficients, respectively. The transmission of the radiation intensity at a certain wavelength (I_λ) in a spherical reference system (spatial coordinates s and Ω) is determined by optical phenomena: the first term on the right hand side describes the absorbed radiation, the second term the out-scattering of radiation and the third the gain of energy due to the in-scattering of radiation.

There are basically two main scenarios in radiation modelling, due to the form in which TiO_2 photocatalyst is used. In case of TiO_2 nanoparticle suspensions, the radiation absorption is volumetric and the local volumetric rate of photon absorption (LVRPA) must be evaluated [125]. The reaction rate is proportional to LVRPA, which in turn is function of lamp power, concentration of absorbing species and photocatalytic reactor geometry. In detail, LVRPA can be estimated as:

$$LVRPA = \int_\lambda I_\lambda \kappa_\lambda \, d\lambda \qquad \text{(e1.20)}$$

Moreover, in case of TiO_2 nanoparticle suspensions the term referring to radiation scattering cannot be neglected and it represents the major challenge for the solution of radiation transfer equation. In addition to the computational effort, the determination of optical properties of TiO_2 suspensions is hard in the presence of scattering, since no direct measurement techniques can be used [78].

In case of immobilized TiO_2, the radiation transfer simplifies, since no scattering phenomena have to be considered, and it reduces to the Beer-Lambert law [46]. Nevertheless, in this case the major issue is given by the estimation of radiation effectively absorbed by TiO_2 surface, which is reflective and semi-transparent [126]. In fact, immobilized systems are normally constituted by a thin layer of TiO_2 deposited or synthetized on a solid support. Therefore, energy balance should consider three terms: the radiation absorbed by the support, the radiation absorbed by the photocatalyst and the reflected radiation. It can be assumed that the ratio between incident and absorbed radiation is the same for a given photocatalyst, whatever the photoreactor [127].

Concerning the solution of radiative transfer equation, the discrete ordinate (DO) model is a numerical algorithm integrated in various CFD codes that transforms the integro-differential form of the radiative transfer equation into a system of algebraic equations [128]. By means of DO model radiative transfer equation has been successfully solved in a variety of reactor designs: slurry [120,122,129], flat plate [126], packed bed [130] and immobilized annular [131] reactors.

- **Fluid dynamics**

The determination of fluid dynamics behaviour is essential in photocatalytic reactors. CFD simulation is especially challenging in case of multi-phase flows, involving the combination of gas and liquid phases. In past research works the solution of Navier-Stokes equation in an Eulerian framework was generally effective for describing the fluid dynamics in a single-phase system. In case of multi-phase flows two different approaches have been tested, namely the Eulerian-Eulerian (E-E) and the Eulerian-Lagrangian (E-L) models, being the former usually preferred because of its ability to simulate large scale reactors with lower computational requirements. In detail, in the E-E model the mass and momentum conservation equations are solved for each phase, being considered as interpenetrating continuous media, while the E-L model is an hybrid approximation, in which the dispersed phase particles are simulated by solving an equation of motion for each particle and the continuous phase is solved in a conventional Eulerian framework [46].

As an example, some previous research works assessed the local concentration of TiO_2 nanoparticles in slurry reactors, since recirculation phenomena or dead-zones can determine significant gradients [120,122]. In figure 1.8 an image adapted from Pareek et al. [120] is reported, showing the modelling of a multi-phase annular slurry reactor by the Eulerian-Eulerian formulation. The presence of non-uniformity in TiO_2 concentration due to the fluid dynamic is highlighted.

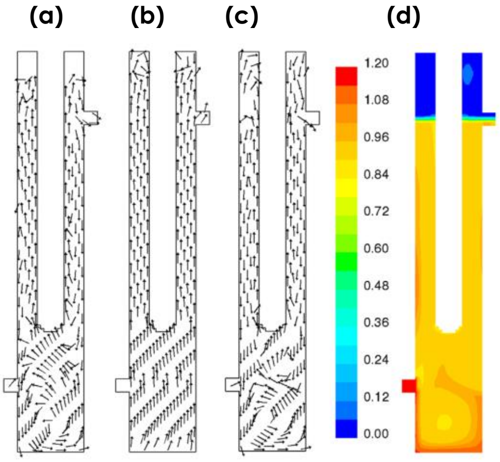

Figure 1.8 Multi-phase modelling of an annular slurry reactor. In the image, adapted from Pareek et al. [120], CFD simulation results are shown: (a) liquid velocity vectors, (b) gas velocity vectors, (c) TiO_2 photocatalyst velocity vector, (d) TiO_2 photocatalyst concentration.

Furthermore, fluid dynamics are fundamental in determining the concentration of compounds in the reactor volume. As a matter of fact, the turbulent diffusion, namely the transport of mass due to random and chaotic time-dependent motions determined by the turbulence, is several orders of magnitude larger than the molecular diffusion. CFD codes are useful tools for assessing the turbulent diffusion in the reactor volume and for describing the mass transport of compounds [100].

- **Chemical reactions**

Optics and fluid dynamics equations have to be solved in advance before dealing with chemical reactions. In most of cases both physics are solved at the time-averaged steady state, having precedence the fluid dynamics in case the fluid flow is determinant for the TiO_2 concentration distribution and, thus, for the radiation transfer, as in multi-phase flows [46]. Chemical reactions are introduced in CFD simulations as source terms by defining the rate of species transformation in each grid element as a function of the local values of the parameters affecting the reaction [100]. In figure 1.9 a schematic flow chart for the CFD simulation of a photocatalytic reactor is reported.

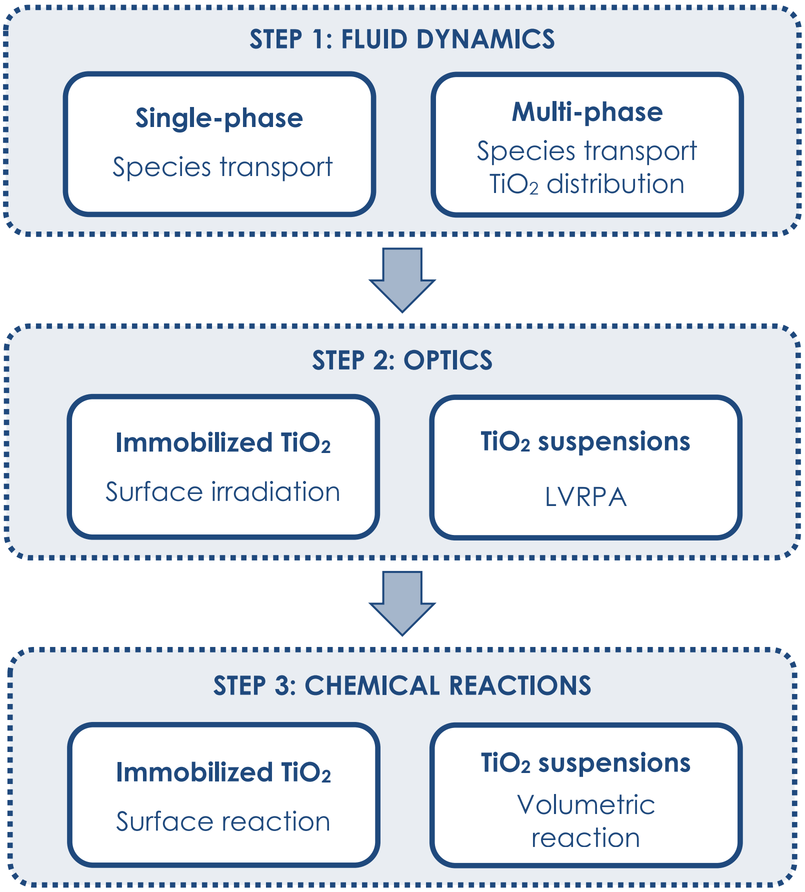

Figure 1.9 Flow chart for the CFD simulation of a photocatalytic reactor, adapted from Boyjoo et al. [46]. Two distinct solution paths are indicated for immobilized (left side) and slurry systems (right side).

Up to now there are two relevant studies in which TiO_2 photocatalysis has been modelled by CFD simulation accounting for optics, fluid dynamics and chemical reaction.

As for TiO_2 nanoparticle suspension, the photocatalytic degradation of dichloroacetic acid (DCA) in an aerated tank photoreactor was simulated using ANSYS Fluent 6.2 by Trujillo et al. [122]. Multi-phase fluid dynamics were described by an Eulerian-Eulerian model, while the radiation fields were assessed by the DO model. The optical properties of TiO_2 suspensions were taken from literature [78] and adapted so as to consider the presence of gas bubbles, whose effect is basically (i) to reduce the absorption coefficient proportionally to the gas hold-up, and (ii) to enhance radiation scattering depending on the characteristics and relative abundance of bubbles. The scattering phase function was assumed as isotropic. The kinetic model was developed according to a previous study [132], based on the following reaction:

$$CHCl_2-COOH+O_2\overset{h\nu}{\rightarrow}2CO_2+2HCl \qquad \text{(e1.21)}$$

The reaction constants for DCA degradation were estimated by fitting a calibration dataset and they were validated in different conditions of TiO_2 and DCA concentration as well as of light intensity, although the results were case-specific with respect to reactor design and lamp type.

Concerning immobilized TiO_2, the photocatalytic degradation of benzoic acid (BA) in two annular reactors was assessed using ANSYS Fluent 6.3 by Duran et al. [131]. Reactor inner wall was coated by composite sol-gel TiO_2. Radiation transfer in reactor volume was simulated by the DO model. A pseudo-first order kinetic model was observed to be effective in experimental data description, while model parameter was estimated by fitting calibration dataset in order to account for the external mass transfer of BA, which was highlighted as the limiting factor for the process in a previous research [133]. The degradation of BA as a function of BA concentration and fluid dynamic conditions was simulated by various turbulence models, achieving a good prediction of experimental data. The integrated model provided a detailed description of the local photoreactor performance, providing valuable indications for reactor design improvement. The main limitation of this study consisted in the scarce insight in process mechanistic phenomena.

In conclusion, the high effectiveness of CFD codes in modelling photocatalytic processes have been highlighted so far. On the other hand, although the cited research works represent a first fundamental step in the assessment of TiO_2 photocatalysis by CFD techniques, further research work should be addressed to two main directions: (i) the mathematical description of mechanistic phenomena allowing for a generalizable modelling approach and (ii) the application of CFD codes to reactor design optimization and scale-up.

1.5 REFERENCES

[1] P. Pichat, Photocatalysis and water purification: from fundamentals to recent applications, Wiley-VCH, 2013.

[2] C. Renz, Light reactions of the oxides of titanium, cerium and earth acids, Helv. Chem. Acta. 4 (1921) 961–968.

[3] A. Fujishima, K. Honda, Electrochemical photolysis of water at a semiconductor electrode, Nature 238 (1972) 37–38.

[4] A. Fujishima, X. Zhang, D. Tryk, TiO_2 photocatalysis and related surface phenomena, Surf. Sci. Rep. 63 (2008) 515–582.

[5] O. Carp, Photoinduced reactivity of titanium dioxide, Prog. Solid State Chem. 32 (2004) 33–177.

[6] C.O. Hendren, X. Mesnard, J. Dröge, M.R. Wiesner, Estimating production data for five engineered nanomaterials as a basis for exposure assessment., Environ. Sci. Technol. 45 (2011) 2562–2569.

[7] A. Weir, P. Westerhoff, L. Fabricius, K. Hristovski, N. von Goetz, Titanium dioxide nanoparticles in food and personal care products., Environ. Sci. Technol. 46 (2012) 2242–50.

[8] L. Windler, C. Lorenz, N. von Goetz, K. Hungerbühler, M. Amberg, M. Heuberger, et al., Release of titanium dioxide from textiles during washing., Environ. Sci. Technol. 46 (2012) 8181–8188.

[9] M.N. Chong, B. Jin, C.W.K. Chow, C. Saint, Recent developments in photocatalytic water treatment technology: a review, Water Res. 44 (2010) 2997–3027.

[10] U.I. Gaya, A.H. Abdullah, Heterogeneous photocatalytic degradation of organic contaminants over titanium dioxide: a review of fundamentals, progress and problems, J. Photochem. Photobiol. C Photochem. Rev. 9 (2008) 1–12.

[11] H. Choi, S.R. Al-Abed, D.D. Dionysiou, E. Stathatos, P. Lianos, TiO_2-based advanced oxidation nanotechnologies for water purification and reuse, Sustain. Sci. Eng. 2 (2010) 229–254.

[12] A. Furube, T. Asahi, H. Masuhara, H. Yamashita, M. Anpo, Direct observation of a picosecond charge separation process in photoexcited platinum-loaded TiO_2 particles by femtosecond diffuse reflectance spectroscopy, Chem. Phys. Lett. 336 (2001) 424–430.

[13] T. Hirakawa, Y. Nosaka, Properties of $O_2^{\bullet-}$ and $OH^{\bullet}$ formed in TiO_2 aqueous suspensions by photocatalytic reaction and the influence of H_2O_2 and some ions, Langmuir (2002) 3247–3254.

[14] T.A. Egerton, P.A. Christensen, Photoelectrocatalysis processes, in: S. Parsons (Ed.), Adv. Oxid. Process. Water Wastewater Treat., IWA Publishing, London, 2004, pp. 167–184.

[15] Y. Zhang, X. Xiong, Y. Han, X. Zhang, F. Shen, S. Deng, et al., Photoelectrocatalytic degradation of recalcitrant organic pollutants using TiO_2 film electrodes: an overview, Chemosphere 88 (2012) 145–154.

[16] K. Ishibashi, A. Fujishima, T. Watanabe, K. Hashimoto, Quantum yields of active oxidative species formed on TiO_2 photocatalyst, J. Photochem. Photobiol. A Chem. 134 (2000) 139–142.

[17] H. De Lasa, B. Serrano, M. Salaices, Photocatalytic reaction engineering, Springer, 2005.

[18] M.I. Litter, Advances in Chemical Engineering - Photocatalytic Technologies, Elsevier, 2009.

[19] K. Nagaveni, G. Sivalingam, M. Hegde, G. Madras, Solar photocatalytic degradation of dyes: high activity of combustion synthesized nano TiO_2, Appl. Catal. B Environ. 48 (2004) 83–93.

[20] N. Serpone, G. Sauvé, R. Koch, H. Tahiri, P. Pichat, P. Piccinini, et al., Standardization protocol of process efficiencies and activation parameters in heterogeneous photocatalysis: relative photonic efficiencies ζr, J. Photochem. Photobiol. A Chem. 94 (1996) 191–203.

[21] D. Jassby, J.F. Budarz, M. Wiesner, Impact of aggregate size and structure on the photocatalytic properties of TiO_2 and ZnO nanoparticles, Environ. Sci. Technol. (2012) 1–10.

[22] M.R. Wiesner, G. V. Lowry, P. Alvarez, D. Dionysiou, P. Biswas, Assessing the risks of manufactured nanomaterials, Environ. Sci. Technol. 40 (2006) 4336–45.

[23] N.T. Loux, Y.S. Su, S.M. Hassan, Issues in assessing environmental exposures to manufactured nanomaterials, Int. J. Environ. Res. Public Health 8 (2011) 3562–3578.

[24] T.E. Doll, F.H. Frimmel, Cross-flow microfiltration with periodical back-washing for photocatalytic degradation of pharmaceutical and diagnostic residues-evaluation of the long-term stability of the photocatalytic activity of TiO_2, Water Res. 39 (2005) 847–54.

[25] P. Fernández-Ibáñez, J. Blanco, S. Malato, F.J. d. Las Nieves, Application of the colloidal stability of TiO_2 particles for recovery and reuse in solar photocatalysis, Water Res. 37 (2003) 3180–3188.

[26] S. Malato, P. Fernández-Ibáñez, M.I. Maldonado, J. Blanco, W. Gernjak, Decontamination and disinfection of water by solar photocatalysis: recent overview and trends, Catal. Today. 147 (2009) 1–59.

[27] R.L. Pozzo, M.A. Baltanás, A.E. Cassano, Supported titanium oxide as photocatalyst in water decontamination: state of the art, Catal. Today. 39 (1997) 219–231.

[28] T. Ochiai, A. Fujishima, Photoelectrochemical properties of TiO_2 photocatalyst and its applications for environmental purification, J. Photochem. Photobiol. C Photochem. Rev. 13 (2012) 247–262.

[29] A. Fujishima, Hydrogen production under sunlight with an electrochemical photocell, J. Electrochem. Soc. 122 (1975) 1487.

[30] N. Negishi, K. Takeuchi, T. Ibusuki, The surface structure of titanium dioxide thin film photocatalyst, Appl. Surf. Sci. 121-122 (1997) 417–420.

[31] A. Fernández, G. Lassaletta, V.M. Jiménez, A. Justo, A.R. González-Elipe, J.-M. Herrmann, et al., Preparation and characterization of TiO_2 photocatalysts supported on various rigid supports (glass, quartz and stainless steel). Comparative studies of photocatalytic activity in water purification, Appl. Catal. B Environ. 7 (1995) 49–63.

[32] H. Wang, T. Wang, P. Xu, Effects of substrate temperature on the microstructure and photocatalytic reactivity of TiO_2 films, J. Mater. Sci. Mater. Electron. 9 (1998) 327–330.

[33] A. Goossens, E.-L. Maloney, J. Schoonman, Gas-phase synthesis of nanostructured anatase TiO_2, Chem. Vap. Depos. 4 (1998) 109–114.

[34] K. Kobayakawa, C. Sato, Y. Sato, A. Fujishima, Continuous-flow photoreactor packed with titanium dioxide immobilized on large silica gel beads to decompose oxalic acid in excess water, J. Photochem. Photobiol. A Chem. 118 (1998) 65–69.

[35] M. Kitano, K.Funatsu, M. Matsuoka, M. Ueshima, M. Anpo, Preparation of nitrogen-substituted TiO_2 thin film photocatalysts by the radio frequency magnetron sputtering deposition method and their photocatalytic reactivity under visible light irradiation, J. Phys. Chem. B 110 (2006) 25266–25272.

[36] K. Takami, T. Adachi, A. Nakajima, K. Hashimoto, T. Watanabe, Inorganic-organic fuctionally-graded films : the role of intermediate layers between TiO_2 coatings and polymer substrates, Surf. Coat. Int. B 85 (2002) 155-158.

[37] Y. Gao, Y. Masuda, Z. Peng, T. Yonezawa, K. Koumoto, Room temperature deposition of a TiO_2 thin film from aqueous peroxotitanate solution, J. Mater. Chem. 13 (2003) 608–613.

[38] N. Berger-Keller, G. Bertrand, C. Filiatre, C. Meunier, C. Coddet, Microstructure of plasma-sprayed titania coatings deposited from spray-dried powder, Surf. Coatings Technol. 168 (2003) 281–290.

[39] M.C. Yang, T.-S. Yang, M.-S. Wong, Nitrogen-doped titanium oxide films as visible light photocatalyst by vapor deposition, Thin Solid Films. 469-470 (2004) 1–5.

[40] T. Miyata, S. Tsukada, T. Minami, Preparation of anatase TiO_2 thin films by vacuum arc plasma evaporation, Thin Solid Films. 496 (2006) 136–140.

[41] G.K. Mor, O.K. Varghese, M. Paulose, K. Shankar, C.A. Grimes, A review on highly ordered, vertically oriented TiO_2 nanotube arrays: fabrication, material properties, and solar energy applications, Sol. Energy Mater. Sol. Cells. 90 (2006) 2011–2075.

[42] C. Turchi, Photocatalytic degradation of organic water contaminants: mechanisms involving hydroxyl radical attack, J. Catal. 122 (1990) 178–192.

[43] J. Herrmann, Heterogeneous photocatalysis: fundamentals and applications to the removal of various types of aqueous pollutants, Catal. Today. 53 (1999) 115–129.

[44] P.C. Maness, S. Smolinski, D.M. Blake, Z. Huang, E.J. Wolfrum, W.A. Jacoby, Bactericidal activity of photocatalytic TiO_2 reaction: Toward an understanding of its killing mechanism, Appl. Environ. Microbiol. 65 (1999) 4094–4098.

[45] I. Grčić, G. Li Puma, Photocatalytic degradation of water contaminants in multiple photoreactors and evaluation of reaction kinetic constants independent of photon absorption, irradiance, reactor geometry, and hydrodynamics, Environ. Sci. Technol. 47 (2013) 13702–13711.

[46] Y. Boyjoo, M. Ang, V. Pareek, Some aspects of photocatalytic reactor modeling using computational fluid dynamics, Chem. Eng. Sci. 101 (2013) 764–784.

[47] J.C. Crittenden, R.R. Trussell, D.W. Hand, K.J. Howe, G. Tchobanoglus, MWH's water treatment: principles and design, Wiley, 2012.

[48] S. Parsons, M. Williams, Introduction, in: S. Parsons (Ed.), Adv. Oxid. Process. Water Wastewater Treat., IWA Publishing, London, 2004, pp. 167–184.

[49] C.B. Mendive, T. Bredow, M.A. Blesa, D.W. Bahnemann, ATR-FTIR measurements and quantum chemical calculations concerning the adsorption and photoreaction of oxalic acid on TiO_2, Phys. Chem. Chem. Phys. 8 (2006) 3232–3247.

[50] K. Naito, T. Tachikawa, M. Fujitsuka, T. Majima, Real-time single-molecule imaging of the spatial and temporal distribution of reactive oxygen species with fluorescent probes: applications to TiO_2 photocatalysts, J. Phys. Chem. C. 112 (2008) 1048–1059.

[51] G. Bartosz, Use of spectroscopic probes for detection of reactive oxygen species, Clin. Chim. Acta. 368 (2006) 53–76.

[52] N. Soh, Recent advances in fluorescent probes for the detection of reactive oxygen species, Anal. Bioanal. Chem. 386 (2006) 532–43.

[53] S.H. Yoon, J.H. Lee, Oxidation mechanism of As(III) in the UV/TiO_2 system: evidence for a direct hole oxidation mechanism, Environ. Sci. Technol. 39 (2005) 9695–9701.

[54] Y. Nosaka, S. Komori, K. Yawata, T. Hirakawa, A.Y. Nosaka, Photocatalytic $OH^•$ radical formation in TiO_2 aqueous suspension studied by several detection methods, Phys. Chem. Chem. Phys. 5 (2003) 4731.

[55] T. Berger, M. Sterrer, O. Diwald, E. Knözinger, D. Panayotov, T.L. Thompson, et al., Light-induced charge separation in anatase TiO_2 particles., J. Phys. Chem. B. 109 (2005) 6061–6068.

[56] K.I. Ishibashi, A. Fujishima, T. Watanabe, K. Hashimoto, Detection of active oxidative species in TiO_2 photocatalysis using the fluorescence technique, Electrochem. Commun. 2 (2000) 207–210.

[57] L. Davydov, P.G. Smirniotis, Quantification of the primary processes in aqueous heterogeneous photocatalysis using single-stage oxidation reactions, J. Catal. 191 (2000) 105–115.

[58] B. Kraeutler, C.D. Jaeger, A.J. Bard, Direct observation of radical intermediates in the photo-Kolbe reaction - heterogeneous photocatalytic radical formation by electron spin resonance, J. Am. Chem. Soc. 100 (1978) 4903–4905.

[59] H. Yoneyama, Y. Takao, H. Tamura, A.J. Bard, Factors influencing product distribution in photocatalytic decomposition of aqueous acetic acid on platinized TiO_2, J. Phys. Chem. 87 (1983) 1417–1422.

[60] G. Merenyi, J. Lind, T.E. Eriksen, The equilibrium reaction of the luminol radical with oxygen and the one-electron-reduction potential of 5-aminophthalazine-1,4-dione, J. Phys. Chem. 88 (1984) 2320–2323.

[61] T. Daimon, Y. Nosaka, Formation and behavior of singlet molecular oxygen in TiO_2 photocatalysis studied by detection of near-infrared phosphorescence, J. Phys. Chem. C. 111 (2007) 4420–4424.

[62] E.J. Rosenfeldt, K.G. Linden, S. Canonica, U. von Gunten, Comparison of the efficiency of •OH radical formation during ozonation and the advanced oxidation processes O_3/H_2O_2 and UV/H_2O_2, Water Res. 40 (2006) 3695–3704.

[63] Y. Nosaka, M. Kishimoto, J. Nishino, Factors governing the initial process of TiO_2 photocatalysis studied by means of in-situ electron spin resonance measurements, J. Phys. Chem. B. 102 (1998) 10279–10283.

[64] C.D. Jaeger, A.J. Bard, Spin trapping and electron spin resonance detection of radical intermediates in the photodecomposition of water at TiO_2 particulate systems, J. Phys. Chem. 83 (1979) 3146–3152.

[65] J. Wang, Y. Guo, B. Liu, X. Jin, L. Liu, R. Xu, et al., Detection and analysis of reactive oxygen species (ROS) generated by nano-sized TiO_2 powder under ultrasonic irradiation and application in sonocatalytic degradation of organic dyes, Ultrason. Sonochem. 18 (2011) 177–183.

[66] J.M. Herrmann, P. Pichat, Heterogeneous photocatalysis. Oxidation of halide ions by oxygen in ultraviolet irradiated aqueous suspension of titanium dioxide, J. Chem. Soc. Faraday Trans. 1. 76 (1980) 1138.

[67] S. Yoon, J.H. Lee, Oxidation Mechanism of As (III) in the UV/TiO_2 system: evidence for a direct hole oxidation mechanism Environ. Sci. Technol. 39 (2005) 9695–9701.

[68] X.J. Chen, H.H. Xu, Y.J. Wang, S. Hu, Z.X Zhang, Y.M. Zhang, Study on active oxygen quantum yield, insecticidal activities and stability of dphenylthiophene, Agric. Sci. China. 6 (2007) 458–465.

[69] T. Hirakawa, K. Yawata, Y. Nosaka, Photocatalytic reactivity for $O_2^{\bullet -}$ and $OH^{\bullet}$ radical formation in anatase and rutile TiO_2 suspension as the effect of H_2O_2 addition, Appl. Catal. A Gen. 325 (2007) 105–111.

[70] K. Naito, T. Tachikawa, S.C. Cui, A. Sugimoto, M. Fujitsuka, T. Majima, Single-molecule detection of airborne singlet oxygen, J. Am. Chem. Soc. 128 (2006) 16430–16431.

[71] T. Tachikawa, T. Majima, Single-molecule detection of reactive oxygen species: Application to photocatalytic reactions, J. Fluoresc. 17 (2007) 727–738.

[72] Y. Nosaka, Y. Yamashita, H. Fukuyama, Application of chemiluminescent probe to monitoring superoxide radicals and hydrogen peroxide in TiO_2 photocatalysis, J. Phys. Chem. B. 101 (1997) 5822–5827.

[73] Y. Nosaka, M. Nakamura, T. Hirakawa, Behavior of superoxide radicals formed on TiO_2 powder photocatalysts studied by a chemiluminescent probe method, Phys. Chem. Chem. Phys. 4 (2002) 1088–1092.

[74] B. Ohtani, Photocatalysis A to Z—What we know and what we do not know in a scientific sense, J. Photochem. Photobiol. C Photochem. Rev. 11 (2010) 157–178.

[75] D. Liu, J. Ducoste, S. Jin, K. Linden, Evaluation of alternative fluence rate distribution models, J. Water SRT - Aqua 52 (2004) 391-408.

[76] J. Moreira, B. Serrano, A. Ortiz, H. De Lasa, Evaluation of photon absorption in an aqueous TiO_2 slurry reactor using Monte Carlo simulations and macroscopic balance, (2010) 10524–10534.

[77] G. Li Puma, A. Brucato, Dimensionless analysis of slurry photocatalytic reactors using two-flux and six-flux radiation absorption-scattering models, Catal. Today. 122 (2007) 78–90.

[78] M.L. Satuf, R.J. Brandi, A.E. Cassano, O.M. Alfano, Experimental method to evaluate the optical properties of aqueous titanium dioxide suspensions, Ind. Eng. Chem. Res. 44 (2005) 6643–6649.

[79] J. Marugán, R. Van Grieken, O.M. Alfano, A.E. Cassano, Optical and physicochemical properties of silica-supported TiO_2 photocatalysts, AIChE J. 52 (2006) 2832–2843.

[80] G. V. Buxton, C.L. Greenstock, W.P. Helman, A.B. Ross, W. Tsang, Critical review of rate constants for reactions of hydrated electrons, J. Phys. Chem. Ref. Data. 17 (1988) 513.

[81] R.L. Pozzo, R.J. Brandi, A.E. Cassano, M.A. Baltanás, Photocatalytic oxidation of oxalic acid in dilute aqueous solution, in a fully illuminated fluidized bed reactor, Chem. Eng. Sci. 65 (2010) 1345–1353.

[82] M. Okuda, T. Tsuruta, K. Katayama, Lifetime and diffusion coefficient of active oxygen species generated in TiO_2 sol solutions., Phys. Chem. Chem. Phys. 11 (2009) 2287–2292.

[83] M. Abdullah, G.K.C. Low, R.W. Matthews, et al., Effects of common inorganic anions on rates of photocatalytic oxidation of organic carbon over illuminated titanium dioxide, J. Phys. Chem. 94 (1990) 6820–6825.

[84] H.Y.Y. Chen, O. Zahraa, M. Bouchy, Inhibition of the adsorption and photocatalytic degradation of an organic contaminant in an aqueous suspension of TiO_2 by inorganic ions, J. Photochem. Photobiol. A Chem. 108 (1997) 37–44.

[85] C. Guillard, E. Puzenat, H. Lachheb, A. Houas, J.M. Herrmann, Why inorganic salts decrease the TiO_2 photocatalytic efficiency, Int. J. Photoenergy. 7 (2005) 1–9.

[86] R.A. Burns, J.C. Crittenden, D.W. Hand, V.H. Selzer, L.L. Sutter, S.R. Salman, Effect of inorganic ions in heterogeneous photocatalysis of TCE, J. Environ. Eng. 125 (1999) 77–85.

[87] A. Lair, C. Ferronato, J.M.M. Chovelon, J.M. Herrmann, Naphthalene degradation in water by heterogeneous photocatalysis: an investigation of the influence of inorganic anions, J. Photochem. Photobiol. A Chem. 193 (2008) 193–203.

[88] J. Gregory, Monitoring particle aggregation processes, Adv. Colloid Interface Sci. 147-148 (2009) 109–123.

[89] F. Gruy, Formation of small silica aggregates by turbulent aggregation., J. Colloid Interface Sci. 237 (2001) 28–39.

[90] C.M. Sorensen, Light scattering by fractal aggregates: a review, Aerosol Sci. Technol. 35 (2001) 648–687.

[91] G.C. Bushell, Y.D. Yan, D. Woodfield, J. Raper, R. Amal, On techniques for the measurement of the mass fractal dimension of aggregates, Adv. Colloid Interface Sci. 95 (2002) 1–50.

[92] M. Hosokawa, K. Nogi, M. Naito, T. Yokoyama, Nanoparticle technology handbook, Elsevier, 2012.

[93] R. Jenkins, R. Snyder, Introduction to X-ray powder diffractometry, Wiley-VCH, 2012.

[94] A. Keller, H. Wang, D. Zhou, H.S. Lenihan, G. Cherr, B.J. Cardinale, et al., Stability and aggregation of metal oxide nanoparticles in natural aqueous matrices, Environ. Sci. Technol. 44 (2010) 1962–1967.

[95] I. Chowdhury, D.M. Cwiertny, S.L. Walker, Combined factors influencing the aggregation and deposition of nano-TiO_2 in the presence of humic acid and bacteria, Environ. Sci. Technol. 46 (2012) 6968–6976.

[96] R.A. French, A.R. Jacobson, B. Kim, S.L. Isley, R. Penn, L. Penn, et al., Influence of ionic strength, pH, and cation valence on aggregation kinetics of titanium dioxide nanoparticles, Environ. Sci. Technol. 43 (2009) 1354–1359.

[97] Y.H. Shih, C.M. Zhuang, C.P. Tso, C.H. Lin, The effect of electrolytes on the aggregation kinetics of titanium dioxide nanoparticle aggregates, J. Nanoparticle Res. 14 (2012).

[98] Y.H. Shih, W.S. Liu, Y.F. Su, Aggregation of stabilized TiO_2 nanoparticle suspensions in the presence of inorganic ions, Environ. Toxicol. Chem. 31 (2012) 1693–1698.

[99] B. Wols, Computational fluid dynamics in drinking water treatment, IWA Publishing, 2011.

[100] H.K. Versteeg, W. Malalaskekera, An introduction to computational fluid dynamics: the finite volume method, Prentice Hall, 2007.

[101] J. Zhang, A.E. Tejada-Martínez, Q. Zhang, Developments in computational fluid dynamics-based modeling for disinfection technologies over the last two decades: a review, Environ. Model. Softw. 58 (2014) 71–85.

[102] J. Bridgeman, B. Jefferson, S. Parsons, The development and application of CFD models for water treatment flocculators, Adv. Eng. Softw. 41 (2010) 99–109.

[103] A.M. Goula, M. Kostoglou, T.D. Karapantsios, A.I. Zouboulis, A CFD methodology for the design of sedimentation tanks in potable water treatment, Chem. Eng. J. 140 (2008) 110–121.

[104] M. Ghadiri, S. Fakhri, S. Shirazian, Modeling and CFD simulation of water desalination using nanoporous membrane contactors, Ind. Eng. Chem. Res. 52 (2013) 3490–3498.

[105] D.M. Desiderio, N.M.M. Nibbering, White's Handbook of Chlorination and Alternative Disinfectants, Wiley-VCH, 2010.

[106] W.B. Rauen, A. Angeloudis, R.A. Falconer, Appraisal of chlorine contact tank modelling practices, Water Res. 46 (2012) 5834–5847.

[107] D.J. Greene, C.N. Haas, B. Farouk, Computational fluid dynamics analysis of the effects of reactor configuration on disinfection efficiency., Water Environ. Res. 78 (2006) 909–919.

[108] W.B. Rauen, B. Lin, R.A. Falconer, E.C. Teixeira, CFD and experimental model studies for water disinfection tanks with low Reynolds number flows, Chem. Eng. J. 137 (2008) 550–560.

[109] R. Amini, R. Taghipour, H. Mirgolbabaei, Numerical assessment of hydrodynamic characteristics in chlorine contact tank, Int. J. Numer. Methods Fluids. 67 (2011) 885–898.

[110] T.-H. Huang, C.J. Brouckaert, M. Pryor, C.A. Buckley, Application of computational fluid dynamics modelling to an ozone contactor, Water SA. 30 (2004) 51–56.

[111] J. Li, J. Zhang, J. Miao, J. Ma, W. Dong, Application of computational fluid dynamics (CFD) to ozone contactor optimization, Wat. Sci. Technol. 6 (2006) 9-16.

[112] J. Zhang, P.M. Huck, W.B. Anderson, G.D. Stubley, A computational fluid dynamics based integrated disinfection design approach for improvement of full-scale ozone contactor performance, Ozone Sci. Eng. 29 (2007) 451–460.

[113] J.J. Ducoste, D. Liu, K. Linden, Alternative approaches to modeling fluence distribution and microbial inactivation in ultraviolet reactors: Lagrangian versus Eulerian, J. Environ. Eng. 131 (2005) 1393–1403.

[114] D.A. Sozzi, F. Taghipour, UV reactor performance modeling by Eulerian and Lagrangian methods, Environ. Sci. Technol. 40 (2006) 1609–1615.

[115] A. Sozzi, F. Taghipour, The importance of hydrodynamics in UV advanced oxidation reactors, Water Sci. Technol., 55 (2007) 53–58.

[116] S. Elyasi, F. Taghipour, Simulation of UV photoreactor for degradation of chemical contaminants: model development and evaluation, Environ. Sci. Technol. 44 (2010) 2056–63.

[117] S.M. Alpert, D.R.U. Knappe, J.J. Ducoste, Modeling the UV/hydrogen peroxide advanced oxidation process using computational fluid dynamics., Water Res. 44 (2010) 1797–808.

[118] D. Santoro, M. Raisee, M. Moghaddami, J. Ducoste, M. Sasges, L. Liberti, et al., Modeling hydroxyl radical distribution and trialkyl phosphates oxidation in UV - H_2O_2 photoreactors using computational fluid dynamics, Environ. Sci. Technol. 44 (2010) 6233–6241.

[119] M. Mohajerani, M. Mehrvar, F. Ein-Mozaffari, CFD modeling of metronidazole degradation in water by the UV/H_2O_2 process in single and multilamp photoreactors, Ind. Eng. Chem. Res. 49 (2010) 5367–5382.

[120] V.K. Pareek, S.J. Cox, M.P. Brungs, B. Young, A.A. Adesina, Computational fluid dynamic (CFD) simulation of a pilot-scale annular bubble column photocatalytic reactor, Chem. Eng. Sci. 58 (2003) 859–865.

[121] D.A. Sozzi, F. Taghipour, Computational and experimental study of annular photo-reactor hydrodynamics, Int. J. Heat Fluid Flow. 27 (2006) 1043–1053.

[122] F.J. Trujillo, T. Safinski, A.A. Adesina, Oxidative photomineralization of dichloroacetic acid in an externally-irradiated rectangular bubble tank reactor: Computational fluid dynamics modeling and experimental verification studies, Ind. Eng. Chem. Res. 49 (2010) 6722–6734.

[123] Y. Boyjoo, M. Ang, V. Pareek, CFD simulation of a pilot scale slurry photocatalytic reactor and design of multiple-lamp reactors, Chem. Eng. Sci. 111 (2014) 266–277.

[124] O. Alfano, A. Negro, Scattering effects produced by inert particles in photochemical reactors. 1. Model and experimental verification, Ind. Eng. Chem. Res. 34 (1995) 488–499.

[125] R.L. Romero, O.M. Alfano, A.E. Cassano, Cylindrical photocatalytic reactors. Radiation absorption and scattering effects produced by suspended fine particles in an annular space, Ind. Eng. Chem. Res. 36 (1997) 3094–3109.

[126] F.J. Trujillo, T. Safinski, A.A. Adesina, CFD analysis of the radiation distribution in a new immobilized catalyst bubble column externally illuminated photoreactor, J. Sol. Energy Eng. 129 (2007) 27.

[127] A. Queffeulou, L. Geron, E. Schaer, Prediction of photocatalytic air purifier apparatus performances with a CFD approach using experimentally determined kinetic parameters, Chem. Eng. Sci. 65 (2010) 5067–5074.

[128] R.L. Romero, O.M. Alfano, A.E. Cassano, Radiationfield in an annular slurry photocatalytic reactor. 2. Model and experiments, Ind. Eng. Chem. Res. 42 (2003) 2479–2488.

[129] V.K. Pareek, A.A. Adesina, Light intensity distribution in a photocatalytic reactor using finite volume, AIChE J. 50 (2004) 1273–1288.

[130] F. Denny, J. Scott, V. Pareek, G. Ding Peng, R. Amal, CFD modelling for a TiO_2-coated glass-bead photoreactor irradiated by optical fibres: photocatalytic degradation of oxalic acid, Chem. Eng. Sci. 64 (2009) 1695–1706.

[131] J.E. Duran, M. Mohseni, F. Taghipour, Computational fluid dynamics modeling of immobilized photocatalytic reactors for water treatment, AIChE J. 57 (2011) 1860–1872.

[132] C.S. Zalazar, R.L. Romero, C.A. Martín, A.E. Cassano, Photocatalytic intrinsic reaction kinetics I: mineralization of dichloroacetic acid, Chem. Eng. Sci. 60 (2005) 5240–5254.

[133] J.E. Duran, F. Taghipour, M. Mohseni, Evaluation of model parameters for simulating TiO_2 coated UV reactors, Water Sci. Technol. 63 (2011) 1366–1372.

CHAPTER 2
DESIGN OF THE RESEARCH

2.1 RATIONALE

TiO_2 photocatalysis for water and wastewater treatment has attracted great research interest, but a scarce development of competitive technological solutions has been achieved so far, representative of the relevant difficulties posed by this research topic. As a matter of fact, in order to outline the research and development scenario concerning TiO_2 photocatalysis, the presence of two fundamental aspects can be noticed: (i) the outstanding photoelectrochemical properties and the potential applications to depolluting technologies as the main driving factor for process assessment, (ii) the important critical issues to be overcome for its real-scale application.

A key element in determining the complexity of this topic is the variety of disciplines that are involved in TiO_2 photocatalysis research, asking for significantly different background, i.e. material science, physics, chemistry and engineering. The multi-disciplinarity is also outlined in the state-of-the-art analysis, presented in chapter 1, where the most important research directions are also highlighted to make TiO_2 photocatalysis an established technology for the advanced oxidation and disinfection of water and wastewater. Three fundamental macro-subjects for further investigation on TiO_2 photocatalysis can be identified, as schematically reported in figure 2.1, and they are briefly presented in the following.

- A <u>mechanistic insight</u> is currently required for a quantitative and valuable description of the complex and mutually-dependent chemical-physical processes involved in TiO_2 photocatalysis. As a matter of fact, so far research works have often been focused on the proof-of-concept of TiO_2-based materials for environmental applications, without considering process engineering. Some important topics belong to this tasks, including: (i) <u>radiation transfer</u>, that is the driving force of the process, for which an accurate description is challenging, (ii) the <u>generation of reactive species</u>, whose peculiar properties have been described in chapter 1, (iii) <u>process modelling</u>, meaning the comprehensive integration of the physics involved in the process, usually optics, fluid dynamics and chemical reactions.

- TiO_2 photocatalysis effective application depends on its <u>optimization and scale-up</u>, in order to display results comparable to other established technologies at sustainable costs. Being this aspect still poorly addressed in the literature, relevant improvements can probably be achieved by the assessment of the <u>reactor design</u>, which is typically a critical aspect for UV-based advanced oxidation processes. In addition, <u>Life Cycle Assessment</u> could represent a useful tool for defining the applicability scenarios for TiO_2 photocatalysis with respect to other established technological competitors.

- Further research works should be devoted to the assessment of the application to water and wastewater, investigating the effectiveness of TiO_2 photocatalysis under realistic operating conditions as polishing treatment for the removal of refractory organics, especially referring to micro-pollutants and emerging contaminants, or for the advanced disinfection of resistant pathogens. Related literature is already consistent, although experimental activities have often been carried out in synthetic media or in conditions not directly generalizable. In particular, concerning the latter situation, future research activities should aim at proposing easy and reliable benchmark methods for comparing processes operated under different conditions, including also other advanced oxidation processes. Finally, the evaluation of the generation of by-products and the eco-toxicity of discharged effluents is a topic that will become increasingly important in the years ahead.

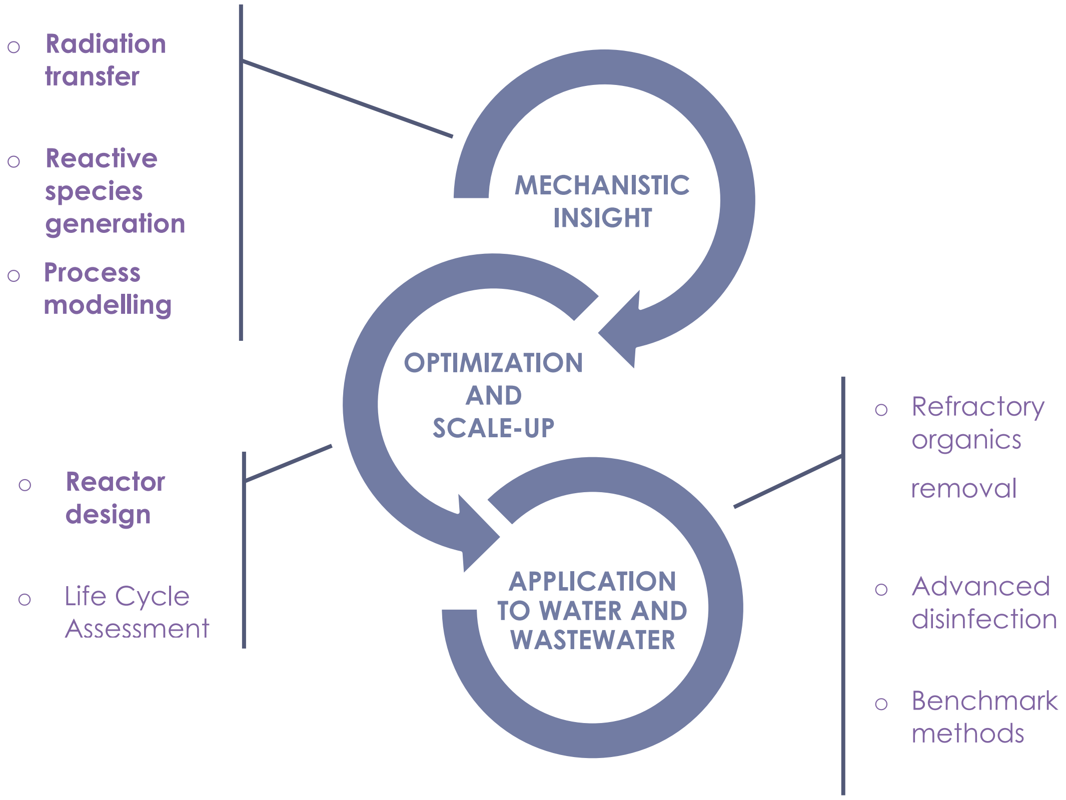

Figure 2.1 Schematic representation of the proposed investigation route on TiO_2 photocatalysis. The topics in bold have been studied in the present work.

Furthermore, future research should consider the opportunities offered by new generation TiO_2-based materials, as TiO_2 grown by anodic oxidation, and by innovative computational techniques, that represent a valuable tool for the optimization and the scale-up of photocatalytic reactors.

In the present work some topics, reported in bold in figure 2.1, have been investigated, basically concerning the mechanistic phenomena insight as well as the optimization and development phases. Such topics were selected to create a multi-disciplinary framework, which has led to the collaboration with scientists and engineers belonging to external institutions and to the acquisition of additional scientific and technological competences. For instance, as introduced in chapter 1, in the present work two innovative subjects were approached, namely nanotechnologies for water and wastewater treatment as well as computational fluid dynamics (CFD) codes.

2.2 RESEARCH DESIGN

The present PhD thesis is organized in five chapter and one appendix, each intended for a publication on international peer-reviewed scientific journal. Each chapter is developed according to an autonomous scheme, including the introduction on current advances in literature, the definition of objectives and experimental methodologies, the presentation and discussion of results and the summary of achievements. In the following the content of chapters is briefly introduced:

- In chapter 3 an innovative methodology for the characterization of the optical properties of TiO_2 suspensions is proposed: experimental measurements were performed by an optical goniometer, followed by a modelling phase, developed by means of a multi-purpose CFD code. The effectiveness of the proposed methodology has been proved by integrating optics, fluid dynamics and chemical reactions in a CFD model, capable of reproducing the behaviour of a semi-batch annular photoreactor.

- In chapter 4 the implementation of two experimental protocols is described for the measurement of reactive species, namely photogenerated holes and hydroxyl radicals, at the laboratory scale. Those protocols were applied for assessing the reactivity of suspensions of commercial TiO_2 nanoparticles. A model for reactive species quenching has been developed, accounting for radiation transfer, TiO_2 nanoparticle aggregation and kinetic reactions, and it was calibrated by means of the collected experimental data. The model has been then validated by measurements carried out in a different experimental setup.

- Chapter 5 is focused on the assessment of the influence of several inorganic anions on the reactivity of commercial TiO_2 nanoparticles in suspension. In detail, the production of reactive species, namely photogenerated holes and hydroxyl radicals, has been monitored over time in the presence of dissolved species in solution. The influence of inorganic anions on TiO_2 aggregation, which has been evaluated, is described too. The detrimental effect of inorganic anions has been discussed and a modelling procedure for the influence of inorganic anions on photogenerated holes based on competitive adsorption is proposed.

- In chapter 6 the influence of several inorganic anions on the reactivity of an innovative engineered nanomaterial, self-ordered nanotubular TiO_2, has been evaluated and discussed. Nanotubular TiO_2 was grown by anodic oxidation and characterized; the detrimental effect of inorganic anions was assessed by monitoring the production of photogenerated holes. A modelling procedure for describing the influence of inorganic anions has been proposed, based on experimental data. A special focus is dedicated to the evaluation of nanotubular TiO_2 fouling and to the definition of a regeneration protocol.

- In chapter 7 an optimal design methodology for an electrophotocatalytic reactor using self-ordered nanotubular TiO_2 for water and wastewater treatment is discussed. Such procedure is based on the use of generated photocurrent as an indicator of TiO_2 photoactivation. In detail, generated photocurrent was monitored as a function of two operating conditions, namely reactor configuration and solution transmittance. Then, a procedure for estimating the generated photocurrent in an electrophotocatalytic reactor was developed, whose effectiveness was validated in a number of reactor configurations.

Finally, the appendix, whose structure is similar to that of the other chapters, is dedicated to the CFD simulation of radiation transfer and fluid dynamics in an unbaffled stirred tank reactor for TiO_2 nanoparticle photocatalysis at the laboratory scale. The effectiveness of CFD code in describing fluid dynamics was proved and the mixing provided by magnetic stirrer was assessed. CFD model was calibrated by radiometric measures and radiation transfer was described, allowing for the determination of radiation intensity and local volumetric rate of photon adsorption in the reactor.

CHAPTER 3

MODELLING THE OPTICAL BEHAVIOUR OF TiO_2 SUSPENSIONS AND OXALIC ACID DEGRADATION IN A PHOTOCATALYTIC REACTOR USING COMPUTATIONAL FLUID DYNAMICS (CFD)

ABSTRACT

A computational fluid dynamic (CFD) model was developed in an Eulerian framework where the optical behaviour of titanium dioxide (TiO_2) suspensions, the flow distribution and the oxalic acid degradation are integrated to describe the treatment performance of a semi-batch annular TiO_2-UV photoreactor. Special attention was paid to characterizing the scattering component of the optical model used in the CFD model, which was calibrated using an optical goniometer by comparing simulated scattering light profiles against irradiance measurements obtained for various TiO_2 concentrations and UV wavelengths. Various scattering phase functions were tested against the experimental data confirming that the Henyey-Greenstein function was the most appropriate for the angular light distribution at 254 and 355 nm irrespective of the TiO_2 concentration.

Using the calibrated scattering phase function, a new approach for quantifying the absorption and scattering coefficients in TiO_2 suspensions was developed. It consists of iteratively solving, using the discrete ordinate model, the radiative transfer equation for various combinations of absorption and scattering coefficients until the error between observed and predicted angular irradiance measurements is minimized. The validity of the optical coefficients identified with the proposed method was validated with independent numerical experiments by modelling the oxalic acid degradation in UV irradiated TiO_2 suspensions in a semi-batch annular photoreactor. CFD simulations, compared with irradiance and oxalic acid degradation data obtained from the literature, indicated an excellent agreement with the observed data confirming the considerable potential of the new, integrated modelling methodology presented for the design, optimization and scale-up of photocatalytic technologies for water and wastewater treatment applications.

The research work described in the present chapter was carried out with the valuable support of

Domenico Santoro, Research scientist, Trojan Technologies, Canada
John de Bruyn, Full professor, University of Western Ontario, Canada
Ferdinando Crapulli, PhD student, University of Western Ontario, Canada

The research work was partially carried out during a 2-month period of international mobility at University of Western Ontario and Trojan Technologies (London, Ontario, Canada).

The present chapter, after an adaptation in terms of formatting style, has been submitted for publication to the journal 'Environmental Science and Technology' and it is currently under review.

3.1 INTRODUCTION

Photocatalytic-based water treatment processes are promising alternatives to conventional advanced oxidation processes [1–3]. However, the complex multi-physics involved and the lack of integrated design frameworks has severely limited their cost-effective deployment at full-scale. Among the several factors causing such delay, the lack of mechanistic models and engineering-friendly tools enabling the detailed understanding and the scale-up of the photo-degradation processes is one of the major barriers to overcome [4,5]. In particular, the accurate and quantitative description of the radiative transfer phenomena occurring in the photoreactor domain plays a key role in the overall design and scale-up as they ultimately determine the extent of photon utilization, i.e. TiO_2 photoactivation, which leads to the efficient generation of highly reactive species directly involved in contaminant degradation.

Although in recent years considerable advancements have been made toward the development of numerical tool for photoreactor design, the accurate and computationally-efficient modelling of fluence rate distribution in photocatalytic systems is still an area of intense research [6–11]. More specifically, predicting the distribution of scattered light induced by TiO_2 nanoparticle suspensions in a photoreactor is of paramount importance as it ultimately dictates the local volumetric rates of photon absorption in the photosystem [6]. For the case of TiO_2 suspensions at low concentrations and particles size larger than the irradiating wavelength [12–14], scattering is usually well described by the Mie theory, which assumes that a photon is scattered only once while crossing the medium and that scattering events are statistically independent from each other. However, while on the one hand the application of the Mie theory only applies to situations when multiple scattering can be neglected (which is hardly found in common TiO_2 applications), on the other hand the simplified theory of light diffusion can be used when an infinite number of scattering events occur [15]. Realistically, TiO_2 photoreactors often operate under an optical regime where photons are scattered more than once but less than an infinite number of times. Therefore, simplified approaches in predicting scattering behaviour of TiO_2 suspensions cannot be used and numerical methods are needed in order to solve, in a generalized framework, the radiative transfer equation (RTE) in the photoreactor liquid domain. Moreover, modelling scattering in TiO_2 suspensions in presence of nanoparticles having a non-uniform particle size and unknown (or non-spherical) shapes presents even more challenges. In such circumstances, a commonly-adopted approach is to introduce semi-empirical probability functions, such as the diffuse reflectance (DR) and the Henyey-Greenstein scattering phase functions (HG), in the attempt of finding an acceptable compromise between mechanistic and empirical models able to predict the optical behaviour of irradiated TiO_2 suspensions while preserving acceptable accuracy and computational efficiency.

Irrespectively of the adopted approach, all the optical properties describing the absorption and scattering behaviour must be known and specified in advance in order to numerically solve RTE.

Once the volumetric absorption coefficient κ_λ, the volumetric scattering coefficient σ_λ and the scattering phase function $p(\Omega' \rightarrow \Omega)$ of the liquid phase are specified, deterministic or stochastic methods can be used to predict the local volumetric rate of photon absorption spatial distribution in a photocatalytic reactor of arbitrary shapes [16–18].

It should be emphasized that the optical properties are dependent on the characteristics of TiO_2 suspensions such as the photocatalyst type and the particle size distribution [7,19]. Moreover, they are somewhat convoluted with each other and cannot be measured individually and independently. As a result, inverse methods are commonly adopted for their quantification and deconvolution [20]. For example, the presence of scattering impedes the direct measurement of the absorption coefficient in TiO_2 suspensions by conventional spectrophotometric techniques and the Beer-lambert law. Under certain geometrical conditions, spectrophotometric measurements of scattering media could be used for estimating the extinction coefficient, that is, a combined measure of absorption and scattering coefficients. In other words, the accurate estimation of optical properties in a scattering suspension requires the deconvolution from the local irradiance measurements of the two contributions of absorption and scattering, while also accounting for the geometrical dependency of optical measurements performed [21,22].

One of the first attempts made to independently estimate the volumetric absorption and scattering coefficients in TiO_2 nanoparticle suspensions has been presented in Cabrera et al. [23]. Their methods consisted of performing spectrophotometric measurements of extinctance and diffuse transmittance, and then using those to estimate the optical properties by solving the RTE in a one-dimensional framework. Since such procedure requires the assumption of the scattering phase function, the diffuse reflectance model was used for the calculations, whose formulation is:

$$p(\theta) = \frac{8}{3\pi}(\sin\theta - \theta\cos\theta) \tag{e3.1}$$

where θ is the radiation scattering angle. Recently, the same method was refined by Satuf et al. [24], who assumed the Henyey-Greenstein scattering phase function instead:

$$p(\theta) = \frac{1}{4\pi}\frac{(1-g_\lambda^2)}{\left(1+g_\lambda^2-2g_\lambda\cos\theta\right)^{\frac{3}{2}}} \tag{e3.2}$$

where g_λ (asymmetry factor) is a wavelength-dependent parameter ranging between -1 (total backward scattering) and +1 (total forward scattering) with $g_\lambda = 0$ indicating isotropic scattering. In the latter case the optical parameters were estimated by performing diffuse reflectance and transmittance spectrophotometric measurements and then solving the RTE in a one-dimensional framework.

To the authors' knowledge, most of the papers available in the literature either refer to the optical parameters estimated by Cabrera et al. [23] and Satuf et al. [24], or make use of the wavelength-dependent averaged values of these optical parameters, as recommended by Romero et al. [26].

Moreover, the lack of a standardized approach and operating procedures for the quantification of the scattering phase function in TiO_2 suspensions lead to two additional consequences: (i) inconsistency in the experimental data describing the anisotropic optical behaviour of scattered light in TiO_2 photoreactors, (ii) uncertainty in the estimated absorption and scattering coefficients, whose accurate quantification depends on the knowledge of the scattering phase function.

A powerful approach for photoreactor modelling relies on the use of computational fluid dynamics (CFD), which is typically conducted using general-purpose CFD softwares, such as ANSYS Fluent, where the RTE can be solved simultaneously with flow transport equations in domains of arbitrary shapes and dimensions [27]. As a matter of fact, in the last decade the use of these CFD models has greatly accelerated the development of new technologies [28–30] and it has been recently extended to TiO_2 photoreactors, where contaminant degradation processes are complex due to the mutual interactions among optics, fluid dynamics and reaction kinetics.

In this research work, a new procedure for the quantification of the scattering phase function and the optical properties of TiO_2 nanoparticle suspensions irradiated under quasi-monochromatic UV light emitting wavelengths with peaks at 254 and 355 nm is presented. Different scattering models were tested against angular light distribution data collected by an optical goniometer and the optical properties (absorption and scattering coefficients) accordingly estimated using an iterative method consisting in solving the RTE for various combinations of those optical coefficients to minimize the error between observed and simulated data. Then, the estimated optical properties were used in a mechanistic CFD model describing the oxalic acid degradation in a semi-batch annular photoreactor and compared against previously-published data [31].

3.2 MATERIAL AND METHODS

3.2.1 Scattering measurements in TiO_2 suspensions

Experiments were performed using P25 Aeroxide TiO_2 nanopowder (Evonik, Germany) suspended in deionized water at various concentrations (40, 100, 400 mg L^{-1}) without pre-sonication. The scattering phase function measurements in TiO_2 suspensions were conducted using an optical goniometer (figure 3.1). About 20 mL of a TiO_2 suspension were poured in a 12 mm diameter quartz tube (external diameter: 14 mm; Quartz Scientific, USA) held in vertical position aligned with the vertical axis of the goniometer. Samples were irradiated by light emitting diodes (UVTOP, SETi, USA) at quasi-monochromatic UV light with emission bands centred at two different wavelengths (254 and 355 nm). The emitted light was collimated using a 5 cm diameter absorbing tube, which was mounted horizontally with its axis parallel to the direction of the radiation incident on the sample in order to cut the off-angle light emitted by the light source. The collimated light beam was focused on the sample by a plano-convex fused silica lens with focal length of 20 cm. A second identical lens was mounted on the rotating arm of the goniometer in order to re-focus the scattered light to the detector.

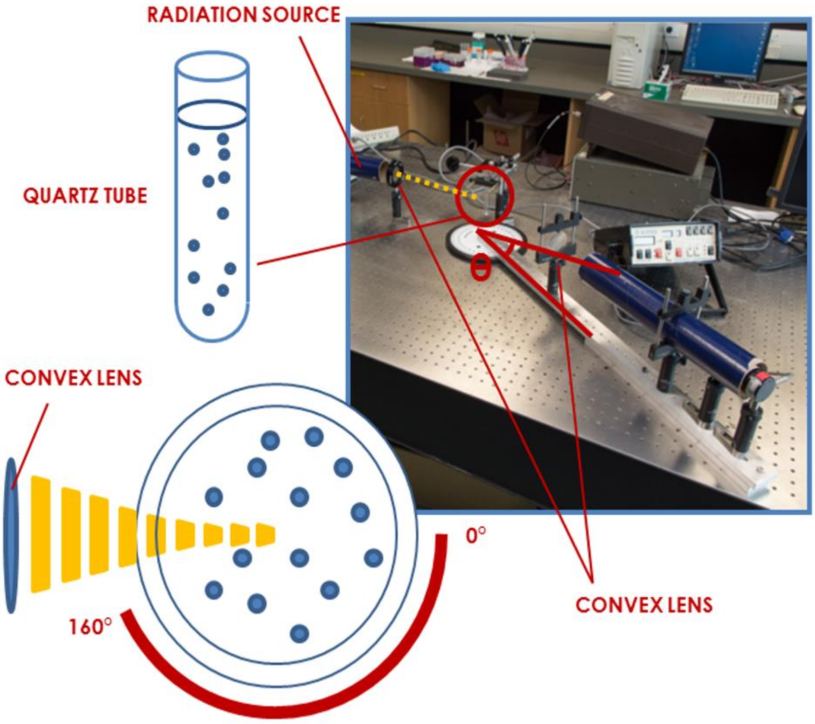

Figure 3.1 Schematic illustration of the experimental setup describing the various components of the optical goniometer used in this study.

The angular distribution of the light scattered by the irradiated sample was measured using a calibrated UV detector (SED100, International Light, USA) connected to a radiometer (ILT1700, International Light). The angle θ at which the scattered light irradiance was measured was varied from the straight irradiation direction (0°) up to an angle of 160° using 5° as angular step interval.

Scattering measurements were corrected by subtracting from the recorded data the corresponding amount of the signal caused by dark current. Measures were taken in quadruplicates for each angular position to allow for the quantification of the associated uncertainty. The absence of significant settling phenomena over the course of experiments and the stability of the experimental measurements were verified prior of testing.

3.2.2 Estimation of optical properties of TiO_2 suspensions

In order to estimate the optical properties of TiO_2 suspensions, the experimental setup was modelled in a 2D-planar CFD framework using ANSYS Fluent 15.0 (ANSYS Inc., Canonsburg, USA). The spatial domain used in the model (figure 3.2) consisted of three concentric sections identifying three domains, namely the suspension domain with dispersed TiO_2, the quartz domain associated with the cylindrical cuvette used during the experiments, and the air domain of arbitrary radius (3 mm thickness) surrounding the sample resulting from the intersection of the 3D-space surrounding the goniometer with the horizontal scattering plane.

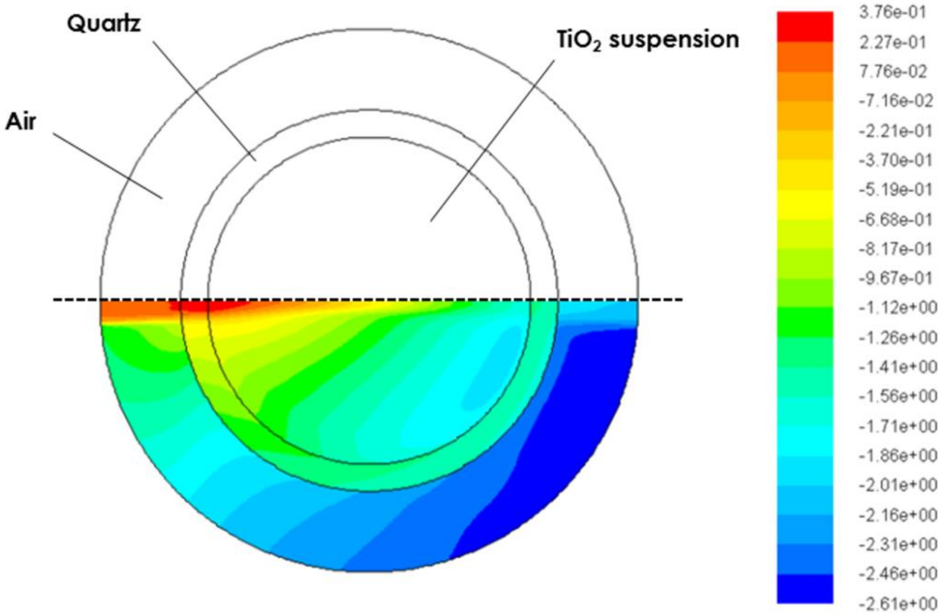

Figure 3.2 Computational domain used for CFD simulations of TiO_2 suspension. In the lower half the simulated UV fluence rate (W m^{-2}) in a logarithmic scale for the case of 400 mg L^{-1} and 355 nm is reported.

The optical properties used for the simulation of the radiation distribution in the quartz tubes were provided by the manufacturer and are reported in table 3.1. Refractive indexes of the liquid were set to 1.349 and 1.376 respectively at 254 and 355 nm, after being measured using a digital multiple wavelength refractometer (DSR-L, Schmidt + Haensch, Germany).

Table 3.1 Optical properties of solid materials.

Material	Wavelength (nm)	Absorption coefficient (m^{-1})	Refractive index
Quartz	254	8.34	1.476
	355	39.3	1.505
Pyrex glass	365	10	1.479
Borosilicate glass	365	10	1.536

The domain indicated in figure 3.2 was discretized with $7 \cdot 10^4$ unstructured triangular elements, almost uniform in size (0.1 mm). In order to simulate the converging behaviour of the UV light after being focused by the optical lens, the emitting light source was set to be as a 1.5 mm curvilinear arc located on the outer circle of the computational domain. The emission profile of the light source was assigned to be normal to the curvilinear arc in order to ensure the converging behaviour of the irradiated light towards the central point of the cuvette containing the TiO_2 suspension. The radiative transfer equation was solved using discrete ordinate (DO) model using a second order upwind discretization scheme. More details about the governing equations and the numerical methods are reported in Supporting Information (SI3.1).

3.2.3 CFD model for oxalic acid degradation

The photoreactor described by Grcic and Li Puma [31], which is referred in their manuscript as PR1, was modelled in an Eulerian framework using the CFD software ANSYS Fluent 15.0. It consists of an annular semi-batch reactor (V=0.134 L), irradiated by an axially-mounted UV polychromatic lamp emitting radiation in the 323-406 nm range with a peak at 365 nm (TL 8W/08 F8 T5/BLB, Philips, Netherlands), connected in recirculation mode to a 2 L mixed tank. The tank containing oxalic acid, dissolved in deionized water and spiked with suspended TiO_2 (P25), was continuously treated and recirculated back in order to keep the solution well-mixed during the degradation experiments. Several combinations of lamp irradiances (I_W = 107.21 W m^{-2}, I_0=89.94 W m^{-2}; I_W = 78.11 W m^{-2}, I_0=63.53 W m^{-2}, where I_W and I_0 represent the UV irradiance at the lamp wall and at reactor inner wall respectively), TiO_2 concentrations (100, 400 mg L^{-1}) and initial oxalic acid concentrations (10, 20, 40 mg L^{-1}) were investigated. Owning to its axis-symmetric configuration, the photoreactor was modelled in a 2D-axisymmetric framework containing four zones representing four cylindrical coaxial volumes: air, Pyrex glass tube, liquid solution, borosilicate glass tube (figure 3.3). Detailed information about the photoreactor geometry are reported in Supporting Information (SI3.2), while the optical properties of glasses, based on supplier datasheets, are included in table 3.1.

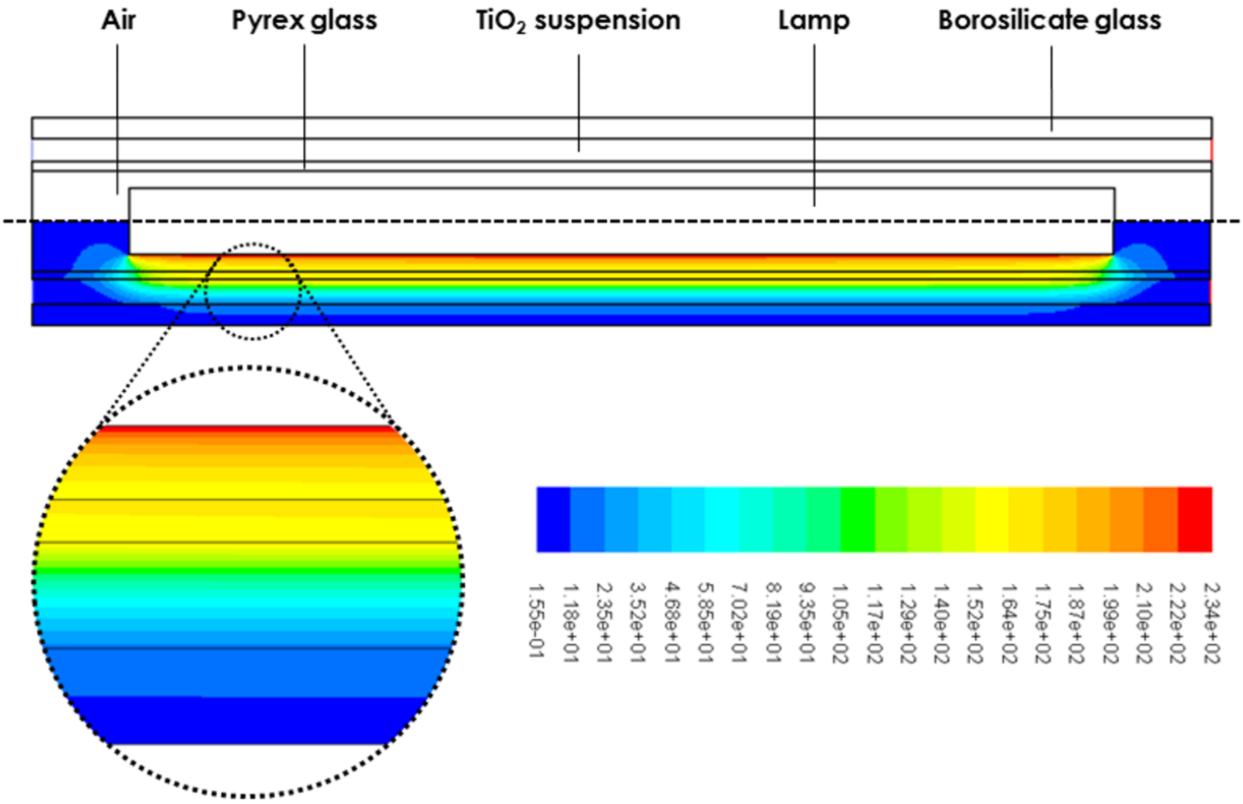

Figure 3.3 Axis-symmetric photoreactor geometry used for the CFD simulation of the oxalic acid degradation. In the lower half, simulated UV irradiance (W m^{-2}) is reported (I_0= 107.21 W/m^2 and TiO_2 = 400 mg L^{-1}).

For all the TiO_2 suspensions used in this study, several combinations for absorption and scattering coefficients (as well as scattering phase function) were used in the CFD model to assess the response of the model and its sensitivity against these parameters. However, the refractive index was measured, as described in the previous paragraph, and kept constant at 1.349 at 365 nm.

The computational domain was discretized in $1.5 \cdot 10^5$ uniform unstructured triangular elements, having an average size of 0.25 mm. The lamp was modelled as a Lambertian monochromatic light source emitting at 365 nm using DO model with second order upwind scheme for solving the RTE in the photoreactor domain. Since the Reynolds number was 1,192, fully-developed laminar flow boundary conditions were prescribed at the reactor inlet as suggested in [32]. More details can be found in Supporting Information (SI3.3).

An additional scalar transport equation with a source term was used in the model to predict the degradation of the oxalic acid in the annular photoreactor. A source term was added to the scalar transport equation using a user-defined function to include the intrinsic degradation kinetics proposed by [31]. The latter kinetic equation was derived from the generalized model developed by Pozzo et al. [17] for photocatalytic degradation of oxalic acid in a fluidized bed reactor, based on adsorption and photodegradation mechanisms studied by Mendive et al. [33]. The proposed intrinsic kinetics for oxalic acid oxidation is reported in equation e3.3:

$$\frac{d[OXA]}{dt} = \left\{k_B\theta(t)[OXA] + k_A[1-\theta(t)]\sqrt{[OXA]}\right\} \cdot \sqrt{LVRPA} \tag{e3.3}$$

where [OXA] is the concentration of oxalic acid, LVRPA is the local volumetric rate of photon absorption and $\Phi(t)$ is the fraction of absorption sites, defined as:

$$\theta(t) = \beta[OXA]_{IN}(1-\alpha t LVRPA) \tag{e3.4}$$

where $\Phi(t)$ is function of initial oxalic acid concentration $[OXA]_{IN}$, time (t) and LVRPA. k_A, k_B, a and β are intrinsic kinetic parameters. The oxalic acid diffusivity was estimated using the equation reported in the Supporting Information (SI3.3). The decrease of oxalic acid concentration over time in the recirculating tank, assumed as a completely mixed reactor, was estimated using the differential mass-balance equation shown in equation e3.5:

$$\frac{d[OXA_{TANK}]}{dt} = \frac{1}{HRT_{TANK}}\left([OXA_{REACTOR,OUT}] - [OXA_{TANK}]\right) \tag{e3.5}$$

where $[OXA_{TANK}]$ is the oxalic acid concentration in the tank, $[OXA_{REACTOR,OUT}]$ is the mass-weighted oxalic acid concentration at reactor outlet and HRT_{TANK} is the hydraulic retention time of the solution in the tank.

3.3 RESULTS AND DISCUSSION

3.3.1 Determination of the scattering phase function

Angular irradiance measurements collected with the optical goniometer are shown in figure 3.4. As it can be noted, the UV irradiance varied strongly as a function of the angle, being at times close to the dark current generated by the ambient light during the measurements (about 10^{-12} W cm^{-2}).

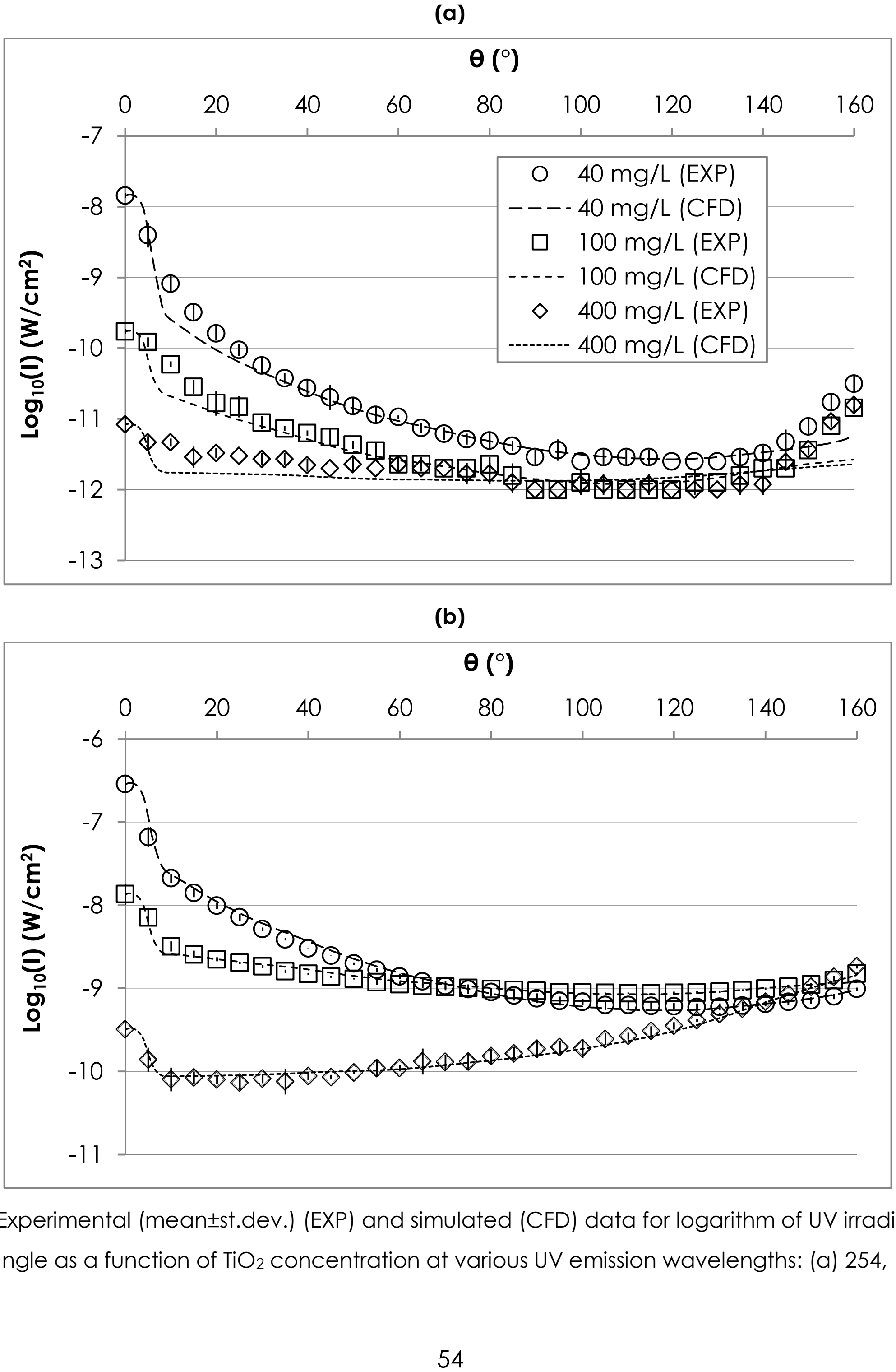

Figure 3.4 Experimental (mean±st.dev.) (EXP) and simulated (CFD) data for logarithm of UV irradiance (I) vs. direction angle as a function of TiO_2 concentration at various UV emission wavelengths: (a) 254, (b) 355 nm.

Irrespective of the investigated wavelengths, a similar behaviour for scattered radiation was observed. The highest irradiance values were detected at the angles close to the straight irradiation direction and at the widest angles, approximately over 135°. While the former was expected, due to the shorter light path associated with the forward direction, less intuitive was the behaviour observed for the backscattered light, probably due to an interference caused by reflection at the widest angles, especially at 254 nm. This behaviour was more pronounced at the lowest TiO_2 concentration and also in the absence of TiO_2 nanoparticles, as reported in Supporting Information (SI3.4), confirming the hypotheses indicated above.

In terms of angular distribution of the scattered light to different TiO_2 concentrations, it was observed, as intuitively expected, an increase in the scattering events with TiO_2 loading. This was evident in the experimental data by looking at the spread of the radiation crossing the glass tube leading to a more uniform distribution of radiation in all angular directions.

The effectiveness of three scattering models reported in literature for describing experimental data was evaluated, namely the Mie theory, the diffuse reflectance model (equation e3.1) and the Henyey-Greenstein function (equation e3.2). In order to account for the disturbances introduced at the widest angles by reflection and refraction, irradiance measurements in correspondence to extreme angles were ignored in the fitting of the scattering phase functions, limiting the angular range between 5° and 120°. The light collected by the sensor in the straight direction (0°) was also excluded since it is not, by definition, a measure of scattered light.

Unsatisfactory fittings were observed both for the Mie theory (not described in this manuscript for brevity) and the diffuse reflectance model (coefficients of determination $R^2<0.6$ for both). These results are probably due to the discrepancies between experimental and modelling assumptions and conditions. In particular, regarding the Mie theory, the number of scattering events was certainly greater than one, as also suggested by the better fitting seen for the low TiO_2 concentration (40 mg L^{-1}). Also, a possible departure for the range of applicability of the Mie theory could be caused by the non-uniformity of the particle size within the TiO_2 suspension. As for the Henyey-Greenstein function, the fitting was carried out by using the asymmetry factor (g_λ) as fitting parameter. Least square regression driven by the simplex algorithm was adopted to determine the best fitting. Consistently with what reported in Satuf et al. [24], experimental data were well described by the Henyey-Greenstein function, as also indicated by the high R^2values under all operating conditions. Estimated asymmetry factors and R^2 values at different UV wavelengths and TiO_2 concentrations are reported in table 3.2. Both for 254 and 355 nm scattering experiments the asymmetry factor decreased with increasing TiO_2 concentration, as a result the scattering characteristic of the solutions reaching more isotropic conditions with increasing concentration of scattering centres in the medium. As also expected, backward scattering was also observed at 355 nm for the highest TiO_2 concentration (TiO_2=400 mg L^{-1}).

In addition, estimated asymmetry factors for TiO_2 concentrations were correlated linearly with TiO_2 concentration (R^2=0.990 for 254 and 355 nm, see Supporting Information, SI3.5), indicating that values at intermediate concentrations can be estimated by linear interpolation. Moreover, the intercepts of the regression lines are close to 1, indicating the theoretical occurrence of perfect forward scattering in case of the absence of TiO_2 nanoparticles at both UV wavelengths. However, their slopes are different for the 254 and 355 nm cases, which support the evidence of scattering being dependent on wavelength.

Table 3.2 Estimated optical properties of TiO_2 suspensions for different UV wavelengths using the Henyey-Greenstein scattering phase function: asymmetry factor (g_λ), absorption coefficient (κ_λ), scattering coefficient (σ_λ) and albedo.

λ (nm)	[TiO_2] (mg L^{-1})	R^2	g_λ (-)	κ_λ (m^{-1})	σ_λ (m^{-1})	Albedo
254	40	0.999	0.929	65	25	0.29
	100	0.973	0.802	180	80	0.31
	400	0.865	0.299	60	180	0.75
355	40	0.976	0.870	15	60	0.80
	100	0.937	0.543	25	135	0.84
	400	0.942	-0.399	80	330	0.81

3.3.2 Estimation of absorption and scattering coefficients in TiO_2 suspensions

The irradiance measurements were numerically modelled by solving the RTE in the computational domain indicated in figure 3.1 using the CFD model. Such approach was deemed appropriate as it was successfully adopted by previous investigators for modelling the radiative transfer in TiO_2 nanoparticles [8,29,30]. It is worth noting that, despite a number of procedures for quantifying the absorption and scattering coefficients in TiO_2 suspensions have already been reported, all of them are based on the assumption that the scattering phase function is known a-priori.

In this research work, the validity of the Henyey-Greenstein function was first confirmed with angular irradiance measurements and then the asymmetry coefficients estimated from those. As a second step, the calibrated HG function was used as input for the CFD model to reduce the unknown optical parameters to two (i.e., the absorption and scattering coefficients), which were then estimated by minimizing the error of observed and predicted angular irradiance data. This procedure, while being similar to the one proposed in Toepfer et al. [34], based on the use of an annular reactor, has as an additional advantage that the measurements used for the coefficient estimation are collected using an apparatus, i.e. an optical goniometer, specifically conceived and designed for the investigation of scattering problems. As such, it could be argued that the precision and the accuracy of this newly developed operating procedure are superior or at least equal to the ones previously reported in the literature.

It should be mentioned that a series of verification steps were taken before the estimation of the optical parameters in order to verify the capability of the CFD model in reproducing the baseline measurements associated with the optical goniometer. For instance, the shape and the width of the radiation beam were first calibrated in absence of TiO_2 nanoparticles by fitting of experimental data obtained at 254 and 355 nm, as reported in Supporting Information (SI3.4), to ensure that the beam divergence and any other potentially interfering optical effects (reflection, refraction) were properly taken into account. This was achieved by normalizing the experimental data against the 0° irradiance measurements.

After the necessary model verification steps illustrated before, the CFD model was used to estimate the actual optical properties of the TiO_2 suspensions. A matrix of CFD simulations were conducted by varying, according to a multi-level full-factorial design of experiments, the absorption and scattering coefficients using 5 m^{-1} as the incremental step. A typical result obtained after numerical convergence is reported in figure 3.2, which refers to the case of 400 mg L^{-1} TiO_2 concentration and 355 nm wavelength. To assess the goodness of fitting for each pairs of coefficients, the error was estimated as overall deviation of simulated data with respect to corresponding experimental data as indicated in equation e3.6:

$$Error = \sum_{Angular\ direction} |\mathrm{Log}_{10} I_{EXP} - \mathrm{Log}_{10} I_{SIM}| \tag{e3.6}$$

where I_{SIM} and I_{EXP} are the simulated irradiance values and the experimentally measured values at the outer boundary for a given angular direction, respectively. The logarithm of radiation intensity was used in order to better incorporate into the estimate the contribution of all irradiance measurements for the various angles (while also mitigating the impact of the highest values). An error surface was generated for each combination of UV wavelength and TiO_2 concentration. As shown in figure 3.5, a minimum can be observed indicating the optimal estimates for the absorption and scattering coefficients at 355 nm wavelength and 400 mg L^{-1} TiO_2 concentration.

Absorption and scattering coefficients estimated by this method are reported in table 3.2 and their graphical representation is given in Supporting Information (SI3.5), while simulated data for the best fitting optical properties are shown in figure 3.4. Interestingly, for 254 nm wavelength, a significant deviation from experimental data was observed at low and high angles at all TiO_2 concentrations. The CFD model was able to predict a sudden change in UV irradiance around the 10° angle, which was not observed by radiometric measures, whose trend gradually decreased with increasing angle. The same variation was detected experimentally at 355 nm wavelength and successfully described by CFD simulations. With respect to high-angle measurements, the increase in sensor response passing the 140° angle was underestimated by the CFD simulations, which reported a slight ascending trend not comparable with the experimental data. Moreover, CFD simulations were not completely satisfactory in reproducing experimental data at 254 nm wavelength and 400 mg L^{-1} TiO_2 concentration, whose trend was slightly decreasing with angle, unlike simulated data.

All error surfaces were characterized by the same shape, showing an absolute minimum and having slopes more pronounced along the axis of the absorption coefficient then the one of the scattering coefficient, thus indicating a greater sensitivity to the former coefficient.

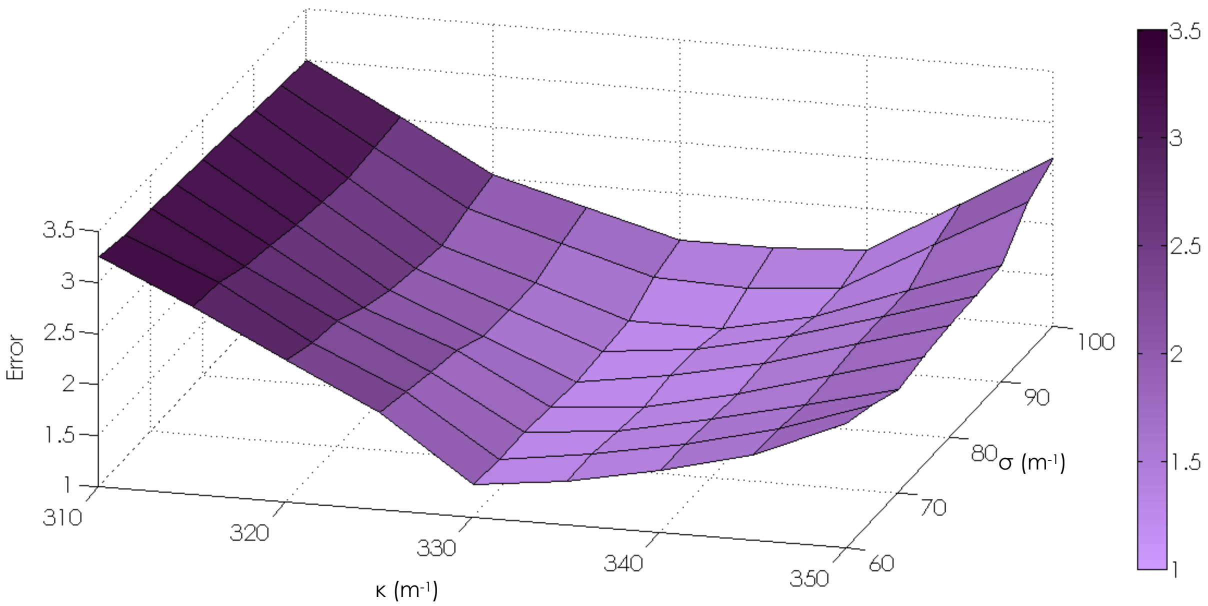

Figure 3.5 Error surface for experimental UV irradiance data fitting by CFD simulations as a function of absorption (κ) and scattering (σ) coefficients at 355 nm wavelength and 400 mg L^{-1} TiO_2 concentration.

An average confidence interval was calculated for the estimated absorption and scattering coefficients by assessing the change in their values required for getting an increase in the overall deviations of a factor of 1.5. This evaluation was carried out as suggested by Press et al. (2007) [35]. Simulated data as a function of absorption and scattering coefficients for 355 nm wavelength and 400 mg L^{-1} TiO_2 concentration are reported in Supporting Information (SI3.6).The results suggest that the uncertainties associated with the estimate around the optimum are ±35 m^{-1} and ±5 m^{-1} for absorption and scattering coefficients, respectively.

A comparison with the optical properties reported in literature was only possible at 355 nm wavelength. The optical properties estimated in this paper are comparable with those determined by Toepfer et al. [34] and subsequently used by Grcic et Li Puma [31], as discussed in detail later.

However, both absorption and scattering coefficients are significantly lower than those reported by Satuf et al. [24], who carried out the estimation on sonicated TiO_2 suspensions. As known, pre-treatment by sonication determines the breakage of TiO_2 aggregates resulting into a particle size distributions dominated by smaller particles. In fact, a value of 125±31 nm (mean±st.dev.) was reported for sonicated P25 Aeroxide TiO_2 suspensions by Jassby et al. [36], while an average particle size of 1642 nm was measured in the absence of sonication by Toepfer et al. [34]. The correlation between extinction coefficient and TiO_2 aggregate size was described by Salaices et al. [7] in a previously published research work.

All cited papers state that albedo is stable as a function of TiO_2 concentration, as also observed in the present study (table 3.2). Moreover, a list of values for albedos was estimated by Satuf et al. [24] and adopted by all the other research works afterwards, reporting a value of 0.778 at 355 nm, which is in good agreement with the present findings.

In the literature, the linear increase of absorption and scattering coefficients with TiO_2 concentration is reported, such as it was observed here (see Supporting Information, SI3.5). The occurrence of aggregation with the increase of TiO_2 concentration, discussed under a theoretical point of view by Kallay and Zalac [37] and possibly causing a decrease in TiO_2 suspension extinctance, was not observed, although an experimental verification was not performed.

At 254 nm wavelength, the albedo was constant at 40 for a 100 mg L^{-1} TiO_2 suspension, indicating a greater impact of absorption over the scattering. The same was not observed for the 355 nm wavelength. This outcome agrees with Satuf et al. [24], who reported this behaviour for wavelengths below 325 nm, although the lower investigated value was 295 nm. Finally, optical properties at 400 mg L^{-1} TiO_2 concentration, whose values conflict with those observed at lower concentrations, emphasize the inability of CFD simulations to deal with this operating condition.

3.3.3 CFD modelling of oxalic acid degradation

The optical parameters estimated in this research work using the new procedure illustrated before have been indirectly validated by predicting, using CFD, the oxalic acid degradation reported in a previous study [31], which employed an annular photoreactor fed with TiO_2 suspensions at concentrations comparable to the one used in the present work.

The validation of the CFD code was performed in steps. As a first step, the CFD analysis focused on the modelling of radiation transfer in the annular photoreactor with the aim of evaluating the local volumetric rate of photon absorption (LVRPA), namely the amount of energy determining TiO_2 photoactivation in each point of the reactor. As a second step, Navier-Stokes equations were solved to describe the velocity fields inside the photoreactor. As a third step, the oxalic acid concentration was simulated by coupling the intrinsic degradation kinetics of oxalic acid with the LVRPA and then solving for an additional scalar transport equation responsible for evaluating its degradation in the photoreactor domain. Finally, as a last step, the decrease in the concentration of oxalic acid inside the external tank, continuously mixed and connected in a recirculation loop with the photoreactor, was simulated.

In the first step, the LVRPA in the photoreactor was simulated using both the optical properties estimated in this research work at 355 nm, accounting for the HG scattering phase function (data in figure 3.3 for 107.21 W m^{-2} irradiance at lamp surface and 400 mg L^{-1} TiO_2 concentration), and the one estimated by [31], accounting for isotropic (ISO) and diffuse reflectance (DR) scattering phase functions. A summary of optical properties is reported in table 3.3.

As shown in figure 3.6, where simulated data are compared to radiometric measures at the lamp surface and at the reactor outer wall [31], CFD simulations were effective in describing irradiation phenomena. Likewise, simulated data obtained adopting the optical properties here estimated using the HG function are comparable to those obtained using absorption and scattering coefficients provided by [31], assuming isotropic scattering. The assumption of diffuse reflectance scattering determined an underestimation of UV irradiance at reactor outer wall, so that a new set of optical parameters was assumed, in order to improve the fitting. Re-estimated absorption and scattering coefficients, complying with the condition of albedo equal to 0.86, are reported in bold in table 3.3. The UV irradiance as a function of the position on the outer wall showed a different trend in the case of CFD simulations with respect to the evaluation carried out by [31] using the six-flux model (SFM). In particular, in CFD simulations the fluence rate distribution was more uniform along the length of the reactor and steepest decreases were observed at the ends, probably due to the better descriptive ability of the DO model, which takes into account the optical behaviour of glass volumes, involving reflection and refraction phenomena.

Table 3.3 Optical properties and intrinsic kinetic parameters used for CFD simulation of the degradation of oxalic acid. Three models were assessed using different scattering phase functions: isotropic (ISO), diffuse reflectance (DR) and Henyey-Greenstein (HG). Absorption (κ) and scattering (σ) coefficients are given at 100 mg L^{-1} and 400 mg L^{-1} TiO_2 concentration for ISO and HG models, unlike for DR model (only at 400 mg L^{-1}). Values for ISO and DR models and kinetic parameters are reported from [31]. Re-estimated κ and σ for DR model are reported in bold.

Model	**ISO**	**DR**	**HG**
κ (m^{-1})	18.7 - 74.8	74.8 > **62.8**	25 - 80
σ (m^{-1})	116.3 - 465.2	465.2 > **390.4**	135 - 330
Albedo (-)	0.86		0.84 - 0.80
k_a (kmol$^{1/2}$ s^{-1} W$^{-1/2}$)	(2.21±0.25)10^{-6}		
k_b (m$^{3/2}$ s^{-1} W$^{-1/2}$)	0.56±0.06		
α (m^3 s^{-1} W^{-1})	45		
β (m^3 kmol^{-1})	(1.3±0.3)10^{-4}		

LVRPA, that was computed as the product of fluence rate times the absorption coefficient, was modelled under the various operating conditions (irradiance at UV lamp surface and TiO_2 concentration) corresponding to the ones tested by [31]; its value at half the reactor length is reported in figure 3.7 vs. dimensionless radial thickness of the reactor (ξ^*) for the three scattering models. Similar results were obtained for ISO and HG models, while a slightly lower curve was observed for DR model, adopting the re-estimated optical properties. Therefore, the integral LVRPA was almost identical for ISO and HG models and lower for DR model, as shown in table 3.4, where the energy balance is given. These results confirm that ISO and HG models are comparable in irradiation modelling, unlike DR model. Being the UV lamp power equal to 1.08 W, obtained as the product of irradiance at UV lamp surface and UV lamp surface (0.0101 m^2), it can be concluded that about only half of the radiative energy is absorbed by the TiO_2 suspension suggesting that, if properly optimized, the energy efficiency of the photoreactor can be roughly doubled. Actually, a significant part of the radiation is lost from external walls (~ 25%) and another part is reflected or back-scattered to UV lamp surface (~ 15%).

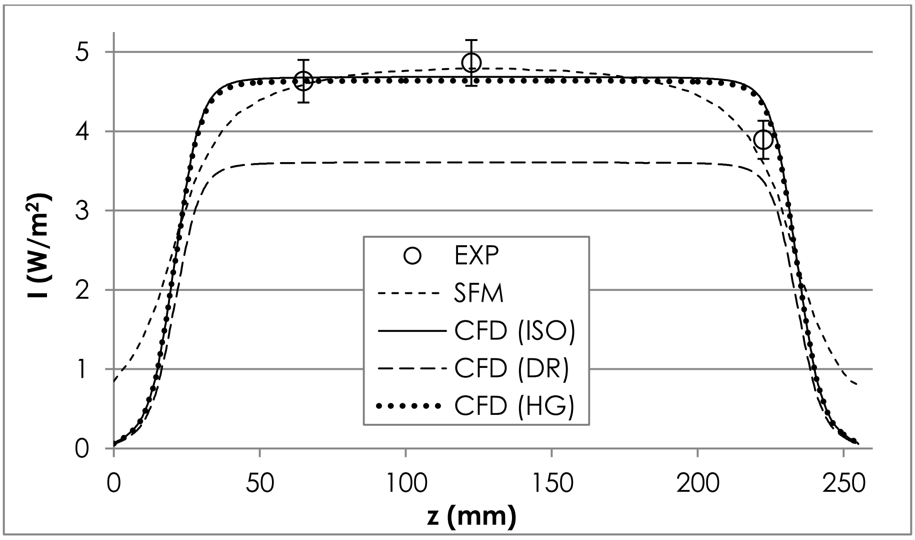

Figure 3.6 UV irradiance at the reactor outer wall (I) vs. position along longitudinal axis at 107.21 W m^{-2} UV irradiance at lamp surface and 400 mg L^{-1} TiO_2 concentration. Experimental (EXP) and six-flux model simulated (SFM) data were derived from [31], while CFD simulated (CFD) data were calculated based on three scattering phase functions: isotropic (ISO), diffuse reflectance (DR) and Henyey-Greenstein function (HG).

As for the second step, laminar velocity profile and hydraulic retention times in the annulus have been simulated and shown in Supporting Information (SI3.7). As expected for the case of laminar flow in an annular reactor, the velocity is minimum at reactor internal walls, where the hydraulic retention time of TiO_2 suspension is significantly higher (~11 s) with respect to the centre (~ 2 s).

Table 3.4 Energy balance at 107.21 W m^{-2} UV irradiance at lamp surface and 400 mg L^{-1} TiO_2 concentration for the three scattering models. Results are given in terms of absorbed Watts and as percentage over total emitted energy. 'UV lamp' refers to radiation returning to UV lamp boundary after emission.

Model	ISO		DR		HG	
Pyrex glass	0.052	4.8%	0.059	5.5%	0.051	4.7%
Liquid volume	0.586	54.3%	0.534	49.3%	0.576	53.4%
Borosilicate glass	0.014	1.3%	0.015	1.4%	0.014	1.3%
External loss	0.262	24.2%	0.269	24.8%	0.259	24.0%
UV lamp	0.165	15.3%	0.206	19.0%	0.180	16.7%

As third step, the degradation of oxalic acid in the annulus was simulated in a single pass to determine the rate of oxalic acid degradation as a function of oxalic acid concentration at reactor inlet. Then, the oxalic acid degradation rate was used for estimating the change in concentration over time in the recirculation tank (i.e., the forth step in the modelling procedure) as in equation e3.5. Simulated data vs. time are compared with experiments in figure 3.8 at different lamp irradiances, TiO_2 concentrations and initial oxalic acid concentrations.

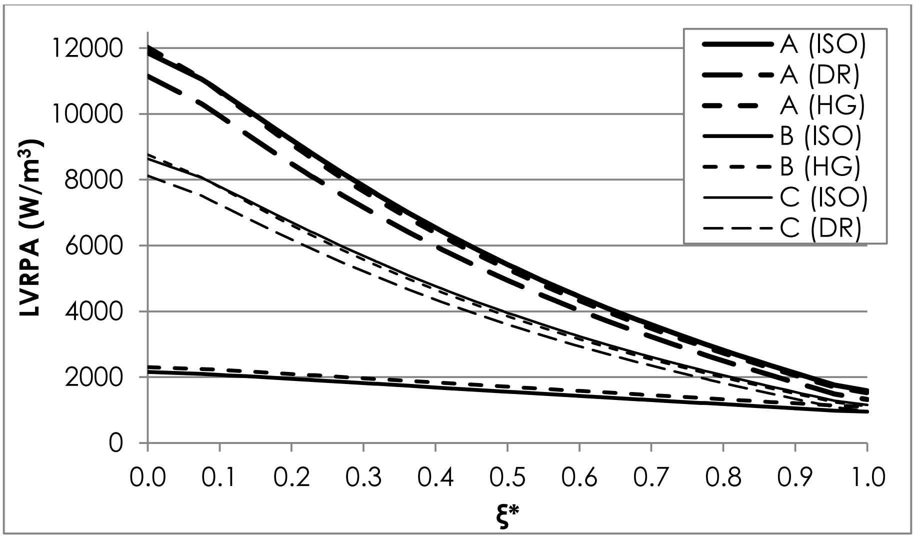

Figure 3.7 Simulated LVRPA vs. reactor dimensionless radial thickness (ξ*) in 3 configurations, as a function of UV irradiance at lamp surface and TiO_2 concentration: (A) 107.21 W m^{-2} - 400 mg L^{-1} TiO_2, (B) 107.21 W m^{-2} - 100 mg L^{-1} TiO_2, (C) 78.11 W m^{-2} - 400 mg L^{-1} TiO_2. Three models were assessed, characterized by different scattering phase functions: isotropic (ISO), diffuse reflectance (DR) and Henyey-Greenstein (HG). DR model has not been simulated in configuration B in the absence of appropriate optical properties.

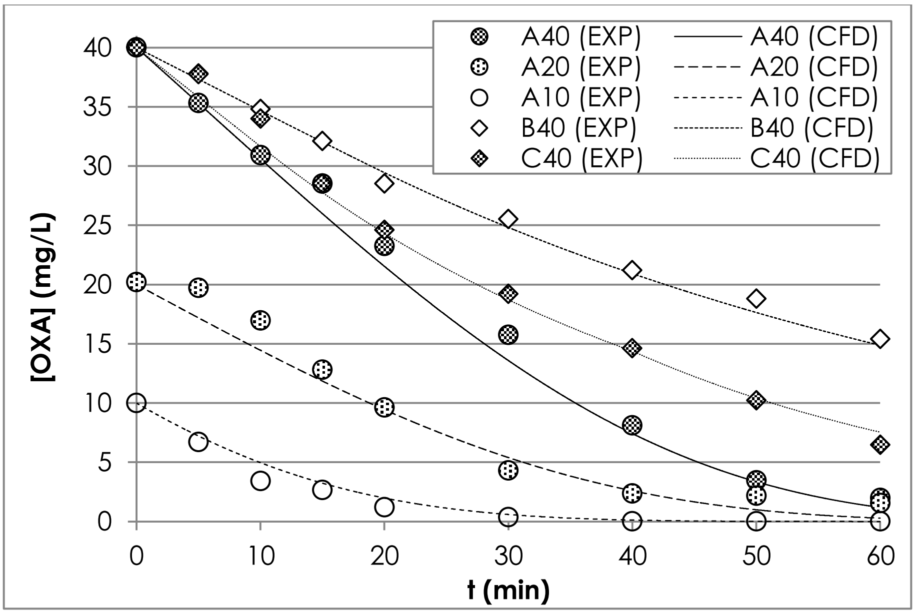

Figure 3.8 Experimental (EXP) and simulated (CFD) oxalic acid (OXA) concentration vs. time in 5 configurations, as a function of irradiance at the lamp surface, TiO_2 concentration and initial oxalic acid (OXA_{IN}) concentration: (A40) 107.21 W/m^2 - 400 mg L^{-1} TiO_2 - 40 mg L^{-1} OXA_{IN}, (A20) 107.21 W/m^2 - 400 mg L^{-1} TiO_2 - 20 mg L^{-1} OXA_{IN}, (A10) 107.21 W/m^2 - 400 mg L^{-1} TiO_2 - 10 mg L^{-1} OXA_{IN}, (B) 107.21 W/m^2 - 100 mg L^{-1} TiO_2 - 40 mg L^{-1} OXA_{IN}, (C) 78.11 W/m^2 - 400 mg L^{-1} TiO_2 - 40 mg L^{-1} OXA_{IN}. Experimental data were derived from [31].

Remarkably CFD simulations predicted very well the oxalic acid degradation under all operating conditions, confirming the accuracy of the optical properties estimated in our study. Moreover, the validity of intrinsic kinetic parameters estimated by [31], and reported in table 3.3, was also confirmed by CFD simulations. Additional simulation results are reported in Supporting Information (SI3.8), including LVRPA, velocity vectors and oxalic acid concentration at the steady state for 40 mg L^{-1} oxalic acid concentration at reactor inlet. Local oxalic acid concentration is related to the combined influence of LVRPA and hydraulic retention time. Lowest concentrations were obtained close to the inner wall, where the amount of absorbed radiation and hydraulic retention time are higher, as shown in Supporting Information (SI3.8).

3.4 CONCLUSIONS

A new methodology based on the combined use of an optical goniometer and a CFD model for the accurate quantification of optical properties for TiO_2 suspensions was successfully developed. In detail, it consists of iteratively solving the radiative transfer equation for various combinations of absorption and scattering coefficients until the error between observed and predicted angular irradiance is minimized. Special attention was paid to characterizing the scattering component. In fact, various scattering phase functions were tested against the experimental data confirming that the Henyey-Greenstein function was the most appropriate approximation. Moreover, a mechanistic CFD model was developed for the detailed description of the photocatalytic degradation of oxalic acid in a semi-batch annular reactor. The model was successfully validated against a previously published work, indicating the considerable potential of CFD-based model for photocatalytic reactor design, optimization and scale-up for water and wastewater treatment applications.

3.5 REFERENCES

[1] M.N. Chong, B. Jin, C.W.K. Chow, C. Saint, Recent developments in photocatalytic water treatment technology: a review, Water Res. 44 (2010) 2997–3027.

[2] K. Nakata, A. Fujishima, TiO_2 photocatalysis: design and applications, J. Photochem. Photobiol. C Photochem. Rev. 13 (2012) 169–189.

[3] C. Turchi, Photocatalytic degradation of organic water contaminants: mechanisms involving hydroxyl radical attack, J. Catal. 122 (1990) 178–192.

[4] V. Pareek, S. Chong, M. Tadé, A.A. Adesina, Light intensity distribution in heterogenous photocatalytic reactors, Asia-Pacific J. Chem. Eng. 3 (2008) 171–201.

[5] C. McCullagh, N. Skillen, M. Adams, P.K.J. Robertson, Photocatalytic reactors for environmental remediation: a review, J. Chem. Technol. Biotechnol. 86 (2011) 1002–1017.

[6] O. Alfano, A. Negro, Scattering effects produced by inert particles in photochemical reactors. 1. Model and experimental verification, Ind. Eng. Chem. Res. 34 (1995) 488–499.

[7] M. Salaices, B. Serrano, H.I. De Lasa, Experimental evaluation of photon absorption in an aqueous TiO_2 slurry reactor, 90 (2002) 219–229.

[8] V.K. Pareek, A. a. Adesina, Light intensity distribution in a photocatalytic reactor using finite volume, AIChE J. 50 (2004) 1273–1288.

[9] G. Li Puma, A. Brucato, Dimensionless analysis of slurry photocatalytic reactors using two-flux and six-flux radiation absorption-scattering models, Catal. Today. 122 (2007) 78–90.

[10] B. Yu, B. Deng, C.N. Kim, Performance evaluation of P-1 model in a photocatalytic reactor, Chem. Eng. Sci. 63 (2008) 5552–5558.

[11] J. Moreira, B. Serrano, A. Ortiz, H. De Lasa, Evaluation of photon absorption in an aqueous TiO_2 slurry reactor using Monte Carlo simulations and macroscopic balance, Ind. Eng. Chem. Res. 49 (2010) 10524–10534.

[12] R.A. French, A.R. Jacobson, B. Kim, S.L. Isley, R.L.E.E. Penn, L. Penn, et al., Influence of ionic strength, pH, and cation valence on aggregation kinetics of titanium dioxide nanoparticles, Environ. Sci. Technol. 43 (2009) 1354–1359.

[13] A.A. Keller, H. Wang, D. Zhou, H.S. Lenihan, G. Cherr, B.J. Cardinale, et al., Stability and aggregation of metal oxide nanoparticles in natural aqueous matrices, Environ. Sci. Technol. 44 (2010) 1962–1967.

[14] Y.H. Shih, C.M. Zhuang, C.P. Tso, C.H. Lin, The effect of electrolytes on the aggregation kinetics of titanium dioxide nanoparticle aggregates, J. Nanoparticle Res. 14 (2012).

[15] C.F. Bohren, D.R. Huffman, Absorption and scattering of light by small particles, Wiley, 1983.

[16] M.L. Satuf, R.J. Brandi, A.E. Cassano, O.M. Alfano, Photocatalytic degradation of 4-chlorophenol: a kinetic study, Appl. Catal. B Environ. 82 (2008) 37–49.

[17] R.L. Pozzo, R.J. Brandi, A.E. Cassano, M. a. Baltanás, Photocatalytic oxidation of oxalic acid in dilute aqueous solution, in a fully illuminated fluidized bed reactor, Chem. Eng. Sci. 65 (2010) 1345–1353.

[18] G. Sagawe, M.L. Satuf, R.J. Brandi, J.P. Muschner, C. Federer, O.M. Alfano, et al., Analysis of photocatalytic reactors employing the photonic efficiency and the removal efficiency parameters: degradation of radiation absorbing and nonabsorbing pollutants, Ind. Eng. Chem. Res. 49 (2010) 6898–6908.

[19] C.A. Martín, M.A. Baltanás, A.E. Cassano, Photocatalytic reactors I. Optical behavior of titanium oxide particulate suspensions, J. Photochem. Photobiol. A Chem. 76 (1993) 199–208.

[20] S.A. Prahl, M.J. van Gemert, A.J. Welch, Determining the optical properties of turbid mediaby using the adding-doubling method., Appl. Opt. 32 (1993) 559–68.

[21] Q. Yang, P. Ling Ang, M.B. Ray, S.O. Pehkonen, Light distribution field in catalyst suspensions within an annular photoreactor, Chem. Eng. Sci. 60 (2005) 5255–5268.

[22] P. Pichat, Photocatalysis and Water Purification: From Fundamentals to Recent Applications, Wiley-VCH, 2013.

[23] M.I. Cabrera, O.M. Alfano, A.E. Cassano, V. Uni, C. Nacional, D.I. V, Absorption and scattering coefficients of titanium dioxide particulate suspensions in water, J. Phys. Chem. 100 (1996) 20043–20050.

[24] M.L. Satuf, R.J. Brandi, A.E. Cassano, O.M. Alfano, Experimental method to evaluate the optical properties of aqueous titanium dioxide suspensions, Ind. Eng. Chem. Res. 44 (2005) 6643–6649.

[25] R.L. Romero, O.M. Alfano, A.E. Cassano, Cylindrical photocatalytic reactors. Radiation absorption and scattering effects produced by suspended fine particles in an annular space, Ind. Eng. Chem. Res. 36 (1997) 3094–3109.

[26] F.J. Trujillo, T. Safinski, A.A. Adesina, Oxidative photomineralization of dichloroacetic acid in an externally-irradiated rectangular bubble tank reactor: Computational fluid dynamics modeling and experimental verification studies, Ind. Eng. Chem. Res. 49 (2010) 6722–6734.

[27] J.E. Duran, M. Mohseni, F. Taghipour, Computational fluid dynamics modeling of immobilized photocatalytic reactors for water treatment, AIChE J. 57 (2011) 1860–1872.

[28] N. Qi, H. Zhang, B. Jin, K. Zhang, CFD modelling of hydrodynamics and degradation kinetics in an annular slurry photocatalytic reactor for wastewater treatment, Chem. Eng. J. 172 (2011) 84–95.

[29] Y. Boyjoo, M. Ang, V. Pareek, CFD simulation of a pilot scale slurry photocatalytic reactor and design of multiple-lamp reactors, Chem. Eng. Sci. 111 (2014) 266–277.

[30] I. Grčić, G. Li Puma, Photocatalytic degradation of water contaminants in multiple photoreactors and evaluation of reaction kinetic constants independent of photon absorption, irradiance, reactor geometry, and hydrodynamics, Environ. Sci. Technol. 47 (2013) 13702–13711.

[31] Papanastasiou T.C., Georgiou G.C., Alexandrou A.N., Viscous fluid flow, CRC Press, 2000.

[32] C.B. Mendive, T. Bredow, M.A. Blesa, D.W. Bahnemann, ATR-FTIR measurements and quantum chemical calculations concerning the adsorption and photoreaction of oxalic acid on TiO_2, Phys. Chem. Chem. Phys. 8 (2006) 3232–3247.

[33] B. Toepfer, A. Gora, G. Li Puma, Photocatalytic oxidation of multicomponent solutions of herbicides: reaction kinetics analysis with explicit photon absorption effects, Appl. Catal. B Environ. 68 (2006) 171–180.

[34] W. Press, S. Teukolsky, W. Vetterling, B. Flannery, Numerical recipes: the art of scientific computing, Cambridge University Press, 1987.

[35] D. Jassby, J.F. Budarz, M. Wiesner, N. Carolina, Impact of aggregate size and structure on the photocatalytic properties of TiO_2 and ZnO nanoparticles, Environ. Sci. Technol. 46 (2012) 6934–6941.

[36] N. Kallay, S. Zalac, Stability of nanodispersions: a model for kinetics of aggregation of nanoparticles., J. Colloid Interface Sci. 253 (2002) 70–76.

3.6 SUPPORTING INFORMATION

SI3.1 Governing equations, models and numerical methods

The Cartesian tensor notation was used for the flow and mass transfer equations. For a steady state incompressible flow, the conservation laws of mass, momentum and concentration are given:

Continuity

$$\frac{\partial U_j}{\partial x_j} = 0 \qquad \text{(eSI3.1)}$$

Momentum

$$\frac{\partial \left(U_j U_i\right)}{\partial x_j} = -\frac{1}{\rho}\frac{\partial P}{\partial x_i} + \frac{\partial}{\partial x_i}\left(\nu \frac{\partial U_i}{\partial x_j} - \overline{u_\iota u_\jmath}\right) \qquad \text{(eSI3.2)}$$

Mass species

$$\frac{\partial \left(U_i Y_j\right)}{\partial x_j} = \frac{\partial}{\partial x_j}\left(\frac{\nu}{Sc}\frac{\partial Y_i}{\partial x_j} - \overline{u_y y_\iota}\right) + R_i \qquad \text{(eSI3.3)}$$

in which ρ, ν and Sc are the density, the kinematic viscosity and the Schmidt number, respectively. In equation eSI3.3 R_i represents the net rate of production due to involved chemical reactions for each component included in the CFD model. The equations are not explained in detail for brevity, for more information the related book by Veersteeg and Malalasekera is recommended [SI1].
The radiative transfer equation is the following:

Radiative transfer equation

$$\begin{aligned}\frac{dI_\lambda}{ds} &= -\kappa_\lambda I_\lambda(s,\Omega) - \sigma_\lambda I_\lambda(s,\Omega) \\ &\quad + \frac{1}{4\pi}\sigma_\lambda \int_0^{4\pi} p(\Omega' \to \Omega) I_\lambda(s,\Omega') I_\lambda(s,\Omega') d\Omega'\end{aligned} \qquad \text{(eSI3.4)}$$

in which I_λ, κ_λ, σ_λ are the radiation intensity, the absorption and the scattering coefficients, respectively. The radiation transmission at a certain wavelength (I_λ) in a spherical reference system (spatial coordinates s and Ω) is determined by optical phenomena described by the terms on the right hand side: the first term describes the absorbed radiation, the second term the out-scattering of radiation and the third term the gain of energy due to the in-scattering of radiation.

The discrete ordinates (DO) radiation model solves the radiative transfer equation (RTE) for a finite number of discrete solid angles, by associating each angle to a direction vector. Basically it transforms the RTE in a transport equation for radiation intensity and it solves as many transport equations as the number of direction vectors. More details are reported in the ANSYS Fluent guide. In case of CFD modelling of TiO_2 suspensions optical properties, the parameters of the DO model were increased on Phi to 64 for angular discretization, both with respect to division and pixelation terms, while Theta values equal to 2 were found to be appropriate. This adaptation was necessary for obtaining a symmetrical beam on the emission plane. When the degradation of oxalic acid was simulated, Phi and Theta values were increased to 8 for division and pixelation terms. In the latter case the adaptation allowed to get a radiation field that varied smoothly in the reactor volume.

Flow equations were solved with 'SIMPLE' algorithm for pressure-velocity coupling and second order upwind discretization. The no-slip boundary condition was employed for all solid walls, whereas an assigned velocity profile and atmospheric pressure boundary conditions were prescribed at inlet and outlet, respectively. The non-linear convection terms in all transport equations were approximated by means of the Power Law scheme.

Solving the radiation intensity, all walls were assumed to be opaque. The quartz and glasses were set as semi-transparent with zero as diffuse fraction. In case of CFD modelling of TiO_2 suspensions optical properties, the UV lamp was modeled as a semi-transparent wall emitting direct radiation, while for CFD simulation of oxalic acid degradation, the UV lamp was set as a semi-transparent wall completely emitting diffuse radiation.

The simulations were performed using a desktop computer equipped with an Intel i7-4770 processor at 3.40 GHz and 16 GB RAM memory. CFD simulations for the modelling of TiO_2 suspensions optical properties required about 2 hours to perform 100 iterations with the DO model, necessary to achieve stable residual values. Concerning CFD simulation of the degradation of oxalic acid, 500 iterations were required for reaching the convergence with the DO model in about 2 hours, while 5000 and 100 iterations were performed for solving respectively the fluid dynamics and the kinetic model within a few minutes. The grid-independence was verified in both cases. The residues were below 10^{-5} for radiative transfer equation, both in case of direct and diffuse irradiation simulation, as well as below 10^{-15} for momentum, continuity and mass species equations.

SI3.2 Geometrical specifications of PR1 reactor

Table SI3.1 Geometrical specifications of PR1 reactor.

Overall	Length (m)	0.255
	Radius (m)	0.0225
Lamp	Bulb length (m)	0.213
	Bulb radius (m)	0.00753
Pyrex glass	Inner radius (m)	0.011
	Outer radius (m)	0.013
Liquid volume	Inner radius (m)	0.013
	Outer radius (m)	0.018
Borosilicate glass	Inner radius (m)	0.018
	Outer radius (m)	0.0225

SI3.3 Radial velocity profile in the annulus and diffusivity of oxalic acid

The radial velocity profile (v) in the annulus was described as [SI2]:

$$v = \frac{2Q}{\pi R^2 \left[(1-\eta^4) - \frac{(1-\eta^2)^2}{\ln\left(\frac{1}{\eta}\right)} \right]} \left[1 - (r^*)^2 + \left(\frac{1-\eta^2}{\ln\left(\frac{1}{\eta}\right)} \right) \ln(r^*) \right] \qquad \text{(eSI3.5)}$$

in which Q is the flow rate, R is the reactor radius at the outer wall of the liquid volume, r* is reactor dimensionless radius and η is the ratio between the inner and the outer walls of the liquid volume.

The diffusivity (Γ) of oxalic acid was set to 9.83E-7 kg m^{-1} s^{-1}, according to the following equation, in which MW is the molecular weight of oxalic acid (90.03 g/mol) [SI3]:

$$\Gamma = \frac{2.4E-8}{MW^{0.71}} \qquad \text{(eSI3.6)}$$

SI3.4 Scattered radiation in the absence of TiO_2 nanoparticles

For 1.5 mm converging beam the best fitting of experimental data was achieved, as shown in figure SI3.1. A good fitting was obtained for low and high angles, while the simulated values were much lower than experimental ones at middle angles, probably because of the radiation intensity values comparable to the ambient light in the measurement chamber, not allowing more accurate measures, although the instrument detection limit was about 10^{-13} W cm^{-2}.

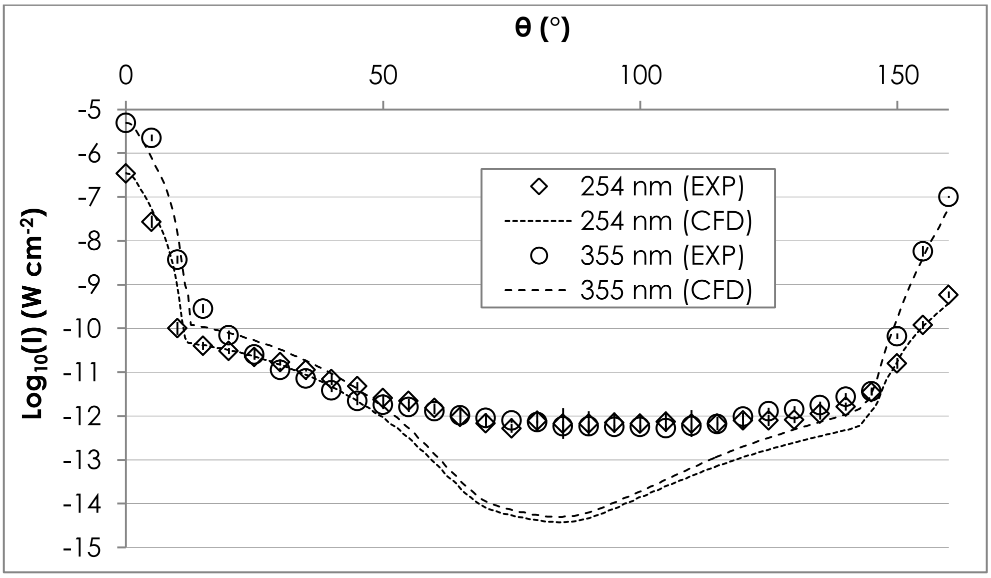

Figure SI3.1 Logarithm of UV radiation intensity (I) vs. direction angle in the absence of TiO_2 nanoparticles in suspension irradiated at 254 and 355 nm: experimental (mean±st.dev.) (EXP) and simulated (CFD) data.

SI3.5 Estimated optical properties of TiO_2 suspensions

The equations for asymmetry coefficients as a function of TiO_2 concentration (in mg L^{-1}) are given:

$$254\text{ nm}: g_\lambda = -0.0017[TiO_2] + 0.9874$$

$$355\text{ nm}: g_\lambda = -0.0034[TiO_2] + 0.9501$$

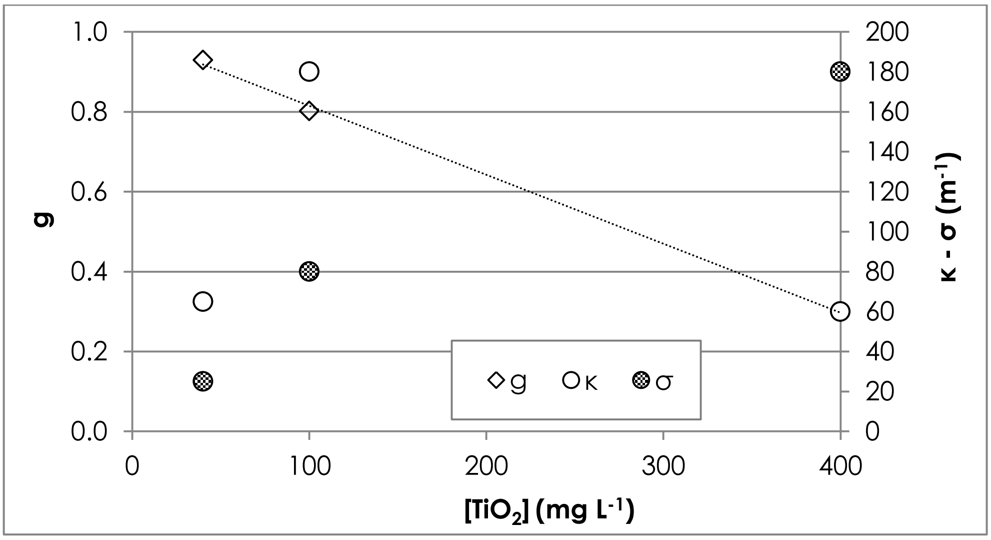

Figure SI3.2 Estimated optical properties of TiO_2 suspensions at 254 nm vs. TiO_2 concentration: asymmetry factor (g), absorption coefficient (κ) and scattering coefficient (σ).

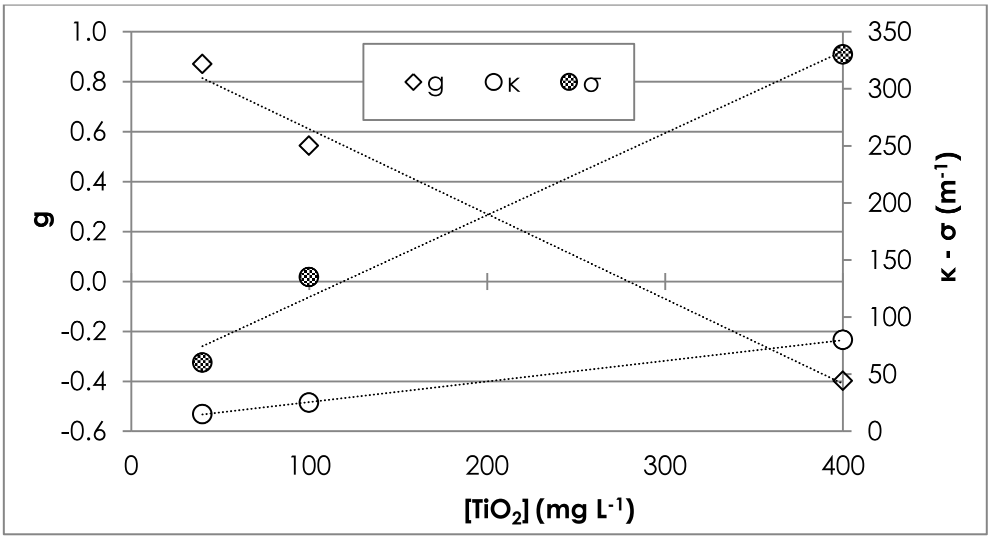

Figure SI3.3 Estimated optical properties of TiO_2 suspensions at 355 nm vs. TiO_2 concentration: asymmetry factor (g), absorption coefficient (κ) and scattering coefficient (σ).

SI3.6 Confidence interval for estimated optical properties

In figure SI3.4 the influence of changing the absorption coefficient was assessed keeping scattering coefficient constant (σ=330 m^{-1}), while in figure SI3.5 the same was repeated for scattering coefficient (κ=80 m^{-1}).

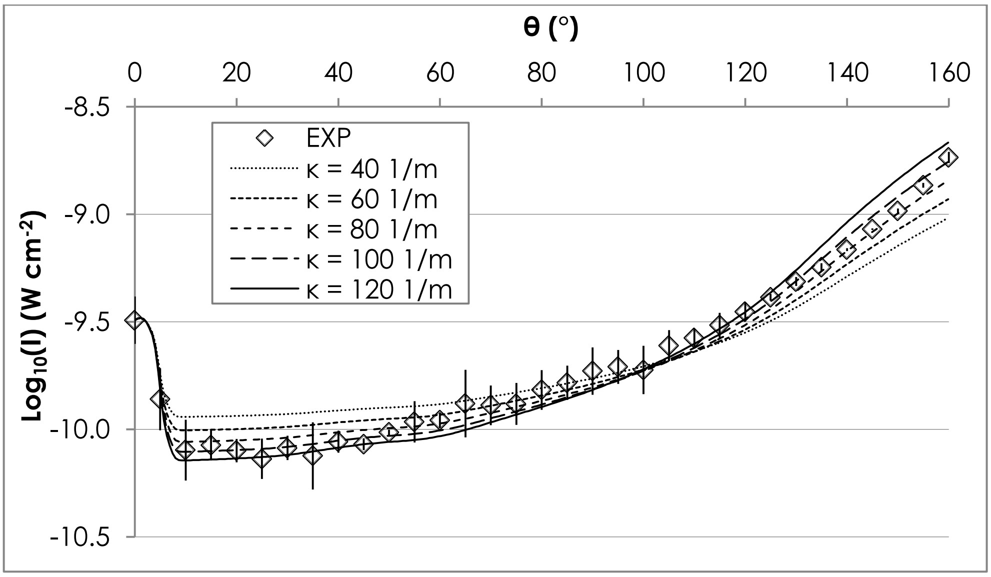

Figure SI3.4 Logarithm of UV radiation intensity (I) vs. direction angle as a function of absorption coefficient (κ) at 400 mg L^{-1} TiO_2 concentration and 355 nm UV emission wavelength: experimental (mean±st.dev.) (EXP) and simulated (CFD) data. Scattering coefficient (σ) in CFD simulations was constant at 330 m^{-1}.

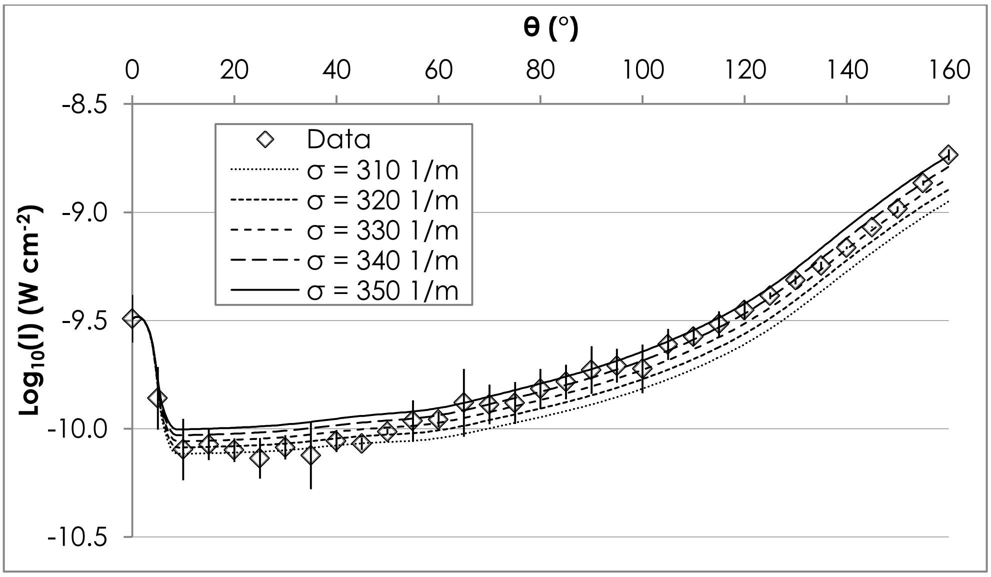

Figure SI3.5 Logarithm of UV radiation intensity (I) vs. direction angle as a function of scattering coefficient (σ) at 400 mg L^{-1} TiO_2 concentration and 355 nm UV emission wavelength: experimental (mean±st.dev.) (EXP) and simulated (CFD) data. Absorption coefficient (κ) in CFD simulations was constant at to 80 m^{-1}.

In table SI3.2 the errors for each combination of absorption and scattering coefficients studied in figure SI3.4 and SI3.5 are given at 355 nm wavelength and 400 mg L^{-1} TiO_2 concentration.

Table SI3.2 Errors for experimental data fitting by CFD simulations as a function of absorption (κ) and scattering (σ) coefficients at 355 nm wavelength and 400 mg L^{-1} TiO_2 concentration. The errors higher than 1.5 times the minimum, namely over 1.857, are reported in bold.

κ (m^{-1})	40	60	80	100	120			80		
σ (m^{-1})			330			310	320	330	340	350
Error	**2.344**	1.324	1.238	1.542	**1.876**	**3.113**	**1.985**	1.238	1.576	2.095

SI3.7 Fluid dynamics in PR1 reactor

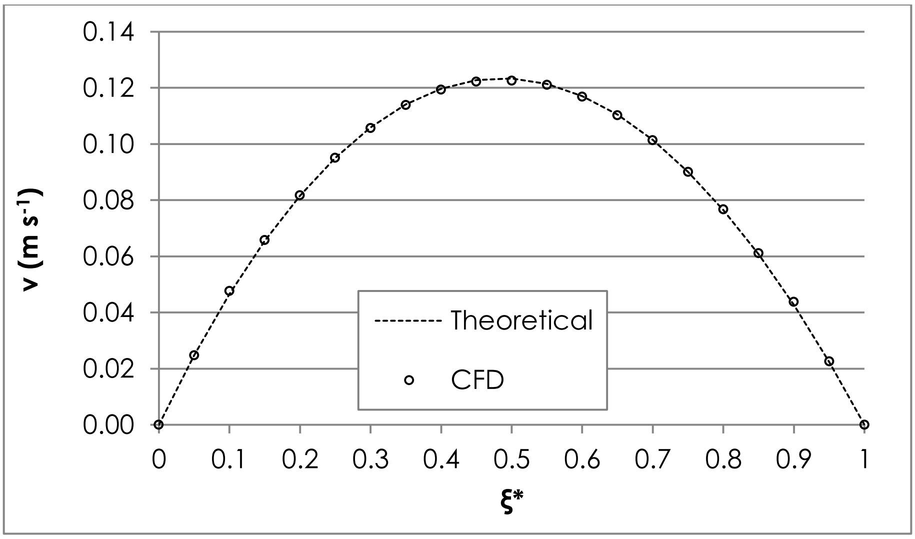

Figure SI3.6 Velocity profile vs. reactor dimensionless radial thickness (ξ*): theoretical and simulated (CFD).

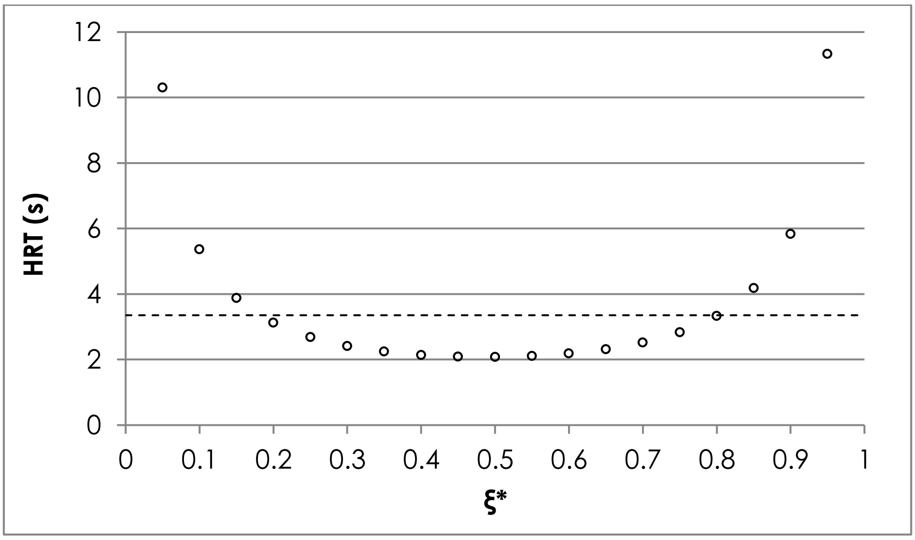

Figure SI3.7 Simulated hydraulic retention time (circles) and average hydraulic retention time (dashed line) vs. reactor dimensionless radial thickness (ξ*).

SI3.8 CFD simulation of oxalic acid degradation in PR1 reactor

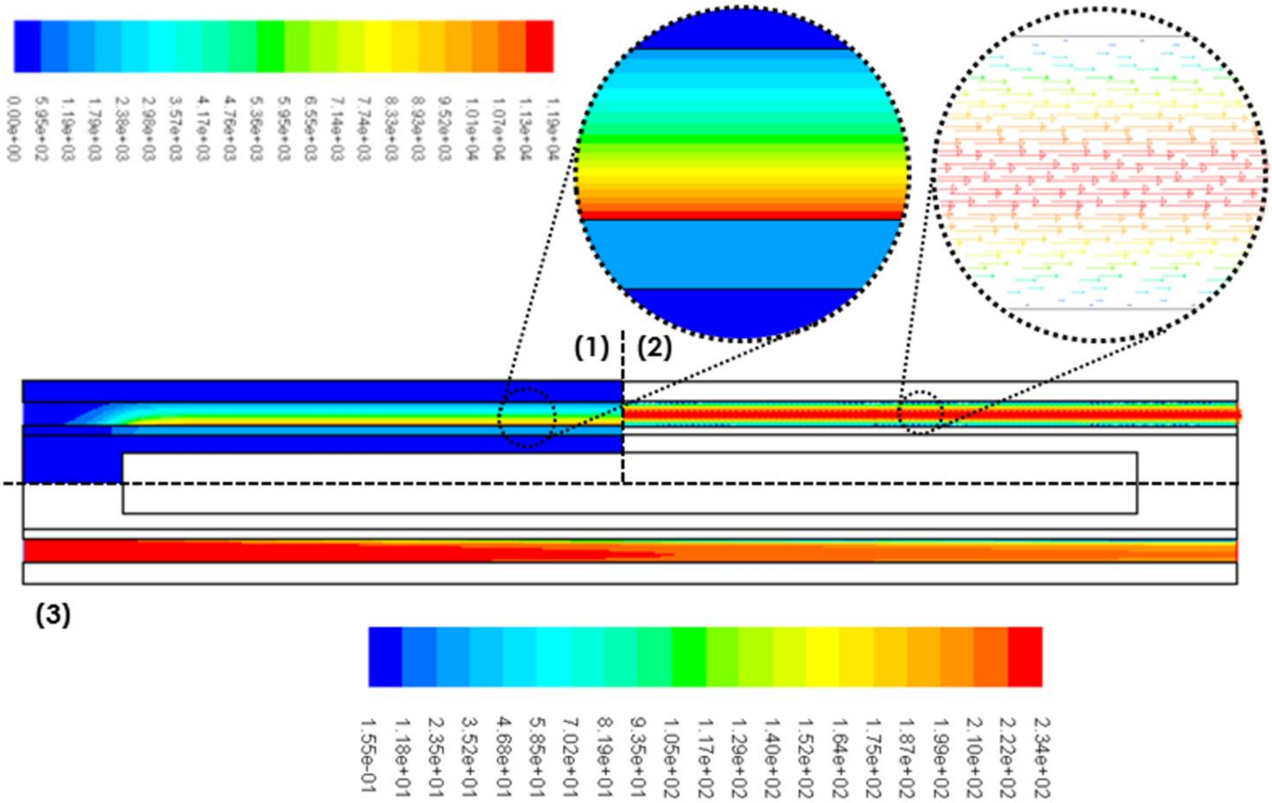

Figure SI3.8 CFD simulation of the degradation of oxalic acid in PR1 reactor at 107.21 W m^{-2} UV lamp radiation intensity and 400 mg L^{-1} TiO_2 concentration: (1) LVRPA (W m^{-3}), (2) velocity vectors, (3) oxalic acid concentration (mol L^{-1}) at the steady state for 40 mg L^{-1} oxalic acid concentration at reactor inlet.

REFERENCES

[SI1] H. Versteeg, W. Malalasekera, An introduction to computational fluid dynamics: the finite volume method, Prentice Hall, 2007.

[SI2] T.C. Papanastasiou, G.C. Georgiou, A.N. Alexandrou, Viscous fluid flow, CRC Press, 1999.

[SI3] R.P.Schwarzenbach, P.M. Gschwend, D.M. Imboden, Environmental organic chemistry, Wiley-VCH, 2003.

CHAPTER 4

EXPERIMENTAL MEASUREMENT AND MODELLING OF REACTIVE SPECIES GENERATION IN TiO_2 NANOPARTICLE PHOTOCATALYSIS

ABSTRACT

The generation of reactive species in titanium dioxide (TiO_2) nanoparticle photocatalysis was assessed in a laboratory scale setup, in which P25 Aeroxide TiO_2 suspensions were photoactivated by means of UV-A radiation. Photogenerated holes and hydroxyl radicals were monitored over time by observing their selective reaction with probe compounds, iodide and terephthalic acid, respectively. TiO_2 aggregate size and structure were characterized over the reaction time. Reactive species quenching was then described by a model, accounting for radiative phenomena, TiO_2 nanoparticle aggregation and kinetic reactions. The interaction between iodide and photogenerated holes was influenced by iodide adsorption on TiO_2 surface, described by a Langmuir-Hinshelwood mechanism, whose parameters were studied as a function of TiO_2 concentration and irradiation time. Iodide oxidation was effectively simulated by modelling the reaction volume as a completely stirred two-dimensional domain, in which irradiation phenomena were described by a two-flux model and the steady state for reactive species was assumed. The kinetic parameters for iodide adsorption and oxidation were estimated and successfully validated in a different experimental setup. The same model was adapted to describe the oxidation of terephthalic acid by hydroxyl radicals. The kinetic parameters for terephthalic acid oxidation were estimated and validated, while the issues in investigating the interaction mechanisms among the involved species have been discussed. The sensitivity of operating parameters on model response was assessed and the most relevant parameters were highlighted.

The research work described in the present chapter was carried out with the valuable support of
Andrea Piazzoli, PhD student, Politecnico di Milano, Italy
Jeffrey Farner Budarz, PhD student, Duke University, United States
Mark Wiesner, Full professor, Duke University, United States

The research work was partially carried out during a 6-month period of international mobility at the Center for the Environmental Implications of NanoTechnologies (CEINT), Duke University (Durham, North Carolina, United States).
The present chapter, after an adaptation in terms of formatting style, has been submitted for publication to the 'Chemical Engineering Journal' and it is currently under review.

4.1 INTRODUCTION

TiO_2 photocatalysis is a promising process arising from the peculiar photoelectrochemical properties of this semiconducting metal oxide. The process has been studied for a number of applications, mainly aimed at contaminant degradation technologies and renewable energy production [1–3]. For water and wastewater treatment applications, TiO_2 photocatalysis belongs to the family of advanced oxidation processes. The absorption of photons of appropriate wavelength ($\lambda<390$ nm) leads to the formation of electron-hole pairs, which can migrate to the surface of the photocatalyst. When in the presence of water and oxygen molecules, this results in the production of reactive oxygen species (ROS), such as hydroxyl radicals and superoxide radical anions [4,5]. The potential of these highly reactive, non-selective species has been reported in previous research for the inactivation of pathogens and the degradation of persistent organic pollutants, such as solvents, dyes, pesticides, pharmaceuticals and personal care products, *inter alia* [6,7]. Despite such interest, the process is still not an established technology, and research efforts continue to seek to develop sustainable technological applications.

Experimental protocols for the measurement of reactive species have been developed, allowing for the monitoring of ROS generation by means of molecular probes, highly selective chemicals whose reaction products can be easily quantified by spectrophotometric and fluorimetric measures [8–12]. The application of these protocols to TiO_2 photocatalysis represents an effective tool to directly assess reactivity and to further increase the knowledge about complex chemical-physical interaction mechanisms, whose comprehension otherwise usually relies on the study of the degradation of model pollutants, reacting simultaneously with different species [13–15].

Regarding photocatalysis by TiO_2 dispersions, reactivity depends strongly on nanoparticle aggregation size and structure [16,17]. When TiO_2 aggregates undergo photoactivation, particles on the inside of the aggregate are effectively shielded from illumination. The extent to which light can penetrate decreases as aggregate density increases, and only exposed nanoparticles can generate electron-hole pairs. Of these pairs, the fraction lost due to recombination is also a function of aggregate density, as closer charges are more likely to undergo recombination [18]. In turn, aggregate size and structure are determined by aqueous matrix properties, such as ionic strength, pH, and solution chemistry [19–23].

In a previous work by Jassby et al. [17] the influence of aggregate size and structure on the generation of hydroxyl radicals by TiO_2 nanoparticle photocatalysis was studied and a good correlation was highlighted. On the other hand, the evaluation of the two main oxidizing species involved, namely photogenerated holes and hydroxyl radicals, and comprehensive modelling throughout the process time have yet to be accomplished for TiO_2 nanoparticle photocatalysis. Indeed, a description of the process in terms of reactive species generation over a geometric domain as a function of operating conditions, and independent of the target contaminants, represents a fundamental step for process engineering and its application to large-scale reactors.

The purpose of this research was to monitor the generation of photogenerated holes (h^+) and hydroxyl radicals ($OH^•$) in TiO_2 nanoparticle photocatalysis, by observing their selective reactions with probe chemicals: iodide (dosed as potassium iodide, KI) to iodine (I_2) [10] and terephthalic acid (TA) to 2-hydroxyterephthalic acid (2-HTA), respectively [8]. P25 Aeroxide TiO_2 nanoparticle suspensions were photoactivated by means of UV-A radiation. The production of photogenerated holes and hydroxyl radicals was observed over time. A model for describing reactive species quenching by probe molecules is formulated, accounting for radiative phenomena, TiO_2 nanoparticle aggregation and kinetic reactions. The same model has been adapted for validation in a different experimental setup. Finally, the modelling of involved radical reactions is discussed, and the sensitivity of operating parameters on model response is assessed.

4.2 MATERIAL AND METHODS

4.2.1 TiO_2 dispersions and reagent solutions

Experiments were performed on P25 Aeroxide TiO_2 nanopowder (Evonik, Germany) suspended in deionized water (DI). TiO_2 stock suspension (100 mg L^{-1}) was prepared by adding 10 mg of P25 TiO_2 to 100 mL of deionized water and mixing on magnetic stirrer for 2 minutes at 120 RPM. KI was purchased from Sigma-Aldrich (USA). A starch solution was prepared adding 5 g of starch (Sigma-Aldrich) to 1 L of boiling deionized water and mixing until complete dissolution. After 12 h settling, the supernatant was collected and 2.5 g of salicylic acid (Merck, USA) were dosed as preservative. TA (0.5 mM) and 2-HTA (0.125 mM) solutions were prepared by adding 16.6 mg of TA (Sigma-Aldrich) and 4.69 mg of 2-HTA (Sigma-Aldrich) in 200 mL of deionized water, adjusting pH to 7.9 by KOH (Sigma-Aldrich) and mixing on magnetic stirrer overnight.

4.2.2 TiO_2 aggregate characterization

TiO_2 aggregate size and structure were investigated by laser light scattering with a Mastersizer 3000 (Malvern, England). TiO_2 stock suspensions were prepared as previously described and diluted to a final concentration of 20 mg L^{-1} in deionized water, with and without 50 mM KI, to observe the effect of the probe compound on aggregate stability. Samples were continuously mixed on a magnetic stirrer (400 RPM) and in-line dynamic light scattering measurements were performed using a peristaltic pump for sample loading located downstream of the instrument. Time resolved size measurements, reported as median diameter (D_{50}) both as number weighted and unweighted intensity, were taken over 30 minutes. To obtain information about aggregate structure, the scattering intensity, I(q), as a function of the scattering vector, q, for each sample was recorded over the same time period. The Mastersizer contains multiple detectors for the red He-Ne laser

(632.8 nm) ranging in angle from 0 to 50 degrees, which allows for the simultaneous collection of scattering intensity data at various angles. Plotting the logarithm of the scattering intensity, log(I(q)), versus the logarithm of the scattering vector, log(q), produces a curve containing the linear fractal region in which the intensity is exponentially proportional to D_f. Aggregate fractal dimension, D_f, is calculated as the negative slope of the linear fit of this region, and the range of q which comprises this region of linearity corresponds to the length scales over which the fractal behaviour holds [24].

4.2.3 TiO_2 nanoparticle reactivity measurement

TiO_2 nanoparticle reactivity measurements were performed in small beakers, in 10 mL batch reactors, continuously mixed on a magnetic stirrer (400 RPM) and irradiated at 365 nm. Experiments were carried out in UV boxes equipped with fluorescent UV lamps and thermostated at room temperature (22±1°C). Two different experimental setups were used, denoted UV1 and UV2. In UV1, samples were irradiated by a single 15 W lamp (Helios Italquartz, Italy), providing a radiation intensity (I) on the upper liquid surface of 1.8±0.1 mW cm^{-2}, measured by means of a radiometer (HD9021, Delta Ohm, Italy). The geometrical characteristics of the beaker (H=1 cm, Ø=5.7 cm) created a liquid layer 0.4 cm in thickness when the stirring bar (3x10 mm) was introduced. In UV2, two 15 W lamps (TL-D 15W BLB SLV, Philips, Netherlands) were mounted, resulting in 1.9±0.1 mW cm^{-2} intensity on the surface of samples, monitored by a ILT1400 radiometer equipped with a SEL033 detector (International Light, USA). The overall thickness of the liquid layer in the beaker (H=3.5 cm, Ø=5 cm) was 0.5 cm. Radiation intensity as a function of emission wavelength at the upper liquid surface of samples for each setup is reported in Supporting Information (SI4.1).

4.2.3.1 Photogenerated holes

Photogenerated hole production was evaluated in UV1 setup in three kind of experiments:

- sample irradiation for 30 minutes as a function of P25 TiO_2 (10, 25 and 40 mg L^{-1}) and KI (10, 30, 50, 75 and 100 mM) concentration,
- sample irradiation at different times (10, 20 and 30 minutes) as a function of KI concentration (10, 30, 50, 75 and 100 mM) for 40 mg L^{-1} P25 TiO_2 concentration,
- sample irradiation at different times (5, 10, 15, 20, 25 and 30 minutes) for 40 mg L^{-1} P25 TiO_2 and 50 mM KI concentration.

Samples were composed of variable volumes of 100 mg L^{-1} P25 TiO_2 stock suspension, 250 mM KI solution and deionized water. After irradiation, a 0.5 mL aliquot of the sample volume was collected and mixed with the starch solution (1:1 volume ratio), which was then transferred to a glass cuvette (10 mm optical path) for absorbance measurement at 585 nm vs. deionized water in spectrophotometer (UV-vis 2, Unicam, USA). Absorbance values were related to iodine concentration by a standard curve that was evaluated by spectrophotometric measurements after subtracting the TiO_2 suspension contribution from non-irradiated samples. The corresponding photogenerated holes concentration was stoichiometrically determined to be twice the produced iodine concentration, according to the following reaction:

$$2I^- + 2h^+ \rightarrow I_2 \qquad \text{(e4.1)}$$

A standard curve was determined using a 0.025 M iodine (Sigma-Aldrich, USA) stock solution that was diluted to obtain solutions at concentrations ranging between 0.00625 and 0.0625 mM (concentration step: 0.00625 mM). The absorbance of different concentrated iodine solutions was measured by a spectrophotometer with the same procedure described for irradiated samples during photocatalytic tests.

Validation tests were carried out in setup UV2 at varying times (5, 10, 15, 20, 25 and 30 minutes) on 20 mg L^{-1} P25 TiO_2 and 50 mM KI concentration samples. The same procedure was used and measures of absorbance were performed with a Cary 100 spectrophotometer (Agilent, USA).

Tests were replicated at least three times for each combination of conditions.

4.2.3.2 Hydroxyl radicals

Hydroxyl radical production tests were performed in setup UV1 on samples containing 40 mg L^{-1} P25 TiO_2 and 0.125 mM TA. Samples, comprised of 4 mL of 100 mg L^{-1} P25 TiO_2 stock solution, 2.5 mL of 0.5 mM TA solution and 1 mL of deionized water, were irradiated for 5, 10, 15, 20, 25 and 30 minutes. After irradiation, 0.5 mL of the volume was sampled, diluted to 1.25 mL with deionized water and centrifuged at 12,000 RPM for 5 minutes in order to separate TiO_2 aggregates. Then, 1 mL of supernatant was removed and transferred to a plastic cuvette (10 mm optical path) for fluorescence measurement (excitation at 315 nm and emission at 425 nm) by means of a Varian Eclipse fluorometer (Agilent). Fluorescence values were related to 2-HTA concentration by a standard curve. The corresponding hydroxyl radical concentration was estimated by the following reaction, assuming that trapping efficiency for OH• radicals by TA is 80% [25]:

$$TA + OH^{\bullet} \rightarrow 2 - HTA \qquad \text{(e4.2)}$$

The standard curve was determined using a 0.125 mM 2-HTA stock solution that was diluted to obtain solutions at concentrations ranging between 0.00125 and 0.0125 mM (concentration step: 0.00125 mM). The fluorescence of different concentrations of 2-HTA solutions was measured as well as for irradiated samples during photocatalytic tests.

Validation tests were carried out in UV2 setup at different times (5, 10, 15, 20, 25 and 30 minutes) on samples containing 20 mg L^{-1} P25 TiO_2 and 125 mM TA.

Measures were repeated at least thrice for each combination of operating conditions.

4.3 RESULTS AND DISCUSSION

4.3.1 TiO_2 aggregate characterization

Measurement conditions were designed to mimic the setup for reactivity measurements. TiO_2 aggregate size evolution was tracked for 30 minutes and, as can be seen in Supporting Information (SI4.2), samples in deionized water were stable with a number weighted D_{50} of 114±0.5 nm over the process time. The unweighted D_{50} indicated an increase from 3.28±0.269 μm initially to 4.17±0.431 μm after 30 minutes. The difference in these values reflects the high polydispersity of TiO_2 suspensions, resulting from the dispersion method. However, the initial number weighted values are all sharply centered around 114 nm indicating that the vast majority of aggregates exist at this smaller size class with relatively few large aggregates influencing the unweighted average size. Samples that were destabilized from the addition of KI (50 mM) showed an increase in the number weighted D_{50} from 111±1.6 nm initially to 681±58.7 nm after 30 minutes, with unweighted D_{50} increasing from 3.45±0.261 to 12.17±0.451 μm. Structure calculations yielded a D_f of 2.17±0.024 for P25 in deionized water which remained unchanged over the 30 minutes. The range of q values for which the scattering response was linear corresponded to length scales ranging from 660 nm to 3.4 μm. These values are consistent with the fractal dimensions reported for P25 by Jassby et al. [17].

4.3.2 TiO_2 nanoparticle reactivity measurement

TiO_2 nanoparticle reactivity tests were carried out in an experimental setup minimizing sample volume and liquid layer thickness so that samples were irradiated as uniformly as possible. Due to the small liquid volume pH and temperature were not monitored over time during irradiation. The pH of TiO_2 suspensions, measured in larger volumes of non-reacted samples, was 6.3±0.1 for photogenerated hole tests and 7.9±0.1 for hydroxyl radical tests. The latter value is higher due to pH adjustment by KOH to allow for the dissolution of TA.

4.3.2.1 Photogenerated holes

The influence of the initial KI concentration on photogenerated hole production was studied at a fixed irradiation time (30 min) for varying P25 TiO_2 concentrations (10, 25 and 40 mg L^{-1}), and at varying irradiation times (10, 20 and 30 min) for a fixed P25 TiO_2 concentration (40 mg L^{-1}). Experimental results are shown in figures 4.1 and 4.2.

For the same KI concentration, an increase in oxidized iodide concentration was observed when increasing the P25 TiO_2 concentration (figure 4.1). This result suggests that a greater amount of photocatalyst involves higher radiation absorption, a greater number of active sites and overall higher photoreactivity, in agreement with Chong et al. (2010) [2].

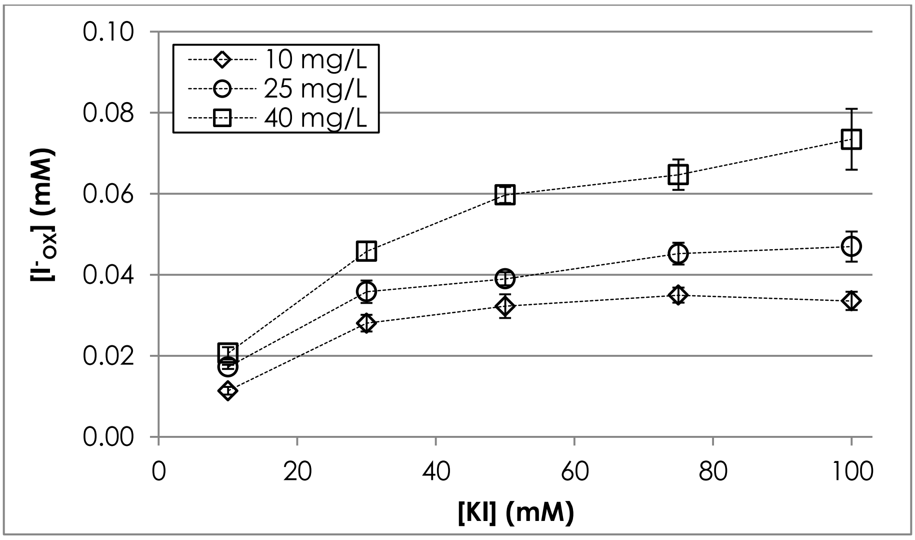

Figure 4.1 Oxidized iodide vs. KI concentration at different TiO_2 concentrations (30 minutes irradiation time, UV1 setup).

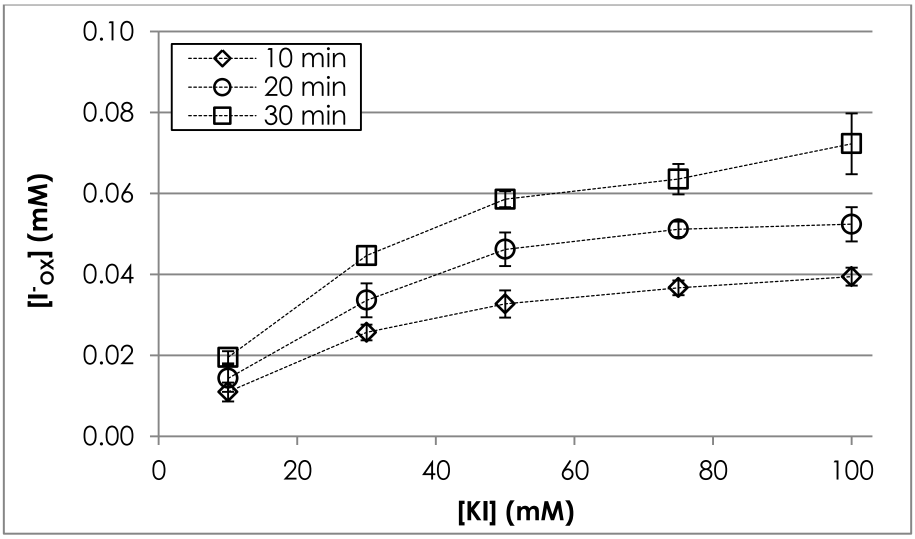

Figure 4.2 Oxidized iodide vs. KI concentration at different irradiation times ($[TiO_2]$=40 mg L^{-1}, UV1 setup).

Moreover, independently from irradiation time (figure 4.2), an increase in photogenerated hole concentration with KI concentration was observed at a fixed P25 TiO_2 concentration, despite the presence of the molecular probe in excess. This behaviour reveals that the reaction between iodide and photogenerated holes is significantly affected by the diffusion of iodide onto nanoparticle surface. Therefore, the effectiveness of the method in quantifying photogenerated holes is strictly related to KI concentration, as previously discussed in Herrmann and Pichat [26], by which the oxidation mechanism of iodide was supposed to depend on iodide adsorption on TiO_2 surface, according to a Langmuir type model. Consequently, the interaction between iodide and photogenerated holes has been described by a Langmuir-Hinshelwood (LH) mechanism [26]:

$$r = \frac{d[I^-]}{dt} = -K_R \cdot \theta_{I^-} = -K_R \cdot \frac{K_A[I^-]}{1 + K_A[I^-]} \tag{e4.3}$$

in which r is the reaction rate, $[I^-]$ is the concentration of iodide, θ_{I^-} is the surface coverage, K_A is the equilibrium constant of adsorption and K_R is the LH reaction constant.

The values of LH coefficients, K_A and K_R, can be estimated by the method of initial rates [27] using experimental results shown in figure 4.1 and 4.2, see Supporting Information (SI4.3). Parameters estimated by linear regression are shown in table 4.1. The coefficients of determination (R^2) of the linear regressions are higher than 0.90, indicating that the LH model is effective in data description. A linear decreasing trend (R^2 = 0.995) was observed for K_A with increasing TiO_2 concentration (for the same time interval, 30 min). This is expected as the equilibrium constant of adsorption is inversely related to the availability of adsorption sites on TiO_2 aggregates, which is a function of the photocatalyst surface [28]. An increasing trend with TiO_2 concentration was determined for K_R at the same time interval (30 min), which is probably due to the enhanced photocatalytic properties of concentrated TiO_2 suspensions in terms of absorption of incident radiation and number of active sites. As reported by Xu et Langford (2000) [29], the estimation of parameters strongly depends on the irradiation time interval chosen for the initial reaction rate calculation, particularly when the operative conditions that affect adsorption and reaction mechanisms change over time. Different time intervals (10, 20 and 30 min) were considered here depending on experimental conditions. For fixed TiO_2 concentration (40 mg L^{-1}) and different irradiation times, K_A maintained a nearly constant value and K_R strongly decreased with time interval. This K_R trend is unexpected and is discussed in paragraph 4.3.3.3.

Table 4.1 Estimated values of K_A and K_R vs. P25 TiO_2 concentration and irradiation time interval (Δt).

$[TiO_2]$ (mgL^{-1})	Δt (min)	K_A (M^{-1})	K_R (Ms^{-1})	R^2
10	30	91.03	2.15E-08	0.905
25	30	64.27	2.97E-08	0.937
40	10	33.20	8.60E-08	0.998
	20	28.61	6.18E-08	0.963
	30	29.62	5.30E-08	0.986

Experimental results illustrate the strong dependence on the method for photogenerated hole measurement from catalyst and probe concentrations. Therefore experiments for the evaluation of photogenerated hole production over 30 min irradiation time were performed with TiO_2 and KI concentrations fixed at 40 mg L^{-1} and 50 mM, respectively, as this was proved to be the best combination. In figure 4.3, oxidized iodide concentration as a function of irradiation time is reported (EXP - UV1). An increasing trend with decreasing slope over time for oxidized iodide was observed in contrast to the normally expected true zero order kinetics for oxidation reactions without interferences. According to Herrmann and Pichat [26], this behaviour is due to light absorption by iodine in solution, whose contribution in terms of absorbance is significant even at small amounts.

The oxidized iodide concentration trend over time will be discussed in paragraph 4.3.3.3.

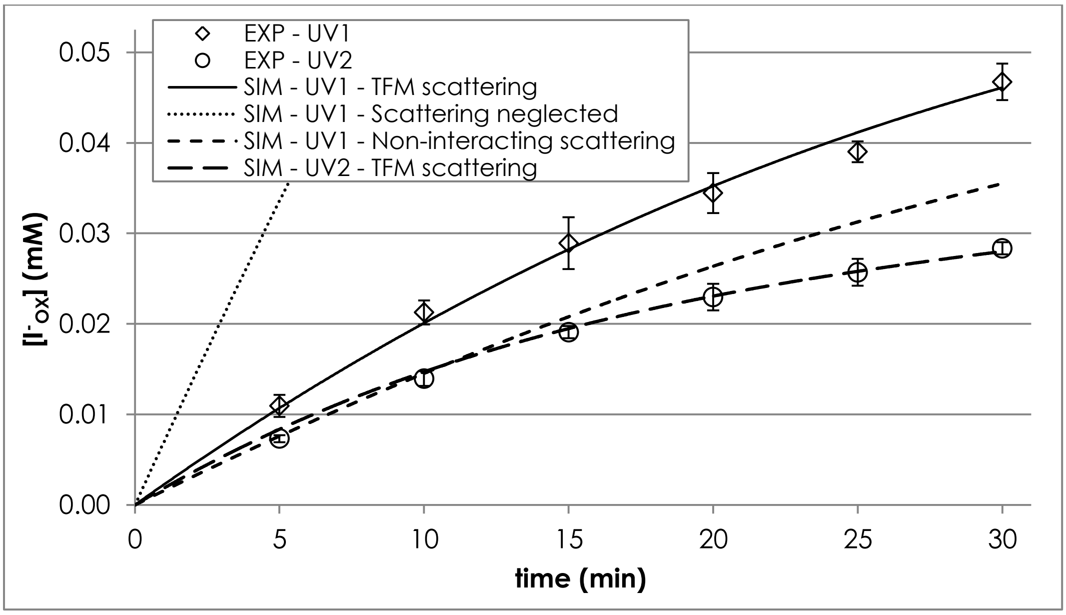

Figure 4.3 Oxidized iodide concentration vs. time: experimental data obtained in UV1 (diamonds) and UV2 (circles) setup, simulated data obtained in UV1 and UV2 setup using different scattering models.

4.3.2.2 Hydroxyl radicals

2-HTA concentrations, corresponding to the oxidation of TA by hydroxyl radicals, as a function of irradiation time (EXP - UV1) are shown in figure 4.4. Similarly to holes, hydroxyl radical production showed an increasing trend with decreasing slope over time, as later discussed in paragraph 4.3.3.3.

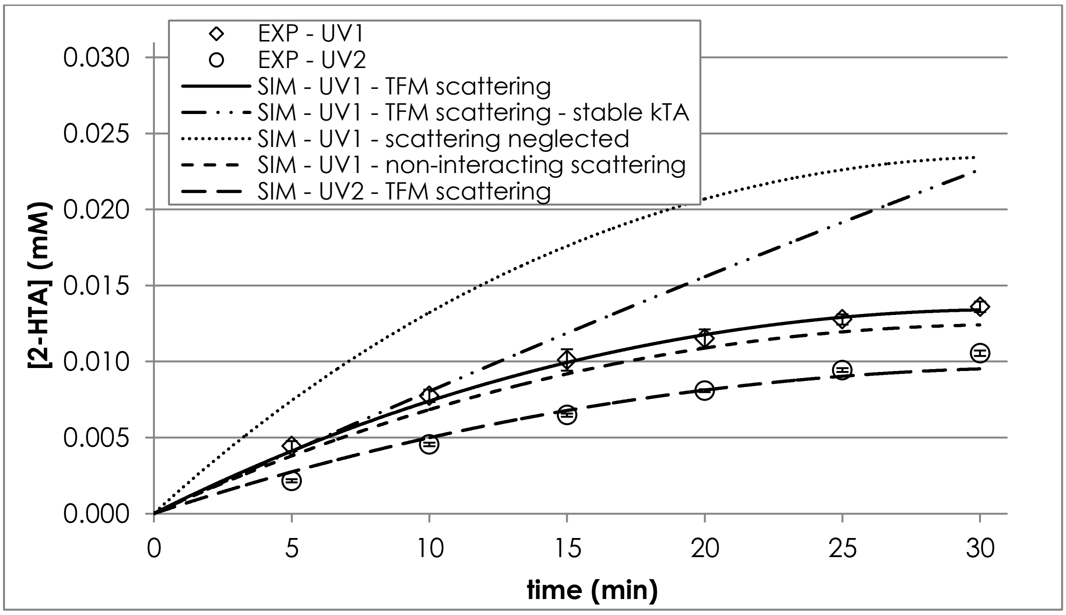

Figure 4.4 2-HTA concentration vs. time: experimental data obtained in UV1 (diamonds) and UV2 (circles) setup, simulated data obtained in UV1 and UV2 setup using different scattering models.

4.3.3 TiO_2 nanoparticle photocatalysis modelling

Modelling criteria proposed in the literature for TiO_2 photocatalysis were adopted and implemented for describing a transient system over the experimental geometric domain. The reactivity measurement setup was modeled as a two-dimensional completely stirred reactor, taking into account both the optical and chemical phenomena involved. The model considers chemical species evolution over time under the assumption of steady state for reactive species [30], as their generation and decay times are several orders of magnitude smaller than those of other species [31]. The proposed irradiation model was developed in order to describe the change in optical properties over time, while the adopted kinetic model accounts for the influence of TiO_2 nanoparticle aggregate size and structure on process yields, as proposed by Jassby et al. [17].

4.3.3.1 Irradiation model

The irradiation model calculates the number of photons absorbed by the photocatalyst per unit of volume in the unit of time, R(t), which is reported in the literature in several ways, including as local volumetric rate of photon absorption (LVRPA), *inter alia* [15,32]. This parameter is a function of time since the optical properties of the aqueous solution change during the process and it was evaluated for the experimental setup as reported in equation e4.4:

$$R(t) = \int_{\lambda} \frac{I_{ABS}(\lambda,t)S}{h\nu(\lambda)N_A} d\lambda \qquad \text{(e4.4)}$$

in which $I_{ABS}(\lambda)$ is the radiation intensity per unit surface absorbed by TiO_2 suspension at a given wavelength in a time step, S is the irradiated surface (25.52 cm^2 and 19.63 cm^2 in UV1 and UV2 setup respectively), $h\nu(\lambda)$ is the energy of a photon at a given wavelength and N_A is the Avogadro's number. For describing the radiation transmission, the total liquid height was divided into layers (z) of equal thickness (Δz = 0.2 mm), as illustrated in figure 4.5. The number of layers was 20 in setup UV1 and 25 in setup UV2.

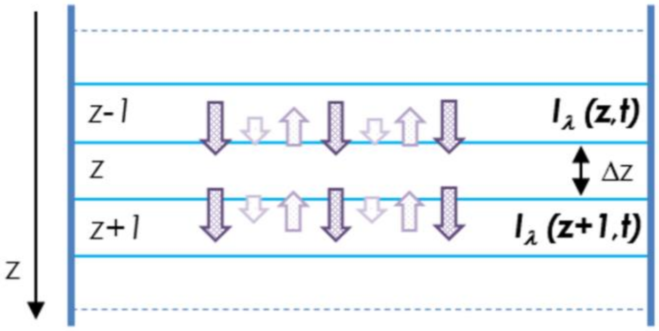

Figure 4.5 2D-domain scheme of the reactor. For a generic layer, incoming radiation intensity (I_λ) is given by the sum of UV lamp direct emission and back-scattering contributions.

The first layer was assumed to be irradiated vertically, while the radiation intensity absorbed by the TiO_2 suspension ($I_{ABS,\lambda}$) in a generic layer z for a given wavelength at each time step per unit surface was calculated by the following expression, derived from the Beer-Lambert law:

$$I_{ABS,\lambda}(z,t) = I_\lambda(z,t) \cdot 10^{-ABS_{SOL,\lambda}(t)} \cdot \left(1 - 10^{-(1-\alpha_\lambda)EXT_{TiO_2,\lambda}(t)}\right) \qquad \text{(e4.5)}$$

in which $ABS_{SOL,\lambda}(t)$ is the volumetric absorbance of the aqueous solution without considering the presence of TiO_2 nanoparticles, $EXT_{TiO_2,\lambda}(t)$ is the volumetric extinction of TiO_2 suspension, accounting for the coexistence of absorption and scattering phenomena, and α_λ is the scattering albedo at a given wavelength [33]. These terms were considered to be identical throughout the liquid volume at any given time step under the assumption of continuous mixing during irradiation. In the present model, specific absorption and scattering coefficients as a function of wavelength reported by Satuf et al. (2005) [34] for P25 TiO_2 were used for determining albedo coefficients and discriminating between the two components in spectrophotometric measures.

I_λ is the incoming radiation intensity in each layer, given by the sum of the radiative contribution from the other layers. In detail, radiation scattering was described by a two-flux model (TFM) [33,35], in which TiO_2 nanoparticle backscattering is introduced, hence the presence of vertical radiative terms in addition to the radiation transmitted from the upper layers and resulting from the direct emission of UV lamps. The total radiation intensity per unit volume (R) was calculated as the sum of the contributions of all the liquid layers R(t) at each step time.

In modelling photogenerated hole production, both absorbance by the aqueous solution and extinction by the TiO_2 suspension were considered to change over time: in the first case due to the production of iodine and in the second because of TiO_2 aggregation mechanisms. The values of $ABS_{SOL,\lambda}(t)$ during process time were obtained by means of absorbance measures of different concentrated iodine solutions (Supporting Information, SI4.4), and the time-dependent values of $EXT_{TiO_2,\lambda}(t)$ were determined by spectrophotometric measures of KI solutions containing P25 TiO_2 in suspension (Supporting Information, SI4.5). In modelling hydroxyl radical production, no significant modifications, neither in aqueous solution absorbance nor in TiO_2 suspension extinction, were observed over time, as reported in the Supporting Information (SI4.6).

4.3.3.2 Kinetic model

The equations for the variation of the concentration of photogenerated holes, promoted electrons and hydroxyl radicals over time were derived from the literature [17,36,37] and experimental results:

$$\frac{d[h^+]}{dt} = \Phi R - k_1[h^+][OH^-] - \varepsilon^{D_f-1}k_2[h^+][e^-] - k_3[h^+][OH^\bullet] - \left\{k_R[h^+]\frac{K_A[I^-]}{1+K_A[I^-]}\right\} \qquad \text{(e4.6)}$$

$$\frac{d[e^-]}{dt} = \Phi R - \varepsilon^{D_f-1}k_2[h^+][e^-] - k_4[e^-][OH^\bullet] - k_5[e^-][O_2] \qquad \text{(e4.7)}$$

$$\frac{d[OH^\bullet]}{dt} = k_1[h^+][OH^-] - k_3[OH^\bullet][h^+] - k_4[OH^\bullet][e^-] - k_6[OH^\bullet]^2 - \{k_{TA}[OH^\bullet][TA]\} \qquad \text{(e4.8)}$$

in which Φ is the quantum yield of the material and R is the radiation intensity per unit volume. $[h^+]$, $[e^-]$, $[OH^-]$, $[OH^\bullet]$, $[I^-]$, $[O_2]$ and [TA] are the molar concentrations of photogenerated holes, promoted electrons, hydroxyl ions, hydroxyl radicals, iodide ions, dissolved oxygen and TA, respectively. k_1, k_2 and k_3 are rate constants for reactions of photogenerated holes with hydroxide ions, promoted electrons and hydroxyl radicals, respectively. k_4 and k_5 are rate constants for reactions of promoted electrons with hydroxyl radicals and dissolved oxygen. k_6 is the rate constant for the self-quenching of hydroxyl radicals and k_{TA} is the rate constants for the reaction of hydroxyl radicals and TA. Regarding TiO_2 aggregate characteristics, ε^{D_f-1} is the parameter that describes the structural characteristics of TiO_2 nanoparticles aggregates, where ε is the porosity and D_f is the fractal dimension of TiO_2 aggregates, and which depends on TiO_2 aggregate hydrodynamic radius (R_h) and on TiO_2 nanoparticle primary radius (R_p) [17,18].

In equation e4.6 the first term on the right side represents photogenerated hole production, the second the hydroxyl radical production, the third the electron-hole recombination and the fourth the reaction between photogenerated holes and hydroxyl radicals. The fifth term refers to the quenching of photogenerated holes by iodide ions adsorbed on TiO_2 nanoparticle surface, assuming that the reaction between iodide and photogenerated holes is described by the Langmuir-Hinshelwood mechanism as discussed previously (paragraph 4.3.2.1). The reaction constant between iodide and photogenerated holes, previously expressed as K_R (equation e4.3), is reported in equation e4.6 as the product between the photogenerated hole concentration and an intrinsic kinetic constant k_R (s^{-1}), showing the direct dependence of the reaction rate on the concentration of photogenerated holes:

$$K_R = k_R[h^+] \qquad \text{(e4.9)}$$

Hence, unlike K_R, the kinetic constant, k_R, is independent from the available photogenerated hole concentration. It is not affected by operating conditions, and it is time-invariant.

In equation e4.7 the first two terms on the right side represent promoted electrons production and recombination, the third the reaction between promoted electrons and hydroxyl radicals and the fourth represents superoxide radical production.

In equation e4.8 the first term on the right side represents hydroxyl radicals generation, the second and the third terms the interaction of hydroxyl radicals with photogenerated holes and promoted electrons, the fourth the hydroxyl radical self-quenching, and the fifth term the quenching of hydroxyl radicals by TA.

In equations e4.6 and e4.8, terms reported in brackets have to be considered only if iodide and TA are present in solution.

Photogenerated hole, promoted electron, and hydroxyl radical concentrations can be calculated at steady state by equating the accumulation of the reactive species over time to zero, which leads to the expressions for the reactive species reported in Supporting Information (SI4.7).

In the described system the iodine production over time can be expressed by equation e4.10:

$$\frac{d[I_2]}{dt} = \frac{1}{2} \cdot k_R \cdot [h^+]_{SS} \cdot \theta_{I^-} = \frac{1}{2} \cdot k_R \cdot [h^+]_{SS} \cdot \frac{K_A[I^-]}{1 + K_A[I^-]} \qquad \text{(e4.10)}$$

On the other hand, the 2-HTA production over time can be evaluated as:

$$\frac{d[2\text{–}HTA]}{dt} = k_{TA}[OH^\bullet]_{SS}[TA] \qquad \text{(e4.11)}$$

The production of iodine and 2-HTA was estimated by solving and integrating the equations over the process time (30 minutes) with a step time of 1 second. The time-independence of the model at this time step was verified.

The values for kinetic constants used in modelling are reported in the Supporting Information (SI4.8), while the values for equilibrium adsorption constant K_A were derived from table 4.1. Experimental values for R_h and D_f were experimentally determined in paragraph 4.3.1, R_p was provided by the manufacturer (~20÷25 nm), while ε was calculated according to the following equation [18]:

$$\varepsilon = {R_h}^{D_f - 3} {R_p}^{3 - D_f} \qquad \text{(e4.12)}$$

Reaction kinetic constants k_R and k_{TA}, characteristic of the iodide oxidation and TA hydroxylation reactions, were determined from the two kinetic models (e4.10 and e4.11) by a least-square optimization procedure, that resulted in the best fitting of experimental data obtained in setup UV1. The validation of kinetic models was carried out using experimental results obtained in setup UV2.

4.3.3.3 Modelling results and sensitivity analysis

The simulated production of I_2 and 2-HTA over time is reported in figure 4.3 and 4.4 (SIM - UV1 - TFM scattering) in comparison with respective experimental results obtained in setup UV1 (EXP - UV1). The values of R, $[h^+]_{SS}$ and $[OH^\bullet]_{SS}$ calculated by the model after 1 and 30 minute process time for setup UV1 are given in table 4.2.

Model calculations of iodide oxidation by photogenerated holes based on the calculated radiation intensity per unit volume (R) shows a strong decrease (-60%) after 30 minutes irradiation time; the reason for this significant reduction in the radiation absorbed by TiO_2 suspension is that the energy balance is modified over time by generated iodine in solution, absorbing an increasing amount of radiation, and by aggregation of TiO_2 particles, lowering the absorbance of the TiO_2 suspension (Supporting Information, SI4.4 and SI4.5). These factors explain the observed slowdown trend in iodide oxidation. As a consequence, the concentrations of photogenerated holes and hydroxyl radicals at the steady state decrease over process time of 60% and 29%, respectively.

Conversely, no energy balance changes are considered in the model describing TA hydroxylation by hydroxyl radicals, so that R and $[h^+]_{SS}$ are constant over process time. $[OH^\bullet]_{SS}$ slightly increases during 30 minutes (+1%) because of the decrease in TA concentration over process time (-11%).

The optimum estimated value for k_R was 8.25 s^{-1}, while linearly decreasing values for k_{TA} from 9.89E03 M^{-1} s^{-1} to 3.96E02 M^{-1} s^{-1} over time resulted in a satisfactory fitting of experimental data. These kinetic parameters yielded R^2 values equal to 0.991 and 0.993 for iodide and TA oxidation, respectively. A variable k_{TA} value was adopted because it provides a better fit with respect to any fixed k_{TA} value, since the strong curvature of experimental data is not predicted otherwise, as can be seen in figure 4.4 (SIM - UV1 - TFM scattering - stable k_{TA}). The latter simulation was run with a k_{TA} value fixed at 9.07E03 M^{-1} s^{-1}, which gave the best match with the initial trend of experimental data. For a comparison with experimental data reported in figures 4.1 and 4.2, the Langmuir-Hinshelwood kinetic constant K_R was calculated over time according to equation e4.9, i.e. as the product between k_R, estimated by the optimization procedure, and $[h^+]_{SS}$, obtaining values decreasing from 6.29E-08 M s^{-1} to 2.47E-08 M s^{-1} over process time, comparable to data in table 4.1. The change in $[h^+]_{SS}$ over process time probably explains the experimental K_R kinetic constant decrease reported in table 4.1 at different irradiation time intervals.

Table 4.2 Values of R, $[h^+]_{SS}$, and $[OH^\bullet]_{SS}$ calculated by models after 1 and 30 minutes process time. Simulated data relative to both experimental setup (UV1 and UV2, used for parameter calibration and validation, respectively) and both models are reported.

Simulated process	**h^+ quenching by I^-**				**$OH^\bullet$ quenching by TA**			
Experimental setup	**UV1**		**UV2**		**UV1**		**UV2**	
Time step (min)	**1**	**30**	**1**	**30**	**1**	**30**	**1**	**30**
R (Einstein L^{-1} s^{-1})	4.08E-05	1.60E-05	3.40E-05	7.24E-06	4.29E-05		2.23E-5	
$[h^+]_{SS}$ (M)	8.68E-09	3.41E-09	5.26E-09	1.54E-09	2.70E-10		1.40E-9	
$[OH^\bullet]_{SS}$ (M)	6.08E-09	4.29E+09	5.08E-09	3.08E-09	1.22E-8	1.23E-8	8.05E-9	8.14E-9

Given the limitations of the method adopted in paragraph 4.3.2.1 for parameter estimation, the agreement between observed and simulated K_R kinetic constant values can be considered satisfactory. On the other hand, the kinetic constant for TA hydroxylation, k_{TA}, estimated here is significantly different from the value proposed in literature, namely 3.30E9 $M^{-1}s^{-1}$ [38]. This discrepancy can be explained assuming that, in a heterogeneous system such as the present one, the TA reaction with hydroxyl radicals could be limited by diffusion on the TiO_2 surface, which is in turn impeded by the pH of solution (higher than the point of zero charge for TiO_2) and by hydroxyl radical effective availability for probe compound hydroxylation. Moreover, the reactivity coefficient reported in literature was estimated in a homogeneous system in which hydroxyl radicals were generated by means of water radiolysis. As already discussed, k_{TA} modification over process time was assumed to reproduce the decreasing trend of experimental data not otherwise described by the model. The model parameters that change over time and that may determine its curvature are TA concentration and solution pH. Regarding TA concentration, its observed slight decrease cannot explain the saturation trend of experimental data for 2-HTA production, since its value does not become limiting for the process. Although it is not monitored throughout the experiment, several simulations were performed at varying pH, however a decreasing trend similar to that shown by experimental data was not observed. Hence, the experimental trend that can be effectively modelled by assuming a linear decrease in TA reactivity over process time is probably due to the changing nature of the interaction between TA and hydroxyl radicals or to modifications in surface chemistry, not related to the morphology of TiO_2 aggregates that was stable over time. Further research should be devoted to the study of the hydroxylation of TA by hydroxyl radicals, possibly involving the use of analytical techniques for monitoring the generation of radical species, such as electron paramagnetic resonance (EPR).

Photogenerated hole and hydroxyl radical consumption by different reactions was assessed on the basis of kinetic constants and concentrations of compounds in solution: in the kinetic model describing iodide oxidation, most of the photogenerated holes are self-quenched in the reaction with promoted electrons (96.8%), some react with hydroxyl ions in the formation of hydroxyl radicals (1.9%) and a fraction is lost in recombination with hydroxyl radicals (1.1%). Only 0.2% of photogenerated holes oxidize iodide in solution. These shares do not change significantly throughout the experiment. The strong detrimental effect of electron-hole recombination on process yield is clear, as this phenomenon is one of the main drawbacks of TiO_2 photocatalysis, whose reduction has been discussed in a number of published papers [39,40]. In the kinetic model describing TA hydroxylation, most of hydroxyl radicals are lost to self-quenching (rising from 95.5% to 99.5% in 30 minutes), while a lower fraction of hydroxyl radicals react with TA. This latter fraction is significantly reduced at the end of the process time, falling from 1.8% to 0.01%, due to the decrease in TA concentration, although this change is not sufficient to explain the strong curvature of experimental data. The fraction of hydroxyl radicals reacting with photogenerated holes is 2.7% at the beginning and 0.5% at the end of the process time, while the reaction with promoted electrons is negligible.

Many authors have pointed out that TiO_2 photocatalysis modelling strongly depends on the evaluation of the volumetric rate of photon absorption, since it represents a fundamental step for the process. In particular, several works highlight the importance of modelling TiO_2 nanoparticle scattering in a slurry reactor, and some formulations for its accurate description have been proposed [15,32]. Two irradiation models have been implemented in addition to that already introduced, one neglecting scattering and a second assuming that radiation no longer interacts with TiO_2 suspension after being scattered once. Results for the UV1 setup are reported in figure 4.3 and 4.4, while similar results were obtained for UV2 setup, here not shown. When light scattering is neglected, the amount of photons absorbed by TiO_2 nanoparticles is abundantly overestimated, resulting in higher I_2 or 2-HTA production (SIM - UV1 - Scattering neglected). Instead, when the absorption of the scattered radiation is not considered, the rate of photon absorption is underestimated (SIM - UV1 - Non-interacting scattering). Hence, a proper consideration of scattering phenomena is fundamental in describing TiO_2 nanoparticles photocatalysis. However, only the photogenerated hole model is strongly affected by scattering, while the differences are less marked in the hydroxyl radical model, probably due to intermediate reactions acting as a limiting step in TA hydroxylation and reducing the direct influence of radiative phenomena.

Kinetic constants k_R and k_{TA}, determined by a least-squares optimization procedure, were validated using data obtained under different experimental conditions (UV2 setup). The values of R, $[h^+]_{SS}$ and $[OH^\bullet]_{SS}$ after 1 and 30 minutes process time for UV2 setup are reported in table 2.

Figure 4.3 and 4.4 show that simulated data for the production of I_2 and 2-HTA over process time (SIM - UV2 - TFM scattering), running the relative kinetic model with the k_R and k_{TA} values previously determined, effectively fit the data obtained under different experimental conditions (EXP - UV2), giving R^2 values equal to 0.994 and 0.962 for iodide and TA oxidation, respectively. The high correspondence observed suggests that both the irradiation and the kinetic model proposed are effective in modelling TiO_2 photocatalysis. However, while the model consistently describes the phenomena related to iodide oxidation by photogenerated holes, it is less reliable for modelling TA hydroxylation by hydroxyl radicals, since the choice of the optimal kinetic parameters, differing from those reported in literature and time-varying, cannot be explained on the basis of involved phenomena and could be due to some neglected mechanisms.

The sensitivity assessment of operating parameters was performed by means of a local sensitivity analysis method, varying one parameter at a time and keeping the others fixed [41]. This methodology was used since all the analyzed parameters are independent. Results are reported in figure 4.6, while more details about sensitivity analysis are given in the Supporting Information (SI4.9).

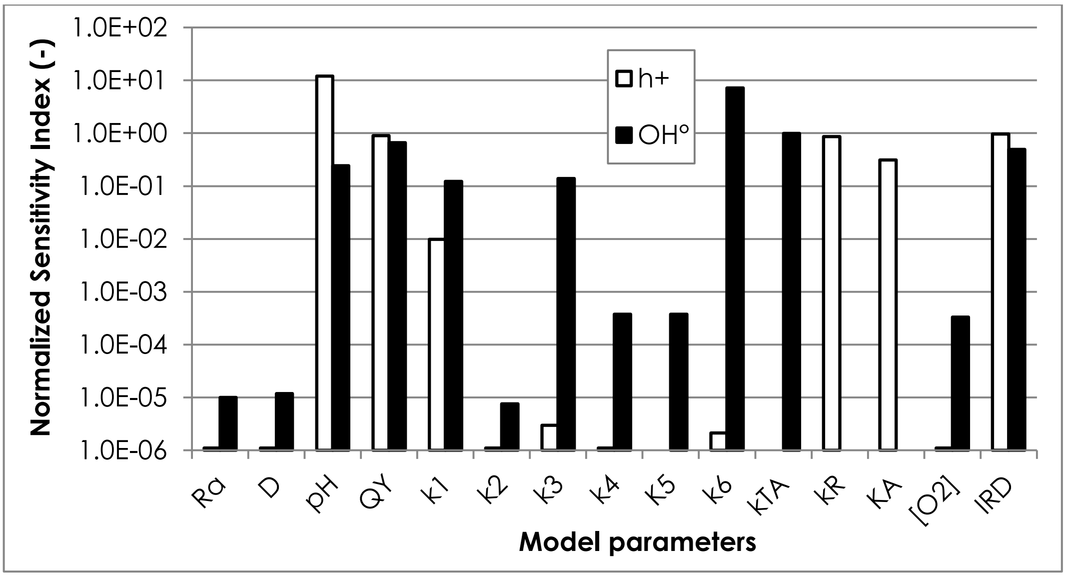

Figure 4.6 Local sensitivity analysis of the parameters of the models for photogenerated holes and hydroxyl radicals production: Normalized Sensitivity Index (NSI) was calculated as the ratio between percentage variation of model outputs and respective parameter values. QY is the quantum yield.

For the model describing photogenerated hole quenching by iodide, the most important parameters affecting the photocatalytic process are pH, radiation intensity, quantum yield, k_R and K_A. TiO_2 aggregates size and structure slightly affect the process, although in the literature these features are described as an important driver for the recombination of electron-hole pairs [17,18].

The most important role of TiO_2 aggregates structure concerns the effects on optical phenomena (absorption, scattering) and it is accounted for in the irradiation model. The strong importance of k_R and K_A is probably distorted by the experimental methodology, involving iodine measurements. For the model describing hydroxyl radicals quenching by TA, the sensitivity analysis indicated that k_6, k_{TA}, quantum yield and radiation intensity are the most important parameters for photocatalysis.

In summary, the reported modelling procedure, integrating the insights of several previous research works with recent protocols for the measurement of reactive species, represents a significant step forward in the description of TiO_2 nanoparticle photocatalysis. The main advantages of the proposed method, whose effectiveness in reproducing time series has been validated in a separate experimental setup, are the independence from the model compound, the estimation of the concentration of the individual reactive species and the potential adaptability to different reactor configurations. Further developments may provide for the implementation of more advanced optical and fluid-dynamic models by means of powerful computational tools, e.g. CFD codes, so that more complex configurations could be described. Additionally, the present model can be extended to other chemical compounds present in water, such as inorganic ions, usually competing for the reactive species and adversely affecting process yields.

4.4 CONCLUSIONS

Two experimental protocols for the measurement of reactive species, namely photogenerated holes and hydroxyl radicals, were successfully applied to the experimental setup. The interaction between iodide and photogenerated holes depended on iodide adsorption on TiO_2 surface, that was described by a Langmuir-Hinshelwood mechanism, whose parameters were studied as a function of TiO_2 concentration and irradiation time. Iodide oxidation was effectively simulated by modelling the reaction volume as a completely stirred two-dimensional domain, in which irradiation phenomena were described by a two-flux model and the steady state for reactive species was assumed. The kinetic parameters for iodide adsorption and oxidation were estimated and successfully validated in a different experimental setup. The same model was adapted to describe the oxidation of terephthalic acid by hydroxyl radicals. The kinetic parameters for terephthalic acid oxidation were estimated and validated, while the issues in investigating the interaction mechanisms among the involved species have been discussed. The sensitivity of operating parameters on model response was assessed and the most relevant parameters were highlighted.

The present work represents a significant advance in the understanding of fundamental chemical-physical processes involved in reactive species generation as well as it provides a valuable modelling methodology accounting for radiation transfer and chemical reactions.

4.5 REFERENCES

[1] O. Carp, Photoinduced reactivity of titanium dioxide, Prog. Solid State Chem. 32 (2004) 33–177.

[2] M.N. Chong, B. Jin, C.W.K. Chow, C. Saint, Recent developments in photocatalytic water treatment technology: a review, Water Res. 44 (2010) 2997–3027.

[3] T. Ochiai, A. Fujishima, Photoelectrochemical properties of TiO_2 photocatalyst and its applications for environmental purification, J. Photochem. Photobiol. C Photochem. Rev. 13 (2012) 247–262.

[4] B. Ohtani, Photocatalysis A to Z—What we know and what we do not know in a scientific sense, J. Photochem. Photobiol. C Photochem. Rev. 11 (2010) 157–178.

[5] P. Pichat, Photocatalysis and water purification: from fundamentals to recent applications, Wiley-VCH, 2013.

[6] S. Malato, P. Fernández-Ibáñez, M.I.I. Maldonado, J. Blanco, W. Gernjak, Decontamination and disinfection of water by solar photocatalysis: recent overview and trends, Catal. Today. 147 (2009) 1–59.

[7] H. Choi, S.R. Al-Abed, D.D. Dionysiou, E. Stathatos, P. Lianos, TiO_2-based advanced oxidation nanotechnologies for water purification and reuse, Sustain. Sci. Eng. 2 (2010) 229–254.

[8] K.I. Ishibashi, A. Fujishima, T. Watanabe, K. Hashimoto, Detection of active oxidative species in TiO_2 photocatalysis using the fluorescence technique, Electrochem. Commun. 2 (2000) 207–210.

[9] T. Hirakawa, K. Yawata, Y. Nosaka, Photocatalytic reactivity for $O_2^{\bullet-}$ and $OH^{\bullet}$ radical formation in anatase and rutile TiO_2 suspension as the effect of H_2O_2 addition, Appl. Catal. A Gen. 325 (2007) 105–111.

[10] S.H. Yoon, J.H. Lee, Oxidation mechanism of As(III) in the UV/TiO_2 system: evidence for a direct hole oxidation mechanism, Environ. Sci. Technol. 39 (2005) 9695–9701.

[11] G. Bartosz, Use of spectroscopic probes for detection of reactive oxygen species., Clin. Chim. Acta. 368 (2006) 53–76.

[12] N. Soh, Recent advances in fluorescent probes for the detection of reactive oxygen species., Anal. Bioanal. Chem. 386 (2006) 532–43.

[13] M.L. Satuf, R.J. Brandi, A.E. Cassano, O.M. Alfano, Photocatalytic degradation of 4-chlorophenol: a kinetic study, Appl. Catal. B Environ. 82 (2008) 37–49.

[14] M. Vezzoli, W.N. Martens, J.M. Bell, Investigation of phenol degradation: true reaction kinetics on fixed film titanium dioxide photocatalyst, Appl. Catal. A Gen. 404 (2011) 155–163.

[15] I. Grčić, G. Li Puma, Photocatalytic degradation of water contaminants in multiple photoreactors and evaluation of reaction kinetic constants independent of photon absorption, irradiance, reactor geometry, and hydrodynamics, Environ. Sci. Technol. 47 (2013) 13702–13711.

[16] H. Lin, C. Huang, W. Li, C. Ni, S. Shah, Y. Tseng, Size dependency of nanocrystalline TiO_2 on its optical property and photocatalytic reactivity exemplified by 2-chlorophenol, Appl. Catal. B Environ. 68 (2006) 1–11.

[17] D. Jassby, J.F. Budarz, M. Wiesner, Impact of aggregate size and structure on the photocatalytic properties of TiO_2 and ZnO Nanoparticles, Environ. Sci. Technol. 46 (2012) 6934-6941.

[18] E.M. Hotze, J.Y. Bottero, M.R. Wiesner, Theoretical framework for nanoparticle reactivity as a function of aggregation state., Langmuir 26 (2010) 11170–11175.

[19] J. Jiang, G. Oberdörster, P. Biswas, Characterization of size, surface charge, and agglomeration state of nanoparticle dispersions for toxicological studies, J. Nanoparticle Res. 11 (2008) 77–89.

[20] A.A. Keller, H. Wang, D. Zhou, H.S. Lenihan, G. Cherr, B.J. Cardinale, et al., Stability and aggregation of metal oxide nanoparticles in natural aqueous matrices, Environ. Sci. Technol. 44 (2010) 1962–1967.

[21] E.M. Hotze, T. Phenrat, G. V. Lowry, Nanoparticle aggregation: challenges to understanding transport and reactivity in the environment, J. Environ. Qual. 39 (2010) 1909.

[22] Y.H. Shih, W.S. Liu, Y.F. Su, Aggregation of stabilized TiO_2 nanoparticle suspensions in the presence of inorganic ions, Environ. Toxicol. Chem. 31 (2012) 1693–1698.

[23] Y.H. Shih, C.M. Zhuang, C.P. Tso, C.H. Lin, The effect of electrolytes on the aggregation kinetics of titanium dioxide nanoparticle aggregates, J. Nanoparticle Res. 14 (2012).

[24] G.C. Bushell, Y.D. Yan, D. Woodfield, J. Raper, R. Amal, On techniques for the measurement of the mass fractal dimension of aggregates, Adv. Colloid Interface Sci. 95 (2002) 1–50.

[25] K. Ishibashi, A. Fujishima, T. Watanabe, K. Hashimoto, Quantum yields of active oxidative species formed on TiO_2 photocatalyst, J. Photochem. Photobiol. A Chem. 134 (2000) 139–142.

[26] J.M. Herrmann, P. Pichat, Heterogeneous photocatalysis. Oxidation of halide ions by oxygen in ultraviolet irradiated aqueous suspension of titanium dioxide, J. Chem. Soc. Faraday Trans. 1. 76 (1980) 1138.

[27] M. Mehrvar, W.A. Anderson, M. Young, P.M. Reilly, Non-linear parameter estimation for a dynamic model in photocatalytic reaction engineering, Chem. Eng. Sci. 55 (2000) 4885–4891.

[28] E. Gerhard, Handbook of heterogeneous catalysis, Wiley-VCH, 2008.

[29] Y. Xu, C.H. Langford, Variation of Langmuir adsorption constant determined for TiO_2-photocatalyzed degradation of acetophenone under different light intensity, 133 (2000) 67–71.

[30] J.H. Esperson, Chemical kinetics and reaction mechanism, McGraw-Hill, 2002.

[31] M.R. Hoffmann, S.T. Martin, W. Choi, D.W. Bahnemannt, Environmental applications of semiconductor photocatalysis, Chem. Rev. 95 (1995) 69–96.

[32] L. Satuf, R.J. Brandi, A.E. Cassano, O.M. Alfano, Quantum efficiencies of 4-chlorophenol photocatalytic degradation and mineralization in a well-mixed slurry reactor, Ind. Eng. Chem. Res. 46 (2007) 43–51.

[33] A. Brucato, L. Rizzuti, Simplified modeling of radiant fields in heterogeneous photoreactors. 2. Limiting 'Two-Flux' model for the case of reflectance greater than zero, Ind. Eng. Chem. Res. 36 (1997) 4748–4755.

[34] M.L. Satuf, R.J. Brandi, A.E. Cassano, O.M. Alfano, Experimental method to evaluate the optical properties of aqueous titanium dioxide suspensions, Ind. Eng. Chem. Res. 44 (2005) 6643–6649.

[35] G. Li Puma, A. Brucato, Dimensionless analysis of slurry photocatalytic reactors using two-flux and six-flux radiation absorption-scattering models, Catal. Today. 122 (2007) 78–90.

[36] C. Turchi, Photocatalytic degradation of organic water contaminants: mechanisms involving hydroxyl radical attack, J. Catal. 122 (1990) 178–192.

[37] R.L. Pozzo, R.J. Brandi, A.E. Cassano, M.A. Baltanás, Photocatalytic oxidation of oxalic acid in dilute aqueous solution, in a fully illuminated fluidized bed reactor, Chem. Eng. Sci. 65 (2010) 1345–1353.

[38] M. Saran, K.H. Summer, Assaying for hydroxyl radicals: hydroxylated terephthalate is a superior fluorescence marker than hydroxylated benzoate., Free Radic. Res. 31 (1999) 429–436.

[39] A. Rincon, Effect of pH, inorganic ions, organic matter and H_2O_2 on E. coli K12 photocatalytic inactivation by TiO_2 implications in solar water disinfection, Appl. Catal. B Environ. 51 (2004) 283–302.

[40] A. Turolla, M. Fumagalli, M. Bestetti, M. Antonelli, Electrophotocatalytic decolorization of an azo dye on TiO_2 self-organized nanotubes in a laboratory scale reactor, Desalination 285 (2012) 377–382.

[41] D.M. Hamby, A review of techniques for parameter sensitivity analysis of environmental models., Environ. Monit. Assess. 32 (1994) 135–54.

4.6 SUPPORTING INFORMATION

SI4.1 Radiation intensity as a function of emission wavelength at the upper liquid surface

Emission spectra of UV lamps, as provided by manufacturers, were used to determine the radiation intensity as a function of emission wavelength at the liquid upper surface of the samples. Results are reported in figure SI4.1. Helios Italquartz 15 W lamp emission spectrum was described by a normal distribution with mean 365nm and standard deviation 15 nm. A normal distribution with mean 365 nm and standard deviation 10 nm was assumed for Philips TL-D 15W BLB SLV spectrum. Radiometric measures were corrected by considering the sensor spectral response, as suggested in [SI1].

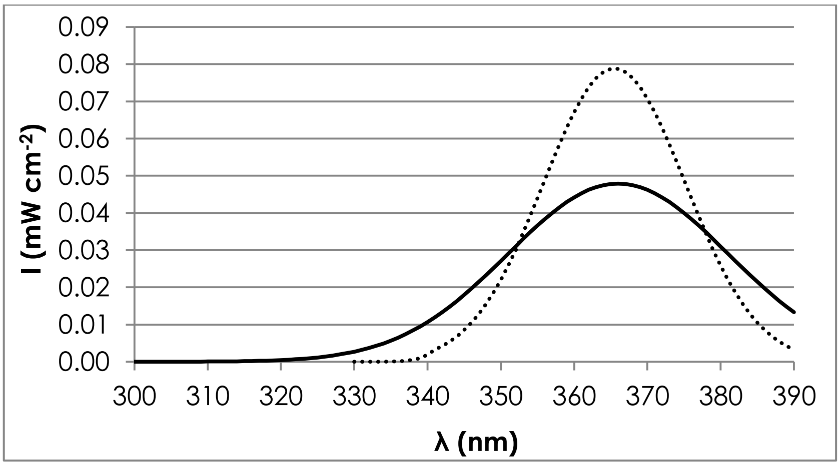

Figure SI4.1 Radiation intensity vs. emission wavelength at the liquid upper surface of samples: (a) Helios Italquartz 15 W (solid line), (b) Philips TL-D 15W BLB SLV (dotted line).

SI4.2 TiO_2 aggregate characterization

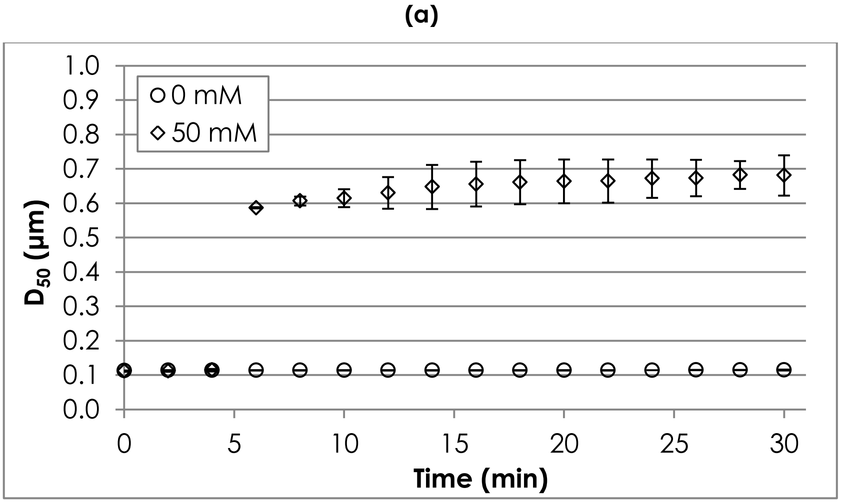

(b)

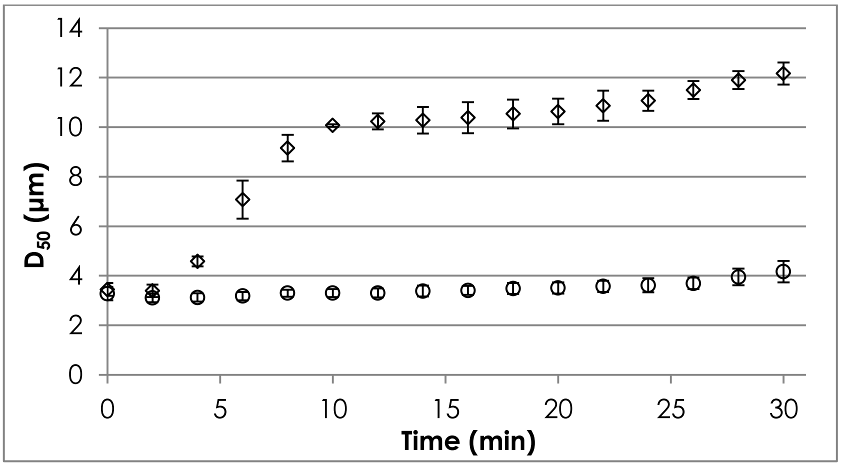

Figure SI4.2 TiO_2 aggregate size (D_{50}) vs. time (mean±st.dev.) as a function of KI concentration (0, 50 mM): (a) value weighted on the number of particles, (b) unweighted value.

(a)

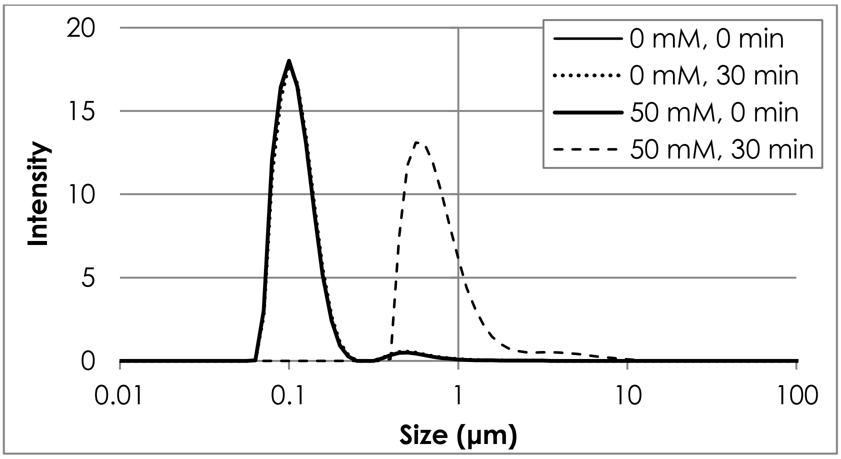

(b)

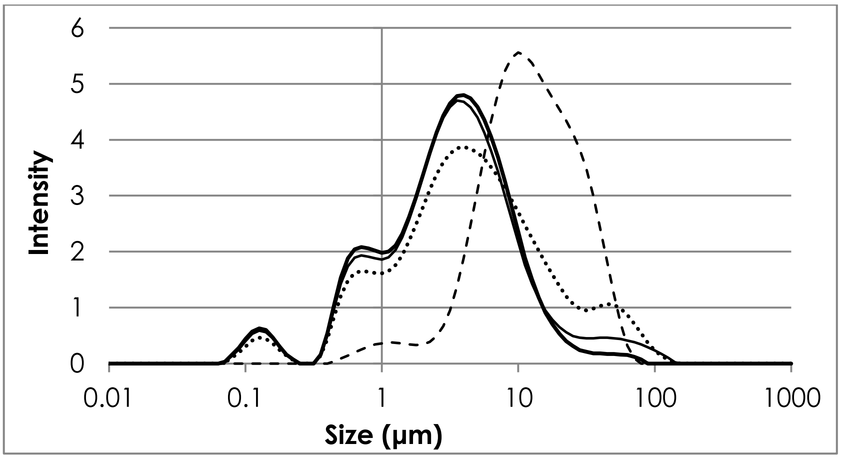

Figure SI4.3 TiO_2 aggregate size distribution as a function of KI concentration (0, 50 mM) at various times (0, 30 min): (a) value weighted on the number of particles, (b) unweighted value.

SI4.3 Langmuir-Hinshelwood linearization procedure for K_A and k_R constants estimation

Equation e4.3 in the manuscript can be expressed showing the linear relationship between the inverse of initial reaction rate ($1/r_0$) and the inverse of initial iodide concentration ($1/[I^-]_0$), as [SI2]:

$$\frac{1}{r_0} = \frac{1}{K_A K_R}\frac{1}{[I^-]_0} + \frac{1}{K_R} = m\,\frac{1}{[I^-]_0} + q \qquad \text{(eSI4.1)}$$

with:

$$K_R = \frac{1}{q} \qquad\qquad K_A = \frac{q}{m}$$

The rate r_0 is obtained from experimental data by calculating the oxidized iodide concentration for each $[I^-]_0$ over irradiation time. K_A and K_R values were calculated by fitting experimental data shown in figure 4.1 and 4.2 with a linear regression, estimating m and q values by the least squares method, as reported in figure SI4.4. Experimental values at the lowest KI concentration (10 mM) were neglected in the calculation to avoid the fact that these points had a decisive influence on the slope of the regression line, as already suggested by Mehrvar et al. (2000) [SI3].

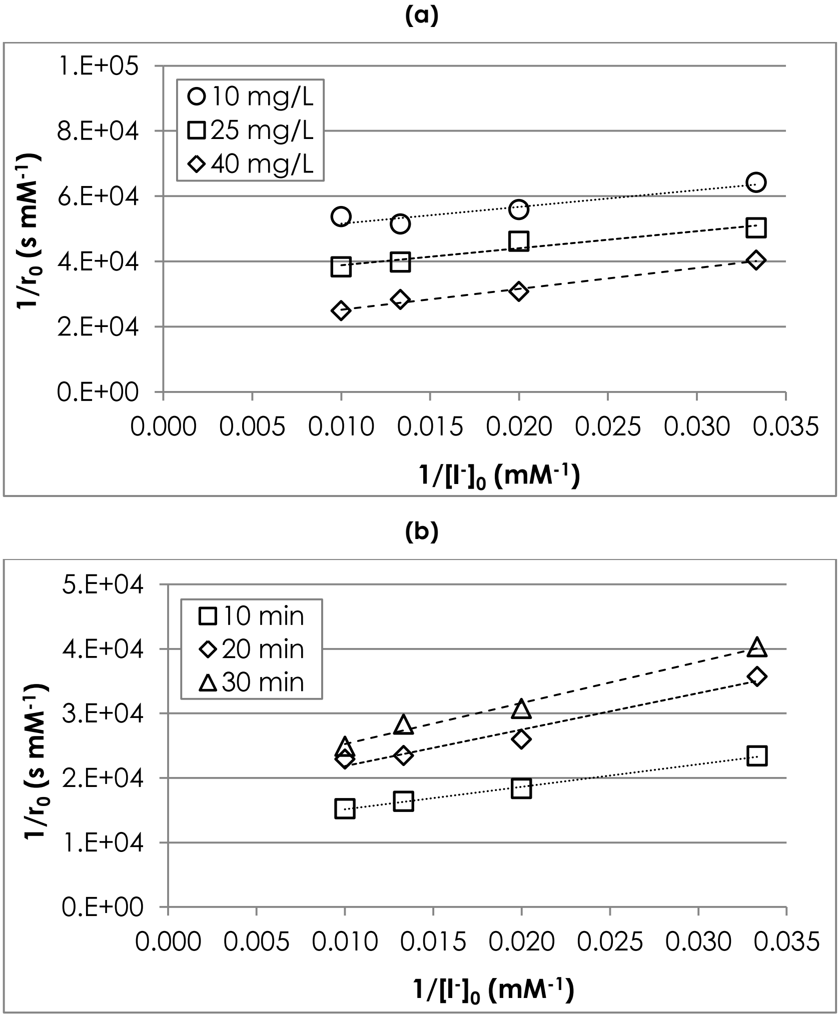

Figure SI4.4 Experimental data linear regressions: (a) fixed irradiation time (30 min) and different P25 TiO_2 concentrations, (b) fixed P25 TiO_2 concentration (40 mg L^{-1}) and different irradiation times.

SI4.4 Absorbance of aqueous solutions as a function of iodine concentration

Absorbance spectra of iodine solutions at different concentrations were measured, obtaining the data shown in figure SI4.5. Deionized water was used as reference. At each wavelength, a second order relationship between absorbance and iodine concentration was highlighted ($R^2 > 0.983$):

$$ABS_{SOL,\lambda} = a_\lambda \cdot [I_2]^2 + b_\lambda \cdot [I_2] + c_\lambda \qquad \text{(eSI4.2)}$$

where $ABS_{SOL,\lambda}$ is aqueous solution absorbance and $[I_2]$ is iodine concentration. Parameter values, estimated by the least squares method, were used in the kinetic model.

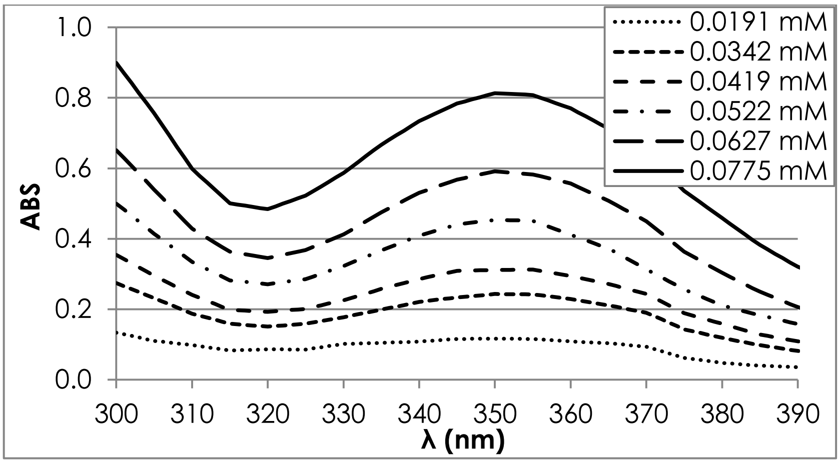

Figure SI4.5 Absorbance spectra of different concentrated iodine solutions.

SI4.5 Absorbance of TiO_2 suspensions in potassium iodide as a function of time

Samples containing two different concentrations of P25 Aeroxide TiO_2 in suspension (40 and 20 mg L^{-1}) and 50 mM KI were mixed on magnetic stirrer (400 RPM) in the same reaction vessel used in photocatalysis tests for different time intervals. At the end of the mixing time, absorbance spectra were measured. Deionized water was used as a reference. Results are shown in figures SI4.6 and SI4.7. At each wavelength two relationships between absorbance and time were investigated: linear (equation eSI4.3) and second order (equation eSI4.4):

$$ABS_{TiO_2,\lambda}(t) = m_\lambda \cdot t + q_\lambda \qquad \text{(eSI4.3)}$$

$$ABS_{TiO_2,\lambda}(t) = a_\lambda \cdot t^2 + b_\lambda \cdot t + c_\lambda \qquad \text{(eSI4.4)}$$

At each wavelength, the best fitting of experimental data was found considering a linear relationship for 40 mg L^{-1} ($R^2>0.968$) and a second order relationship for 20 mg L^{-1} ($R^2>0.994$).

Regression parameters, estimated by the least squares method, were used in the kinetic model to evaluate $ABS_{TiO_2,\lambda}$ changing over time.

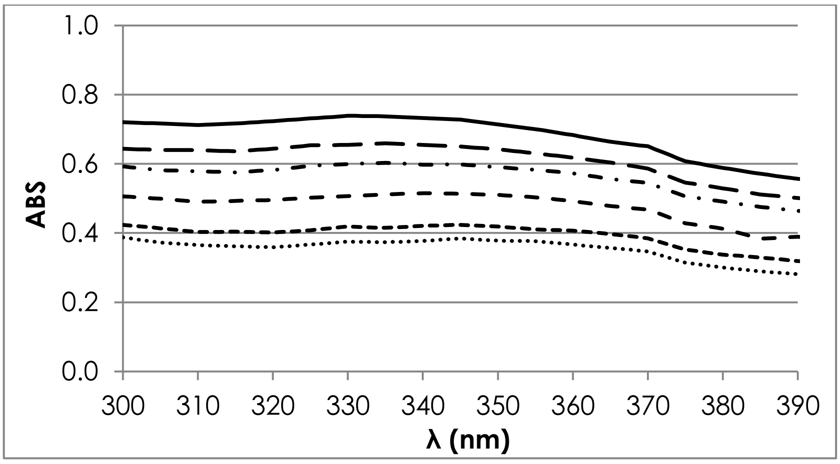

Figure SI4.6 Absorbance spectra of 40 mg L^{-1} P25 TiO_2 suspensions vs. time ([KI]=50 mM).

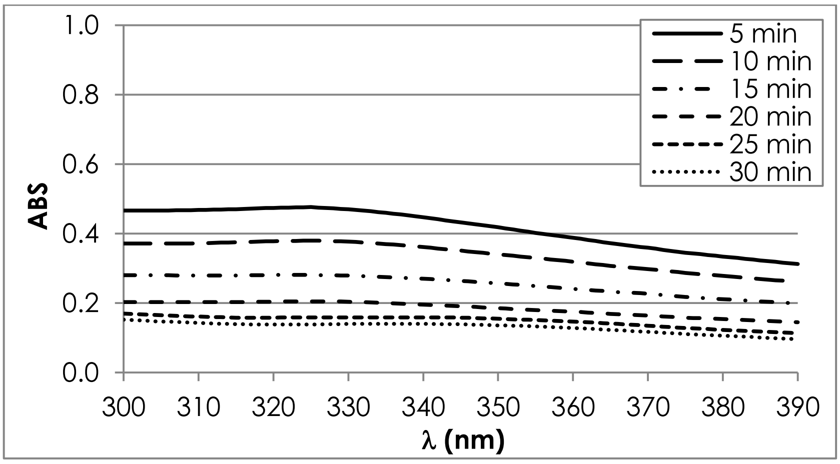

Figure SI4.7 Absorbance spectra of 20 mg L^{-1} P25 TiO_2 suspensions vs. time ([KI]=50 mM).

SI4.6 Absorbance of TiO_2 suspensions in terephthalic acid as a function of time

Samples containing two different concentrations of P25 Aeroxide TiO_2 in suspension (40 and 20 mg L^{-1}) and 0.125 mM TA, buffered to pH 7.8 by means of 5 mM phosphate buffer, were mixed on a magnetic stirrer (400 RPM) in the same reaction vessel used in photocatalysis tests for different time intervals. At the end of the mixing time, absorbance spectra were measured against deionized water was as the reference.

Results, reported in figure SI4.8, show that no significant changes in TiO_2 suspension absorbance were observed over time. In the kinetic model, the $ABS_{TiO2,\lambda}$ value at a given wavelength was considered to be time-independent and calculated as the average of absorbance values measured at each time interval. It was also verified that neither TA nor 2-HTA significantly absorb incident radiation in the investigated wavelength range, confirming that the absorbance of solution $ABS_{sol,\lambda}$ was negligible during tests for hydroxyl radical measurement.

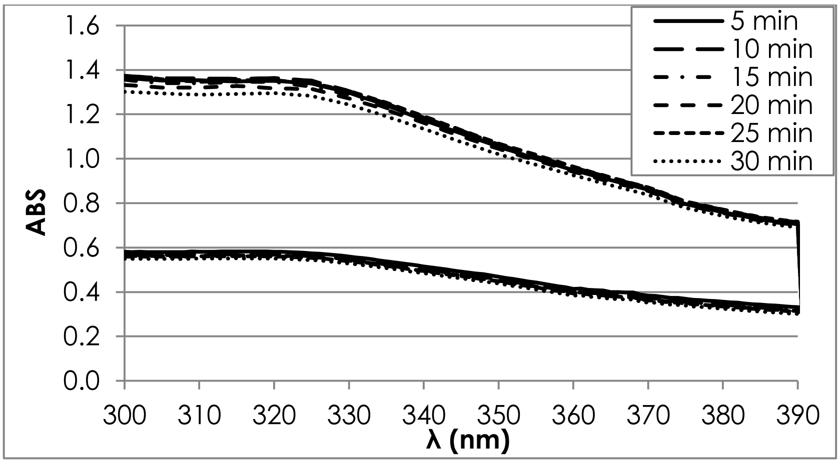

Figure SI4.8 Absorbance spectra of 40 mg L^{-1} (higher series) and 20 mg L^{-1} (lower series) P25 TiO$_2$ suspensions vs. time ([TA]=0.125 mM, pH buffered to 7.9 by means KOH).

SI4.7 Steady state equations for reactive species

Steady state equations for reactive species were obtained by:

- equating the relation for promoted electrons variation (8) to zero,
- deriving from this relation the expression for photogenerated holes concentration (eSI4.5),
- equating the relation for photogenerated holes variation (7) to zero,
- introducing in this relation the expression (eSI4.5) for photogenerated holes concentration,
- deriving the relation for promoted electrons concentration (equation eSI4.6),
- equating the relation for hydroxyl radicals variation (9) to zero,
- solving this relation as a quadratic and explicating the relation for hydroxyl radicals concentration (eSI4.7).

$$[h^+]_{SS} = \frac{k_5[e^-]_{SS}[O_2]}{k_1[OH^-] + k_3[OH^\bullet]_{SS} + k_R \frac{K_A[I^-]}{1 + K_A[I^-]}} \qquad \text{(eSI4.5)}$$

$$[e^-]_{SS} = \frac{-b + \sqrt{b^2 - 4ac}}{2\alpha} \qquad \text{(eSI4.6)}$$

$$a = \varepsilon^{D-1}k_2k_5[O_2] + k_2k_4[OH^\bullet]_{SS}$$

$$b = k_5[O_2]k_1[OH^-] + k_4[OH^\bullet]_{SS}k_1[OH^-] + k_3[OH^\bullet]_{SS}k_5[O_2] + k_3k_4{[OH^\bullet]_{SS}}^2 + k_5[O_2]k_R\frac{K_A[I^-]}{1 + K_A[I^-]} + k_4[OH^\bullet]_{SS}k_R\frac{K_A[I^-]}{1 + K_A[I^-]}$$

$$c = -\Phi R\left(k_1[OH^-] + k_3[OH^\bullet]_{SS} + k_R\frac{K_A[I^-]}{1 + K_A[I^-]}\right)$$

$$[OH^{\bullet}]_{SS} = \frac{-(k_3[h^+]_{SS} + k_4[e^-]_{SS} + k_{TA}[TA]) + \sqrt{(k_3[h^+]_{SS}+k_4[e^-]_{SS}+k_{TA}[TA])^2 + 4k_6k_1[OH^-][h^+]_{SS}}}{2k_6} \quad \text{(eSI4.7)}$$

SI4.8 Values for reaction rate constants used in TiO_2 photocatalysis modelling

Table SI4.1 Reaction constants used in TiO_2 nanoparticle photocatalysis modelling.

Parameter	Value [$M^{-1}\,s^{-1}$]	Reference	Parameter	Value [$M^{-1}\,s^{-1}$]	Reference
Φ	0.02	[SI4]	k_4	$3.00 \cdot 10^{10}$	[SI7]
k_1	$4.00 \cdot 10^{9}$	[SI5]	k_5	$1.90 \cdot 10^{10}$	[SI7]
k_2	$1.66 \cdot 10^{9}$	[SI6]	k_6	$5.50 \cdot 10^{9}$	[SI7]
k_3	$7.00 \cdot 10^{9}$	[SI7]	k_{TA}	$3.30 \cdot 10^{9}$	[SI8]

SI4.9 Kinetic model sensitivity analysis

The sensitivity of parameters of the kinetic models as evaluated by a one-parameter-at-a-time method [SI9]. The concentration of iodine and 2-HTA obtained at the end of simulation (30 minutes of irradiation time) was chosen as the reference model output for the evaluation of the influence of the variation of parameters. The Normalized Sensitivity Index (NSI) was calculated by normalizing the output values using the following expression:

$$NSI = \frac{OUTPUT_{max} - OUTPUT_{min}}{OUTPUT_{max}} \cdot \frac{\delta_{max}}{\delta_{max} - \delta_{min}} \quad \text{(eSI4.8)}$$

where $[OUTPUT]_{max}$ and $[OUTPUT]_{min}$ are the maximum and the minimum output values obtained when varying a model parameter in a range of values between δ_{max} and δ_{min}. Parameters related to experimental procedures were varied in an admissible range of values, considering the uncertainty in their determination, while kinetic constants were increased and decreased by one order of magnitude. The range of variation and the obtained NSI values for each parameter are summarized in table SI4.2.

Table SI4.2 Sensitivity analysis of kinetic models (pH from 6.3 to 6.4 in h^+ model, from 7.7 to 7.9 in $OH^{\bullet}$ model).

			h^+ model	$OH^{\bullet}$ model
Parameter	δ_{min}	δ_{max}	**NSI**	
R_a (m)	1.00E-07	1.50E-06	<1.00E-05	<1.00E-05
D (-)	1.1	3	<1.00E-05	1.18E-05
I (mW cm^{-2})	1.6	2.0	9.60E-01	4.97E-01
pH (-)	6.3/7.8	6.4/8.0	1.20E+01	2.41E-01
Φ (-)	0.01	0.05	9.01E-01	6.59E-01
$[O_2]$ (M)	2.84E-05	2.84E-04	<1.00E-05	3.32E-04

k_1 (M^{-1} s^{-1})	4.00E+08	4.00E+10	9.89E-03	1.22E-01
k_2 (M^{-1} s^{-1})	1.66E+08	1.66E+10	<1.00E-05	<1.00E-05
k_3 (M^{-1} s^{-1})	7.00E+08	7.00E+10	<1.00E-05	1.39E-01
k_4 (M^{-1} s^{-1})	3.00E+09	3.00E+11	<1.00E-05	3.77E-04
k_5 (M^{-1} s^{-1})	1.90E+09	1.90E+11	<1.00E-05	3.77E-04
k_6 (M^{-1} s^{-1})	5.50E+08	5.50E+10	<1.00E-05	7.24E+00
k_R (s^{-1})	6.25E+00	8.25E+00	8.60E-01	-
K_A (M^{-1})	2.86E+01	3.32E+01	3.10E-01	-
k_{TA} (M^{-1} s^{-1})	5.94E+03	5.94E+05	-	9.93E-01

REFERENCES

[SI1] I. Grcic, G. Li Puma, Photocatalytic degradation of water contaminants in multiple photoreactors and evaluation of reaction kinetic constants independent of photon absorption, irradiance, reactor geometry, and hydrodynamics, Environ. Sci. Technol. 47 (2013) 13702-13711.

[SI2] J.M. Herrmann, P. Pichat, Oxidation of halide ions by oxygen in ultraviolet irradiated aqueous suspension of titanium dioxide. J.C.S. Faraday I 76 (1980) 1138-1146.

[SI3] M. Mehrvar, W.A. Anderson, et al., Non-linear parameter estimation for a dynamic model in photocatalytic reaction engineering. Chem. Eng. Sci. 55 (2000) 4885-4891.

[SI4] K. Ishibashi, A. Fujishima, T. Watanabe, K. Hashimoto, Detection of active oxidative species in TiO_2 photocatalysis using the fluorescence technique. Electrochem. Commun. 2 (2000) 207-210.

[SI5] D. Jassby, J.F. Budarz, M. Wiesner, Impact of aggregate size and structure on the photocatalytic properties of TiO_2 and ZnO nanoparticles. Environ. Sci. Technol. 12 (2012) 6934-6941.

[SI6] B. Ohtani, R.M. Bowman, D.P. Colombo, H. Kominami, H. Noguchi, K. Uosaki, Femtosecond diffuse reflectance spectroscopy of aqueous titanium (IV) oxide suspension: correlation of electronhole recombination kinetics with photocatalytic activity. Chem. Lett. (1998) 579–580.

[SI7] G.V. Buxton, C.L. Greenstock, W.P. Helman, A. Ross, Critical review of rate constants for reactions of hydrated electrons, hydrogen atoms and hydroxyl radicals ($^{\bullet}OH/^{\bullet}O^{-}$) in aqueous solution. J. Phys. Chem. Ref. Data 17 (1988) 513–886.

[SI8] M. Saran, K.H. Summer, Assaying for hydroxyl radicals: hydroxylated terephthalate is a superior fluorescence marker than hydroxylated benzoate. Free Radical Res. 31 (1999) 429–436.

[SI9] D.M. Hamby, A review of techniques for parameter sensitivity analysis of environmental models. Environ. Monit. Assess. 32 (1994) 135-154.

CHAPTER 5

INFLUENCE OF INORGANIC ANIONS ON THE REACTIVITY OF NANOPARTICLES IN TiO_2 PHOTOCATALYSIS

ABSTRACT

The influence of inorganic anions on the reactivity of titanium dioxide (TiO_2) nanoparticles was assessed by monitoring the production of reactive species over time by P25 Aeroxide TiO_2 suspensions in the presence of inorganic ions (i.e. carbonate, chloride, nitrate, phosphate and sulfate) dosed as potassium salts at several concentrations. The production of photogenerated holes and hydroxyl radicals was measured by observing their selective reaction with two probe compounds, respectively iodide and terephthalic acid. TiO_2 nanoparticles were dispersed in solution with anionic species and photoactivated by UV-A radiation, while TiO_2 aggregates were characterized over process time.

The influence of inorganic anions was different for photogenerated holes and hydroxyl radicals. For iodide oxidation, a strong decrease was determined by carbonate and phosphate, whose interaction with TiO_2 nanoparticles was successfully described by a Langmuir-Hinshelwood mechanism and effectively related to the characteristics of TiO_2 aggregates. Therefore, the detrimental effect was attributed to a reduction of active sites on TiO_2 surface available for iodide oxidation. On the other hand, a decrease in terephthalic acid oxidation was observed for all inorganic anions, with the extent of inhibition a function of anionic species, where carbonate > chloride > phosphate > nitrate > sulfate. In this case inorganic anions probably acted via two mechanisms in reducing TiO_2 reactivity: (i) by substituting hydroxyl radicals precursors, i.e. hydroxyl ions, on TiO_2 surface and (ii) by quenching hydroxyl radicals.

The research work described in the present chapter was carried out with the valuable support of

Jeffrey Farner Budarz, PhD student, Duke University, United States
Jean-Yves Bottero, Research scientist, CEREGE, University Aix-Marseille, France
Mark Wiesner, Full professor, Duke University, United States

The research work was partially carried out during a 6-month period of international mobility at the Center for the Environmental Implications of NanoTechnologies (CEINT), Duke University (Durham, North Carolina, United States).

The present chapter, after a further internal review and an adaptation in terms of formatting style, will be submitted within a short time for publication to the journal ‘Langmuir’.

5.1 INTRODUCTION

Titanium dioxide (TiO_2) nanoparticles are widespread and used in a multitude of commercial products, including food, personal care products, paints, coatings, paper, and fibers due to their brightness, high refractive index, and UV resistance [1–3]. Other applications related to the peculiar photoelectrochemical properties of titanium dioxide are also of research interest, namely solar energy conversion, photocatalytic depolluting and photo-induced superhydrophilicity [4,5]. In particular, TiO_2 nanoparticle photocatalysis is a promising process for water and wastewater treatment, based on the advanced oxidation and disinfection of chemical pollutants and pathogens by reactive species generated when TiO_2 nanoparticles in suspension are irradiated by photons of wavelength below 390 nm [6]. The potential of TiO_2 photocatalysis for degrading a number of contaminants has already been highlighted [7,8], although the process is still not a technology as established as ozone or hydrogen peroxide combined UV radiation advanced oxidation. In order to be widely adopted, further investigations are required to improve its cost-efficiency and to develop its application at the full scale [9].

An important constraint is represented by the presence of compounds in water and wastewater that adversely affect the reactivity of TiO_2 nanoparticles against target pollutants. Of these, inorganic ions are the most ubiquitous, as significant quantities are normally present in fresh water. This research focuses on the ability of inorganic anions to significantly affect TiO_2 reactivity by (i) directly interfering with chemical-physical reactions (direct mechanism), and by (ii) influencing the aggregation state of TiO_2 nanoparticles, in turn altering reactivity (indirect mechanism) [6].

Concerning the direct mechanism, several research works have already been published indicating that inorganic anions impact the fundamental chemical-physical processes taking place in TiO_2 photocatalysis, namely photon absorption, surface adsorption and photocatalytic degradation [10–17]. As a matter of fact, UV screening by nitrate was reported [18] as well as the adsorption of various anions, such as phosphate [19]. In the latter case anions compete for the active sites on TiO_2 surface, preventing the reaction of pollutants, which have to be necessarily adsorbed before degradation, and reducing the amount of hydroxide ions sorbed to TiO_2 surface, precursors of radical species. On the other hand, the photocatalytic degradation is inhibited when reactive species are directly quenched by anions. This phenomenon is related to the specific reactivity of each compound with the generated reactive species [20].

The cited research was conducted by using various model pollutants, such as dyes or organic solvents, whose reaction pathways are complex and mostly unknown. As such, only overall reactivity assessments were conducted given the difficulty in differentiating the involved chemical reactions. Moreover, most of the studies assessing the influence of inorganic ions on TiO_2 suspensions were carried out without a detailed characterization of TiO_2 aggregates.

Apart from these considerations, with respect to the indirect mechanism, the influence of inorganic anions on TiO_2 nanoparticle aggregation has been extensively documented for nanoparticles diffusion and transport in aquatic systems [21–25]. This area of research is of particular interest due to the increasing concern for environmental implications of nanomaterials. In particular, the interactions among TiO_2 nanoparticles are effectively described by the DLVO theory, developed by Derjaguin, Landau, Verwey and Overbeek, which accounts for the two forces influencing nanoparticles, namely the van der Waals attraction and the electrical double layer repulsion, the sum of which is decisive in determining the potential for aggregation [24]. Generally the repulsive energy of the electric double layer is dominant for TiO_2 nanoparticles suspended in water in the absence of inorganic ions, while the energy barrier decreases with increasing the concentration of ions, corresponding to a greater presence of charge in solution and, therefore, to a weakening of the repulsive forces. The ionic strength of the solution has been successfully related to the stability of a nanoparticle suspension [22]. Nevertheless there remains a lack of understanding about the relationship between the characteristics of TiO_2 suspensions and their reactivity.

The detection and measurement of reactive species can be performed using highly selective chemical probes, *inter alia* [26–28]. This enables the present investigation of the specific influence of inorganic ions on the availability of the various reactive species in the development of radical pathways. Such research has strong implications not only for TiO_2 photocatalysis engineering but also for the assessment of the risk related to the environmental dispersion of this manufactured nanomaterial. In fact, toxicological studies are usually performed in synthetic or natural media containing inorganic ions, whose overlook may result in relevant misjudgments [29–31].

In this work, the reactivity of TiO_2 suspensions in the presence of inorganic species was assessed at the laboratory scale by monitoring the selective reaction of reactive species with probe compounds. In detail, reactions for photogenerated holes (h^+) and hydroxyl radicals ($OH^•$) were, respectively, iodide (dosed as potassium iodide, KI) to iodine (I_2) and terephthalic acid (TA) to 2-hydroxyterephthalic acid (2-HTA). The products of these reactions are easily measurable by spectrometric and fluorimetric techniques (chapter 4). TiO_2 nanoparticles suspensions were created by different procedures, involving either the use of probe sonication or stirring, and the inorganic species (carbonate, chloride, nitrate, phosphate and sulfate) were dosed as potassium salts at several concentrations. TiO_2 suspensions were photoactivated by UV-A irradiation, and the reactive species concentration was evaluated over time along with TiO_2 aggregate characterization.

5.2 MATERIAL AND METHODS

5.2.1 Reagent solutions

KOH, KI, I_2, $KHCO_3$, KCl, KNO_3, KH_2PO_4, K_2HPO_4 and K_2SO_4 were purchased from VWR International (USA). Mono-salt stock solutions of inorganic anions (0.1 M) were prepared in deionized water for carbonate, chloride, nitrate and sulfate. Phosphate stock solution (0.1 M) was prepared by dosing 0.1495 g of KH_2PO_4 and 1.55 g of K_2HPO_4 in 100 mL of deionized water.

The starch solution was prepared by adding 0.5 g of starch (VWR International) in 100 mL of boiling deionized water and mixing until complete dissolution. After 12 h settling, the supernatant was collected. TA (0.5 mM) and 2-HTA (0.125 mM) solutions were prepared by dosing 16.72 mg of TA (Sigma-Aldrich, USA) and 4.69 mg of 2-HTA (Sigma-Aldrich) in 200 mL of deionized water, adjusting pH to 7.9 with KOH, and mixing on magnetic stirrer overnight.

5.2.2 TiO_2 dispersion and suspension characterization

Experiments were performed on P25 Aeroxide TiO_2 nanopowder (Evonik, Germany). TiO_2 stock suspension (40 mg L^{-1}) was prepared by adding 2 mg of P25 TiO_2 to 50 mL liquid volume, consisting of a combination of water and stock solutions of inorganic anions depending on the test conditions. Two different procedures for TiO_2 nanoparticle dispersion were used: (i) mixing on magnetic stirrer for 2 minutes at 120 RPM, (ii) probe sonication (Q700, QSonica, USA) for 6 minutes in pulse mode (12 s ON / 3 s OFF) with 1/2” diameter tip.

Three procedures were used for sample preparation, depending on the dispersion method of TiO_2 nanoparticles and on the timing of dosage of the inorganic anions in solution:

- Sonicated with inorganic anions (S): TiO_2 nanoparticles were dispersed by probe sonication in the presence of inorganic ions, added to TiO_2 stock suspension before probe sonication.
- Sonicated without inorganic anions (S+A): TiO_2 nanoparticles were dispersed by probe sonication in the presence of a small concentration of inorganic anions (1 mM), while the remaining mass of inorganic anions was added after sonication in the reaction beaker.
- Non-sonicated (NS): TiO_2 nanoparticles were dispersed in deionized water by mixing on magnetic stirrer and inorganic anions were added later in the reaction beaker.

After sonication or mixing, a fraction of the volume was collected and transferred to the reaction beaker for sample preparation in reactivity measurement tests. When TiO_2 was dispersed by sonication, pH was adjusted to 7.9 with KOH (0.1 M) after sonication.

A laser diffraction particle analyser (Mastersizer 3000, Malvern, England) was used to determine TiO_2 aggregate size and fractal dimension. 300 mL of TiO_2 suspensions were prepared and continuously mixed on a magnetic stirrer (400 RPM), then in-line light scattering measurements were performed using a peristaltic pump for sample loading located downstream of the instrument. Time resolved size measurements, reported in terms of median diameter (D_{50}) both as number weighted and volume weighted intensity, were taken over 30 minutes. Meanwhile, measurements of the scattering intensity, I(q), over a range of scattering vectors, q, corresponding to 0 - 50° for each sample were recorded simultaneously by an array of detectors. The aggregate fractal dimension, D_f, was then calculated as the negative slope of the linear fitting region emerging when plotting log(I(q)) vs. log(q) [32].

5.2.3 TiO_2 nanoparticle reactivity measurement

The experimental setup consisted of a UV box equipped with two 15 W fluorescent UV lamps (TL-D 15W BLB SLV, Philips, Netherlands) and thermostated at room temperature (22±1°C), in which a 10 mL reaction beaker was continuously mixed on a magnetic stirrer (400 RPM). The radiation intensity at the liquid upper surface was 1.9 mW cm^{-2}, centered at 365 nm (see Supporting Information (SI5.1)) and monitored by means of a ILT1400 radiometer, mounting a SEL033 sensor (International Light Technologies, USA). Geometrical characteristics of the reaction beaker (H=3.5 cm, Ø=5 cm) determined a 0.5 cm thickness liquid layer when the stirring bar (3 x 10 mm) was inset.

5.2.3.1 Photogenerated holes

The production of photogenerated holes was first measured as a function of iodide concentration, by irradiating 20 mg L^{-1} TiO_2 suspensions for 30 minutes at various KI concentrations (25, 37.5, 75, 100 mM) in the absence of other inorganic anions. Every 5 minutes a small volume (0.5 mL) was sampled and, after starch addition at a 1:1 volume ratio, the absorbance at 585 nm was measured in a plastic cuvette (10 mm optical path) vs. deionized water by spectrophotometer (Cary 100, Agilent, USA). Absorbance values were related to iodine concentration by a standard curve, after subtracting TiO_2 suspension contribution, which was evaluated by spectrometric measures on non-irradiated samples. The photogenerated holes concentration was stoichiometrically estimated as twice the produced iodine concentration, according to the following reaction:

$$2I^- + 2h^+ \rightarrow I_2 \qquad \text{(e5.1)}$$

A standard curve was determined using a 0.025 M iodine stock solution, that was diluted to obtain solutions at concentration between 0.0125 and 0.125 mM (concentration step: 0.0125 mM), and adopting the same procedure as for the samples.

For evaluating photogenerated hole production in the presence of inorganic anions (carbonate, chloride, nitrate, phosphate, sulfate), reaction beakers containing 20 mg L^{-1} P25 TiO_2, 50 mM KI and various concentrations of inorganic anions (0, 0.5, 1, 2.5, 5, 12.5 mM) were irradiated for 30 minutes, and photogenerated holes were evaluated by the same procedure already reported.

All tests were repeated four times.

5.2.3.2 Hydroxyl radicals

Hydroxyl radical production tests were performed on samples consisting of 20 mg L^{-1} P25 TiO_2, 0.125 mM TA, and various concentrations of inorganic anions (0, 0.5, 2.5, 5, 12.5, 25 mM of carbonate, chloride, nitrate, phosphate and sulfate), irradiated for 30 minutes. Every 5 minutes a 0.5 mL aliquot was added to 0.75 mL deionized water in a 2 mL centrifuge tube. Samples were then centrifuged for 5 minutes at 12,000 RPM to separate the TiO_2 from the solution. Afterwards, 1 mL of the supernatant was transferred in a plastic cuvette (10 mm optical path) for fluorescence measurement in a Varian Eclipse fluorometer (Agilent, USA) with the excitation wavelength set at 315 nm and emission set at 425 nm. Fluorescence values were related to the 2-HTA concentration by a standard curve. Hydroxyl radical concentrations were estimated by the following reaction, assuming 80% trapping efficiency for $OH^\bullet$ by TA [33] and considering sample dilution in deionised water:

$$TA + OH^\bullet \rightarrow 2 - HTA \tag{e5.2}$$

A standard curve was determined using a 0.125 mM 2-HTA stock solution, that was diluted to obtain solutions at 0.0025, 0.005, 0.01, 0.025, 0.05, 0.075 and 0.1 M, and adopting the same procedure as for the samples.

All tests were replicated four times.

5.3 RESULTS AND DISCUSSION

The strong influence of inorganic anions on TiO_2 nanoparticle photocatalysis, resulting from a complex combination of chemical-physical phenomena, was observed in experimental results. In the following, the characteristics of TiO_2 aggregate suspensions (i.e. size and fractal dimension) as a function of operating conditions are argued in paragraph 5.3.1. The influence of inorganic anions on TiO_2 reactivity is subsequently discussed by differentiating experimental data according to the detected reactive species, namely photogenerated holes and hydroxyl radicals.

5.3.1 TiO_2 aggregate characterization

The measurement technique for photogenerated holes is characterized by an important constraint, in that large quantities of an inorganic salt (potassium iodide) are dosed in solution as a probe compound. Aggregation of TiO_2 nanoparticles occurred immediately after iodide dosage, whereas TiO_2 suspensions were stable in deionized water, irrespectively of the dispersion method, over the experimental timeframe. Significant aggregation was not observed when terephthalic acid was dosed for the experimental determination of hydroxyl radicals. This is due to the fact that terephthalic acid was dosed at very low concentrations, resulting in a negligible increase of the solution ionic strength, and TiO_2 suspensions maintained a size distribution similar to that observed in deionized water. Experimental size data, both as number weighted and volume weighted D_{50}, over time for non-sonicated TiO_2 suspensions at various iodide concentrations (0, 50 mM) are reported in figure 5.1, while relative size distributions are reported in Supporting Information (SI5.2, figure SI5.2). Furthermore, size distribution vs. time for non-sonicated TiO_2 suspensions at various iodide concentrations (0, 0.5, 5, 50 mM) are reported in Supporting Information (SI5.2, figure SI5.3).

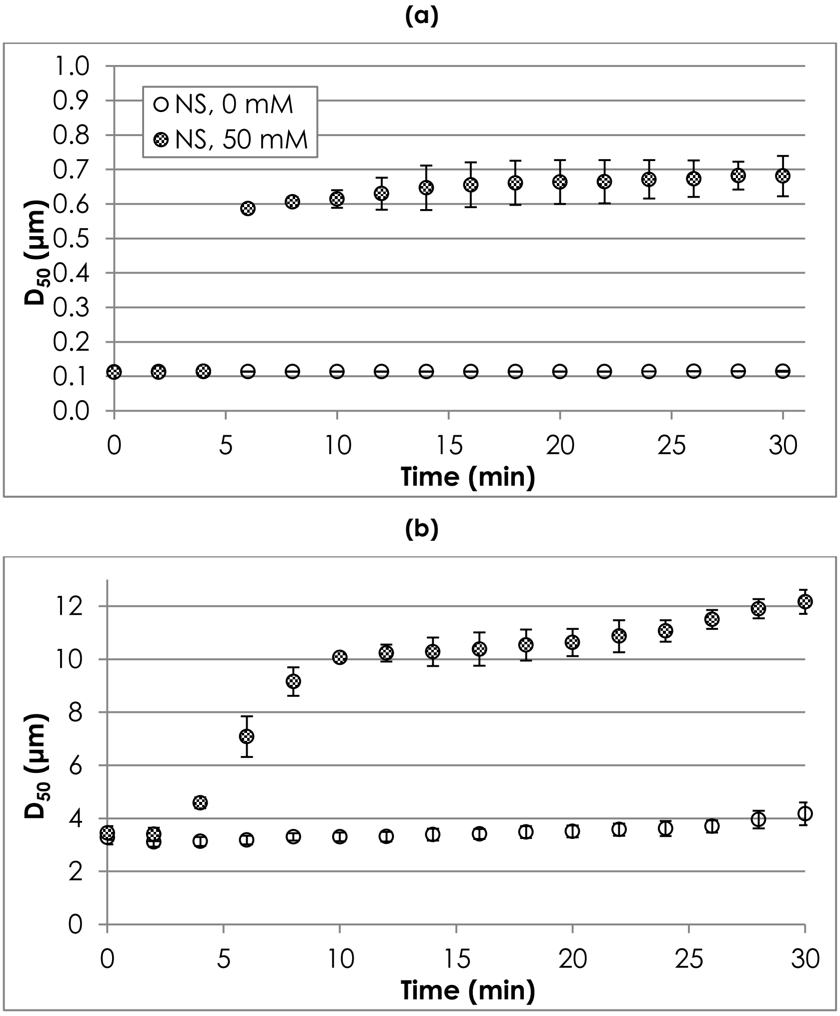

Figure 5.1 TiO_2 aggregate size (D_{50}), number (a) and volume (b) weighted, vs. time (mean±st.dev.) as a function of iodide concentration (0, 50 mM) for non-sonicated TiO_2 dispersions.

In detail, non-sonicated TiO_2 nanoparticles in deionized water created aggregates with a stable number weighted D_{50} of 114±0.5 nm and volume weighted D_{50} slightly increasing from 3.28±0.269 µm to 4.17±0.431 µm over 30 minutes. The difference in values using different weighting methods arises from the high polydispersity of TiO_2 suspensions, indicating that the vast majority of aggregates exist at the smaller size class with relatively few large aggregates influencing the volume weighted D_{50}. Although the number weighted D_{50} was comparable with and without sonication, the dispersion method strongly influenced the polydispersity of the aggregate size distribution, with sonication breaking up TiO_2 large aggregates (data not shown).

The introduction of KI resulted in the aggregation of TiO_2 nanoparticles for both dispersion methods, so that, for instance, the number weighted D_{50} increased over 30 minutes to 681±58.7 nm for non-sonicated TiO_2 suspensions. In agreement with DLVO theory, the promotion of aggregation was generally observed with increasing anion concentration, as it can be observed in figure SI5.3.

However, the introduction of inorganic ions to samples already containing KI did not significantly altered aggregation except at concentrations above 12.5 mM. For samples not containing KI, the presence of low concentrations (0.5 mM) of carbonate and phosphate during sonication resulted in the reduction of initial aggregate sizes. Both of these species buffered the pH at about 7.9, far from the isoelectric point (about 6.71 [34]), whereas a significant pH decrease was observed when TiO_2 nanoparticles were sonicated either in deionized water or other anions (e.g. nitrate). The pH decrease, due to the formation of hydroxyl groups on TiO_2 surface and, thus, to the subtraction of hydroxyl ions from solution, produces a more favorable condition for TiO_2 aggregation.

As for the fractal dimension, structure calculations yielded a D_f around 2.17 for all the tested operating conditions, which remained unchanged over the 30 minutes. The range of q values for which the scattering response was linear corresponded to length scales ranging from about 660 nm to 3.4 μm, being the totality of experimental data, including those shown in chapter 4, comparable.

5.3.2 Photogenerated holes

The influence of inorganic anions on the production of photogenerated holes was assessed by monitoring the oxidation of iodide as a function of the concentration of inorganic anions. Initially, the production of photogenerated holes was measured at various iodide concentrations in the absence of other inorganic anions. Experimental results indicated a saturation trend (figure 5.2), as observed previously in chapter 4. Oxidized iodide concentrations as a function of time at various iodide concentrations are shown in Supporting Information (SI5.3). Higher reactivity, monitored as greater iodide oxidation, was observed for non-sonicated TiO_2 suspensions. This is likely due to the differences in solution pH due to sonication. In fact, at lower pH, as is seen in sonicated suspensions, the surface of the TiO_2 will be less negatively charged, decreasing electrostatic repulsion and increasing the probability of iodide ion sorption on the TiO_2 surface.

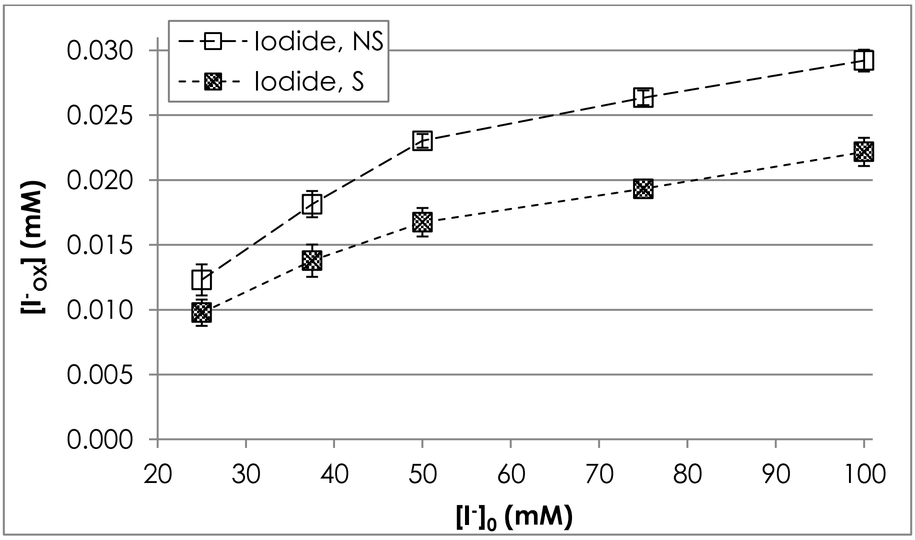

Figure 5.2 Oxidized iodide concentration (mean±st.dev.) vs. initial iodide concentration after 30 minutes irradiation time as a function of TiO_2 dispersion method (S: Sonicated, NS: Non-sonicated).

A change in the rate of iodide oxidation was only observed in the presence of carbonate and phosphate, while chloride, nitrate and sulfate did not cause any significant change at concentrations between 0.5 and 12.5 mM. Experimental results after 30 minutes of irradiation for carbonate and phosphate anion concentrations and TiO_2 dispersion methods are shown in figure 5.3. Oxidized iodide concentrations as a function of irradiation time at various carbonate and phosphate concentrations are shown in Supporting Information (SI5.4). Experimental data for chloride, nitrate and sulfate are not shown, since oxidized iodide concentrations as a function of irradiation time were not significantly different from results obtained for TiO_2 suspensions without inorganic ions. Hence, oxidized iodide concentrations for chloride, nitrate and sulfate were equal to the values reported in Supporting Information (SI5.4) for null concentrations of carbonate and phosphate. The lack in statistically significant differences between series with or without anions for chloride, nitrate and sulfate was verified by means of Student's t-test (p-value 0.005).

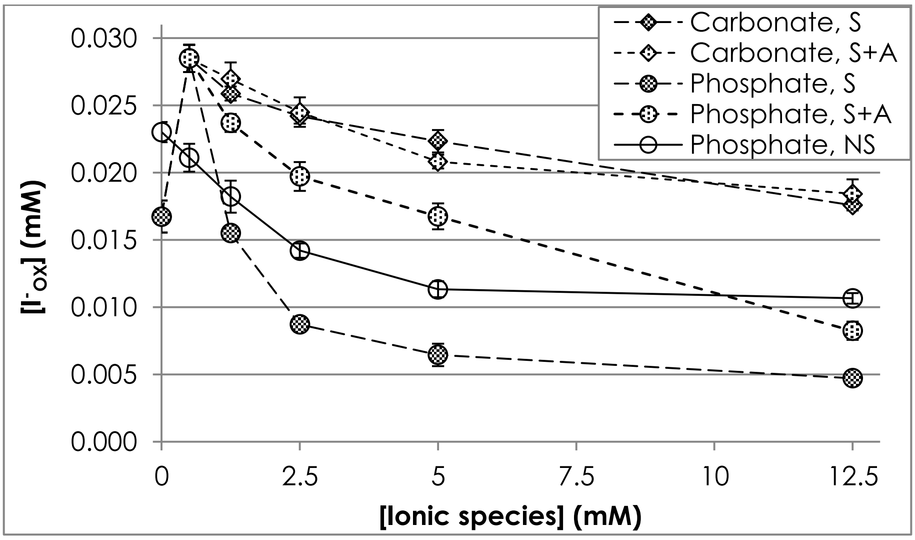

Figure 5.3 Oxidized iodide concentration (mean±st.dev.) vs. inorganic anion concentration after 30 minutes irradiation time (50 mM KI) as a function of species in solution (carbonate, phosphate) and TiO_2 dispersion method (S: Sonicated with inorganic ions, S+A: Sonicated without inorganic ions, NS: Non-sonicated).

For sonicated TiO_2 stock suspensions, an increase in reactivity was observed at 0.5 mM carbonate and phosphate concentrations. The presence of a low amount of either carbonate or phosphate anions in solution during sonication produced the same increase in reactivity. This is probably due to the stabilizing effect of these inorganic anions on TiO_2 aggregates. Furthermore, because the concentration of anions added was small, little negative effect on reactivity was observed, and the overall effect due to both direct and indirect mechanisms was an increase in reactivity.

At concentrations of 1 mM and above, inorganic anions reduced the reactivity of TiO_2 suspensions. The detrimental effect of phosphate addition is greater than carbonate, and the effect of dispersion method is more pronounced as well for phosphate. For non-sonicated TiO_2 suspensions, a monotonic decrease in reactivity was observed when increasing phosphate concentration.

Non-reproducible results were obtained for non-sonicated TiO_2 suspensions in the presence of carbonate, with data variability so high (standard error>50%) that a trend with carbonate concentration could not be determined. An explanation for these results is probably related to the different influence of inorganic anions, exerting phosphate a stabilizing effect on TiO_2 suspensions, unlike carbonate. Thus, the result is non-stable TiO_2 aggregates in presence of carbonate, since the solution pH, at 6.3±0.1, was not adjusted after dispersion and was close to the isoelectric point.

A relevant effect of the dispersion method on the photocatalytic process consists in the modification of the optical properties of TiO_2 suspensions. Absorption and scattering coefficients are about four times higher in case of sonication in deionized water [35,36], due to the higher number of small TiO_2 aggregates. Thus, higher reactivity is generally expected for sonicated TiO_2 suspensions [37]. In the present case the only possible comparison in terms of photogenerated holes between sonicated and non-sonicated TiO_2 suspensions was for phosphate dosage and no unambiguous indications were obtained. In fact, as already discussed, iodide oxidation was consistently higher only at 0.5 mM phosphate concentration in sonicated TiO_2 suspensions, unlike in the absence of phosphate in solution, while in non-sonicated TiO_2 suspension reactivity declined more slowly with increasing phosphate concentration. Hence, other parameters, such as solution pH, have to be considered. As an example, pH in non-sonicated TiO_2 suspensions was about 6.3 and it was not adjusted to 7.9, as was done for sonicated TiO_2 suspensions. This has two consequences for reactivity: (i) TiO_2 nanoparticles were less negatively charged and iodide transport to the aggregate surface was more favorable than for the sonicated samples at higher pH, and (ii) fewer hydroxide ions were present in solution and able to react with photogenerated holes to generate hydroxyl radicals.

The interaction mechanism between anions and TiO_2 nanoparticles has been discussed by Chen et al. [11], indicating that inorganic species are adsorbed on TiO_2 surface, according to a Langmuir type model. The adsorption of iodide, including the presence of other anions in solution, and subsequent reaction by TiO_2 photocatalysis can then be modelled as a Langmuir-Hinshelwood (LH) mechanism [38]:

$$r = \frac{d[I^-]}{dt} = -K_R \cdot \theta_{I^-} = -K_R \cdot \frac{K_{A,I}[I^-]}{1 + K_{A,I}[I^-] + \sum_{Anion} K_{A,Anion}\,[Anion]} \qquad \text{(e5.3)}$$

in which r is the reaction rate, θ_{I^-} is the surface coverage by iodide, $[I^-]$ is the concentration of iodide, $K_{A,I}$ is the equilibrium constant of adsorption for iodide, $K_{A,Anion}$ is the equilibrium constant of adsorption for a certain anionic species and K_R is the LH reaction constant for iodide oxidation. A procedure for $K_{A,I}$ and K_R estimation in the absence of other anionic species and considering iodide as the only compound involved in photocatalysis on TiO_2 surface was applied to experimental data reported in figure 5.2 as it has been suggested previously [38] (see Supporting Information (SI5.5)).

Estimated $K_{A,I}$ and K_R values are shown in table 5.1. The high values of the determination coefficient (R^2) indicate that LH mechanism is appropriate in describing iodide oxidation. Estimated K_A values were similar irrespective of the dispersion method, indicating that no significant differences in the number of active sites were induced by the sonication for the iodide adsorption on TiO_2 nanoparticles during reactivity measurement. On the other hand, experimental trends can be justified as a function of the K_R values, determined by a number of operating conditions, including pH. This finding supports the previous discussion that the importance of solution pH is greater than the changes in TiO_2 nanoparticle structure induced by the dispersion procedure in affecting reactivity results. Moreover, data processing results are in agreement with previous results on TiO_2 aggregate characterization, showing no relevant modification in TiO_2 aggregate size distribution by sonication, at least not as concerns the presence of active sites on the surface. These values are comparable with those obtained in chapter 4 for iodide oxidation in non-sonicated suspensions at 40 mg L^{-1} TiO_2 concentration.

Table 5.1 Estimated values of the equilibrium adsorption coefficient, K_A, for iodide, carbonate and phosphate and estimated values of LH reaction constants for iodide oxidation, K_R, in case it is the only anionic species or a competitor of other inorganic anions (carbonate or phosphate). Parameters were determined as a function of TiO_2 dispersion method (S: Sonicated with inorganic ions, S+A: Sonicated without inorganic ions, NS: Non-sonicated). The values of the coefficients of determination, R^2, are reported.

Ionic species	**K_A (M^{-1})**	**K_R (M s^{-1})**	**R^2**
Iodide, NS	10.1	3.51E-08	0.974
Iodide, S	13.2	2.24E-08	0.988
Carbonate, S	93.9	3.96E-08	0.930
Carbonate, S+A	142.7	4.16E-08	1.000
Phosphate, NS	309.9	3.75E-08	0.983
Phosphate, S	1370.8	4.41E-08	0.946
Phosphate, S+A	251.8	4.02E-08	0.954

Similarly, the LH mechanism was used for modelling the effect of inorganic anions on the formation of photogenerated holes. Here it is essential to take into account the competition for the active sites in LH mechanism among inorganic anions. A procedure for $K_{A,Anion}$ and K_R estimation in the presence of anionic competition for surface adsorption has been applied in the Supporting Information (SI5.5) in which the equilibrium constant of adsorption for iodide was taken from the previous calculation in the absence of other inorganic anions. Estimated $K_{A,Anion}$ and K_R values are also reported in table 5.1. Even for this case, experimental data are well fitted by the LH mechanism (R^2>0.930). Relevant differences were noticed in $K_{A,Anion}$ values as a function of the anionic species and the dispersion method, resulting greater values of $K_{A,Anion}$ in higher efficiency of active site occupation as a function of the inorganic anion concentration. Hence, comparing the various anionic species, iodide is the least favored in adsorption on TiO_2 surface under the present operating conditions. $K_{A,Anion}$ values for phosphate were much higher than for carbonate, highlighting that the stronger detrimental effect of phosphate on reactivity is probably due to a greater adsorbability on TiO_2 surface. Concerning the influence of the dispersion method, iodide oxidation was greatly reduced for sonicated TiO_2 suspensions in the presence of phosphate, indicating that phosphate creates surface bonds during sonication, unlike carbonate, and that the occupation of actives sites prevents the subsequent sorption and reaction of iodide. Instead, for the simultaneous dosage of phosphate and iodide, the two anionic species compete at the same time on the TiO_2 surface so that the adsorption of iodide in this case is greater. In addition, K_R values were comparable among various configurations, meaning that surface adsorption of inorganic anions is the most relevant phenomena in determining TiO_2 reactivity for the same conditions.

The adsorption on TiO_2 surface has previously been characterized for the inorganic anions studied here by assessing the competitive effects on the degradation of model pollutants, and the LH mechanism was effectively adopted for process modelling [10,16]. However, in the present work only carbonate and phosphate inhibited the oxidation of iodide, which has been recognized as a selective probe for photogenerated holes. Therefore, assuming that all anionic species are adsorbed on TiO_2 surface according to the affinity scale reported by Chen et al. [11] (chloride < nitrate < carbonate < sulfate < phosphate), there are two possible explanations for the observed experimental results: (i) the existence of different types of active sites governing the interactions of iodide, carbonate and phosphate on the TiO_2 surface, and (ii) the adsorption of chloride, nitrate and sulfate creates weak bonds with respect to other species, where these anions are easily displaced from TiO_2 surface by iodide. These hypotheses should be verified by means of analytical techniques capable of investigating TiO_2 surface chemistry, such as the surface-enhanced Raman spectroscopy [39].

A final remark concerns the influence of the associated cation, i.e. potassium in the present situation, whose effect on TiO_2 reactivity was considered negligible in previous works. The same can be predicted for other counter-ions, such as sodium [40].

5.3.3 Hydroxyl radicals

The generation of hydroxyl radicals as a function of inorganic anion concentration was evaluated for TiO_2 suspensions prepared with S+A dispersion method. 2-hydroxyterephthalic acid concentrations as a function of inorganic anion concentration after 30 minute irradiation time for various anionic species are shown in figure 5.4, while relative time series are reported in Supporting Information (SI5.6) in comparison with TiO_2 suspensions sonicated in the absence of anionic species. As in case of the iodide oxidation measurements, a small amount of anionic species dosed during sonication (0.5 mM) determined a strong change in TiO_2 suspension reactivity with respect to TiO_2 suspensions sonicated in the absence of inorganic anions. In detail, an increase was noticed for carbonate and chloride as well as a decrease for nitrate, phosphate and sulfate.

A detrimental effect on the generation of hydroxyl radicals was observed for each of the anionic species, although affecting TiO_2 reactivity with different magnitude. For normalization purposes, experimental results were divided by 2-HTA concentration obtained at 0.5 mM inorganic anion concentration for any anionic species, as shown in Supporting Information (SI5.7). Hence, anionic species can be sorted as a function of their detrimental effect on TiO_2 reactivity, obtaining the following decreasing scale: carbonate > chloride > phosphate > nitrate > sulfate. In particular, extreme values were observed for carbonate, since 25 mM anion concentration reduced terephthalic acid oxidation by about 70% after 30 minute irradiation time, and sulfate, for which an effect of a few percentage points was obtained at the same concentration.

The intensity of inorganic anion influence on TiO_2 reactivity differs from what has been reported in past research works [10,11,16], among which, however, there is no general consensus. In particular, the discrepancies in the results seem to be related to different adopted operating conditions, especially solution pH, model contaminants and TiO_2 characteristics, resulting in a change in the balance among the involved chemical-physical processes. A generalization is difficult and a case-by-case assessment is usually required for studying anionic species influence.

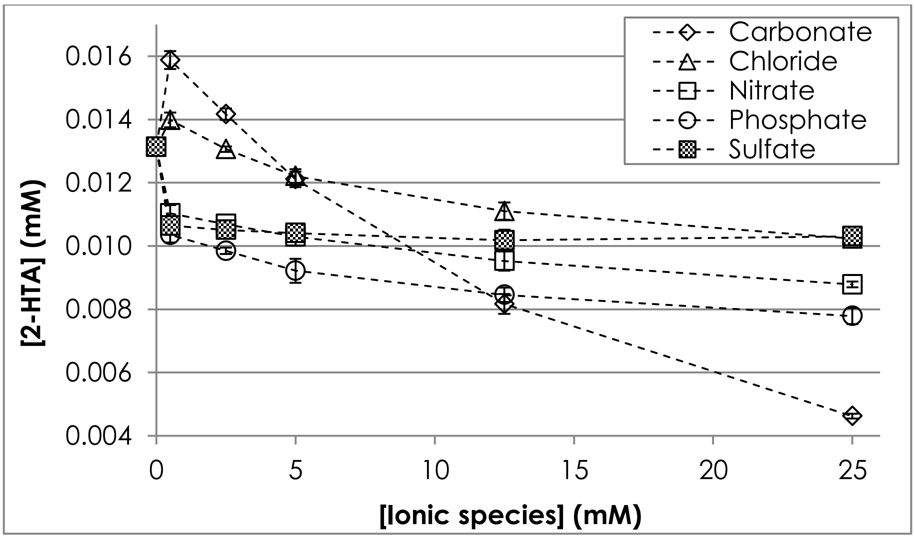

Figure 5.4 2-hydroxyterephthalic acid concentration (mean±st.dev.) vs. inorganic anion concentration after 30 minute irradiation time as a function of species in solution. TiO_2 suspensions were dispersed by S+A method.

Most of literature works refer to contaminants that undergo adsorption before photocatalytic degradation, such as dichloroethane for Chen et al. [11] and methylene blue for Guillard et al. [16], usually competing model pollutants for active sites on TiO_2 surface, likewise discussed for iodide. As for terephthalic acid, the occurrence of photocatalytic degradation in the absence of surface adsorption has been reported [26]. Moreover, terephthalic acid is a probe compound selective to hydroxyl radicals, whose reaction happens via a single step hydroxylation process, making possible a quantification of TiO_2 reactivity independent of pollutant characteristics. A further remark concerns solution pH, imposed to 7.9 for allowing the dissolution of terephthalic acid and, thus, determining the negative charge of TiO_2 surface. In such conditions terephthalic acid anionic molecules are rejected from TiO_2 surface that, in turn, is characterized by the presence of a large number of surface bonds with hydroxyl ions, given the high content in solution, as previously discussed in chapter 4.

Therefore, the negative influence of inorganic anions on terephthalic acid oxidation can be probably explained by means of two main phenomena: (i) a reduction in hydroxyl radical generation due to the occupation of active sites by anionic species instead of hydroxyl ions, (ii) the direct quenching of hydroxyl radicals by inorganic anions. The absorption of photons by inorganic anions, such as nitrate, has been excluded for these operating conditions in a previous work [16].

Rate constants for hydroxyl radicals and inorganic anions, reported in Supporting Information (SI5.8), do not provide a comprehensive explanation for observed results, being the expected reactivity scale at solution pH (sulfate > chloride > nitrate > carbonate > phosphate) different from experimental results. In fact, as an example, sulfate reactivity with hydroxyl radicals is four orders of magnitude higher than carbonate, although experimental results showed an opposite behaviour.

Hence, since the interaction between TiO_2 surface and probe compound is negligible as well as TiO_2 aggregate characteristics are comparable among different cases, the process is probably driven by the adsorption of inorganic anions on TiO_2 surface. Then, the adsorption of inorganic anions on TiO_2 surface could justify the asymptotic trend of experimental data, limiting the decrease of TiO_2 reactivity with increasing inorganic anion concentration. Otherwise, the poor description given by LH mechanism ($R^2<0.7$) and the differences in carbonate and phosphate influence with respect to iodide suggest that results are due to a combination of phenomena, possibly also having mass transfer and electrostatic interaction a relevant role.

Concerning 2-hydroxyterephthalic acid concentration over time, as can be seen in Supporting Information (SI5.6), different trends were observed in correspondence to various anionic species, in contrast to results obtained in the measurement of photogenerated holes. In particular, a significant slowdown in oxidation kinetics was observed for chloride, nitrate and sulfate as well as for carbonate in a more limited extent. This behaviour is probably due to the change of solution pH, decreasing over process time and reducing the availability of precursor molecules, hydroxyl ions, for the generation of hydroxyl radicals. In case of carbonate and phosphate the same phenomenon was respectively reduced and absent because of the pH buffering effect.

5.4 CONCLUSIONS

Experimental measurements indicated that inorganic anions have a significant impact on TiO_2 reactivity, determining their presence in water the occurrence of several chemical-physical phenomena. The most important is inorganic anion adsorption on TiO_2 surface, that happens via Langmuir model and that determines a competition for active sites with any other compound in solution, both contaminants and hydroxyl ions. Therefore, the detrimental effect of inorganic ions as a consequence of adsorption on TiO_2 surface can consist in: (i) hindering the interaction of pollutants, (ii) suppressing the generation of hydroxyl radicals by substituting hydroxyl ions. Moreover, inorganic ions can quench hydroxyl radicals, proportionally to specific rate constants.

Since the presence of inorganic ions is a common feature in water and wastewater, a preliminary assessment should be carried out for determining process performance and for evaluating the opportunity of preliminary inorganic anions removal, usually a complex and expensive alternative. Finally, as for the disturbances that can be caused by the presence of inorganic anions on experimental activities, such as in case of toxicological assays cited in the introduction, blank tests have to be conducted for estimating anionic species contribution, both in terms of direct and indirect effects, so that these could be discounted from experimental results.

5.5 REFERENCES

[1] C.O. Hendren, X. Mesnard, J. Dröge, M.R. Wiesner, Estimating production data for five engineered nanomaterials as a basis for exposure assessment, Environ. Sci. Technol. 45 (2011) 2562–2569.

[2] A. Weir, P. Westerhoff, L. Fabricius, K. Hristovski, N. von Goetz, Titanium dioxide nanoparticles in food and personal care products., Environ. Sci. Technol. 46 (2012) 2242–50.

[3] L. Windler, C. Lorenz, N. von Goetz, K. Hungerbühler, M. Amberg, M. Heuberger, et al., Release of titanium dioxide from textiles during washing., Environ. Sci. Technol. 46 (2012) 8181–8.

[4] O. Carp, Photoinduced reactivity of titanium dioxide, Prog. Solid State Chem. 32 (2004) 33–177.

[5] A. Fujishima, X. Zhang, D. Tryk, TiO_2 photocatalysis and related surface phenomena, Surf. Sci. Rep. 63 (2008) 515–582.

[6] M.N. Chong, B. Jin, C.W.K. Chow, C. Saint, Recent developments in photocatalytic water treatment technology: a review, Water Res. 44 (2010) 2997–3027.

[7] S. Malato, P. Fernández-Ibáñez, M.I.I. Maldonado, J. Blanco, W. Gernjak, Decontamination and disinfection of water by solar photocatalysis: recent overview and trends, Catal. Today. 147 (2009) 1–59.

[8] H. Choi, S.R. Al-Abed, D.D. Dionysiou, E. Stathatos, P. Lianos, TiO_2-based advanced oxidation nanotechnologies for water purification and reuse, Sustain. Sci. Eng. 2 (2010) 229–254.

[9] P. Pichat, Photocatalysis and water purification: from fundamentals to recent applications, Wiley-VCH, 2013.

[10] M. Abdullah, G.K.C. Low, R.W. Matthews, Effects of common inorganic anions on rates of photocatalytic oxidation of organic carbon over illuminated titanium dioxide, J. Phys. Chem. 94 (1990) 6820–6825.

[11] H.Y.Y. Chen, O. Zahraa, M. Bouchy, Inhibition of the adsorption and photocatalytic degradation of an organic contaminant in an aqueous suspension of TiO_2 by inorganic ions, J. Photochem. Photobiol. A Chem. 108 (1997) 37–44.

[12] R.A. Burns, J.C. Crittenden, D.W. Hand, V.H. Selzer, L.L. Sutter, S.R. Salman, Effect of inorganic ions in heterogeneous photocatalysis of TCE, J. Environ. Eng. 125 (1999) 77–85.

[13] M. Mehrvar, W. a. Anderson, M. Young, Photocatalytic degradation of aqueous organic solvents in the presence of hydroxyl radical scavengers, Int. J. Photoenergy. 3 (2001) 187–191.

[14] K. Wang, J. Zhang, L. Lou, S. Yang, Y. Chen, UV or visible light induced photodegradation of AO7 on TiO_2 particles: the influence of inorganic anions, J. Photochem. Photobiol. A Chem. 165 (2004) 201–207.

[15] M.H. Habibi, A. Hassanzadeh, S. Mahdavi, The effect of operational parameters on the photocatalytic degradation of three textile azo dyes in aqueous TiO_2 suspensions, J. Photochem. Photobiol. A Chem. 172 (2005) 89–96.

[16] C. Guillard, E. Puzenat, H. Lachheb, A. Houas, J.M. Herrmann, Why inorganic salts decrease the TiO_2 photocatalytic efficiency, Int. J. Photoenergy. 7 (2005) 1–9.

[17] A. Lair, C. Ferronato, J.-M.M. Chovelon, J.M. Herrmann, Naphthalene degradation in water by heterogeneous photocatalysis: an investigation of the influence of inorganic anions, J. Photochem. Photobiol. A Chem. 193 (2008) 193–203.

[18] A. Mills, R.H. Davies, D. Worsley, Water purification by semiconductor photocatalysis, Chem. Soc. Rev. 22 (1993) 417-425.

[19] M. Kerzhentsev, C. Guillard, J. Herrmann, P. Pichat, case study of the total degradation of the insecticide fenitrothion, 27 (1996) 215–220.

[20] U. Diebold, The surface science of titanium dioxide, Surf. Sci. Rep. 48 (2003) 53–229.

[21] A. Fernández-Nieves, F.J. De Las Nieves, The role of ζ potential in the colloidal stability of different TiO_2/electrolyte solution interfaces, Colloids Surfaces A Physicochem. Eng. Asp. 148 (1999) 231–243.

[22] R.A. French, A.R. Jacobson, B. Kim, S.L. Isley, R.L.E.E. Penn, L. Penn, et al., Influence of ionic strength, pH, and cation valence on aggregation kinetics of titanium dioxide nanoparticles, Environ. Sci. Technol. 43 (2009) 1354–1359.

[23] A.A. Keller, H. Wang, D. Zhou, H.S. Lenihan, G. Cherr, B.J. Cardinale, et al., Stability and aggregation of metal oxide nanoparticles in natural aqueous matrices, Environ. Sci. Technol. 44 (2010) 1962–1967.

[24] A.R. Petosa, D.P. Jaisi, I.R. Quevedo, M. Elimelech, N. Tufenkji, Aggregation and deposition of engineered nanomaterials in aquatic environments: role of physicochemical interactions., Environ. Sci. Technol. 44 (2010) 6532–49.

[25] Y.H. Shih, W.S. Liu, Y.F. Su, Aggregation of stabilized TiO_2 nanoparticle suspensions in the presence of inorganic ions, Environ. Toxicol. Chem. 31 (2012) 1693–1698.

[26] K.I. Ishibashi, A. Fujishima, T. Watanabe, K. Hashimoto, Detection of active oxidative species in TiO_2 photocatalysis using the fluorescence technique, Electrochem. Commun. 2 (2000) 207–210.

[27] G. Bartosz, Use of spectroscopic probes for detection of reactive oxygen species, Clin. Chim. Acta. 368 (2006) 53–76.

[28] N. Soh, Recent advances in fluorescent probes for the detection of reactive oxygen species, Anal. Bioanal. Chem. 386 (2006) 532–43.

[29] L.K. Adams, D.Y. Lyon, P.J.J. Alvarez, Comparative eco-toxicity of nanoscale TiO_2, SiO_2, and ZnO water suspensions., Water Res. 40 (2006) 3527–32.

[30] M. Heinlaan, A. Ivask, I. Blinova, H.-C. Dubourguier, A. Kahru, Toxicity of nanosized and bulk ZnO, CuO and TiO_2 to bacteria Vibrio fischeri and crustaceans Daphnia magna and Thamnocephalus platyurus., Chemosphere 71 (2008) 1308–16.

[31] M. Giovanni, C.Y. Tay, M.I. Setyawati, J. Xie, C.N. Ong, R. Fan, et al., Toxicity profiling of water contextual zinc oxide, silver, and titanium dioxide nanoparticles in human oral and gastrointestinal cell systems, Environ. Toxicol. (2014).

[32] G.C. Bushell, Y.D. Yan, D. Woodfield, J. Raper, R. Amal, On techniques for the measurement of the mass fractal dimension of aggregates, Adv. Colloid Interface Sci. 95 (2002) 1–50.

[33] K. Ishibashi, A. Fujishima, T. Watanabe, K. Hashimoto, Quantum yields of active oxidative species formed on TiO_2 photocatalyst, J. Photochem. Photobiol. A Chem. 134 (2000) 139–142.

[34] P. Fernández-Ibáñez, J. Blanco, S. Malato, F.J. d. Las Nieves, Application of the colloidal stability of TiO_2 particles for recovery and reuse in solar photocatalysis, Water Res. 37 (2003) 3180–3188.

[35] M.L. Satuf, R.J. Brandi, A.E. Cassano, O.M. Alfano, Experimental method to evaluate the optical properties of aqueous titanium dioxide suspensions, Ind. Eng. Chem. Res. 44 (2005) 6643–6649.

[36] B. Toepfer, A. Gora, G. Li Puma, Photocatalytic oxidation of multicomponent solutions of herbicides: reaction kinetics analysis with explicit photon absorption effects, Appl. Catal. B Environ. 68 (2006) 171–180.

[37] M. Salaices, B. Serrano, H.I. De Lasa, Experimental evaluation of photon absorption in an aqueous TiO_2 slurry reactor, 90 (2002) 219–229.

[38] J.M. Herrmann, P. Pichat, Heterogeneous photocatalysis. Oxidation of halide ions by oxygen in ultraviolet irradiated aqueous suspension of titanium dioxide, J. Chem. Soc. Faraday Trans. 1. 76 (1980) 1138.

[39] M. Moskovits, Surface-enhanced Raman spectroscopy: a brief retrospective, J. Raman Spectrosc. 36 (2005) 485–496.

[40] A. Rincon, Effect of pH, inorganic ions, organic matter and H_2O_2 on E. coli K12 photocatalytic inactivation by TiO_2. Implications in solar water disinfection, Appl. Catal. B Environ. 51 (2004) 283–302.

5.6 SUPPORTING INFORMATION

SI5.1 Radiation intensity as a function of emission wavelength at the upper liquid surface

Emission spectrum of UV lamps, as provided by the manufacturer, was used to determine the radiation intensity as a function of the emission wavelength at the liquid upper surface of the samples. Results are reported in figure SI5.1. A normal distribution with mean 365 nm and standard deviation 10 nm was assumed for Philips TL-D 15W BLB SLV spectrum. Radiometric readings were corrected by taking into account the spectral response of the sensor, as suggested in [SI1].

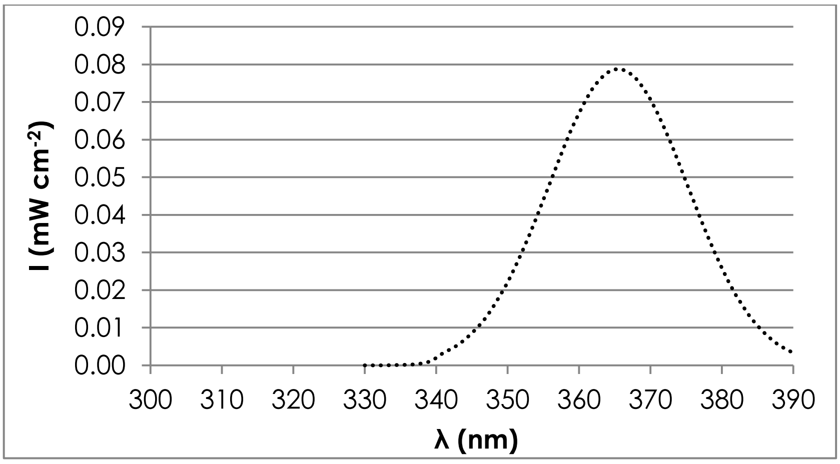

Figure SI5.1 Radiation intensity vs. emission wavelength at the liquid upper surface of samples.

SI5.2 Characterization of size distribution of TiO_2 aggregates as a function of operating conditions

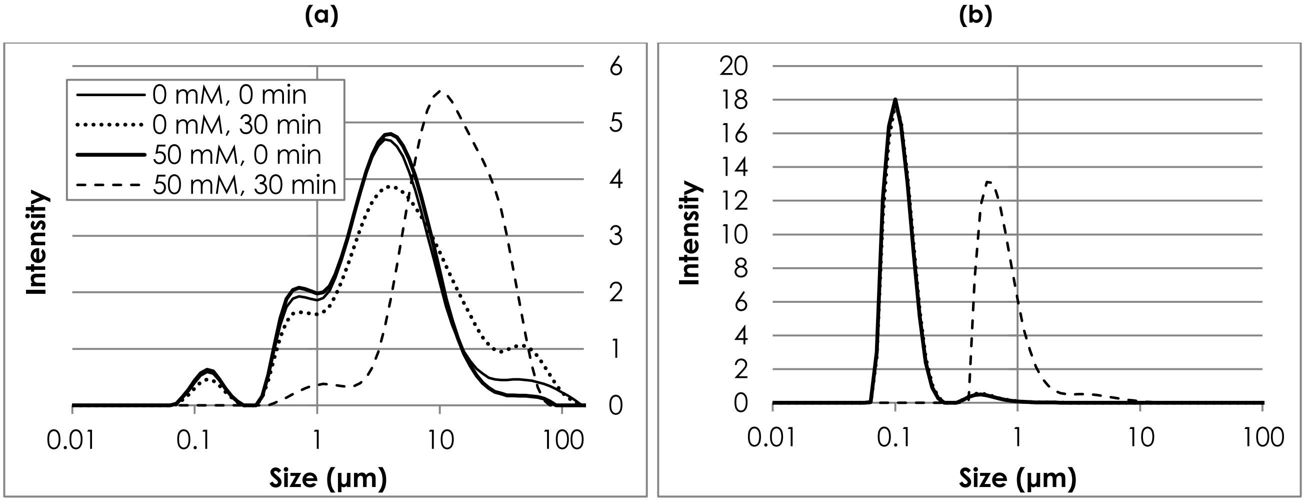

Figure SI5.2 TiO_2 aggregate size distribution as a function of KI concentration (0, 50 mM) at various times (0, 30 min) for non-sonicated TiO_2 dispersions. Experimental results are expressed both as particle number weighted (a) and volume weighted (b).

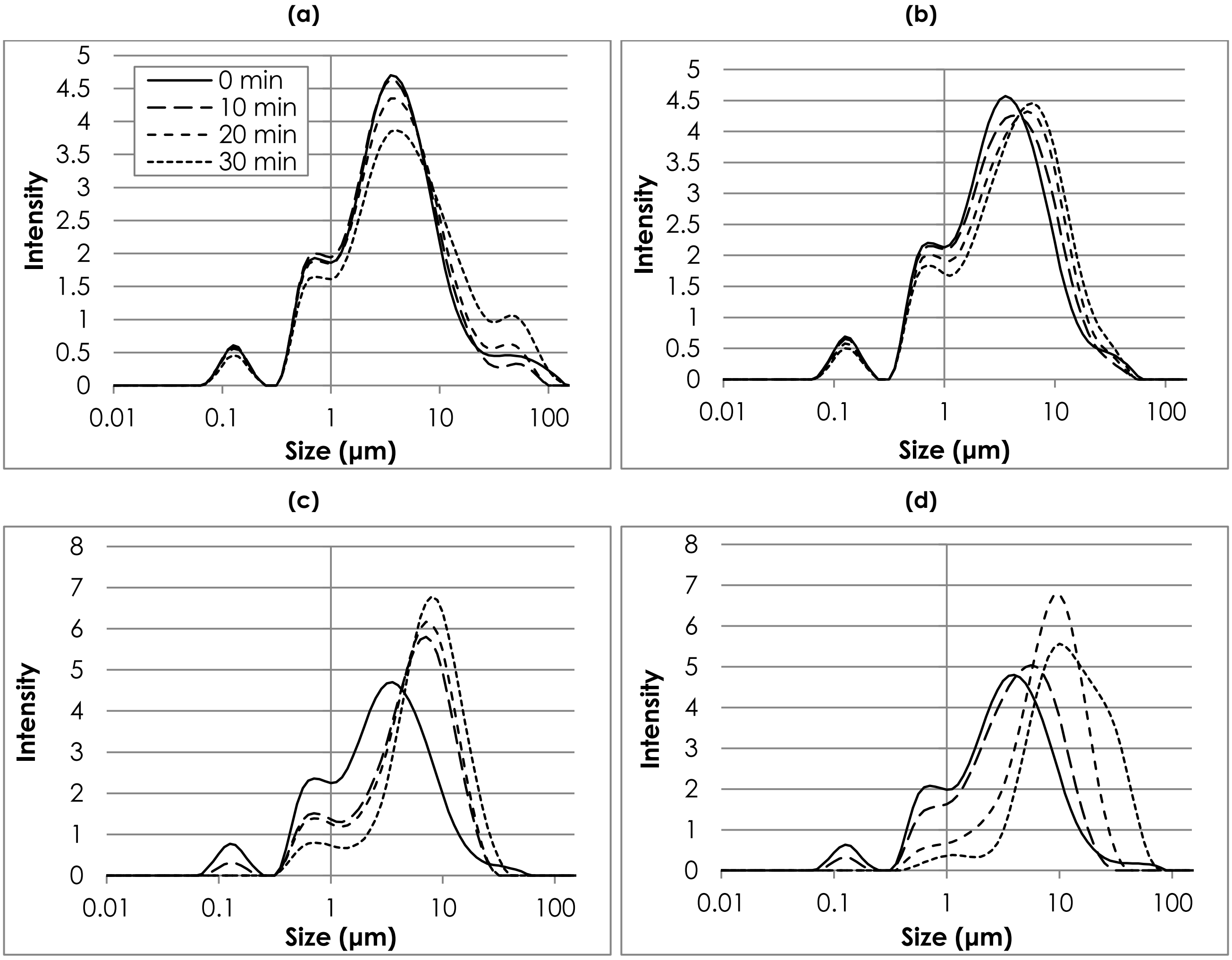

Figure SI5.3 TiO_2 aggregate size distribution vs. time at various KI concentration: (a) 0, (b) 0.5, (c) 5, (d) 50 mM for non-sonicated TiO_2 dispersions. Experimental results are expressed both as particle number weighted.

SI5.3 Time series for iodide oxidation as a function of iodide concentration

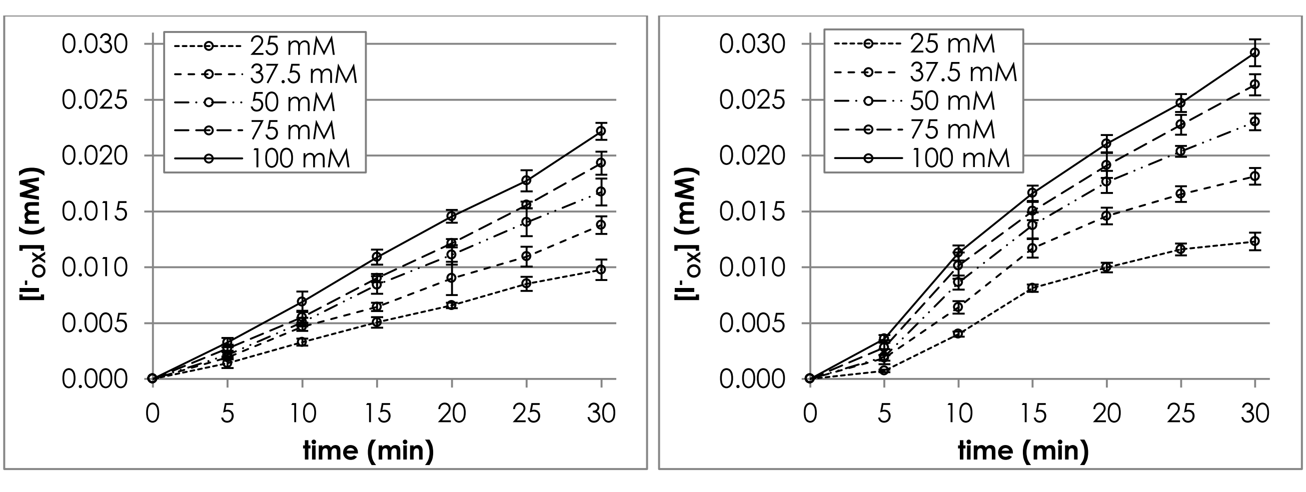

Figure SI5.4 Oxidized iodide concentration (mean±st.dev.) vs. time as a function of iodide concentration and TiO_2 dispersion method, i.e. sonicated (a) and non-sonicated (b).

SI5.4 Time series for iodide oxidation as a function of inorganic anion concentration

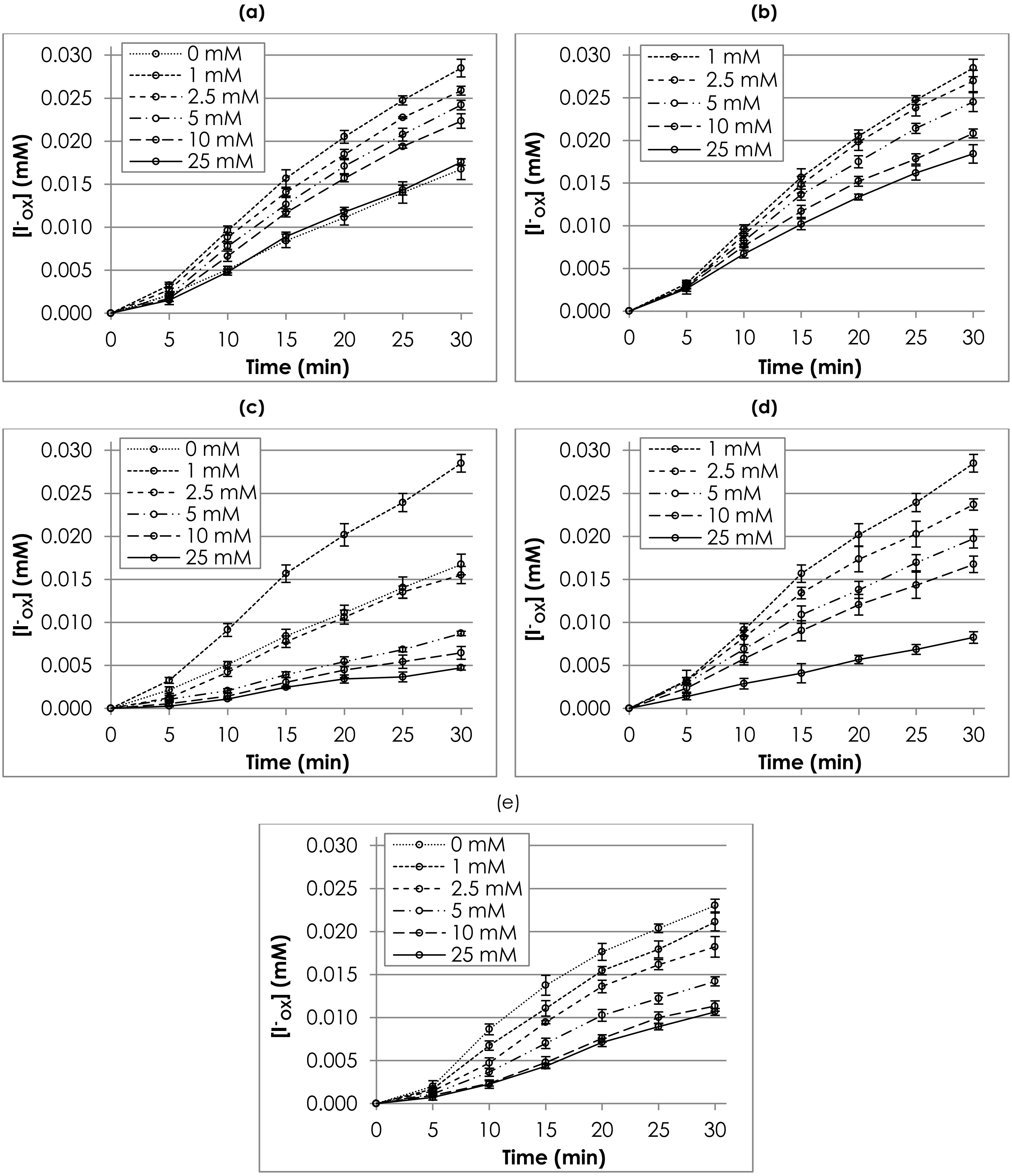

Figure SI5.5 Oxidized iodide concentration (mean±st.dev.) vs. time as a function of inorganic anion concentration, i.e. carbonate (a,b) and phosphate (c,d,e), as well as TiO_2 dispersion methods, i.e. sonicated with inorganic ions (a,c), sonicated without inorganic ions (b,d) and non-sonicated (e).

SI5.5 Langmuir-Hinshelwood linearization procedure for K_A and K_R constants estimation

By neglecting the presence of inorganic anions other than iodide, equation e5.3 in the manuscript can be simplified and expressed showing the linear relationship between the inverse of initial reaction rate and the inverse of initial iodide concentration, as follows [SI2]:

$$\frac{1}{r_0} = \frac{1}{K_{A,I^-}\, K_R}\,\frac{1}{[I^-]_0} + \frac{1}{K_R} = m\,\frac{1}{[I^-]_0} + q \qquad \text{(eSI5.1)}$$

with

$$K_R = \frac{1}{q} \qquad\qquad K_A = \frac{q}{m}$$

The rate r_0 is obtained from experimental data by calculating the oxidized iodide concentration for each $[I^-]_0$ over time. K_A and K_R values were calculated by fitting experimental data shown in figure 5.2 with a linear regression, estimating m and q values by least square method, as in figure SI5.6.

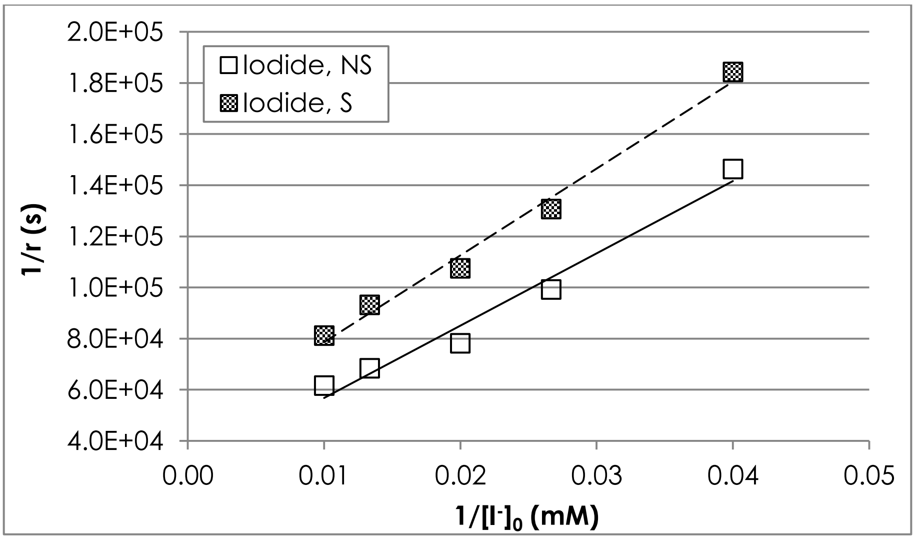

Figure SI5.6 Experimental data linear regressions ($1/r$ vs. $1/[I^-]_0$) for iodide adsorption via Langmuir-Hinshelwood mechanism as a function of TiO_2 dispersion method (S: sonicated, NS: non-sonicated).

Equation e5.3 in the manuscript can be transformed so as to highlight the linear relationship between the inverse of the initial reaction rate and the initial inorganic anion concentration, as it follows [SI3]:

$$\frac{1}{r_0} = \frac{K_{A,Anion}}{K_R K_{A,I^-}\,[I^-]_0}\,[Anion] + \frac{1 + K_{A,I^-}\,[I^-]_0}{K_R K_{A,I^-}\,[I^-]_0} = m\,[Anion] + q \qquad \text{(eSI5.2)}$$

with

$$K_R = \frac{1+K_{A,I^-}\,[I^-]_0}{q\cdot K_{A,I^-}\,[I^-]_0} \qquad\qquad K_A = m\cdot K_R K_{A,I^-}\,[I^-]_0$$

In calculation procedure experimental values at 0 and 12.5 mM were neglected because of the observed modifications in TiO_2 suspension characteristics, as discussed in paragraph 5.3.1. Results for linearization of experimental data by the proposed procedure are reported in figure SI5.7.

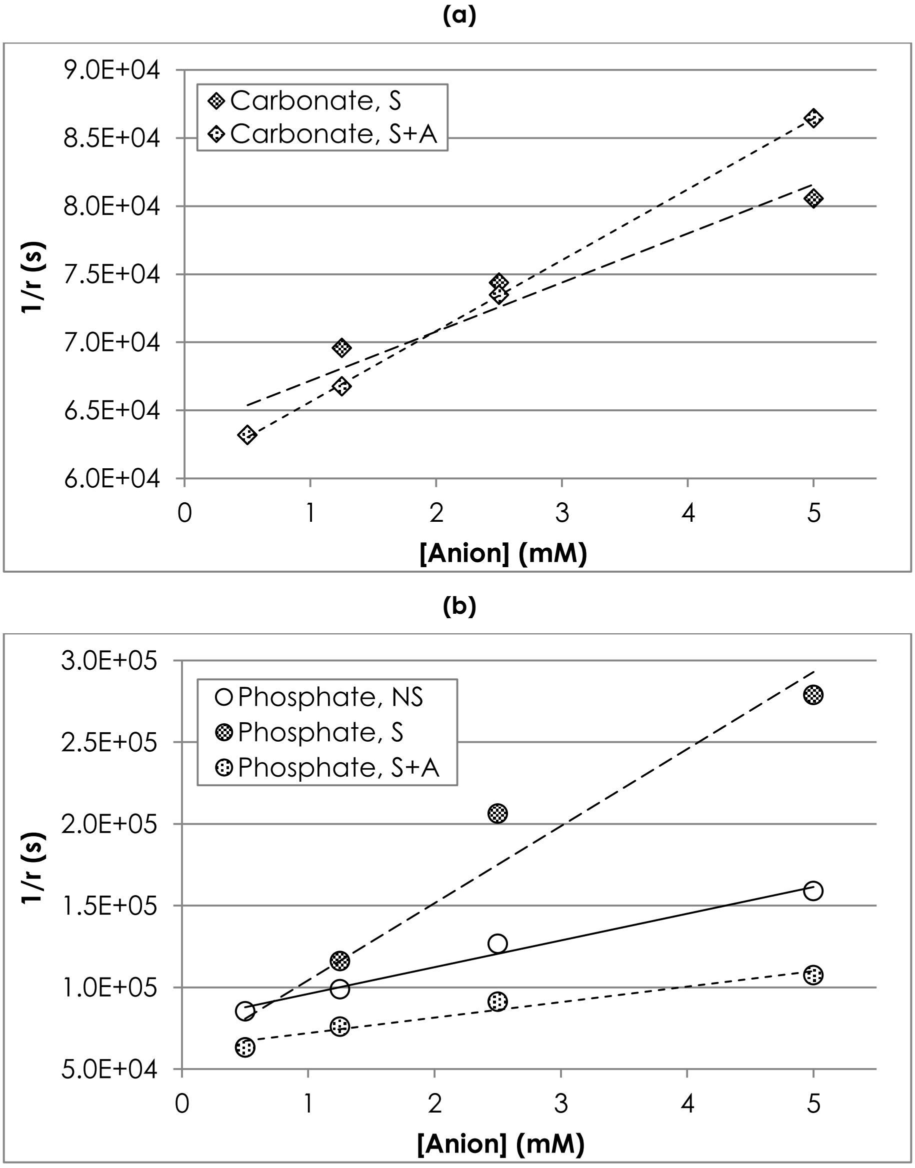

Figure SI5.7 Experimental data linear regressions (1/r vs. [Anion]) for the competitive adsorption of inorganic anions with iodide via Langmuir-Hinshelwood mechanism as a function of TiO_2 dispersion method (S: sonicated, NS: non-sonicated) for various anionic species, i.e. carbonate (a) and phosphate (b).

SI5.6 Time series for terephthalic acid oxidation as a function of inorganic anion concentration

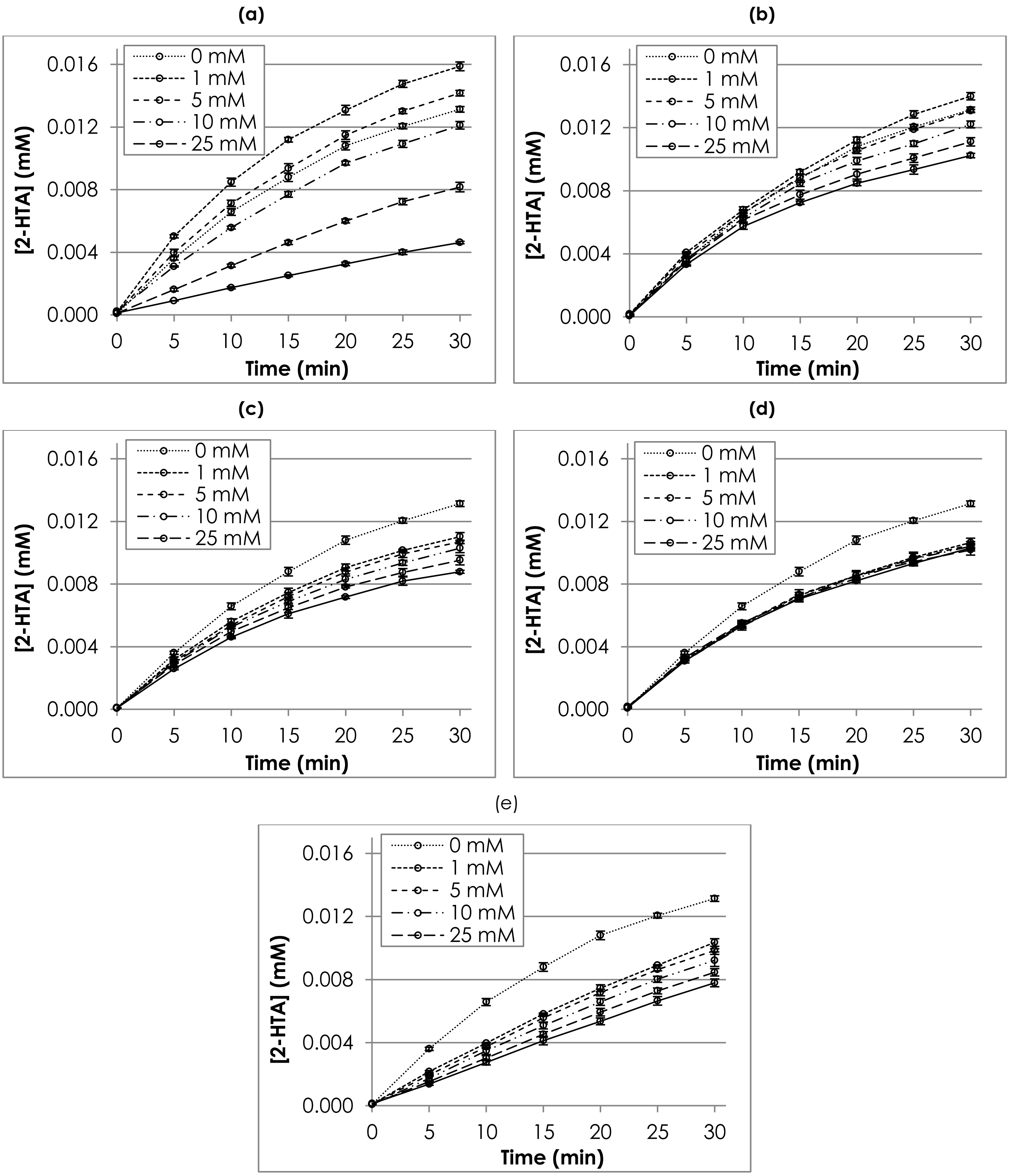
(a)
(b)
(c)
(d)
(e)

Figure SI5.8 2-hydroxyterephthalic acid concentration (mean±st.dev.) vs. time as a function of inorganic anion concentration for various anionic species, i.e. carbonate (a), chloride (b), nitrate (c), sulfate (d) and phosphate (e). TiO_2 suspensions were dispersed by S+A method.

SI5.7 Normalized hydroxyl radical generation as a function of inorganic anion concentration

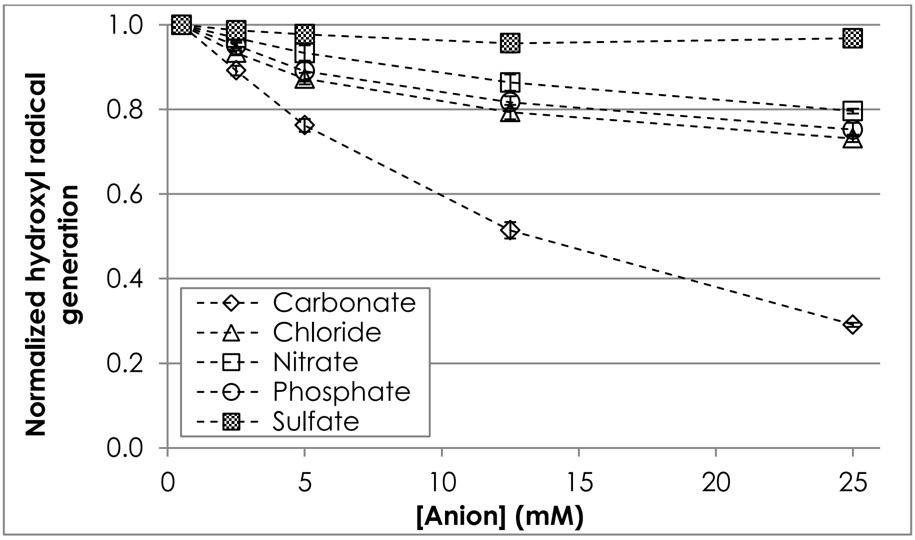

Figure SI5.9 Normalized hydroxyl radical generation vs. inorganic anion concentration after 30 minute irradiation time as a function of anionic species in solution. TiO_2 suspensions were dispersed by S+A method.

SI5.8 Rate constants for reaction between hydroxyl radicals and inorganic anions

Table SI5.1 Rate constants for hydroxyl radicals and inorganic anions.

Anionic species	Value ($M^{-1}\,s^{-1}$)	Reference
HCO_3^-	$8.5\cdot10^6$	[4]
CO_3^{2-}	$3.9\cdot10^8$	[4]
Cl^-	$4.3\cdot10^9$	[4]
NO_3^-	$1.4\cdot10^8$	[5]
$H_2PO_4^-$	$2\cdot10^4$	[6]
HPO_4^{2-}	$6\cdot10^5$	[6]
SO_4^{2-}	$1.0\cdot10^{10}$	[7]

REFERENCES

[SI1] I. Grcic, G. Li Puma, Photocatalytic degradation of water contaminants in multiple photoreactors and evaluation of reaction kinetic constants independent of photon absorption, irradiance, reactor geometry, and hydrodynamics, Environ. Sci. Technol. 47 (2013) 13702-13711.

[SI2] J.M. Herrmann, P. Pichat, Oxidation of halide ions by oxygen in ultraviolet irradiated aqueous suspension of titanium dioxide. J.C.S. Faraday I 76 (1980) 1138-1146.

[SI3] H.Y. Chen, O. Zahraa, M. Bouchy, Inhibition of the adsorption and photocatalytic degradation of an organic contaminant in an aqueous suspension of TiO_2 by inorganic ions. J. Photochem. Photobiol. A 108 (1997) 37-44.

[SI4] G.V. Buxton, C.L. Greenstock, W.P. Helman, A. Ross, Critical review of rate constants for reactions of hydrated electrons, hydrogen atoms and hydroxyl radicals ($^{\bullet}OH/^{\bullet}O^{-}$) in aqueous solution. J. Phys. Chem. Ref. Data 17 (1988) 513–886.

[SI5] Y. Katsumura , P.Y. Jiang, R. Nagaishi, T. Oishi, K. Ishigure, Y. Yoshida, Pulse radiolysis study of aqueous nitric acid solutions: formation mechanism, yield, and reactivity of NO_3 radical. J. Phys. Chem. 95 (1991) 4435-4439.

[SI6] J. Kochany, E. Lipczynska-Kochany, Application of the EPR spin-trapping technique for the investigation of the reactions of carbonate, bicarbonate, and phosphate anions with hydroxyl radicals generated by the photolysis of H_2O_2. Chemosphere 25 (1992) 1769-1782.

[SI7] J. Holcman, T. Logager, K. Sehested, V. Klaning, Reactions of peroxodisulfate and SO_4^- with selected radicals in aqueous solution, in Laboratory studies on atmospheric chemistry, York, September 23–25, 1991.

CHAPTER 6

INFLUENCE OF INORGANIC ANIONS ON THE PHOTOCATALYTIC REACTIVITY OF SELF-ORDERED NANOTUBULAR TiO_2

ABSTRACT

The influence of several inorganic anions, namely carbonate, chloride, nitrate, phosphate and sulfate, on the photocatalytic reactivity of self-ordered nanotubular titanium dioxide (TiO_2) was assessed by monitoring the production of reactive species. Self-ordered nanotubular TiO_2 was grown by anodic oxidation directly on wire mesh titanium substrate, and then characterised by scanning electron microscopy and X-Ray diffractometry. The photocatalyst was photoactivated by means of UV-A radiation in the presence of inorganic anions dosed as sodium salts at several concentrations, while photogenerated holes were measured by observing their selective reaction with a probe compounds, i.e. iodide. Moreover, the occurrence of self-ordered nanotubular TiO_2 fouling was evaluated in terms of reactivity decay, in order to define a photocatalyst surface regeneration protocol. A detrimental effect on iodide oxidation was observed only for carbonate and phosphate and it was effectively modelled by Langmuir-Hinshelwood mechanism, being the concentration of inorganic anions at TiO_2 surface limited by the external mass transfer in the stagnant film layer. The multiple-use of photocatalyst determined an initial irreversible drop in reactivity and two reversible phenomena, namely the unpredictable fluctuation of nanotubular TiO_2 reactivity in consecutive tests and a decrease in reactivity when TiO_2 surface was exposed to inorganic anions. A regeneration protocol was identified, consisting in electrophotocatalytic cleaning of TiO_2 photocatalyst after washing in sodium hydroxide solution.

The research work described in the present chapter was carried out with the valuable support of
Francesca Zanchi, MSc student, Politecnico di Milano, Italy
Andrea Piazzoli, PhD student, Politecnico di Milano, Italy

The present chapter, once integrated with experimental tests on the influence of inorganic anions on the generation of hydroxyl radicals and after an adaptation in terms of formatting style, will be submitted for publication to the journal 'Applied Catalysis B: Environmental'.

6.1 INTRODUCTION

In recent years titanium dioxide (TiO_2) has been widely investigated as a photocatalyst for the advanced oxidation of refractory organic pollutants and for the advanced disinfection of pathogens due to its promising properties [1–3]. TiO_2 has numerous benefits, such as low cost, durability, photostability and non-toxicity, which have been offset so far due to: (ii) the heterogeneous phase of the photocatalyst, involving many drawbacks, and (ii) the low process yield with respect to other oxidation processes, such as ozone or H_2O_2/UV [4]. As a consequence, TiO_2 photocatalysis is far from an effective application for water and wastewater treatment.

The potential of TiO_2 as photocatalyst has been mainly investigated using TiO_2 as a suspension of nanoparticles in slurry phase. This mode of use necessarily requires a complex and expensive downstream separation stage in case of application to water and wastewater treatment [5], potentially consisting in a filtration [6] or coagulation [7] process. In order to avoid the need for a separation stage, previous research has been addressed to the development of TiO_2 immobilization techniques, leading to the additional advantage of a continuous use of the photocatalyst without its replacement [8]. Among the most investigated methods for TiO_2 immobilization there are sol-gel [9,10], chemical vapour deposition (CVD) [11,12] and thermal treatment [13,14]. Beyond these, nanotubular TiO_2, grown by anodic oxidation on a titanium (Ti) substrate, is lately emerging as an innovative material and attracting considerable interest [15,16].

Nanotubular TiO_2 is constituted by self-ordered nanotube arrays, aligned perpendicularly to the Ti substrate and strongly bounded to it. Besides the high specific surface, nanotubular TiO_2 may be biased due to the good backside electrical contact provided by the metallic substrate [17]. In detail, an anodic polarization can be applied enhancing the removal of a part of the promoted electrons from the conduction band, being them forced to move through the electrical circuit. Thus, a reduction in the electron-hole pair recombination can be achieved. The positive effect of polarization on process yield has been reported in several works, *inter alia* [18,19], including our previous paper [20]. The application of nanotubular TiO_2 for water and wastewater decontamination has been discussed both in case of photocatalysis [21,22] and electrophotocatalysis [23,24], the latter involving the use of an electrical polarization. Anyway, research has been mostly performed at laboratory scale, aimed at assessing the degradability of model pollutants, usually spiked in synthetic media prepared in deionized water. However, synthetic media are generally scarcely representative with respect to real water and wastewater in predicting photocatalytic degradation efficiency. In fact, the presence in solution of other compounds than target pollutant can result in a strong detrimental effect on TiO_2 reactivity, lowering the process yield, as already discussed for TiO_2 nanoparticles in chapter 5.

Inorganic anions are definitely among the most diffuse affecting compounds and their relevance for TiO_2 photocatalytic reactivity has been reported in a number of published works, *inter alia* [25–27]. In fact, inorganic anions significantly influence process efficiency by (i) directly interfering with chemical-physical reactions involved in TiO_2 photoactivation, and (ii) by changing the superficial and morphological characteristics of the photocatalyst. As for the latter, in case of TiO_2 nanoparticle suspensions, reduced reactivity is related to the modifications induced in nanoparticle aggregation state [2]. In case of immobilized TiO_2, which undergoes to a continuous use, reduced reactivity is related to the fouling of TiO_2 surface. In fact, several inorganic anions, as phosphate, were observed to form persistent bonds with TiO_2 surface, resulting in reduced reactivity [28].

To the best of the authors' knowledge, the influence of inorganic anions has never been thoroughly studied with reference to nanotubular TiO_2 reactivity. Detailed information about reactive species generation in the presence of inorganic anions is lacking, as well as about the regeneration of fouled nanotubular TiO_2. It should be mentioned that the development of a regeneration protocol is crucial for the efficient application of nanotubular TiO_2 to real water and wastewater. As for reactive species generation, the assessment of inorganic anion influence has been usually based on the study of the degradation of model pollutants, such as dyes or organic solvents, reacting simultaneously with different reactive species according to complex and mostly unknown reaction pathways. Actually, the introduction of experimental protocols for the selective measurement of reactive species by means of probe compounds allow a significant step forward, permitting to evaluate the influence of inorganic anions on individual reactive species production according to a known reaction pathway [29,30].

In the present research the influence of inorganic anions on the photocatalytic reactivity of self-ordered TiO_2 nanotubes was assessed by monitoring the production of reactive species. In particular, photogenerated holes (h^+) were measured by a selective probe compound, namely iodide (dosed as potassium iodide, KI), which was oxidized to iodine (I_2). Nanotubular TiO_2 was grown by anodic oxidation directly on wire mesh Ti substrate as well as characterised by Environmental Scanning Electron Microscope (ESEM) and X-Ray Diffractometer (XRD) analyses. It was photoactivated by means of UV-A radiation in the presence of inorganic anions, dosed as sodium salts at several concentrations, while iodine concentration was monitored over time by a spectrometric technique. Moreover, nanotubular TiO_2 fouling by inorganic anions was monitored as reactivity decay for defining a regeneration protocol.

6.2 MATERIAL AND METHODS

6.2.1 Nanotubular TiO_2 photocatalyst

Nanotubular TiO_2 was grown by anodic oxidation of a commercial titanium (grade 1) wire mesh (TTM Rossi, Italy), whose optical microscope image is shown in figure 6.1a. The anodization procedure, which was carried out in fluoride containing solution, is described in previously published works [20,31]. Nanotubular TiO_2 morphology and crystalline structure were characterized respectively by ESEM (Zeiss EVO 50 EP, Germany) and XRD (Philips PW-1830, Netherlands), before and after the annealing treatment. Flat samples (5x5 cm) were prepared, whose specific surface was about 20 cm^2, calculated by the procedure reported in Supporting Information (SI6.1).

6.2.2 Reagents

KI, I_2, NaOH, $NaHCO_3$, NaCl, $NaNO_3$, NaH_2PO_4, Na_2HPO_4 and Na_2SO_4 were purchased from Sigma-Aldrich (USA). Mono-salt stock solutions of inorganic anions (0.1 M) were prepared in deionized water (DI) for carbonate, chloride, nitrate and sulfate. Phosphate stock solution (0.1 M) at pH 7.9 was prepared by dosing 0.1495 g of NaH_2PO_4 and 1.55 g of Na_2HPO_4 in 100 mL of deionized water. When needed, solution pH was adjusted by NaOH (0.1 M). Starch solution was prepared by adding 0.5 g of starch (Sigma-Aldrich) in 100 mL of boiling deionized water and mixing until complete dissolution. After 12 h settling, the supernatant was collected and 2.5 g of salicylic acid (Merck, USA) were dosed as preservative.

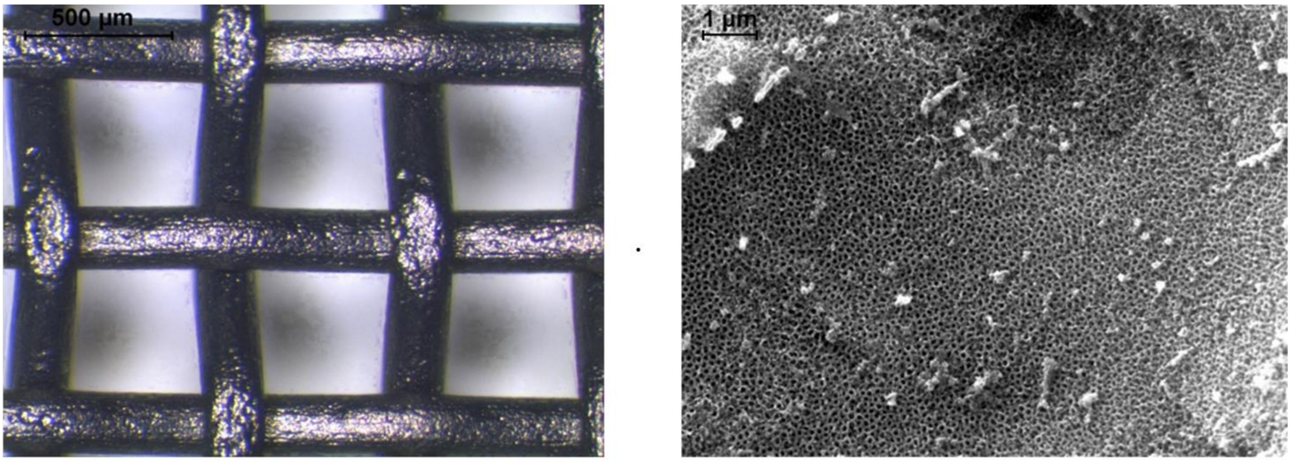

Figure 6.1 Surface structure of TiO_2 photocatalyst samples: (a) optical microscope image of Ti support, (b) ESEM image of nanotubular TiO_2.

6.2.3 Nanotubular TiO_2 reactivity measurements

Experiments were performed in a thermostated (22±1°C) UV box equipped with a 15 W fluorescent UV lamp (Helios Italquartz, Italy), whose emission spectrum had a peak at 365 nm and a distribution comparable to a normal curve with 15 nm standard deviation. A reaction beaker (H=1.5 cm, Ø=7 cm) was used, containing 30 mL solution which determined 1 cm thickness liquid layer when the stirring bar (4.4 x 14 mm) was inset; it was continuously mixed on a magnetic stirrer (400 RPM) and irradiated by the lamp located horizontally over the beaker. Nanotubular TiO_2 sample was immersed and immobilized by a PTFE support at about 4 mm below upper liquid surface. The effective mixing of the described configuration was preliminary verified in tracer tests using methylene blue. Radiation intensity, monitored by a radiometer (HD9021, Delta Ohm, Italy), was on average 1.6±0.1 mW cm^{-2} at the upper liquid surface, while the values as a function of emission wavelength are shown in Supporting Information (SI6.2).

Nanotubular TiO_2 reactivity was assessed by photogenerated holes measurements in three types of tests. First, the influence of solution pH on the production of photogenerated holes was assessed in 60 minute irradiation tests, using 50 mM iodide solution at various pH (6.3, 7.9, 8.8). Then, the production of photogenerated holes was measured as a function of iodide concentration (6.25, 12.5, 25, 37.5 and 50 mM) in 15 minute tests at pH 7.9. Finally, the influence of inorganic anions (carbonate, chloride, nitrate, phosphate, sulfate) on the production of photogenerated holes was evaluated in 60 minute irradiation tests by dosing 50 mM iodide and various concentrations of inorganic anions (6.25, 12.5, 18.75, 25 and 50 mM) at pH 7.9. Each test was repeated at least thrice.

Nanotubular TiO_2 was regenerated after every reactivity test by means of 20 minute batch washing in 0.1 M NaOH solution followed by 40 minute electrophotocatalytic cleaning with non-recirculated flowing of 3 KCl washing solution at a flow rate of 50 mL/min, as described in paragraph 6.2.3.1.

6.2.3.1 Regeneration protocol

Several regeneration methods for nanotubular TiO_2 were tested:

(a) washing in deionized water (DI): sample was immersed for 1 h in a 100 mL beaker (H=2 cm, Ø=9 cm) filled with deionized water and continuously mixed on a magnetic stirrer (600 RPM);

(b) photocatalytic cleaning (PC): sample was immersed similarly to (a) and irradiated for 1 h with the equipment used for reactivity measurement (2.0±0.1 mW cm^{-2} on liquid surface);

(c) electrophotocatalytic cleaning (EPC): sample was immersed in the reactor described in Supporting Information (SI6.3) and used as a photo-anode, irradiated by 30 W low pressure Hg vapour UV lamp (Helios Italquartz, Italy), emitting at 254±10 nm (mean±st.dev.) and determining 0.8±0.1 mW cm^{-2} radiation intensity at photocatalyst surface, as well as biased at 1.5 V vs. Ag/AgCl with a potentiostat/galvanostat (515, Material Mates, Italy). A 3 mM KCl cleaning solution was continuously circulated throughout the reactor by a peristaltic pump having 50 mL/min flow rate, in order to providing a base conductivity (about 450 µS/cm). Three EPC configurations were studied: (1) 0.5 L cleaning solution was recirculated for 40 minutes in a closed loop, (2) 1 L cleaning solution was flushed for 20 minutes, (3) 2 L cleaning solution was flushed for 40 minutes;

(d) washing in NaOH + electrophotocatalytic cleaning (NaOH+EPC): sample was first immersed for 20 min in a 100 mL beaker (H=2 cm, Ø=9 cm) filled with 0.1 M NaOH solution and continuously mixed on a magnetic stirrer (600 RPM), then it was subjected to electrophotocatalytic cleaning, as described in (c), carried out by configuration 3.

Nanotubular TiO_2 regeneration methods were compared by assessing the variability, in terms of standard error, of the production of photogenerated holes over 60 minute irradiation time in at least three reactivity tests repeated under same operating conditions and following each one the application of a given regeneration protocol. Reactivity measurements were conducted in absence and in presence of phosphate in solution (0, 50 mM).

6.2.3.2 Measurement protocol

A small volume (2 mL) of solution was sampled every 15 minutes and, after starch addition (1:1 volume ratio), absorbance at 585 nm was measured in a glass cuvette (10 mm optical path) vs. deionized water by spectrophotometer (Unicam UV-Vis 2, USA). Subsequently, absorbance was related to iodine concentration by a standard curve. The concentration of photogenerated holes in solution was stoichiometrically estimated as twice the produced iodine concentration, according to the reaction:

$$2I^- + 2h^+ \rightarrow I_2 \qquad \text{(e6.1)}$$

Standard curve was determined using a 0.025 M iodine stock solution that was diluted to obtain solutions at concentration between 0.0125 and 0.125 mM (concentration step: 0.0125 mM). After starch addiction (1:1 volume ratio), solutions were transferred in a glass cuvette (10 mm optical path) for absorbance measurements at 585 nm vs. deionized water in spectrophotometer.

6.3 RESULTS AND DISCUSSION

6.3.1 Nanotubular TiO_2 characterization

The film morphology, as shown in figure 6.1b, was compact and uniform, composed of nanotubes having a thickness of about 500-600 nm and an average diameter of 100-150 nm. The crystalline phase distribution was estimated by XRD spectra, reported in figure 6.2, according to the method described by Jenkins and Snyder [32]: nanotubular TiO_2 consisted of 70-80% anatase and 20-30% rutile. Nanotubular TiO_2 specific surface, which is a case-specific feature related to the morphological structure of TiO_2 nanotubes, should be experimentally evaluated by means of appropriate analytical techniques, such as BET. No valuable indications are provided in literature.

6.3.2 Nanotubular TiO_2 reactivity

The influence of inorganic anions on nanotubular TiO_2 reactivity was assessed by using the photocatalyst in presence of various concentrations of anionic species. However, unlike the assessment of the influence of inorganic anions on TiO_2 nanoparticle photocatalysis (chapter 5), immobilised TiO_2 is reused multiple times, so that probe compounds and inorganic anions may bond to TiO_2 surface and affect the photocatalyst reactivity in consecutive experiments. Therefore, the identification of a regeneration protocol is a basic requirement for the reliability and the accuracy of reactivity measurements. Besides, it is also fundamental for process engineering, since the presence of anionic species could determine a progressive decline of performance over time.

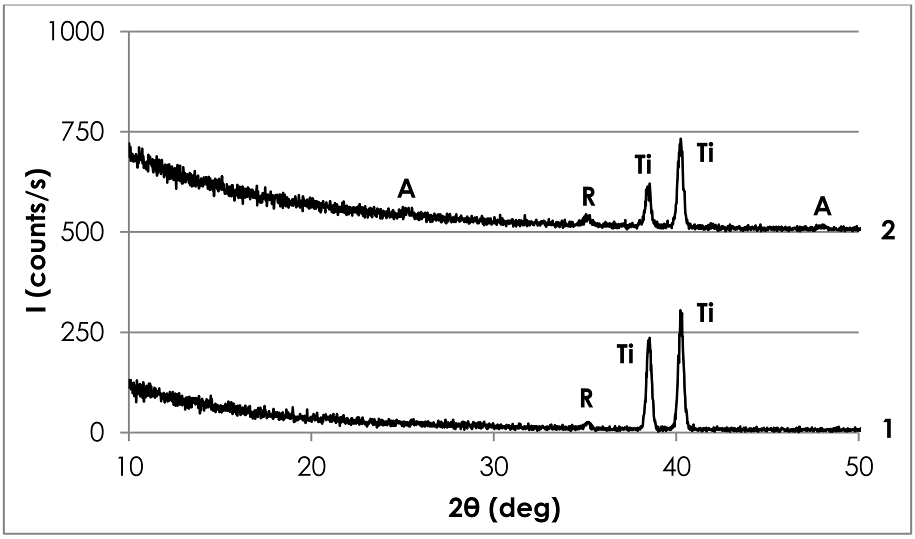

Figure 6.2 XRD spectra of oxidized TiO_2 before (1) and after (2) annealing treatment. Crystalline peaks are marked: anatase (A), rutile (R), titanium (Ti).

First, a progressive and irreversible decline in reactivity was observed in newly-synthesised nanotubular TiO_2 samples, leading to a stable reduction in photogenerated holes of about 30-40% over a few hours of photocatalyst use. This loss in photocatalyst activity can probably be ascribed to the fouling of the photocatalyst surface by some compounds in solution, such as inorganic anions, gradually accumulating on active sites and not subsequently released. This initial loss in reactivity has not be restored by any regeneration method that has been tested.

After reactivity stabilization, the results obtained in photogenerated hole measurements in the absence of photocatalyst regeneration highlighted a scarce repeatability under same operating conditions. Moreover, a memory effect was observed in sequential reactivity tests when photocatalyst regeneration was not carried out in between (data not shown). This behaviour was observed even if TiO_2 surface was not exposed to inorganic anions, suggesting a detrimental effect of KI and I_2, which foul the photocatalyst surface. The memory effect did not necessarily result in a decrease in TiO_2 reactivity, being the photocatalytic behaviour in consequential tests essentially unpredictable. In addition, a significant decrease in reactivity was observed in measurements performed on TiO_2 samples previously immersed in phosphate-containing solutions, although the extent of detrimental effect changed from time to time. Phosphate was therefore selected as an indicator in regeneration tests, given its ability to strongly and persistently bound on TiO_2 surface [2].

6.3.2.1 Assessment of the regeneration protocol for nanotubular TiO_2

The efficiency of some regeneration protocols was evaluated by comparing variability in the production of photogenerated holes, adopting various regeneration methods preliminarily to every reactivity tests. In figure 6.3 the variability is shown as a function of phosphate concentration (0, 50 mM). A maximum value of 5% was defined as a reference threshold for standard error so as to have accurate and reliable data on reactivity.

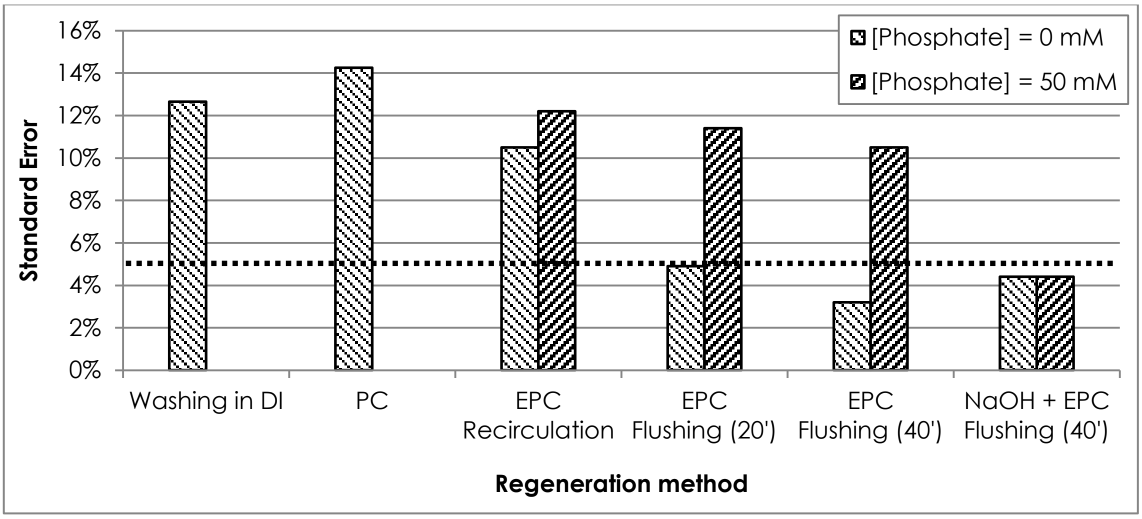

Figure 6.3 Variability, as standard error of at least three measures, in the production of photogenerated holes over 60 minute irradiation time using various regeneration methods preliminarily to the reactivity tests as a function of phosphate concentration in solution (0, 50 mM).

Washing in deionized water and photocatalytic cleaning were ineffective as regeneration methods, even in the absence of phosphate, leading to standard error over 10%. In the absence of phosphate experimental data variability was instead significantly reduced in case of electrophotocatalytic cleaning, being the beneficial effect improved in case of non-recirculated configuration and for larger volumes of washing solution. As a consequence, the regeneration protocol based on TiO_2 sample electrophotocatalytic cleaning without recirculation of washing solution was identified as the best protocol, when KI and I_2 are the only species in solution. However, such regeneration method was insufficient to get desired standard error in presence of phosphate in solution during reactivity tests. In presence of phosphate, standard error lower than 5% was achieved only by performing a preliminary washing of TiO_2 sample in 0.1 M NaOH solution, as suggested in a previous work [25]. In figure 6.3 the standard error bars are not shown for 50 mM phosphate in case of “washing in DI” and PC regeneration protocols. This absence is due to the fact that a preliminary assessment of the regeneration protocol was conducted in the absence of phosphate, and then the better options were validated in presence of phosphate.

Reactivity reduction is probably related to TiO_2 complex surface chemistry. Even if no detailed and reliable mechanistic explanations can be proposed at this time, the occurrence of two different mechanisms can be argued:

(i) A change in the surface state of nanotubular TiO_2 occurs during photocatalysis, persisting after the process and determining a sound alteration in photocatalytic properties of the photocatalyst. This alteration affects the performance of the photocatalyst in its following use. This hypothetical change in TiO_2 surface chemistry does not depend necessarily on the presence of certain compounds in solution, and it seems to be resettable by coupling the action of irradiation at 254 nm and anodic polarization.

(ii) The fouling of TiO_2 surface determined by some specific anions, such as phosphate, whose removal requires the use of regeneration solutions, such as NaOH, in order to promote the detachment of these inorganic anions from TiO_2 surface.

Therefore, in order to verify this hypothesis, further investigations should be devoted to the topic hereafter, possibly taking advantage of specific techniques for TiO_2 surface analysis.

6.3.2.2 Photogenerated holes in absence of anionic species

In the following experimental results on the influence of inorganic anions on photogenerated holes production are presented, being expressed in terms of oxidized iodide concentration. In fact, only a quote of total photogenerated holes could be monitored, namely that involved in the oxidation reaction of iodide, as already discussed in chapter 4. However, preliminarily the influence of two fundamental process parameters has been assessed, i.e. solution pH and iodide concentration.

Solution pH has been highlighted in literature as a fundamental parameter in defining TiO_2 reactivity. In fact, solution pH determines the superficial charge of TiO_2 photocatalyst, affecting the electrostatic attraction of charged compounds and, thus, their adsorption on TiO_2 surface [33]. Moreover, it influences the production of hydroxyl radicals, since a higher concentration of hydroxyl ions results in a higher hydroxyl radical production [28]. Concerning the superficial charge, a fundamental parameter is the point zero change, which is the pH value corresponding to the neutral charge, usually around pH 6 for TiO_2 nanoparticle, although an accurate estimation for nanotubular TiO_2 has not been provided yet. In the present work TiO_2 reactivity was assessed from an almost neutral (pH 6.3) to a strongly negative (pH 8.8) surface charge condition. Although an anionic species, i.e. iodide, was used as probe compound for photogenerated holes, no significant influence was observed on reactivity at three tested values of pH (6.3, 7.9, 8.8), as shown in figure 6.4. Such experimental results are in contrast with the previous work on TiO_2 nanoparticles (chapter 5), indicating the strong influence of solution pH in affecting reactivity. In fact, a decrease in reactivity with increasing solution pH could be expected, determined both by a reduced attraction of iodide anions on TiO_2 surface and by a larger quote of photogenerated holes involved in hydroxyl radical generation. In case of nanotubular TiO_2, the negligible influence of solution pH has probably to be ascribed to mass transfer limitations, already highlighted as the main driving factor in photocatalysis on immobilized TiO_2, *inter alia* [34–37], even none of these works is explicitly referred to nanotubular TiO_2.

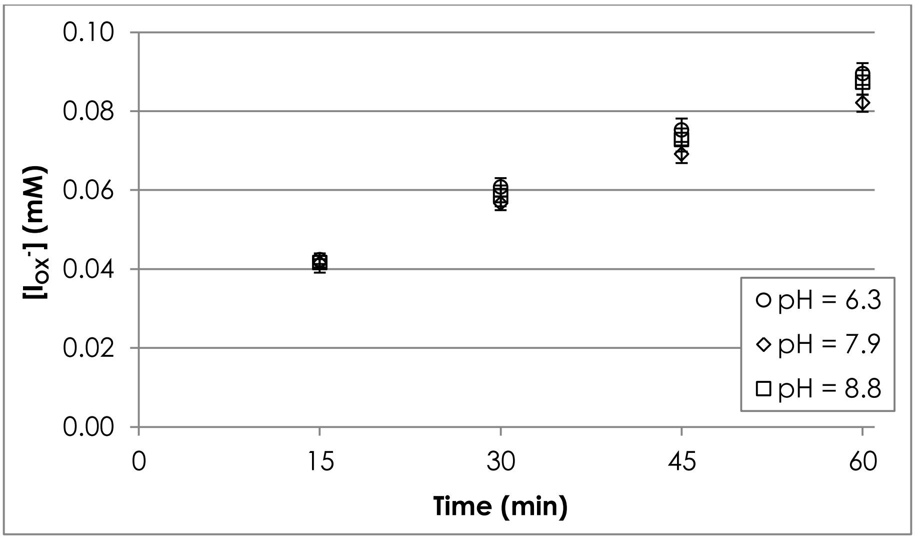

Figure 6.4 Oxidized iodide concentration (mean±st.dev.) vs. time as a function of solution pH.

The influence of iodide concentration on the production of photogenerated holes was then assessed, since the oxidation of iodide was observed to depend on its adsorption on TiO_2 surface, in turn function of iodide concentration in solution [38]. Experimental results are reported in figure 6.5.

An increase in the production of photogenerated holes with iodide concentration was observed, approaching oxidized iodide a plateau at about 37.5 mM iodide concentration. Experimental data were analysed by a Langmuir-Hinshelwood (LH) model, describing the adsorption of iodide on TiO_2 surface by a Langmuir mechanism and its further oxidation. LH model formulation, accounting for other compound competing in adsorption with iodide, is reported:

$$r = \frac{d[I^-]}{dt} = -K_R \cdot \theta_{I^-} = -K_R \cdot \frac{K_{A,I}[I^-]}{1 + K_{A,I}[I^-] + \sum_{Anion} K_{A,Anion}\,[Anion]} \qquad \text{(e6.2)}$$

in which r is the reaction rate, $[I^-]$ is the concentration of iodide, K_R is the LH reaction constant for iodide oxidation, θ_{I^-} is the surface coverage by iodide, , $K_{A,I}$ is the equilibrium constant of adsorption for iodide, $K_{A,Anion}$ is the equilibrium constant of adsorption for a certain anionic species. The effectiveness of such model in describing the photocatalytic oxidation of model pollutants has already been pointed out in literature [26], while its applicability in case of iodide oxidation was highlighted in chapter 4 and 5 in case of TiO_2 nanoparticle suspensions. Experimental data reported in figure 6.5 were used to estimate $K_{A,I}$ and K_R in the absence of other anionic species and considering iodide as the only compound involved in photocatalysis on TiO_2 surface, according to the procedure suggested by [39]; the method is described in detail in Supporting Information (SI6.4). Estimated values for $K_{A,I}$ and K_R and for the coefficient of determination (R^2) are reported in table 6.1. The good fitting of linearized data (R^2=0.992) indicates the effectiveness of LH model in describing experimental data trend.

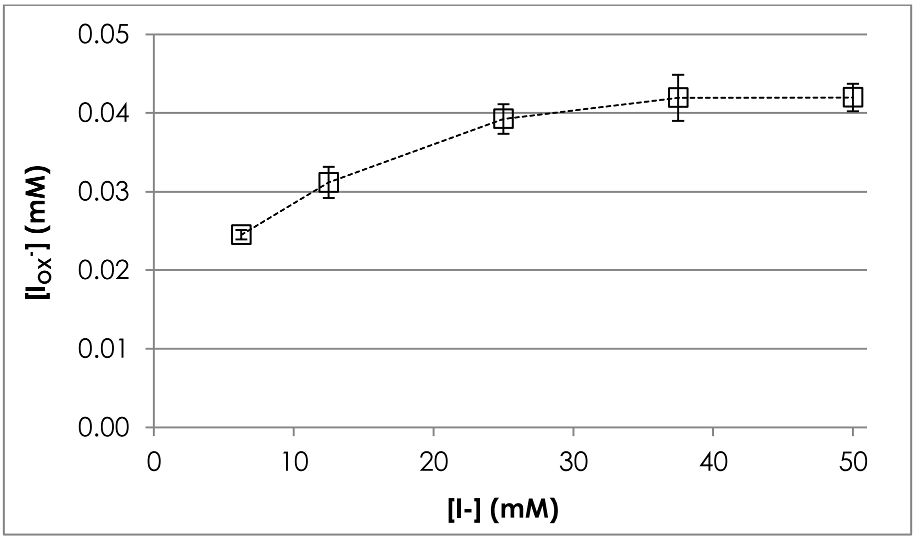

Figure 6.5 Oxidized iodide concentration (mean±st.dev.) vs. initial iodide concentration after 15 minutes irradiation time.

A comparison can be carried out between equilibrium adsorption coefficient, $K_{A,I}$, and LH reaction constant for iodide oxidation, K_R, estimated here for nanotubular TiO_2 and in chapter 5 for TiO_2 nanoparticle suspensions. It should be noticed that optical phenomena involved in TiO_2 photoactivation are completely different for the two types of photocatalysts and consequently the comparison has to be considered as rough. As for the K_R coefficient, the values of LH reaction constant for iodide oxidation are comparable between the two cases. As for $K_{A,I}$ coefficient, $K_{A,I}$ is one order of magnitude larger for TiO_2 nanoparticles, probably due to two distinct phenomena, potentially having a role at the same time: the availability of active sites and the occurrence of mass transfer limitations. Concerning the former, $K_{A,I}$ is inversely related to their availability of active sites for iodide adsorption and, consequently, to TiO_2 surface. Actually, it is possible that a lower number of active sites is present on the photoactivated surface of nanotubular TiO_2 sample with respect to the TiO_2 nanoparticle suspension used in chapter 5 (4 mg of P25 Aeroxide TiO_2). Moreover, a discrepancy between the overall nanotubular TiO_2 surface, that can be estimated by BET, and the fraction effectively participating in the photocatalytic process could exist, since the contribution of TiO_2 surface depends on irradiation and molecular diffusion related phenomena. As a matter of fact, the photocatalytic process on immobilized TiO_2 is usually limited by mass transfer [37], which can be typically neglected in case of TiO_2 suspensions [40]. In particular, immobilized TiO_2 may suffer from external mass transfer and internal diffusion limitations, being the latter frequently negligible. As for external mass transfer, it can be modelled by means of the stagnant film model [41], whose generic mass balance for iodide over a liquid film is reported:

$$\frac{d[I^-]_S}{dt} = -K_M([I^-]_B - [I^-]_S) \tag{e6.3}$$

in which K_M is the mass transfer coefficient for iodide, while $[I^-]_B$ and $[I^-]_S$ are the bulk and surface concentrations of iodide, respectively. At the steady state, when iodide is the only compound involved in photocatalysis, the rate of mass transfer must be equal to the rate of reaction [34], as:

$$K_M([I^-]_B - [I^-]_S) = K_R \cdot \frac{K_{A,I}[I^-]_S}{1 + K_{A,I}[I^-]_S} \tag{e6.4}$$

In equation e6.4 it is assumed that the Langmuir-Hinshelwood is assessed on the basis of the iodide concentration at TiO_2 surface, while $K_{A,I}$ was estimated as a function of the bulk iodide concentration in data processing. On the other hand, surface iodide concentration is unknown, being its value a function of the decrease in iodide concentration from the bulk concentration due to the linear descent across the boundary layer determined by the external mass transfer. However, in the present situation a more detailed quantitative assessment is complicated by the scarce knowledge of fundamental parameters characterizing the boundary layer, as local turbulent state.

Table 6.1 Estimated values of the equilibrium adsorption coefficient, K_A, for iodide, carbonate and phosphate and estimated values of LH reaction constants for iodide oxidation, K_R, in case it is the only anionic species or a competitor of other inorganic anions (carbonate or phosphate). Coefficients of determination, R^2, are shown.

Ionic species	**K_A (M^{-1})**	**K_R ($M\ s^{-1}$)**	**R^2**
Iodide	166.2	5.30E-08	0.992
Carbonate	46.6	2.45E-08	0.981
Phosphate	107.0	2.55E-08	0.955

6.3.2.3 Photogenerated holes in presence of anionic species

A significant decrease in the oxidation of iodide in the presence of inorganic anions in solution was observed only for carbonate and phosphate, while chloride, nitrate and sulfate did not resulted in a measurable effect in the studied range of concentrations.

The concentration of oxidized iodide over 60 minutes irradiation time as a function of carbonate and phosphate concentration is reported in figure 6.6, while time series for iodide oxidation as a function of carbonate and phosphate concentration are shown in Supporting Information (SI6.5). Experimental data for chloride, nitrate and sulfate are not shown explicitly in figure 6.6, since they did not determined a relevant effect on reactivity, as proved by means of Student's t-test (p-value 0.05). Time series for these inorganic anions were identical to results obtained for null concentrations of phosphate and carbonate, irrespectively of their concentration in solution.

Concerning the absence of any influence by chloride, nitrate and sulfate on the oxidation of iodide, which is a selective probe for photogenerated holes, an explanation has been proposed in chapter 5, where the same experimental results were obtained. In fact, assuming that all studied inorganic anions are adsorbed on TiO_2 surface, as demonstrated by Chen et al. [26], two mechanisms were suggested: (i) the existence of different types of active sites, but occurring the interaction of iodide, carbonate and phosphate on TiO_2 surface in the same type of active sites, (ii) the adsorption of chloride, nitrate and sulfate creates weak bonds with respect to other species, being these anions easily displaced from TiO_2 surface by iodide. As in chapter 5, it has to be stressed the importance of further research works aimed at a deeper insight using analytical techniques capable of investigating TiO_2 surface chemistry, such as surface-enhanced Raman spectroscopy [42].

A decreasing trend going to plateau was observed both in presence of phosphate and carbonate, so that the Langmuir-Hinshelwood model was applied to describe the competitive adsorption of inorganic anions on TiO_2 surface by means of the procedure reported in Supporting Information (SI6.4), in which the equilibrium constant of adsorption for iodide was assumed from the previous calculation in the absence of other inorganic anions. Data processing results are reported in table 6.1. The effectiveness of LH mechanism in experimental data fitting was observed, as indicated by the high values of the coefficients of determination for both anionic species ($R^2>0.95$). The greater detrimental effect of phosphate on iodide oxidation is evidenced by the estimated value of $K_{A,Anion}$, being twofold with respect to the value of $K_{A,Anion}$ for carbonate. In case of negligible mass transfer limitations this would imply a higher affinity of phosphate for adsorption.

By comparing these results with those for TiO_2 nanoparticles (chapter 5), it is possible to observe that carbonate and phosphate determined respectively a decrease in iodide oxidation at maximum concentration (50 mM) of about 25% and 45% for nanotubular TiO_2, in contrast with TiO_2 nanoparticles, whose reactivity was reduced by 40% and 70% by carbonate and phosphate. Therefore, the relative importance in interfering in the production of photogenerated holes is maintained: phosphate plays the major role and the proportion in reactivity reduction is about twofold for phosphate with respect to carbonate. Anyway, nanotubular TiO_2 seems to be less sensitive to the presence of phosphate and carbonate. Such difference in reactivity is reflected by the different values of $K_{A,Anion}$ for the two types of materials. The peculiar behaviour of nanotubular TiO_2 could be related to two different phenomena:

(i) a difference in active site morphology with respect to TiO_2 nanoparticles, resulting in a different selectivity towards anionic species, being this situation scarcely probable according to related literature [28];
(ii) the process is regulated by other chemical-physical phenomena, negligible in case of TiO_2 nanoparticles, such as external mass transfer, in agreement with the above discussed results about iodide concentration dependence.

The latter hypothesis is supported by the strong linear relation observed between equilibrium adsorption coefficients, $K_{A,Anion}$, and molecular weights of inorganic anions ($R^2=0.997$), which is:

$$K_{A,Anion} = 0.560MW + 34.251 \quad \text{(e6.5)}$$

in which MW is the molecular weight of the anionic species.

As a matter of fact, molecular weight is a fundamental factor in determining the diffusion coefficient of compounds [41], which control the transport of inorganic anions across the boundary layer. As a consequence, diffusion coefficient is directly correlated to the relative concentration of anionic species at TiO_2 surface, in turn affecting the photocatalytic process. Therefore, iodide oxidation is limited by the diffusion of anionic species in the boundary layer, conditioning the concentration of compounds at TiO_2 surface, while the active sites on nanotubular TiO_2 surface are probably not fully occupied by inorganic anions, so that their competition for adsorption and, thus, their affinity for TiO_2 surface are not determinant, as for TiO_2 nanoparticles. Accordingly to these results, the limitations to photocatalytic process that could be due to internal diffusion and oxygen concentration, indicated in literature as possibly relevant [35], can be neglected here.

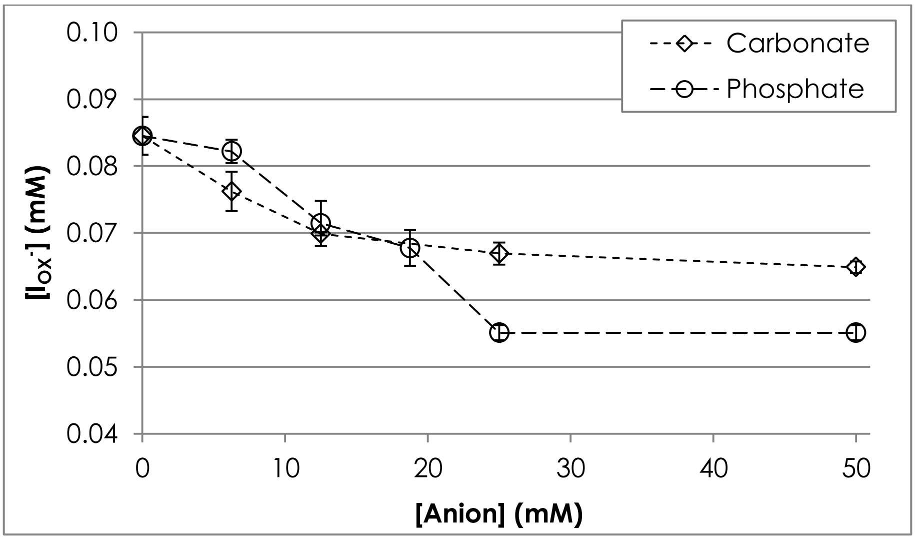

Figure 6.6 Oxidized iodide concentration (mean±st.dev.) vs. inorganic anion concentration after 60 minutes irradiation time (50 mM KI) as a function of species in solution (carbonate, phosphate).

6.4 CONCLUSIONS

Reactivity measurement tests evidenced the occurrence of a detrimental effect on iodide oxidation in presence carbonate and phosphate, unlike for other tests inorganic anions. These results are in agreement with previous results on TiO_2 nanoparticles, although the extent of reactivity reduction was significantly lower in nanotubular TiO_2. The influence of inorganic anions was effectively modelled by Langmuir-Hinshelwood mechanism, being the concentration of inorganic anions at TiO_2 surface limited by the external mass transfer in the stagnant film layer. In particular, the molecular weight of anionic species was crucial in determining their diffusion on TiO_2 surface. The reuse of photocatalyst determined an initial irreversible drop in reactivity and two reversible phenomena, namely the unpredictable fluctuation of nanotubular TiO_2 reactivity in consecutive tests and a decrease in reactivity when TiO_2 surface was exposed to inorganic anions. A regeneration protocol was identified, consisting in electrophotocatalytic cleaning of TiO_2 photocatalyst after washing in sodium hydroxide solution. These results represent a significant advance in the view of process engineering, which involves the continuous usage of the photocatalyst inside reactors and its exposure to anionic species normally present in fresh water.

6.5 REFERENCES

[1] A. Fujishima, X. Zhang, D. Tryk, TiO_2 photocatalysis and related surface phenomena, Surf. Sci. Rep. 63 (2008) 515–582.

[2] M.N. Chong, B. Jin, C.W.K. Chow, C. Saint, Recent developments in photocatalytic water treatment technology: a review, Water Res. 44 (2010) 2997–3027.

[3] P. Pichat, Photocatalysis and water purification: from fundamentals to recent applications, Wiley-VCH, 2013.

[4] H. Choi, S.R. Al-Abed, D.D. Dionysiou, E. Stathatos, P. Lianos, TiO_2-based advanced oxidation nanotechnologies for water purification and reuse, Sustain. Sci. Eng. 2 (2010) 229–254.

[5] H. De Lasa, B. Serrano, M. Salaices, Photocatalytic reaction engineering, Springer, 2005.

[6] T.E. Doll, F.H. Frimmel, Cross-flow microfiltration with periodical back-washing for photocatalytic degradation of pharmaceutical and diagnostic residues-evaluation of the long-term stability of the photocatalytic activity of TiO_2, Water Res. 39 (2005) 847–54.

[7] P. Fernández-Ibáñez, J. Blanco, S. Malato, F.J. d. Las Nieves, Application of the colloidal stability of TiO_2 particles for recovery and reuse in solar photocatalysis, Water Res. 37 (2003) 3180–3188.

[8] A.Y. Shan, T.I.M. Ghazi, S.A. Rashid, Immobilisation of titanium dioxide onto supporting materials in heterogeneous photocatalysis: a review, Appl. Catal. A Gen. 389 (2010) 1–8.

[9] Y. Li, X. Li, J. Li, J. Yin, Photocatalytic degradation of methyl orange by TiO_2-coated activated carbon and kinetic study, Water Res. 40 (2006) 1119–26.

[10] Y. Chen, E. Stathatos, D.D. Dionysiou, Microstructure characterization and photocatalytic activity of mesoporous TiO_2 films with ultrafine anatase nanocrystallites, Surf. Coatings Technol. 202 (2008) 1944–1950.

[11] H. Nizard, M.L. Kosinova, N.I. Fainer, Y.M. Rumyantsev, B.M. Ayupov, Y. V. Shubin, Deposition of titanium dioxide from TTIP by plasma enhanced and remote plasma enhanced chemical vapor deposition, Surf. Coatings Technol. 202 (2008) 4076–4085.

[12] C.W.H. Dunnill, Z.A. Aiken, J. Pratten, M. Wilson, D.J. Morgan, I.P. Parkin, Enhanced photocatalytic activity under visible light in N-doped TiO_2 thin films produced by APCVD preparations using t-butylamine as a nitrogen source and their potential for antibacterial films, J. Photochem. Photobiol. A Chem. 207 (2009) 244–253.

[13] N.M. Mahmoodi, M. Arami, Bulk phase degradation of Acid Red 14 by nanophotocatalysis using immobilized titanium(IV) oxide nanoparticles, J. Photochem. Photobiol. A Chem. 182 (2006) 60–66.

[14] A.H. Fostier, M. do S.S. Pereira, S. Rath, J.R. Guimarães, Arsenic removal from water employing heterogeneous photocatalysis with TiO_2 immobilized in PET bottles., Chemosphere 72 (2008) 319–24.

[15] G.K. Mor, O.K. Varghese, M. Paulose, K. Shankar, C.A. Grimes, A review on highly ordered, vertically oriented TiO_2 nanotube arrays: fabrication, material properties, and solar energy applications, Sol. Energy Mater. Sol. Cells. 90 (2006) 2011–2075.

[16] K. Shankar, J.I. Basham, N.K. Allam, O.K. Varghese, G.K. Mor, X. Feng, et al., Recent advances in the use of TiO_2 nanotube and nanowire arrays for oxidative photoelectrochemistry, J. Phys. Chem. C. 113 (2009) 6327–6359.

[17] Y. Zhang, X. Xiong, Y. Han, X. Zhang, F. Shen, S. Deng, et al., Photoelectrocatalytic degradation of recalcitrant organic pollutants using TiO_2 film electrodes: an overview, Chemosphere 88 (2012) 145–154.

[18] J.M. Macak, H. Tsuchiya, A. Ghicov, K. Yasuda, R. Hahn, S. Bauer, et al., TiO_2 nanotubes: self-organized electrochemical formation, properties and applications, Curr. Opin. Solid State Mater. Sci. 11 (2007) 3–18.

[19] M. Zlamal, J.M. Macak, P. Schmuki, J. Krýsa, Electrochemically assisted photocatalysis on self-organized TiO_2 nanotubes, Electrochem. Commun. 9 (2007) 2822–2826.

[20] A. Turolla, M. Fumagalli, M. Bestetti, M. Antonelli, Electrophotocatalytic decolorization of an azo dye on TiO_2 self-organized nanotubes in a laboratory scale reactor, Desalination 285 (2012) 377–382.

[21] A. Kar, Y.R. Smith, V. Subramanian, Improved photocatalytic degradation of textile dye using titanium dioxide nanotubes formed over titanium wires, Environ. Sci. Technol. 43 (2009) 3260–3265.

[22] N. Baram, D. Starosvetsky, J. Starosvetsky, M. Epshtein, R. Armon, Y. Ein-Eli, Photocatalytic inactivation of microorganisms using nanotubular TiO_2, Appl. Catal. B Environ. 101 (2011) 212–219.

[23] Y.S. Sohn, Y.R. Smith, M. Misra, V. Subramanian, Electrochemically assisted photocatalytic degradation of methyl orange using anodized titanium dioxide nanotubes, Appl. Catal. B Environ. 84 (2008) 372–378.

[24] M.F. Brugnera, K. Rajeshwar, J.C. Cardoso, M.V.B. Zanoni, Bisphenol A removal from wastewater using self-organized TIO_2 nanotubular array electrodes, Chemosphere 78 (2010) 569–575.

[25] M. Abdullah, G.K.C. Low, R.W. Matthews, Effects of common inorganic anions on rates of photocatalytic oxidation of organic carbon over illuminated titanium dioxide, J. Phys. Chem. 94 (1990) 6820–6825.

[26] H.Y.Y. Chen, O. Zahraa, M. Bouchy, Inhibition of the adsorption and photocatalytic degradation of an organic contaminant in an aqueous suspension of TiO_2 by inorganic ions, J. Photochem. Photobiol. A Chem. 108 (1997) 37–44.

[27] C. Guillard, E. Puzenat, H. Lachheb, A. Houas, J. Herrmann, Why inorganic salts decrease the TiO_2 photocatalytic efficiency 7 (2005) 1–9.

[28] O. Carp, Photoinduced reactivity of titanium dioxide, Prog. Solid State Chem. 32 (2004) 33–177.

[29] G. Bartosz, Use of spectroscopic probes for detection of reactive oxygen species, Clin. Chim. Acta. 368 (2006) 53–76.

[30] N. Soh, Recent advances in fluorescent probes for the detection of reactive oxygen species, Anal. Bioanal. Chem. 386 (2006) 532–43.

[31] M. Bestetti, S. Franz, M. Cuzzolin, P. Arosio, P.L. Cavallotti, Structure of nanotubular titanium oxide templates prepared by electrochemical anodization in H_2SO_4/HF solutions, Thin Solid Films 515 (2007) 5253–5258.

[32] R. Jenkins, R. Snyder, Introduction to X-ray powder diffractometry, A Wiley-InterScience Publication, 2012.

[33] S. Malato, P. Fernández-Ibáñez, M.I.I. Maldonado, J. Blanco, W. Gernjak, Decontamination and disinfection of water by solar photocatalysis: recent overview and trends, Catal. Today. 147 (2009) 1–59.

[34] D. Chen, F. Li, A.K. Ray, External and internal mass transfer effect on photocatalytic degradation, Catal. Today 66 (2001) 475–485.

[35] M.F.J. Dijkstra, H.J. Panneman, J.G.M. Winkelman, J.J. Kelly, A.A.C.M. Beenackers, Modeling the photocatalytic degradation of formic acid in a reactor with immobilized catalyst, Chem. Eng. Sci. 57 (2002) 4895–4907.

[36] D.D. Dionysiou, M.T. Suidan, I. Baudin, J.M. Laîné, Oxidation of organic contaminants in a rotating disk photocatalytic reactor: reaction kinetics in the liquid phase and the role of mass transfer based on the dimensionless Damköhler number, Appl. Catal. B Environ. 38 (2002) 1–16.

[37] M. Vezzoli, W.N. Martens, J.M. Bell, Investigation of phenol degradation: true reaction kinetics on fixed film titanium dioxide photocatalyst, Appl. Catal. A Gen. 404 (2011) 155–163.

[38] J.M. Herrmann, P. Pichat, Heterogeneous photocatalysis. Oxidation of halide ions by oxygen in ultraviolet irradiated aqueous suspension of titanium dioxide, J. Chem. Soc. Faraday Trans. 1. 76 (1980) 1138.

[39] M. Mehrvar, W.A. Anderson, M. Young, P.M. Reilly, Non-linear parameter estimation for a dynamic model in photocatalytic reaction engineering, Chem. Eng. Sci. 55 (2000) 4885–4891.

[40] M. de los M. Ballari, R. Brandi, O. Alfano, A. Cassano, Mass transfer limitations in photocatalytic reactors employing titanium dioxide suspensions. II. External and internal particle constrains for the reaction, Chem. Eng. J. 136 (2008) 242–255.

[41] J.C. Crittenden, R.R. Trussell, D.W. Hand, K.J. Howe, G. Tchobanoglus, MWH's water treatment: principles and design, Wiley, 2012.

[42] M. Moskovits, Surface-enhanced Raman spectroscopy: a brief retrospective, J. Raman Spectrosc. 36 (2005) 485–496.

6.6 SUPPORTING INFORMATION

SI6.1 TiO_2 photocatalyst surface calculation

Calculations are based on the assumption that all the Ti wires are identical, and that each mesh is characterized by an orthogonal texture. The complex structure of the wire mesh was divided into a sequence of identical wires across vertical and horizontal direction. These wires were considered as cylindrical structures, so that the surface of each wire (S_W) was estimated as:

$$S_W = 2\pi R_W L \qquad \text{(eSI6.1)}$$

in which R_W is the wire radius, having a dimension of approximately 100 μm.

Subsequently, the surface of each wire in vertical and horizontal direction was multiplied by the number of wires constituting the mesh in the two directions (n_V, n_O). The surface lost (S_L) due to the overlap of the wires in the texture has been evaluated according to:

$$S_L = 2(n_V n_O)(2R_W)^2 \qquad \text{(eSI6.2)}$$

As a matter of fact, each overlap determines approximately the loss of a square surface having a side dimension equal to the wire section on each involved wire. Wires overlap as many times as the product of the number of wires that are present along the two dimensions in the wire mesh. The specific surface was obtained as the ratio between the active surface and the apparent surface of the cylindrical TiO_2 sample, resulting in 0.8 cm^2 per apparent cm^2.

SI6.2 Radiation intensity as a function of emission wavelength at the upper liquid surface

Emission spectrum of UV lamps, as provided by the manufacturer, was used to determine the radiation intensity as a function of the emission wavelength at the liquid upper surface of the samples. Results are reported in figure SI6.1. Radiometric readings were corrected by taking into account the spectral response of the sensor, as suggested in [SI1].

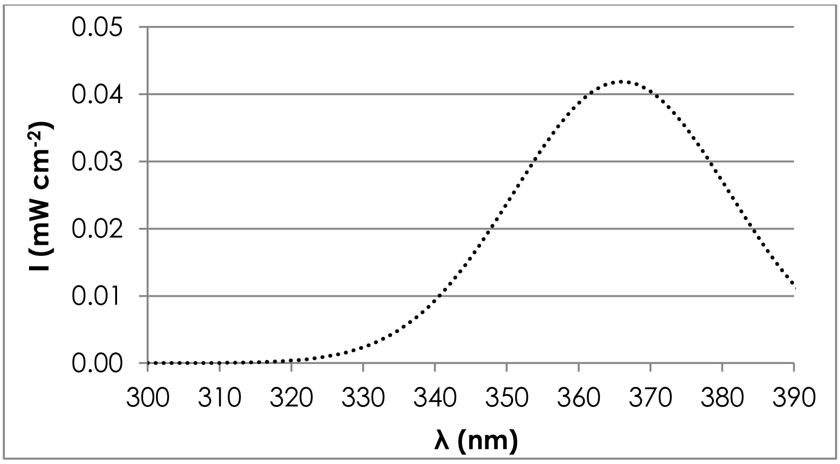

Figure SI6.1 Radiation intensity vs. emission wavelength at the liquid upper surface of samples.

SI6.3 Electrophotocatalytic reactor for nanotubular TiO_2 regeneration

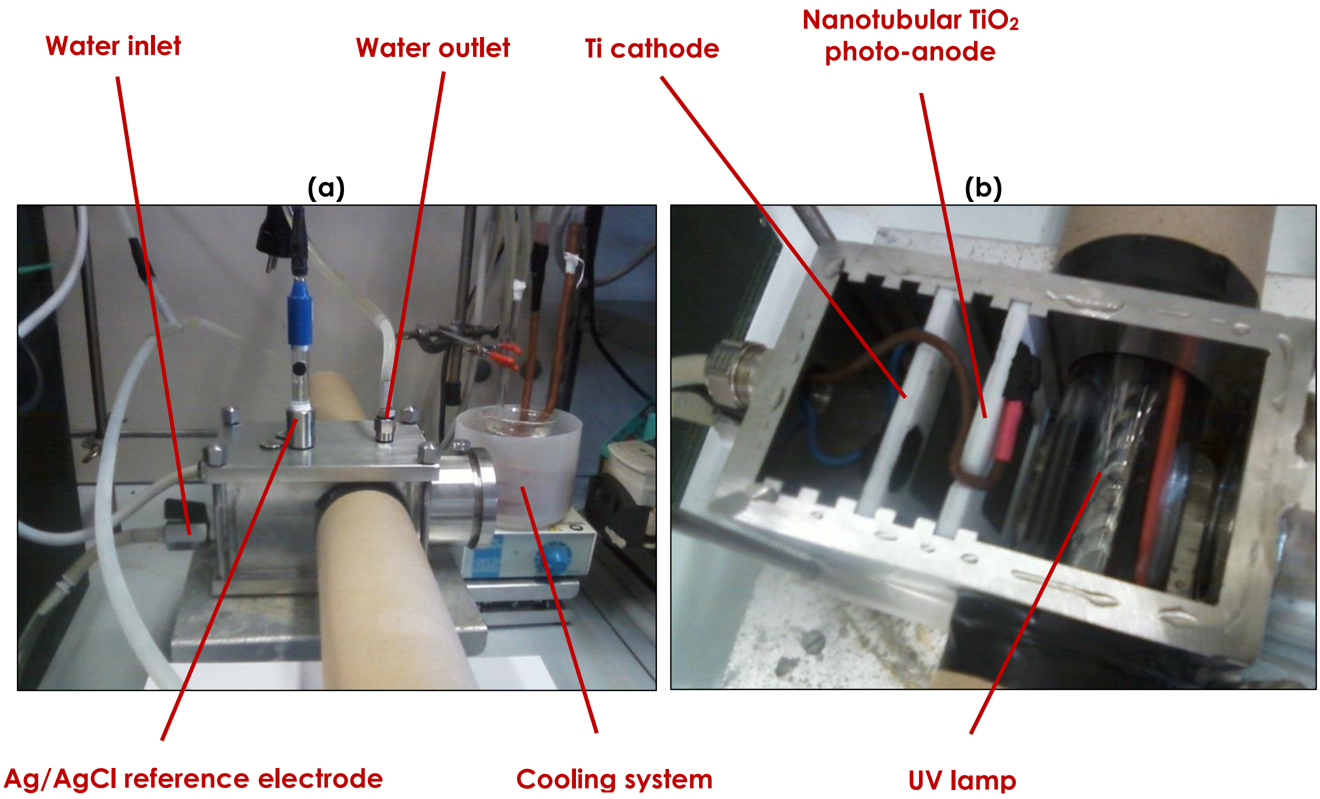

Figure SI6.2 Electrophotocatalytic reactor for nanotubular TiO_2 regeneration: (a) side view of the reactor while operating, (b) top view of the reactor during a cleaning procedure (the cover is removed).

SI6.4 Langmuir-Hinshelwood linearization procedure for K_A and K_R constants estimation

Equation e6.2 can be modified in order to describe the oxidation of iodide in the absence of other inorganic anions, highlighting the linear relationship between the inverse of initial reaction rate and the inverse of initial iodide concentration, as follows [SI2]:

$$\frac{1}{r_0} = \frac{1}{K_{A,I^-} K_R} \frac{1}{[I^-]_0} + \frac{1}{K_R} = m \frac{1}{[I^-]_0} + q \qquad \text{(eSI6.3)}$$

with

$$K_R = \frac{1}{q} \qquad\qquad K_A = \frac{q}{m}$$

The rate r_0 is obtained from experimental data by calculating the oxidized iodide concentration for each $[I^-]_0$ over time. K_A and K_R values were calculated by fitting experimental data shown in figure 6.5 with a linear regression, estimating m and q values by least square method, as in figure SI6.3.

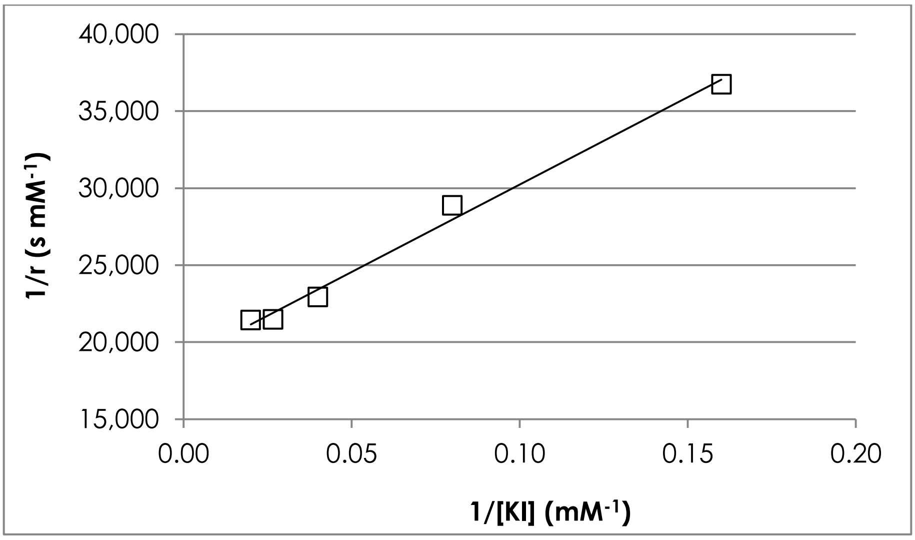

Figure SI6.3 Experimental data linear regressions (1/r vs. 1/$[I^-]_0$) for iodide adsorption via Langmuir-Hinshelwood model.

Equation e6.2 in the manuscript can be transformed so as to highlight the linear relationship between the inverse of the initial reaction rate and the initial inorganic anion concentration, as it follows [SI3]:

$$\frac{1}{r_0} = \frac{K_{A,Anion}}{K_R K_{A,I^-}\,[I^-]_0}\,[Anion] \quad + \frac{1 + K_{A,I^-}\,[I^-]_0}{K_R K_{A,I^-}\,[I^-]_0} = m\,[Anion] \quad + q \qquad \text{(eSI6.4)}$$

with

$$K_R = \frac{1+K_{A,I^-}\,[I^-]_0}{q\cdot K_{A,I^-}\,[I^-]_0} \qquad\qquad K_A = m \cdot K_R K_{A,I^-}\,[I^-]_0$$

In calculation procedure experimental values at 50 mM were neglected because plateau has already been reached at this concentration, that resulted, as a consequence, in a distortion in data processing. Results for linearization of experimental data are reported in figure SI6.4.

(a)

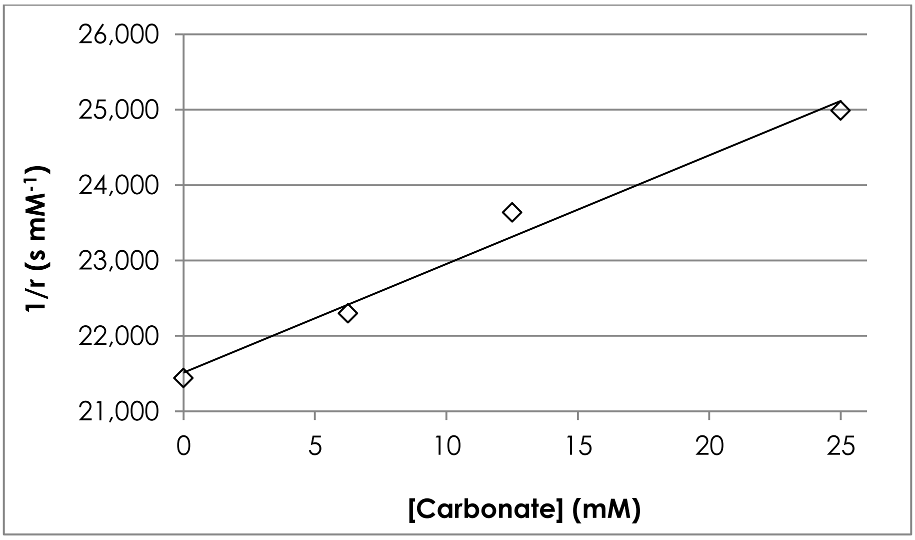

(b)

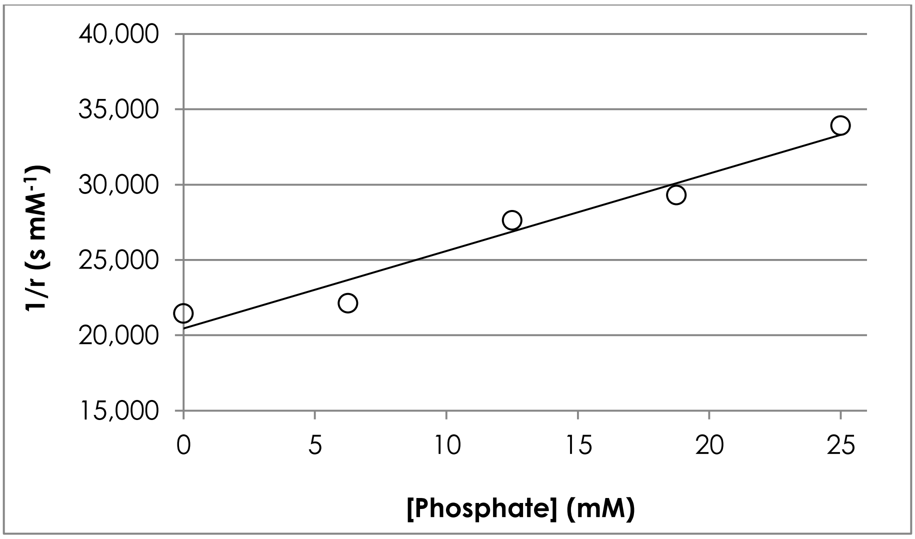

Figure SI6.4 Experimental data linear regressions (1/r vs. [Anion]) for the competitive adsorption of inorganic anions with iodide via Langmuir-Hinshelwood mechanism as a function of TiO_2 dispersion method (S: sonicated, NS: non-sonicated) for various anionic species, i.e. carbonate (a) and phosphate (b).

SI6.5 Time series for iodide oxidation as a function of inorganic anion concentration

(a)

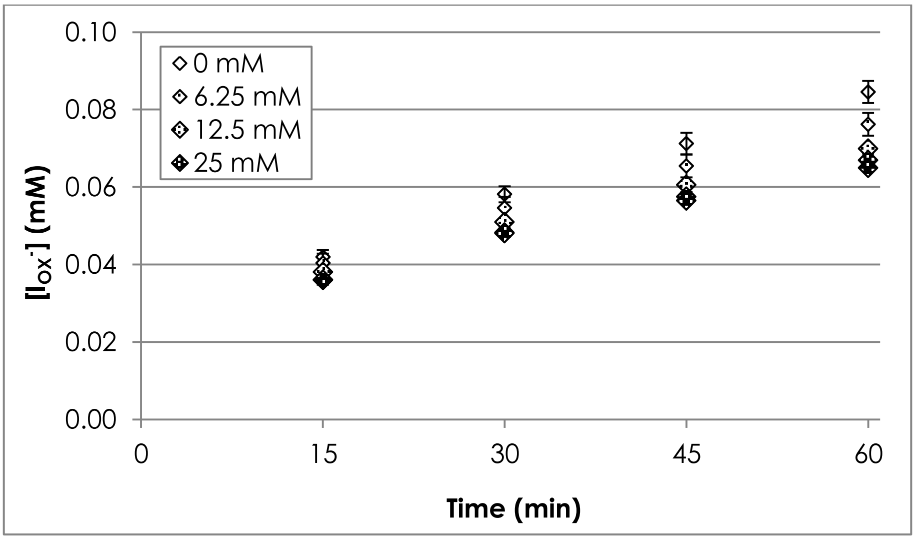

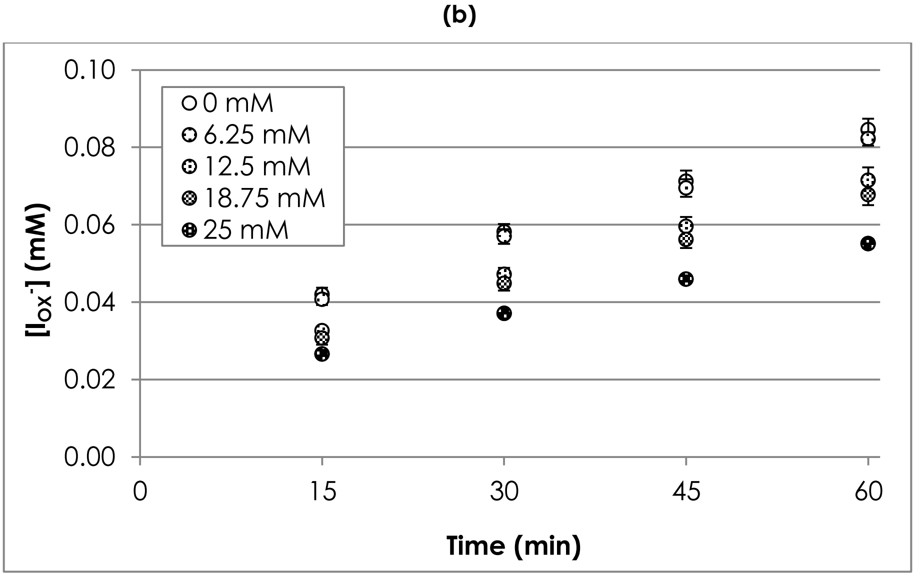

Figure SI6.5 Oxidized iodide concentration (mean±st.dev.) vs. time as a function of inorganic anion concentration for (a) carbonate and (b) phosphate.

REFERENCES

[SI1] I. Grcic I., G. Li Puma, Photocatalytic degradation of water contaminants in multiple photoreactors and evaluation of reaction kinetic constants independent of photon absorption, irradiance, reactor geometry, and hydrodynamics, Environ. Sci. Technol. 47 (2013) 13702-13711.

[SI2] J.M. Herrmann, P. Pichat, Oxidation of halide ions by oxygen in ultraviolet irradiated aqueous suspension of titanium dioxide. J.C.S. Faraday I 76 (1980) 1138-1146.

[SI3] H.Y. Chen, O. Zahraa M. Bouchy, Inhibition of the adsorption and photocatalytic degradation of an organic contaminant in an aqueous suspension of TiO_2 by inorganic ions. J. Photochem. Photobiol. A 108 (1997) 37-44.

CHAPTER 7

DESIGN AND OPTIMISATION OF AN ELECTROPHOTOCATALYTIC PROCESS BASED ON SELF-ORDERED NANOTUBULAR TiO_2 FOR WATER AND WASTEWATER TREATMENT

ABSTRACT

Electrophotocatalysis on nanotubular titanium dioxide (TiO_2) is a promising advanced oxidation process, potentially overcoming constrains of photocatalysis on immobilized TiO_2, namely the low process yield and the difficult process engineering. In the present work an optimal design methodology for an electrophotocatalytic reactor using self-ordered nanotubular TiO_2 has been proposed. The photocatalyst, subjected to a bias, was used as a photo-anode in a modular reactor (25 L), in which the positioning of a variable number of UV lamps (0 to 5) and photocatalyst surfaces (0 to 5) was varied. A textile azo-dye (Reactive Red 243, RR243) was used as model compound, to vary the solution transmittance. TiO_2 photoactivation was monitored in terms of generated photocurrent as a function of the operating conditions, namely reactor geometrical configuration and solution transmittance. A model to predict the overall generated photocurrent in the electrophotocatalytic reactor was developed and calibrated on experimental data. The effectiveness of generated photocurrent as proxy variable to predict TiO_2 photoactivation was proved, both by photocurrent measurements and by RR243 degradation tests, performed in modular configurations based on various arrangements of a basic unit. RR243 decolorization kinetic was successfully described by Langmuir-Hinshelwood model and the kinetic coefficients were well correlated to generated photocurrent. Finally, this approach was applied for reactor design, assessing several modular configurations on the basis of energy consumption to obtain a selected TiO_2 photoactivation extent as a function of solution transmittance. Guidelines for reactor design optimization and scale-up were indicated.

The research work was partially carried out within the research project 'TITANO' (Ricerca di nuovi materiali catalizzatori e loro integrazione in dispositivi per processi di elettrofotocatalisi eterogenea per la rimozione di inquinanti refrattari e patogeni resistenti dalle acque, ID 13726167), funded by Regione Lombardia (ATP 2009) and involving several national industrial and academic partners:

Ozono Elettronica Internazionale srl - Helios Italquartz srl - AMEL Electrochemistry srl -
CSMT Gestione scarl - TTM ROSSI srl - Department of Chemistry, Materials and Chemical
Engineering "Giulio Natta" (CMIC), Politecnico di Milano, Italy

The present chapter, after an adaptation in terms of formatting style, will be submitted within a short time for publication to the 'Journal of Environmental Chemical Engineering'.

7.1 INTRODUCTION

The relevant potential of TiO_2 photocatalysis for the removal of refractory pollutants and pathogens in water and wastewater has been pointed out over the last 30 years [1–3]. Anyway, so far TiO_2 photocatalysis cannot yet be included among established technologies for water and wastewater treatment, unlike other UV-based advanced oxidation processes, such as hydrogen peroxide combined to UV radiation [4]. Actually the underdevelopment of photocatalytic technologies at real scale has to be mainly ascribed to low process yield and complex process engineering [5,6].

The low process yield descends directly from the low TiO_2 quantum yield, which is a measure of the fraction of absorbed photons generating reactive species. This low photoactivation efficiency is mainly due to the recombination of most electron-hole pairs, inhibiting the progress of reductive and oxidative pathways [7]. For instance, the quantum yield has been estimated to be around 2% for hydroxyl radicals in a previous research work [8].

Concerning process engineering, current challenges in reactor design differ depending on TiO_2 structure. When TiO_2 suspensions are used, a downstream separation stage is required, as filtration [9] or coagulation [10], in order to avoid nanoparticle release in the effluent. However, TiO_2 immobilization, despite it does not ask for a post-separation stage, typically implies a reduction in the number of active sites and the occurrence of mass transfer limitations [11]. Although several TiO_2 immobilization techniques have been reported in past years [12], most of the research works are focused on material manufacturing and its application at the proof-of-concept scale for the degradation of model pollutants [13–16]. As a result, reactor design optimization and scale-up are still an area of research compared to photocatalytic processes on immobilized TiO_2 applied for gas-phase purification [17–19]. As a matter of fact, this research lag is mostly related to: (i) the greater complexity of a quantitative and accurate description in liquid phase of all the phenomena involved (radiation transfer, fluid dynamics and mass transport phenomena); (ii) the good performance achieved by photocatalysis on TiO_2 suspensions in slurry phase which cannot be applied in gas-phase purification.

A viable solution to by-pass the constraints related to the low process yield is represented by electrophotocatalysis on nanotubular TiO_2. Nanotubular TiO_2 is grown by anodic oxidation directly on a titanium (Ti) substrate and it is composed by nanometric oxide cylinders which are aligned perpendicularly to the Ti substrate and strongly bounded to it [20]. As a consequence, an anodic polarization can be applied to nanotubular TiO_2, which would act as photo-anode in a photoelectrochemical cell. Polarization voltage represents the driving force for the removal of promoted electrons from TiO_2 surface, determining the significant inhibition of electron-hole pair recombination and therefore enhancing reactive species generation [21,22]. Hence electrophotocatalysis on nanotubular TiO_2 can be considered a promising technology which has been attracting considerable interest in recent years [23], as proved by several studies carried out at the laboratory scale on the removal of refractory pollutants, as bisphenol A [24], pentachlorophenol [25], methyl orange [26], 4-chlorophenol [27], aromatic amines [28].

Actually even for electrophotocatalysis on nanotubular TiO_2, the challenge of the process engineering persists, since the definition of an accurate and reproducible methodology is first required for process optimization and reactor scale-up. In optimization problems a common issue is the identification of a reference variable which is representative of the overall process efficiency and independent from specific working conditions. So far the radiation delivered at TiO_2 surface [29] and the degradation of model pollutants [30] have been chosen as indicators in modelling of photocatalysis on immobilized TiO_2. However, on the one hand, the solution of radiative transfer equation in the reactor volume and its integration with fluid dynamics and process chemistry are not commonly affordable; on the other hand, the results from the degradation of model pollutants are usually not directly generalizable. A great advantage in electrophotocatalysis on nanotubular TiO_2 is that TiO_2 photoactivation can be assessed by measuring the generated photocurrent, which is a direct consequence of charge separation at photocatalyst surface. Generated photocurrent is a measurable and reliable proxy variable, which is commonly used in determining TiO_2 electrodes efficiency for other applications, but it can be also effectively implemented in water and wastewater treatment [31,32], in order to monitor reactive species generation.

In the present work an optimal design methodology for an electrophotocatalytic reactor using self-ordered nanotubular TiO_2 for water and wastewater treatment has been proposed, using generated photocurrent as an indicator of TiO_2 photoactivation. TiO_2 photocatalyst was used as a photo-anode in a batch reactor (25 L) in which a variable number of UV lamps (up to 5) and photocatalysts (up to 5) can be positioned in various geometries. While it was irradiated by UV monochromatic radiation at 254 nm and subjected to anodic polarization, nanotubular TiO_2 photoactivation was monitored by means of photoelectrochemical tests as a function of solution transmittance and reactor configuration (number of lamps and photocatalysts and relative positioning). A textile azo-dye (Reactive Red 243, RR243) was used as model compound, to modify the solution transmittance. A model to predict the overall generated photocurrent in the electrophotocatalytic reactor was developed and calibrated on experimental data and then validated by RR243 degradation tests, obtaining a good correlation with Langmuir-Hinshelwood decolorization kinetic coefficients. Finally, the modelling approach was applied to a modular reactor scale-up, assessing several modular configurations, composed by assembling basic units of various geometries, on the basis of energy consumption required for a selected TiO_2 photoactivation extent as a function of solution transmittance. The parametric analyses performed permitted to define guidelines for reactor design optimization and scale-up.

7.2 MATERIAL AND METHODS

7.2.1 Nanotubular TiO_2 photocatalyst and reagents

Nanotubular TiO_2 was supplied by Nanomaterials.it (Italy). It was grown by anodic oxidation of a commercial titanium (grade 1) wire mesh (TTM Rossi, Italy), shown in figure 7.1a. Anodic oxidation was carried out in a fluoride containing solution, according to the procedure described in previously published works [33,34]. Nanotubular TiO_2 morphology and its crystalline structure were characterized respectively by Environmental Scanning Electron Microscope (ESEM, Zeiss EVO 50 EP, Germany) and X-Ray Diffractometer (XRD, Philips PW-1830, Netherlands), before and after the annealing treatment. An ESEM image of nanotubular TiO_2 is reported in figure 7.1b: the film morphology is compact and uniform, composed of nanotubes having a thickness of about 500-600 nm and an average diameter of 100-150 nm. Based on XRD spectra, reported in Supporting Information (SI7.1), anatase and rutile phases were estimated to be respectively 70-80% and 20-30% [35]. Three types of cylindrical photocatalyst samples were used, having the same length (H=40 cm) and differing in the diameter (Ø=4.5, 5.5, 6.5 cm). The specific surface area of the cylindrical samples has been calculated according to the procedure reported in Supporting Information (SI7.2), obtaining 958, 1171,1384 cm^2 for the samples with a diameter of 4.5, 5.5, 6.5 cm respectively.

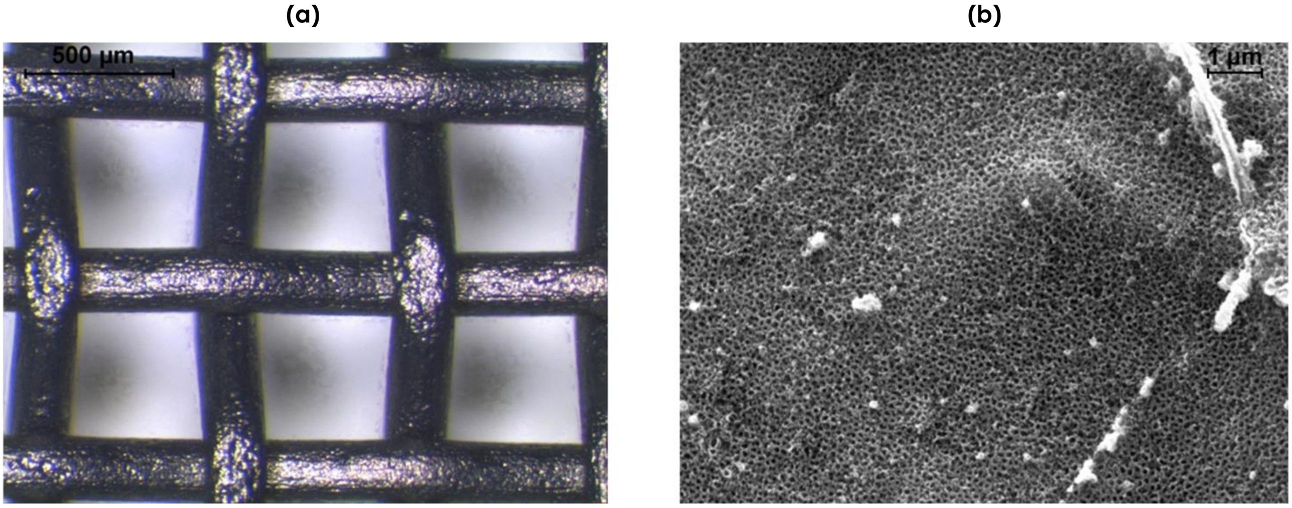

Figure 7.1 Surface structure of nanotubular TiO_2 photocatalyst samples: (a) optical microscope image of Ti support, (b) ESEM image of nanotubular TiO_2.

A textile organic azo dye (Reactive Red 243, RR243) was selected as model compound for refractory organic pollutants, being its molecular structure shown in Supporting Information (SI7.3). RR243 solutions were prepared in deionized water (5 to 25 mg L^{-1}) and potassium chloride (KCl, 4.2 mM) was added to adjust initial conductivity at 635±15 $\mu S\ cm^{-1}$, comparable to drinking water values in Milan urban area. RR243 has three characteristic absorbing wavelengths at 287, 515 and

545 nm: calibration lines at these wavelengths were determined using solutions at various dye concentrations (1 to 25 mg L^{-1}). No significant modifications in solution conductivity were determined by the presence of RR243. The mathematical function for correlating solution transmittance and RR243 concentration was determined by experimental data fitting:

$$T = 1.010e^{-0.043[RR243]} \qquad (R^2=0.99996)$$

where T is the solution transmittance and [RR243] is RR243 concentration (mg L^{-1}).

7.2.2 Electrophotocatalytic reactor

Electrophotocatalytic reactor was constituted by a 25 L stainless steel vessel (H=50 cm, Ø=26.7 cm) in which up to 5 UV lamps and up to 5 cylindrical TiO_2 samples, coaxially located around UV lamps, can be vertically positioned in various geometries, as shown in figure 7.2. Low pressure Hg vapour UV lamps (30 W, Helios Italquartz, Italy) were used, each one placed in a quartz sleeve (Ø=3.4 cm). The UV emission spectrum had a peak at 254 nm and it was described by a normal distribution curve having standard deviation of 10 nm. TiO_2 cylindrical samples were used as photo-anodes and biased at 1.5 V vs. Ag/AgCl with a potentiostat/galvanostat (515, Material Mates, Italy). Cathodes consisted of four stainless steel bars (40x1 cm) placed vertically in the reactor, while the Ag/AgCl reference electrode (373/SSG/12, AMEL, Italy) was immersed vertically close to one of the TiO_2 cylindrical samples. Electrophotocatalytic reactor was continuously mixed by air bubbling from the bottom by means of an upward flow of 0.27 L h^{-1} cm^{-2}, also maintaining oxygen concentration at saturation level.

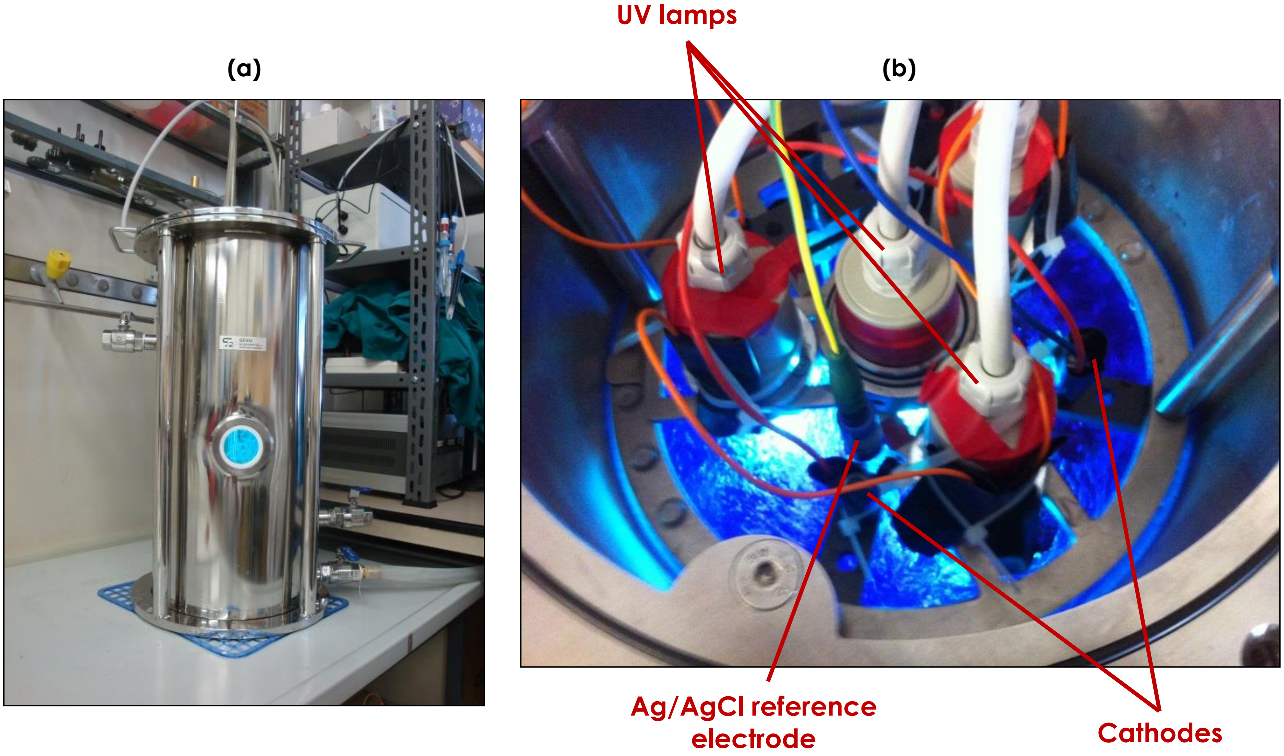

Figure 7.2 Electrophotocatalytic reactor scheme: (a) side view, (b) top view.

7.2.3 Photoelectrochemical tests on nanotubular TiO_2

Photocurrent generated by irradiated and biased nanotubular TiO_2 was quantified by chrono-amperometric measures. In detail, the current intensity (mA) displayed by the photocatalyst in dark (60 s) and light (300 s) conditions was recorded with a time step of 1 s in tests lasting 360 s. Current intensity in dark conditions accounts for faradic side reactions taking place in the experimental setup, specifically depending on electrode geometry and configuration. Current intensity measured under irradiation conditions accounts for both the promoted electrons and the electrons circulating in the circuit imposed between electrodes. The generated photocurrent intensity was calculated as the difference between the mean value of the last 60 s signal and the mean value of the first 60 s signal. The photocurrent density (mA cm^{-2}) was then calculated as the ratio between photocurrent intensity and photocatalytic surface area (cm^2). Three types of tests were performed to evaluate the extent of TiO_2 photoactivation depending on reactor configuration:

(1) A UV lamp was located centrally and vertically in the reactor, coaxially surrounded by a TiO_2 cylindrical sample, which was thus irradiated from inside. In total, 18 tests were performed, considering the combinations of the following parameters: diameter of the cylindrical photocatalyst (4.5, 5.5 and 6.5 cm), RR243 concentration (0 to 25 mg L^{-1}; 5 mg L^{-1} step).

(2) A TiO_2 cylindrical sample was located centrally and vertically in the reactor and irradiated from outside by a UV lamp vertically positioned at variable distance. In total, 144 tests were performed, considering the combinations of the following parameters: diameter of the cylindrical photocatalyst (4.5, 5.5 and 6.5 cm), irradiation distance of the UV lamp (0.5 to 4 cm; 0.5 cm step), RR243 concentration (0 to 25 mg L^{-1}; 5 mg L^{-1} step).

(3) Seven reactor configurations (#1 to #7) were defined, differing in the number of UV lamps and TiO_2 cylindrical samples (diameter: 4.5 cm), but having fixed at 2.5 cm the distance between the external UV lamps and the photocatalyst. The configuration schemes are reported in figure 7.3. RR243 concentration was varied from 0 to 25 mg L^{-1} (5 mg L^{-1} step). A total number of 42 tests were performed.

Absorbance (254, 287, 515 and 545 nm), conductivity and pH were monitored before and after each trial. The absence of significant RR243 degradation phenomena was verified in any operating condition, indicating the stability of optical properties during tests.

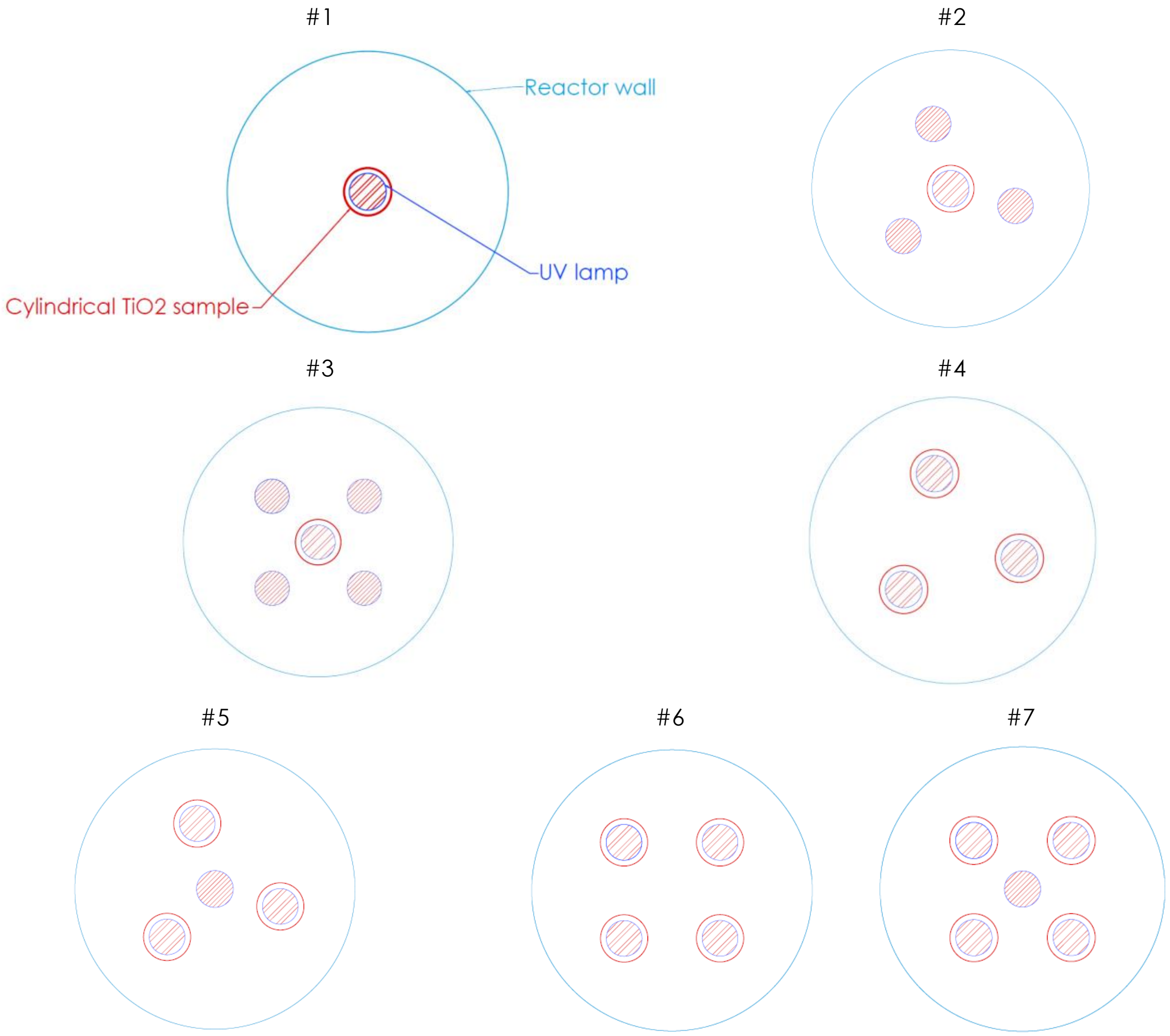

Figure 7.3 Reactor configurations based on multiple UV lamps and TiO_2 cylindrical samples

7.2.4 Electrophotocatalytic degradation tests

Electrophotocatalytic degradation tests were performed in configurations from #1 to #7. The initial RR243 concentration was 25 mg L^{-1}. Tests lasted 240 minutes in configurations from #1 to #4 (samples collected every 30 minutes) and 120 minutes in configurations from #5 to #7 (samples collected every 15 minutes). Absorbance (254, 287, 515 and 545 nm), conductivity, pH and chloride concentration were monitored. Each test was carried out in triplicate.

7.2.5 Analytical methods

Solution absorbance (254, 287, 515 and 545 nm), conductivity, pH and chloride concentration were measured according to Standard Methods [36]. Absorbance was measured by a Unicam UV-Vis 2 spectrophotometer (optical path 1 cm). Conductivity and pH were respectively monitored by Eutech pH 6+ (Thermo Scientific, USA) and Eutech Cond 6+ (Thermo Scientific).

7.3 RESULTS AND DISCUSSION

Generated photocurrent is an indicator of the separation of charges on TiO_2 surface induced by irradiation, and thus it is directly related to nanotubular TiO_2 photoactivation [37]. It should be mentioned that this proxy variable does not provide a quantitative measure of promoted electrons, but its variations are proportional to the extent of charge separation on TiO_2 surface. Moreover, it is an effective proxy variable when the estimation of the radiation delivered to the photocatalyst surface is complex and not reliable due to semi-transparent and reflective characteristics of the photocatalyst [38]. As a matter of fact, in the present case, radiation transfer modelling is further complicated by: (i) the complex morphology of the photocatalyst at the macro and micro-scale, which enhance superficial reflective phenomena; (ii) the relative positioning of photocatalysts and UV lamps, which results in a wide range of radiation incident angles often far from perpendicularity.
The robustness of generated photocurrent as proxy variable in predicting TiO_2 nanotubular photoactivation in an electrophotocatalysis process has been here assessed in 3 steps. First, the photoactivation of a TiO_2 cylindrical sample was experimentally evaluated when irradiated by one UV lamp, located in turn inside and outside the photocatalytic surface, as a function of irradiation distance and solution transmittance. Experimental data were used to develop a generated photocurrent prediction model. Then, in the second step, the model was validated comparing experimental and simulated generated photocurrent data in multi-lamp and multi-catalyst reactor configurations, constituted by a different number of catalysts and lamps differently positioned. Moreover, the model has been validated against experimental data collected in dye degradation tests in the same reactor configurations. In the third step, the model has been used as optimisation tool, to fix the best base unit geometries, and scale-up tool to define the shape, size and characteristics of modular reactors, designed by assembling such base units, in order to maximise generated photocurrent and minimise energy requirements as a function of transmittance.
It should be emphasised that the definition of guidelines for reactor design optimization and scale-up would permit to successfully extend the use of TiO_2 cylindrical meshed supports, which resulted as an optimal alternative in our previous work on a single-lamp reactor setup [39], to a multiple-lamp setup. In fact, most of immobilized TiO_2 has been prepared on flat supports so far, essentially because of more favorable fabrication procedures, but enforcing strong restrictions in reactor design. As a matter of fact, two main configurations have been described in the past [4,5,12]: (i) tubular structures coaxially illuminated by an artificial radiation source, in which TiO_2 photocatalyst usually covers the reactor outer wall, and (ii) planar structures frontally positioned with respect to the incident direction of radiation, being this last configuration suitable also in case of solar irradiation in addition to artificial sources. In the present case, nanotubular TiO_2 was produced on a wire mesh, allowing for the development of alternative and more flexible configurations, such as reactor setup with photocatalyst irradiation on both sides or liquid phase flow not parallel to the catalytic support, to enhance local turbulence at the micro-scale.

7.3.1 Experimental measurements and modelling of nanotubular TiO_2 photoactivation in a mono-lamp and mono-photocatalyst configuration

Concerning cylindrical TiO_2 samples internally irradiated by a UV lamp, generated photocurrent intensity values are shown in figure 7.4 as a function of cylinder diameter and RR243 concentration. As it can be noted in the figure, with the exception of data collected in the absence of RR243, generated photocurrent intensity decreases according to an exponential trend, depending both on the optical path, which coincides with cylinder radius, and the optical properties of the solution, which depend on RR243 concentration. Therefore, as expected, TiO_2 photoactivation is disadvantaged by low solution transmittance, being reduced the radiation energy transfer to the photocatalytic surface; as a consequence, the reduction of the irradiation distance is beneficial in such conditions. As proved in our previous work [39], TiO_2 photoactivation can be effectively described by a relation similar to the Beer-Lambert law, which describes the transmission of radiation through a non-scattering liquid medium, depending on both the radiation optical path and the optical properties of the solution [40]. Therefore, the following relation can be written for generated photocurrent density (PCD):

$$PCD_x = PCD_0 e^{-\delta x} \qquad \text{(e7.1)}$$

where:

PCD_x ($\mu A\ cm^{-2}$) = generated photocurrent density at x [cm] distance from UV lamp,
PCD_0 ($\mu A\ cm^{-2}$) = generated photocurrent density at null distance from UV lamp,
δ (cm^{-1}) = decay coefficient for generated photocurrent density.

The proposed model defines the generated photocurrent density at a given distance from UV lamp as a fraction of the maximum generated photocurrent density (PCD_0), which corresponds to null distance between photocatalyst and UV lamp. The decrease in generated photocurrent is mathematically described by a dimensionless factor ranging between 0 and 1, which depends on the radiation optical path (x) and the photocurrent decay coefficient (δ). The decay coefficient δ is a function of the optical properties of the solution, particularly it depends on RR243 concentration, according to the following relation:

$$\delta = \delta_0 e^{\gamma C} \qquad \text{(e7.2)}$$

where:

δ_0 (cm^{-1}) = decay coefficient for generated photocurrent density at null RR243 concentration,
γ ($L\ mg^{-1}$) = decay coefficient for generated photocurrent density at given RR243 concentration,
C ($mg\ L^{-1}$) = RR243 concentration.

The values of model parameters, δ_0 and γ, were estimated in [39] and here applied:

$$\delta = 0.2358 e^{0.075\mathbf{C}} \qquad (R^2=0.997)$$

The relation for describing generated photocurrent intensity (PC) by TiO_2 cylindrical samples can be obtained combining equations e7.1 and e7.2, and multiplying by the cylindrical surface area of the photocatalyst sample (S):

$$PCI_x = PCD_0 e^{-\delta_0 e^{\gamma C} x} S \tag{e7.3}$$

The only unknown parameter was PCD_0, which was estimated from the experimental data of generated photocurrent intensity by least square method, obtaining a value of 128.5 mA (R^2>0.968), and by dividing this outcome for cylindrical surface area of the photocatalyst sample.

The prediction curves obtained by e7.3 are shown in figure 7.4: the good agreement between experimental and predicted data confirms that the model is effective in describing photoactivation of cylindrical TiO_2 samples when irradiated from inside. It is interesting to note the not-intuitive data trend in the absence of RR243 (solution transmittance equal to 100%). In this case, the increase of superficial area with the radius prevails over the decrease of generated photocurrent due to the optical path increase. Thus the irradiation distance does not determine a negative effect on TiO_2 photoactivation, rather the opposite, when optical properties are optimal.

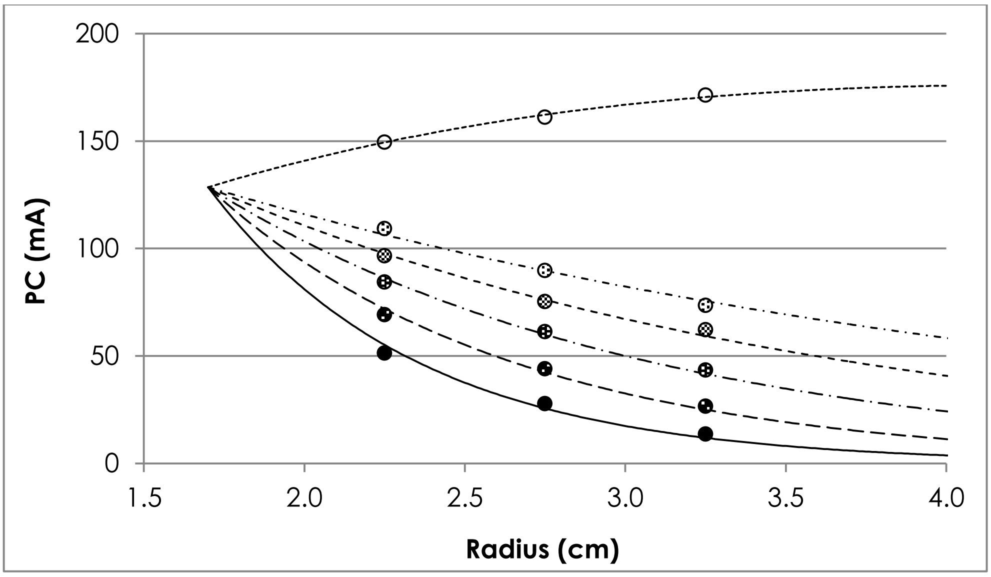

Figure 7.4 Generated photocurrent intensity (PC) vs. radius as a function of RR243 concentration. Experimental data (dots) are sorted by color, being the chromatic order related to the increase in RR243 concentration from 0 to 25 mg L^{-1} (step 5 mg L^{-1}). Identically, simulated data (lines) are sorted so as the higher the RR243 concentration and the more continuous the line referred to it.

As for the external irradiation of a cylindrical TiO_2 sample by a UV lamp, experimental data are shown in figure 7.5 for some of the tested RR243 concentrations. They were processed using equation e7.3, and the best fitting curves are shown in figure 7.5 too. All experimental and simulated data are reported in Supporting Information (SI7.4). As in the case of irradiation from inside, the model successfully describes TiO_2 photoactivation, displaying coefficients of determination (R^2) higher than 0.972 under any operating condition. Having defined the solution transmittance (dye concentration) and the irradiation distance (distance of the lamp from the axis of the photocatalyst), the generated photocurrent depends on the photocatalyst diameter, being higher for the larger cylinder. This is associated to a variation in the photocatalyst irradiated surface, as a function of the width of the irradiation cone, but it has to be mainly ascribed to a different extent of energy delivered to the photocatalyst surface, as a function of the radiation incident angles. As a consequence, when the photocatalyst is irradiated from outside, three values for PC_0 and for δ_0 were estimated, a pair for each photocatalyst radius: 34.9, 36.9 and 39.8 mA for PC_0 and 0.148, 0.159 and 0.178 for δ_0, respectively for cylinders having radius 4.5, 5.5 and 6.5 cm. Both PC_0 and δ_0 showed a linear trend against the cylinder radius (R) in the studied range, as:

$$PC_0 = 5.01R + 31.91 \qquad (R^2 = 0.99) \tag{e7.4}$$

$$\delta_0 = 0.03R + 0.13 \qquad (R^2 = 0.98) \tag{e7.5}$$

The influence of RR243 concentration on generated photocurrent decay, expressed by coefficient γ, was found invariant irrespectively of the cylinder radius.

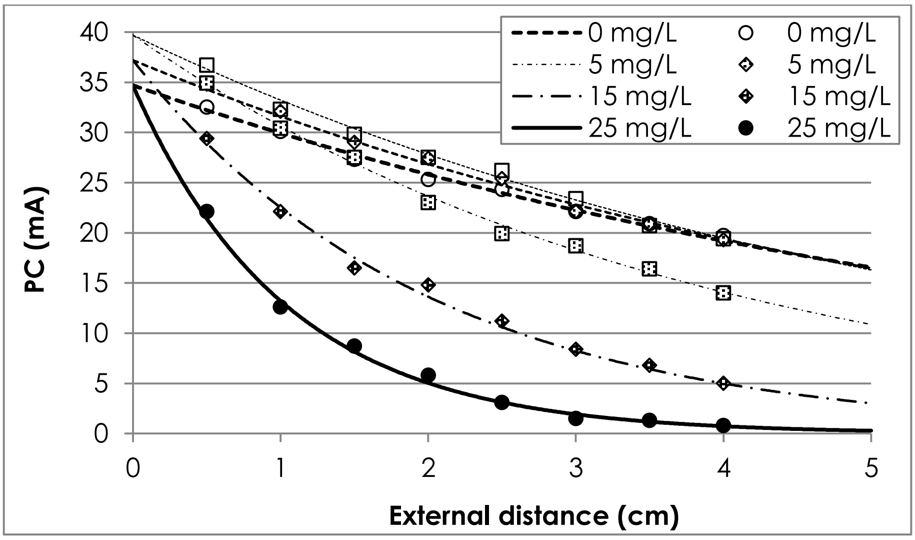

Figure 7.5 Generated photocurrent intensity (PC) vs. external irradiation distance as a function of cylinder radius and RR243 concentration. Experimental data (dots) are sorted by color in relation to RR243 concentration, as specified in the legend, and by shape in relation to the cylinder radius: 4.5 cm, circle - 5.5 cm, diamond, 6.5 cm - square. Simulated data (lines) are sorted by the type of hatch in relation to RR243 concentration, as specified in the legend, and by line thickness in relation to cylinder radius, having finer line at increasing cylinder radius.

7.3.2 Modelling validation of photoactivation in configurations with multiple lamps and photocatalysts

In order to validate the photocurrent model, a cylindrical TiO_2 sample internally and externally irradiated has been assumed as base unit to design more complex geometries, but modular. Since equation e7.3 can be used to predict TiO_2 photoactivation in such base unit, the total generated photocurrent intensity (PC_{TOT}) in a photocatalytic reactor having any geometry based on that base unit, can be modelled as:

$$PC_{TOT} = \sum_k \left(PC_{k,i} + PC_{k,e}\right) = \sum_k \left(DPC_{0,i} e^{-\delta_i R_k S} + DPC_{0,e} e^{-\delta_e d_{e,k} S}\right) \qquad \text{(e7.6)}$$

This equation states that the total generated photocurrent intensity is the sum of the photocurrent intensity generated by every cylindrical TiO_2 sample in the reactor, when irradiated by UV lamps from inside and outside.

To validate the proposed method, TiO_2 photoactivation was monitored in configurations from #1 to #7, equipped with multiple UV lamps and TiO_2 cylindrical samples. Experimental measures of generated photocurrent intensity were compared to simulated values using equation e7.6 adopting the previously estimated parameters. Results for two RR243 concentrations (0, 25 mg L^{-1}) are summarised in table 7.1, in which the percentage error of predictions is reported. This method is effective in predicting TiO_2 photoactivation, having an error lower than 5% for any configuration.

Table 7.1 Experimental (PC_{EXP}) and simulated (PC_{SIM}) total generated photocurrent intensity in photocatalytic reactor for various lamp/catalyst configurations and RR243 concentrations (0, 25 mg L^{-1}). The error in prediction is given (Δ). Reactor electrical energy consumption (P) and PC/P index are reported for each condition as well as the reaction constants for first-order (k_1) and Langmuir-Hinshelwood (k_{LH}) models in 25 mg L^{-1} RR243 solution decolorization.

Configuration	[RR243] (mg L^{-1})	PC_{EXP} (mA)	PC_{SIM} (mA)	Δ	P (W)	PC/P (mA W^{-1})	k_1		k_{LH}	
							(s^{-1})	R^2	(mg L^{-1} min^{-1})	R^2
#1	0	153.8	149.0	3.2%	30	4.967	0.0041	0.98	0.279	0.87
	25	76.2	73.0	4.1%		2.433				
#2	0	226.5	220.4	2.8%	120	1.837	0.0063	0.98	0.259	0.90
	25	84.1	82.3	2.1%		0.686				
#3	0	255.6	244.2	4.7%	150	1.628	0.0096	0.98	0.321	0.95
	25	83.7	85.4	2.8%		0.569				
#4	0	430.2	447.1	3.8%	90	4.968	0.0140	0.99	0.576	0.93
	25	229.8	219.0	4.6%		2.433				
#5	0	500.9	518.4	3.4%	120	4.320	0.0180	0.97	0.475	0.92
	25	218.7	228.4	4.6%		1.903				
#6	0	613.7	596.1	3.0%	120	4.968	0.0313	0.95	0.734	0.96
	25	297.0	292.1	1.7%		2.433				
#7	0	721.0	691.3	4.3%	150	4.609	0.0354	0.91	0.761	0.88
	25	315.5	304.5	3.4%		2.030				

The proposed methodology results to be simple and reproducible for determining TiO_2 photoactivation, providing a practical tool for reactor modelling. As a matter of fact, no complex measurements are required, as radiometric measures, possibly using an optical fibre terminal to quantify the irradiance values at photocatalyst surface, or diffuse reflectance measures to characterize the photocatalyst optical properties. Concerning reactor modelling, no heavy calculation have to be implemented, as advanced numerical or stochastic techniques require, such as computational fluid dynamics (CFD) codes or Monte Carlo method, which are essential for estimating radiation transfer across reactor volume.

A further validation of the effectiveness of generated photocurrent as proxy variable for the optimisation and scale-up of electrophotocatalysis processes has been performed by dye degradation tests. The decolorization of RR243 solution was monitored over process time in configurations from #1 to #7. Results for configurations #1, #3 and #7 are reported in figure 7.6. It can be noticed that the configurations #6 and #7 are the most efficient in decolorization, as expected on the basis of generated photocurrent values (see table 7.1). Experimental data were fitted by two kinetic models that have been reported in literature as effective in describing photocatalytic degradation, namely first-order and Langmuir-Hinshelwood (LH) models:

First order kinetics:
$$\frac{d[RR243]}{dt} = -k_1 \cdot [RR243] \qquad \text{(e7.7)}$$

LH kinetics:
$$\frac{d[RR243]}{dt} = -K_{LH} \cdot \frac{K_A[RR243]}{1 + K_A[RR243]} \qquad \text{(e7.8)}$$

where:

k_1 (s^{-1}) = first-order kinetic reaction constant,
k_{LH} (mg L^{-1} min^{-1}) = Langmuir-Hinshelwood reaction constant,
K_A (L mg^{-1}) = equilibrium constant of adsorption.

Unlike to first-order kinetics, LH kinetics takes into account the pollutant adsorption on TiO_2 surface, according to a Langmuir mechanism, that has been reported as a fundamental step in the degradation of many compounds [3]. The K_{LH} and K_A parameters are determined by a linearization procedure, as described in Supporting Information (SI7.5). Estimated model parameters for first-order and LH models as well as the coefficients of determination are reported in table 7.1. A good fitting of experimental data was obtained by means of both models, displaying R^2 values over 0.875. Anyway, as shown in figure 7.6, the first-order model is less effective at higher decolorization rates, when data seem to display a quasi-linear trend. Unlike first-order model, LH model is effective in describing such composite trends, since it takes into account at the same time two distinct behaviors depending on the pollutant concentration. In detail, when pollutant concentration is high (K_A [RR243]>>1), the second factor in the right term of equation e7.8 becomes negligible, so that the LH model is comparable to a zero-order model.

The dependence of reaction constants (k_1, k_{LH}) from generated photocurrent intensity (PC_{SIM}) at initial time was evaluated for the various configurations. A linear relation between reaction constants and generated photocurrent intensity was observed for both first-order and LH models, respectively resulting in:

$$k_1 = 0.00011 \cdot PC - 0.00370 \qquad (R^2=0.89)$$

$$k_{LH} = 0.00202 \cdot PC - 0.11516 \qquad (R^2=0.95)$$

Thus, generated photocurrent is confirmed to be a good proxy variable for electrophotocatalysis processes, effectively describing RR243 decolorization.

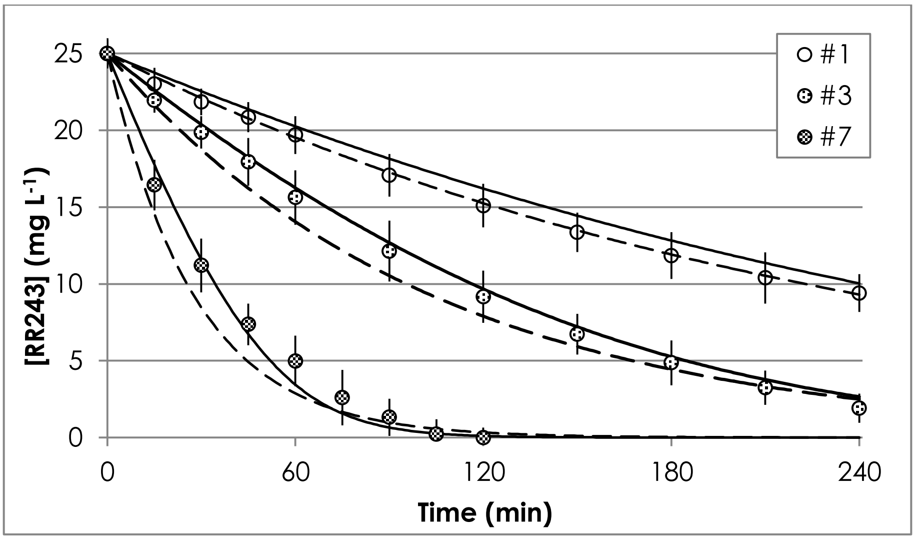

Figure 7.6 RR243 concentration vs. time in decolorization tests in various reactor configurations (#1, #3, #7): experimental (dots) and simulated (lines) data for first-order (dashed line) and LH (solid line) model.

The electrophotocatalytic process determined also a strong decrease in 254 nm absorbance over time, suggesting that not only decolorization occurs but also a degradation of RR243 molecules. The significant increase in solution transmittance (experimental data referred to configurations #1, #3 and #7 are reported in Supporting Information, SI7.6) implies a modification of the reactor operating conditions, which is expected to enhance the photocatalytic degradation rate during the process time. Such dynamic behaviour is reflected in a progressive increase in generated photocurrent over time, as already observed in our past work [39]. In fact, in that case the degradation rate was not well described by the LH model, which was modified for accounting the continuous variation of operating conditions over time. Anyway, in the present case, only a slight increase was observed in generated photocurrent throughout process time in the various configurations, much smaller than the values predicted by equation e7.6 on the basis of the increase in solution transmittance. Experimental and simulated values of generated photocurrent over time are reported in Supporting Information (SI7.6) for configurations #1, #3 and #7. Coherently with the quite stable generated photocurrent, the unmodified LH model, as reported in equation e7.8, reveals effective in describing RR243 decolorization.

As proved in decolorization tests in various configurations with multiple elements, generated photocurrent can be successfully adopted as a proxy variable for supporting reactor optimization.

It should be mentioned that TiO_2 (electro)photocatalysis is an energy-intensive process, and its economic sustainability is strictly related to its efficiency in order to limit operating costs. Among the various costs, electricity for UV lamp supply has been highlighted as the most relevant in case of TiO_2 (electro)photocatalysis and UV-based advanced oxidation technologies [41]. As an example, in the present work the energy consumption of each UV lamp was 30 W, while the consumption associated to the anodic polarization of each cylindrical TiO_2 sample was about 0.5-1 W, calculated as the product of cell potential and current intensity. Thus, the energy consumption for anodic polarization can be usually neglected.

Consequently, the design and optimization of a TiO_2 (electro)photocatalysis reactor have to take into account not only the maximization of TiO_2 photoactivation, but also the minimization of the overall energy consumption, which display diverging trends. Hence, generated photocurrent is not sufficient as proxy variable, accounting only for TiO_2 photoactivation, and has to be integrated with another proxy variable accounting for energy consumption. As a matter of fact, a new proxy variable (PC/P) was introduced accounting for both these two conflicting aspects. It consists in the ratio between generated photocurrent and UV lamp power, providing the indication of the electrical watt required to obtain a selected extent of TiO_2 photoactivation. The maximization of this comprehensive proxy variable provides an estimation of system efficiency, irrespectively of the number of UV lamps involved.

In table 7.1 the energy consumption and PC/P for every configuration are reported. In case of low transmittance, configurations #1, #4 and #6 are the most energetically efficient, although the maximum values of energy consumption and total generated photocurrent pertain to configuration #7. Differently, when transmittance is very high, only configurations #2 and #3 are energetically inefficient. In conclusion, the defined proxy variables help in the assessment of the energetic efficiency of the various configurations, to be used as modular base units for a reactor scale-up, but it is fundamental to take into account also the liquid transmittance in the scale-up process.

7.3.3 Scale-up of a reactor based on modular units

The proposed reactor optimization procedure based on PC/P values has been applied to compare three configurations constituting the base units for modular reactors, respectively triangular, quadrangular and hexagonal. In detail, such configurations are composed by respectively three, four or six lamps, each surrounded by a photocatalytic cylinder, equidistant from a central lamp, which externally irradiates all the photocatalysts. Specifically, the schemes of triangular and quadrangular units are the same used in configurations #5 and #7, respectively.

In order to define the optimal geometry of the base units, a parametric study was performed to calculate the PC/P values for each configuration as a function of solution transmittance and of geometrical parameters, namely the radius of cylindrical TiO_2 samples and the external irradiation distance, which define the overall size of the three base units. The relation between RR243 concentration and solution transmittance was determined, as reported in paragraph 7.2.1, so that the previous modeling equations were transformed in order to describe TiO_2 photoactivation as a function of solution transmittance at irradiation wavelength (254 nm) and, thus, to provide a generalizable methodology for rector optimization depending on the liquid optical properties. Independently on the shape of the base units, a structural constraint was imposed to reactor design, consisting in a 0.5 cm minimum distance among each UV lamp and photocatalyst, due to (i) the presence of ascending bubbles in the reactor, and (ii) the need to avoid electrical contacts between polarized photocatalysts. Another limitation was due to the geometric feasibility of the reactor configuration, since no every combination of cylinder radius and external irradiation distance are admissible.

Optimization results are reported in figure 7.7 and table 7.2, where the maximum PC/P values as a function of solution transmittance are reported for the three studied base unit configurations. In table 7.2, the base unit configurations in which multiple-lamp setups overcome single-lamp setup are highlighted in bold.

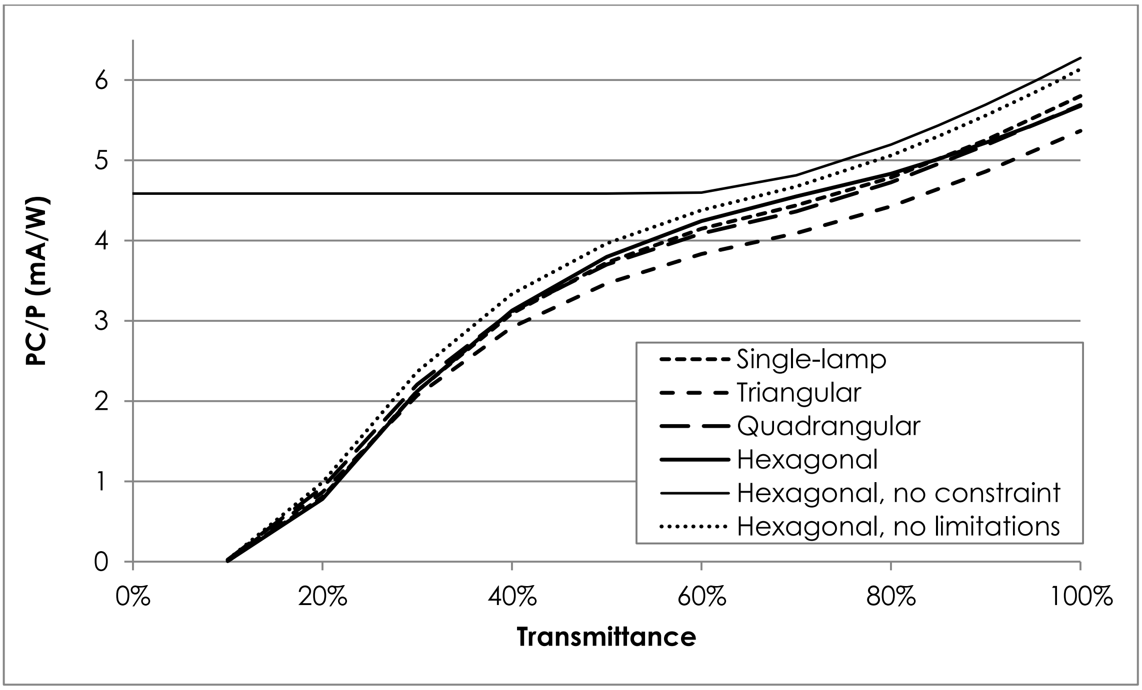

Figure 7.7 Maximum PC/P values as a function of solution transmittance displayed by the optimized base unit configurations. In case of hexagonal configuration two more cases are reported:
(i) no constraint is applied on the minimum distance between cylindrical TiO_2 sample and UV lamp,
(ii) geometric limitations are not considered.

Table 7.2 Maximum PC/P (mA W^{-1}) values as a function of transmittance displayed by the optimized base unit configurations. Values in bold refer to situations in which multiple-lamp setups are more efficient than single-lamp setup.

Transmittance	10%	20%	30%	40%	50%	60%	70%	80%	90%	100%
Single-lamp	0.010	0.808	2.128	3.094	3.727	4.148	4.439	4.784	5.249	5.802
Triangular	**0.024**	**0.867**	2.071	2.92	3.468	3.831	4.09	4.428	4.862	5.368
Quadrangular	**0.025**	**0.924**	**2.209**	**3.115**	3.702	4.086	4.363	4.723	5.186	5.689
Hexagonal	0.009	0.783	2.124	**3.129**	**3.796**	**4.242**	**4.551**	**4.833**	5.217	5.678

In figure 7.8 the geometric parameters of the optimized base unit configurations are shown as a function of solution transmittance. As an example, for the triangular base unit configuration and three transmittance values (100, 60 and 10%), in Supporting Information (SI7.7) PC/P values are plotted as a function of geometrical parameters.

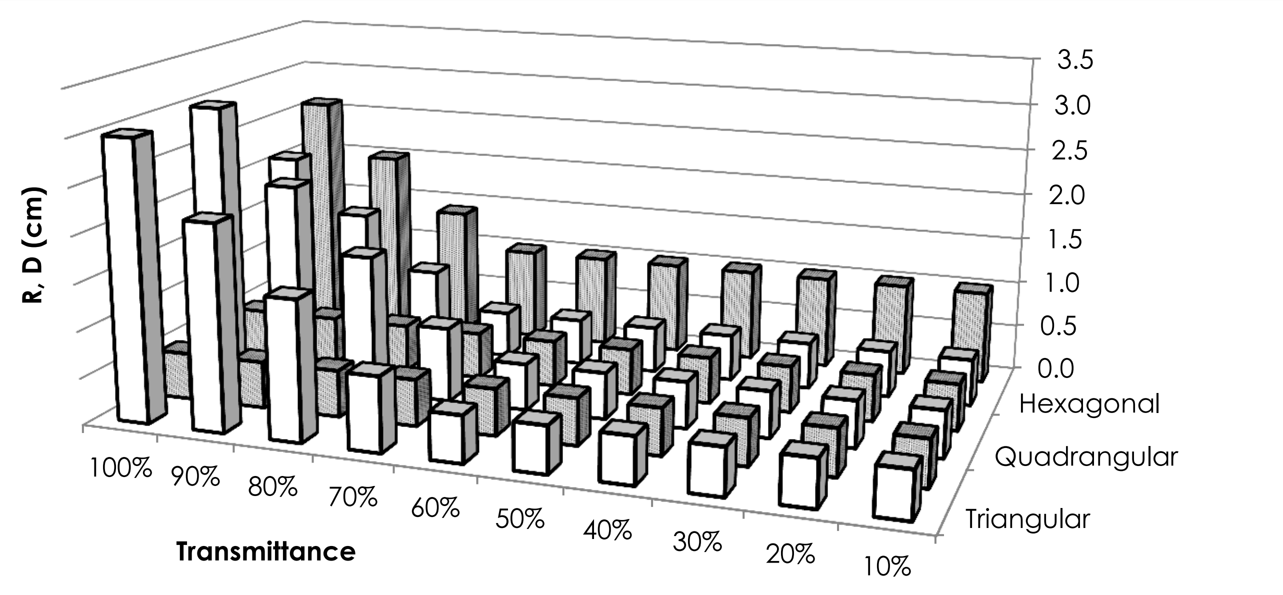

Figure 7.8 Optimal geometric parameters, namely cylinder radius R (white bars) and external irradiation distance D (dotted grey bars), for base unit configurations as a function of solution transmittance.

In general, optimal PC/P decays non-linearly as a function of transmittance, specifically the decreasing trend can be approximated to two curves having different slopes above and below about 60% transmittance. As for internal irradiation, the optimized configuration is obtained by increasing cylinder radius at high transmittance, where the positive effect of increasing photocatalytic surface predominates over the decrease in generated photocurrent due to the increase in optical path. Otherwise, when transmittance is lower than 60%, the optimum cylinder radius moves down, as shown in figure 7.8. For instance, in case of triangular and quadrangular base units, the optimum cylinder radius decreases with transmittance from 3 cm to 0.5 cm, i.e. the minimum admissible radius. However, the optimal condition below 60% transmittance would be to bring the TiO_2 photocatalyst as close as possible to UV lamp, potentially up to contact. As an example, the case in which the structural constraint is removed is shown for hexagonal configuration in figure 7.7: PC/P values stabilize on the value corresponding to the photocurrent ideally generated by the TiO_2 catalyst placed in contact with the UV lamp surface at transmittance lower than 60%. On the other hand, concerning external irradiation, the best configurations are expected when the distance between TiO_2 catalysts and central UV lamp is as short as possible.

PC/P maximum value generally increases with the number of cylindrical TiO_2 samples that are externally irradiated, as shown in figure 7.7 and table 7.2, until reaching values comparable to the single-lamp setup in case of four or more UV lamps around the central one. Unfortunately, geometric limitations, rising from positioning 6 catalysts around one central UV lamp, bound the efficiency of hexagonal base unit configuration, which would be by far the preferable. As a comparison, PC/P value over transmittance neglecting geometric limitations is reported in figure 7.7. Therefore, triangular and quadrangular base unit configurations are preferable with respect to a single-lamp setup at low transmittances (<40%), while a hexagonal base unit configuration displays better performance at medium-high transmittances (40-80%). A single-lamp is optimal for transmittances over 80%. As a matter of fact, the optimization of an electrophotocatalytic reactor is a dynamic problem, being the reactor design strongly affected by operating conditions, especially by liquid transmittance, as already highlighted by experimental data.

Then, the modular reactor scale-up was assessed by assembling a variable number of base units. In particular, the combination of several base units was simulated for evaluating the influence of changing the ratio between the number of UV lamps irradiating cylindrical TiO_2 photocatalysts from the inside and the outside. In fact, in a modular reactor a number of elements (photocatalysts and lamps) are shared among different base units located side by side, as shown in figure 7.9. The total number of base units and, thus, the total number of elements are conditioned by the geometry of every base unit, while composite configurations are designed so as to achieve structures that could be housed in a circular or rectangular section vessel. The main characteristics of the studied configuration are reported in table 7.3. Modeling results, which are reported in Supporting Information (SI7.8), indicate that a change in maximum PC/P values occur when the reactor is scaled-up. In detail, since the increase in the number of base units results in a reduction of the ratio between the number of UV lamps irradiating cylindrical TiO_2 samples from the inside and the outside, a positive effect is obtained when the irradiation from the outside is enhanced, such as for low transmittance values. Therefore, in such conditions the modular reactor generates a relevant quote of photocurrent from external irradiation of cylindrical TiO_2 catalysts.

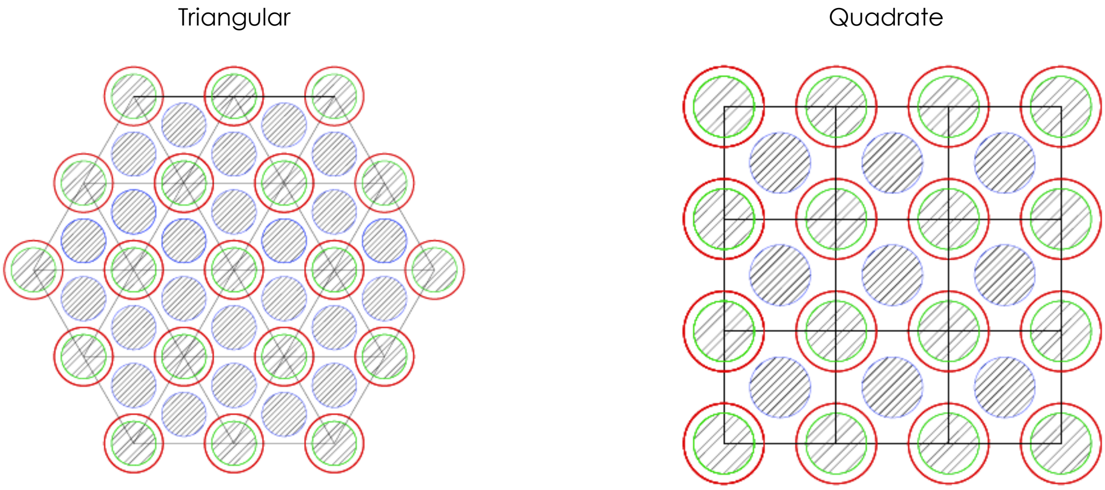

Figure 7.9 Modular configurations for reactor scale-up. Filling hatch is different for internally and externally irradiating UV lamps, loose in the former case and dense in the latter.

Table 7.3 Modular configurations for reactor scale-up.

Configuration	# modular units	# Internal lamps (#I)	# external lamps (#E)	# total lamps	Ratio (#I/#E)
Triangular	1	3	1	4	3.00
	2	4	2	6	2.00
	6	7	6	13	1.17
	24	19	24	43	0.79
	54	37	54	91	0.69
Quadrate	1	1	4	5	4.00
	2	4	9	13	2.25
	3	9	16	25	1.78
	4	16	25	41	1.56
	5	25	36	61	1.44
	6	36	49	85	1.36
Hexagonal (regular)	1	6	1	7	6.00
	7	30	7	37	4.29
	19	72	19	91	3.79
Hexagonal (honeycomb)	1	6	1	7	6.00
	7	24	7	31	3.43
	19	54	19	73	2.84

7.4 CONCLUSIONS

An optimal design methodology for an electrophotocatalytic reactor using self-ordered nanotubular TiO_2 has been proposed based on two proxy variables to monitor and assess the electrophotocatalysis process. First, generated photocurrent reveals a reliable and easy-to-monitor variable to describe the extent of TiO_2 photoactivation in complex reactors including multiple lamps and photocatalysts. Then, to take into account also the energy consumption, which can be an important constrain for electrophotocatalysis deployment at full scale, another proxy variable was introduced, normalizing generated photocurrent intensity with respect to overall power consumption by UV lamps. Based on these two proxy variables, capable to match the conflicting trend typical of TiO_2 photoactivation (to be maximized) and energy consumption (to be minimized), guidelines for reactor design optimization and scale-up were indicated, based on the assembling of modular base units. It should be emphasised that such guidelines are a function of solution transmittance, since the optimization reveals a dynamic problem, being the reactor design strongly affected by operating conditions, especially by liquid transmittance.

7.5 REFERENCES

[1] C. Turchi, Photocatalytic degradation of organic water contaminants: mechanisms involving hydroxyl radical attack, J. Catal. 122 (1990) 178–192.

[2] J. Herrmann, Heterogeneous photocatalysis: fundamentals and applications to the removal of various types of aqueous pollutants, Catal. Today. 53 (1999) 115–129.

[3] S. Malato, P. Fernández-Ibáñez, M.I.I. Maldonado, J. Blanco, W. Gernjak, Decontamination and disinfection of water by solar photocatalysis: recent overview and trends, Catal. Today. 147 (2009) 1–59.

[4] H. Choi, S.R. Al-Abed, D.D. Dionysiou, E. Stathatos, P. Lianos, TiO_2-based advanced oxidation nanotechnologies for water purification and reuse, Sustain. Sci. Eng. 2 (2010) 229–254.

[5] H. De Lasa, B. Serrano, M. Salaices, Photocatalytic reaction engineering, Springer, 2005.

[6] M.I. Litter, Advances in Chemical Engineering - Photocatalytic Technologies, Elsevier, 2009.

[7] A. Fujishima, X. Zhang, D. Tryk, TiO_2 photocatalysis and related surface phenomena, Surf. Sci. Rep. 63 (2008) 515–582.

[8] P. Pichat, Photocatalysis and water purification: from fundamentals to recent applications, Wiley-VCH, 2013.

[9] T.E. Doll, F.H. Frimmel, Cross-flow microfiltration with periodical back-washing for photocatalytic degradation of pharmaceutical and diagnostic residues-evaluation of the long-term stability of the photocatalytic activity of TiO_2, Water Res. 39 (2005) 847–54.

[10] P. Fernández-Ibáñez, J. Blanco, S. Malato, F.J. d. Las Nieves, Application of the colloidal stability of TiO_2 particles for recovery and reuse in solar photocatalysis, Water Res. 37 (2003) 3180–3188.

[11] R.L. Pozzo, M.A. Baltanás, A.E. Cassano, Supported titanium oxide as photocatalyst in water decontamination: state of the art, Catal. Today. 39 (1997) 219–231.

[12] T. Ochiai, A. Fujishima, Photoelectrochemical properties of TiO_2 photocatalyst and its applications for environmental purification, J. Photochem. Photobiol. C Photochem. Rev. 13 (2012) 247–262.

[13] H. Hu, W.J. Xiao, J. Yuan, M.X. Chen, Shang Guan W.F., Preparations of TiO_2 film coated on foam nickel substrate by sol-gel processes and its photocatalytic activity for degradation of acetaldehyde, J. Environ. Sci. 19 (2007) 80–85.

[14] Y. Zhang, J. Wan, Y. Ke, A novel approach of preparing TiO_2 films at low temperature and its application in photocatalytic degradation of methyl orange, J. Hazard. Mater. 177 (2010) 750–4.

[15] K. Nakata, T. Kagawa, M. Sakai, S. Liu, T. Ochiai, H. Sakai, et al., Preparation and photocatalytic activity of robust titania monoliths for water remediation, ACS Appl. Mater. Interfaces. 5 (2013) 500–4.

[16] Y. Chen, Y. Li, A. Zhu, Y. Huang, Z. Liu, K. Yan, Degradation of aqueous Rhodamine B by plasma generated along the water surface and its enhancement using nanocrystalline Fe-, Mn-, and Ce-doped TiO_2 films., Environ. Sci. Pollut. Res. Int. 21 (2014) 9948–58.

[17] G.E. Imoberdorf, A.E. Cassano, H.A. Irazoqui, O.M. Alfano, Optimal design and modeling of annular photocatalytic wall reactors, Catal. Today. 129 (2007) 118–126.

[18] J.M.G. Hernandez, B.S. Rosales, H. de Lasa, The photochemical thermodynamic efficiency factor (PTEF) in photocatalytic reactors for air treatment, Chem. Eng. J. 165 (2010) 891–901.

[19] C. Passalía, O.M. Alfano, R.J. Brandi, Optimal design of a corrugated wall photocatalytic reactor Using efficiencies in series and computational fluid dynamics (CFD) Modeling, Ind. Eng. Chem. Res. Artic. 52 (2013) 6916–6922.

[20] G.K. Mor, O.K. Varghese, M. Paulose, K. Shankar, C.A. Grimes, A review on highly ordered, vertically oriented TiO_2 nanotube arrays: fabrication, material properties, and solar energy applications, Sol. Energy Mater. Sol. Cells. 90 (2006) 2011–2075.

[21] J.M. Macak, H. Tsuchiya, A. Ghicov, K. Yasuda, R. Hahn, S. Bauer, et al., TiO_2 nanotubes: self-organized electrochemical formation, properties and applications, Curr. Opin. Solid State Mater. Sci. 11 (2007) 3–18.

[22] M. Zlamal, J.M. Macak, P. Schmuki, J. Krýsa, Electrochemically assisted photocatalysis on self-organized TiO_2 nanotubes, Electrochem. Commun. 9 (2007) 2822–2826.

[23] Y. Zhang, X. Xiong, Y. Han, X. Zhang, F. Shen, S. Deng, et al., Photoelectrocatalytic degradation of recalcitrant organic pollutants using TiO_2 film electrodes: an overview, Chemosphere. 88 (2012) 145–154.

[24] M.F. Brugnera, K. Rajeshwar, J.C. Cardoso, M.V.B. Zanoni, Bisphenol A removal from wastewater using self-organized TiO_2 nanotubular array electrodes, Chemosphere. 78 (2010) 569–575.

[25] X. Quan, X. Ruan, H. Zhao, S. Chen, Y. Zhao, Photoelectrocatalytic degradation of pentachlorophenol in aqueous solution using a TiO_2 nanotube film electrode., Environ. Pollut. 147 (2007) 409–414.

[26] Y.S. Sohn, Y.R. Smith, M. Misra, V. Subramanian, Electrochemically assisted photocatalytic degradation of methyl orange using anodized titanium dioxide nanotubes, Appl. Catal. B Environ. 84 (2008) 372–378.

[27] N. Wang, X. Li, Y. Wang, X. Quan, G. Chen, Evaluation of bias potential enhanced photocatalytic degradation of 4-chlorophenol with TiO_2 nanotube fabricated by anodic oxidation method, Chem. Eng. J. 146 (2009) 30–35.

[28] J.C. Cardoso, T.M. Lizier, M.V.B. Zanoni, Highly ordered TiO_2 nanotube arrays and photoelectrocatalytic oxidation of aromatic amine, Appl. Catal. B Environ. 99 (2010) 96–102.

[29] A.L.L. Zazueta, H. Destaillats, G. Li Puma, Radiation field modeling and optimization of a compact and modular multi-plate photocatalytic reactor (MPPR) for air/water purification by Monte Carlo method, Chem. Eng. J. 217 (2013) 475–485.

[30] M.A. Behnajady, M. Hajiahmadi, N. Modirshahla, Enhancement of removal rate of an organic pollutant in thepresence of immobilized TiO_2 nanoparticles with inorganic anions combination: optimization using Taguchi approach, Ind. Eng. Chem. Res. 51 (2012) 15324–15330.

[31] O.K. Varghese, C.A. Grimes, Appropriate strategies for determining the photoconversion efficiency of water photoelectrolysis cells: a review with examples using titania nanotube array photoanodes, Sol. Energy Mater. Sol. Cells. 92 (2008) 374–384.

[32] J.R. Jennings, A. Ghicov, L.M. Peter, P. Schmuki, A.B. Walker, Dye-sensitized solar cells based on oriented TiO_2 nanotube arrays: transport, trapping, and transfer of electrons, J. Am. Chem. Soc. 130 (2008) 13364–13372.

[33] M. Bestetti, S. Franz, M. Cuzzolin, P. Arosio, P.L. Cavallotti, Structure of nanotubular titanium oxide templates prepared by electrochemical anodization in H_2SO_4/HF solutions, Thin Solid Films. 515 (2007) 5253–5258.

[34] A. Turolla, M. Fumagalli, M. Bestetti, M. Antonelli, Electrophotocatalytic decolorization of an azo dye on TiO_2 self-organized nanotubes in a laboratory scale reactor, Desalination 285 (2012) 377–382.

[35] R. Jenkins, R. Snyder, Introduction to X-ray powder diffractometry, A Wiley-InterScience Publication, 2012.

[36] L.S.C. Eugene W. Rice, Rodger B. Baird, Andrew D. Eaton, Standard methods for the examination of water and wastewater, Am. Water Work. Assoc. Public Work. Assoc. Environ. Fed. (2012) 1469.

[37] O. Carp, Photoinduced reactivity of titanium dioxide, Prog. Solid State Chem. 32 (2004) 33–177.

[38] A.A. Donaldson, Z. Zhang, UV absorption by TiO_2 films in photocatalytic reactors: effect of fold curvature, AIChE J. 58 (2012) 1578–1587.

[39] A. Turolla, M. Bestetti, M. Antonelli, Electrophotochemical assessment for the optimization of heterogeneous electrophotocatalysis on TiO_2 self-organized nanotubes, In preparation.

[40] J.G. Calvert, J.N. Pitts, Photochemistry, John Wiley & Sons, Inc., New York, 1966.

[41] T.A. Egerton, P.A. Christensen, Photoelectrocatalysis processes, in: S. Parsons (Ed.), Adv. oxid. process. water wastewater treat., IWA Publishing, London, 2004, 167–184.

7.6 SUPPORING INFORMATION

S7.1 XRD spectra of nanotubular TiO_2

The XRD spectra of a sample before and after annealing is reported in figure SI7.1. The change in TiO_2 crystalline structure can be observed in terms of an increase of both anatase and rutile peaks after heat treatment.

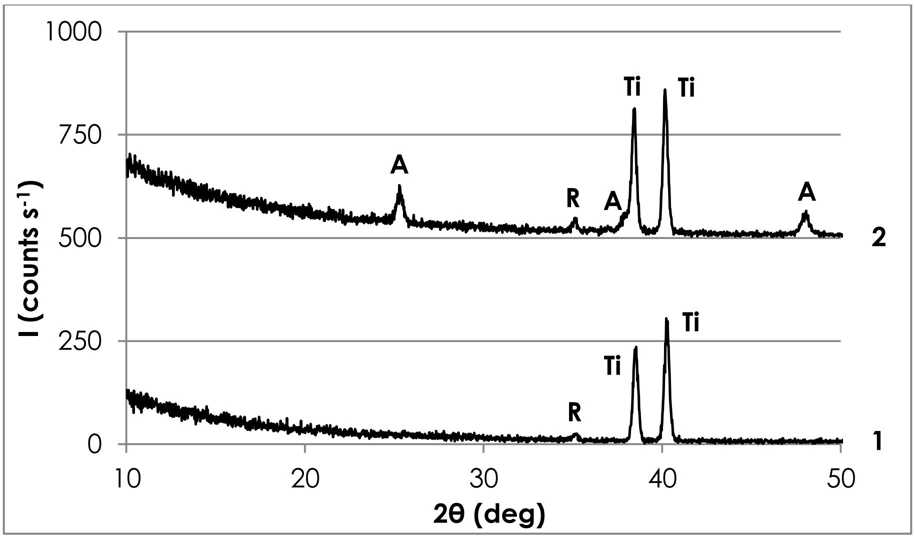

Figure SI7.1 XRD spectra of oxidized TiO_2 before (1) and after (2) annealing treatment. Crystalline peaks are marked: anatase (A), rutile (R), titanium (Ti).

SI7.2 TiO_2 photocatalyst surface calculation

Calculations are based on the assumption that all the Ti wires are identical, and that each mesh is characterized by an orthogonal texture. In the following the calculation procedure is reported for a cylindrical TiO_2 sample of 4.5 cm radius. The complex structure of the wire mesh was divided into a sequence of identical wires across vertical and horizontal direction, respectively having an approximate length (L) of 40 and 14.13 cm. These wires were considered as cylindrical structures, so that the surface of each wire (S_W) was estimated as:

$$S_W = 2\pi R_W L \tag{eSI7.1}$$

in which R_W is the wire radius, having a dimension of approximately 100 μm.

Subsequently, the surface of each wire, respectively 2.5 cm^2 and 0.9 cm^2 in vertical and horizontal direction, was multiplied by the number of wires constituting the mesh in the two directions (n_V, n_O), namely 224 and 556. Therefore, the overall surface of each cylindrical TiO_2 sample was 1,057 cm^2. The surface lost (S_L) due to the overlap of the wires in the texture has been evaluated according to:

$$S_L = 2(n_V n_O)(2R_W)^2 \tag{eSI7.2}$$

As a matter of fact, each overlap determines approximately the loss of a square surface having a side dimension equal to the wire section on each involved wire. Wires overlap as many times as the product of the number of wires that are present along the two dimensions in the wire mesh, giving an overall loss of surface area equal to about 100 cm^2, thus reducing the active surface to 958 cm^2. Finally, the specific surface was obtained as the ratio between the active surface and the apparent surface (1,130 cm^2) of the cylindrical TiO_2 sample, resulting in 0.8 cm^2 per apparent cm^2.

SI7.3 Molecular structure of Reactive Red 243 (RR243)

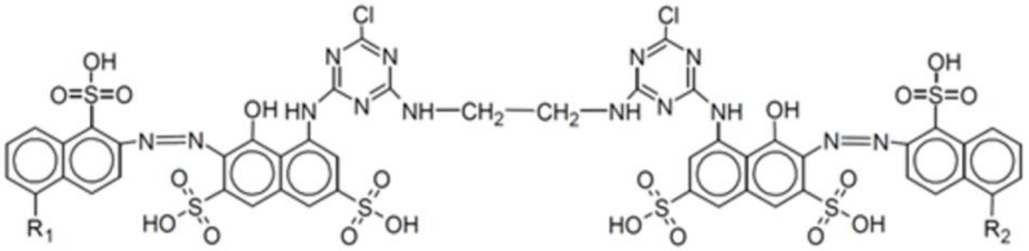

Figure SI7.2 Molecular structure of RR243. Three different molecular configurations are possible: (1) $R_1=R_2=SO_3H$ - (2) $R_1= SO_3H$, $R_2=H$ - (3) $R_1=R_2=H$.

SI7.4 External irradiation of cylindrical TiO_2 samples

(a)

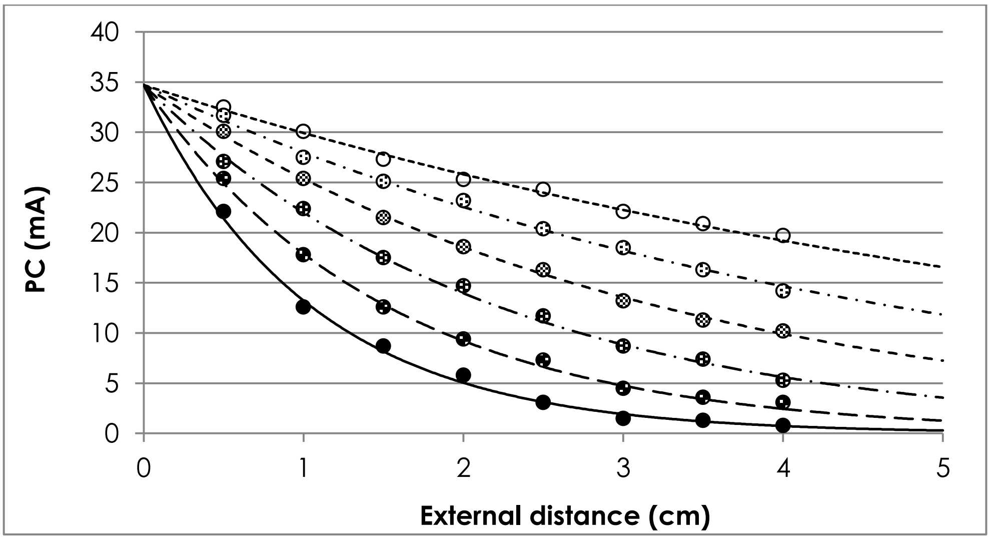

(b)

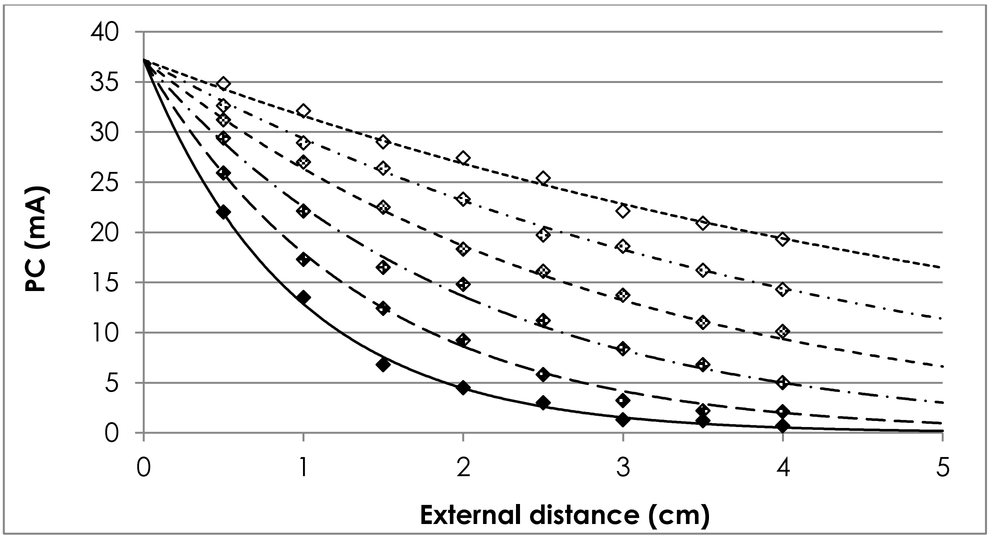

(c)

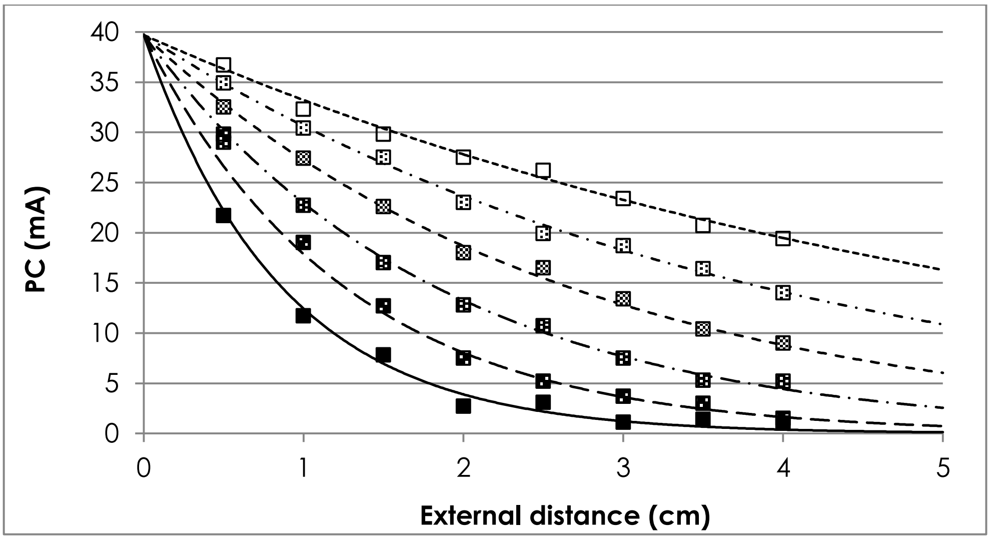

Figure SI7.3 Generated photocurrent (PC) vs. external distance as a function of RR243 concentration. Experimental data (dots) are sorted by color in relation to RR243 concentration, being the chromatic order related to the increase in RR243 concentration from 0 to 25 mg L^{-1} (step 5 mg L^{-1}). Simulated data (lines) are sorted by the type of hatch in relation to RR243 concentration, so as the higher the RR243 concentration and the more continuous the line referred to it from 0 to 25 mg L^{-1} (step 5 mg L^{-1}). Experimental and simulated data for various cylinder radius are reported in different images: (a) 4.5 cm, (b) 5.5 cm, (c) 6.5 cm.

SI7.5 Langmuir-Hinshelwood linearization procedure for K_A and K_{LH} constants estimation

Equation e7.8 in the manuscript can be expressed showing the linear relationship between the inverse of initial reaction rate (1/r) and the inverse of RR243 concentration (1/[RR243]), as:

$$\frac{1}{r} = \frac{1}{K_A K_{LH}} \frac{1}{[RR243]} + \frac{1}{K_{LH}} = m \frac{1}{[RR243]} + q \qquad \text{(eSI7.3)}$$

with:

$$K_{LH} = \frac{1}{q} \qquad K_A = \frac{q}{m}$$

The rate r is obtained from experimental data by calculating the decrease in RR243 concentration over a time interval. K_A and K_{LH} values were determined by plotting (1/r, 1/[RR243] and fitting these data with a linear relation, in which the slope (m) and the intercept (q) were estimated by the least squares method.

SI7.6 Generated photocurrent in electrophotocatalytic degradation tests

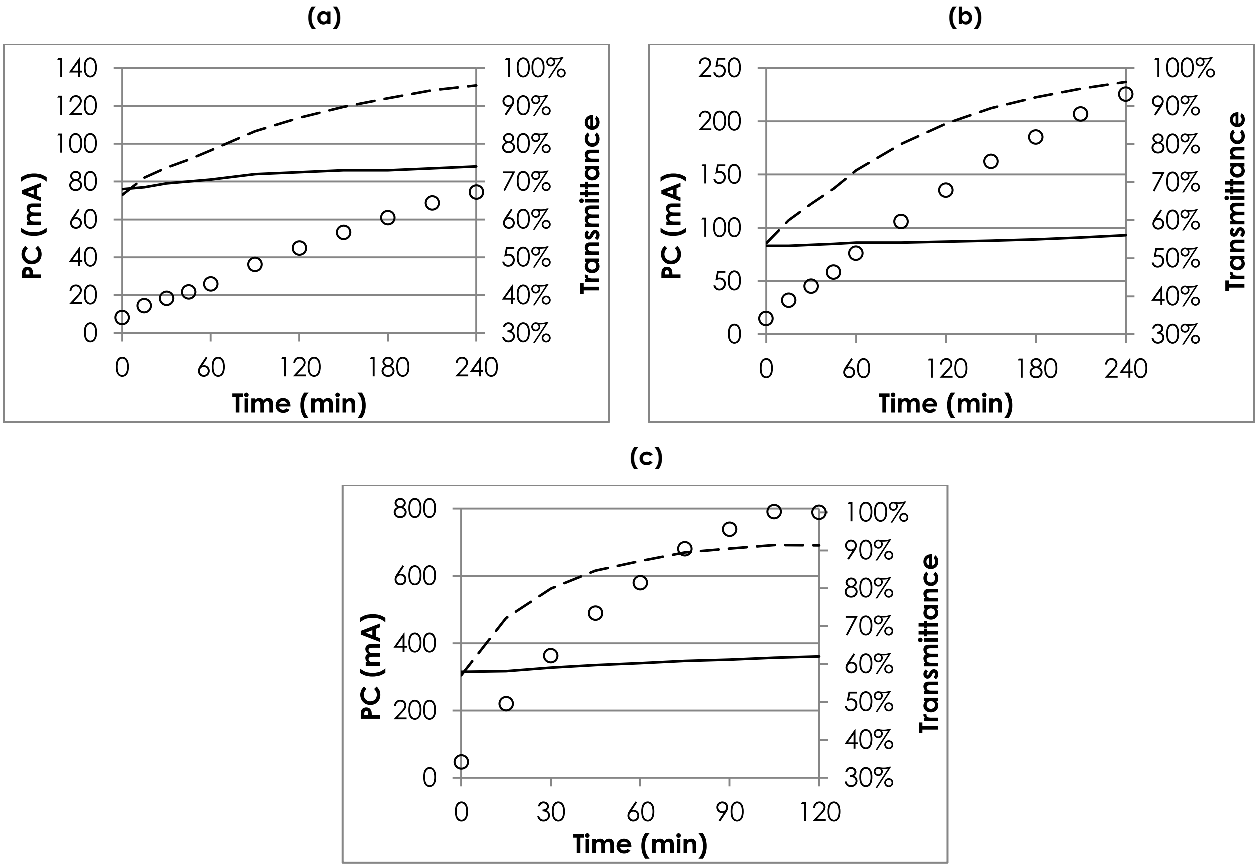

Figure SI7.4 Generated photocurrent (PC) vs. time in electrophotocatalytic degradation tests. Experimental (solid lines) and simulated (dashed lines) are shown for various reactor configurations: (a) #1, (b) #3, (c) #7. Solution transmittance at irradiation wavelength is reported (dots).

SI7.7 PC/P surfaces as a function of geometric characteristics

(a)

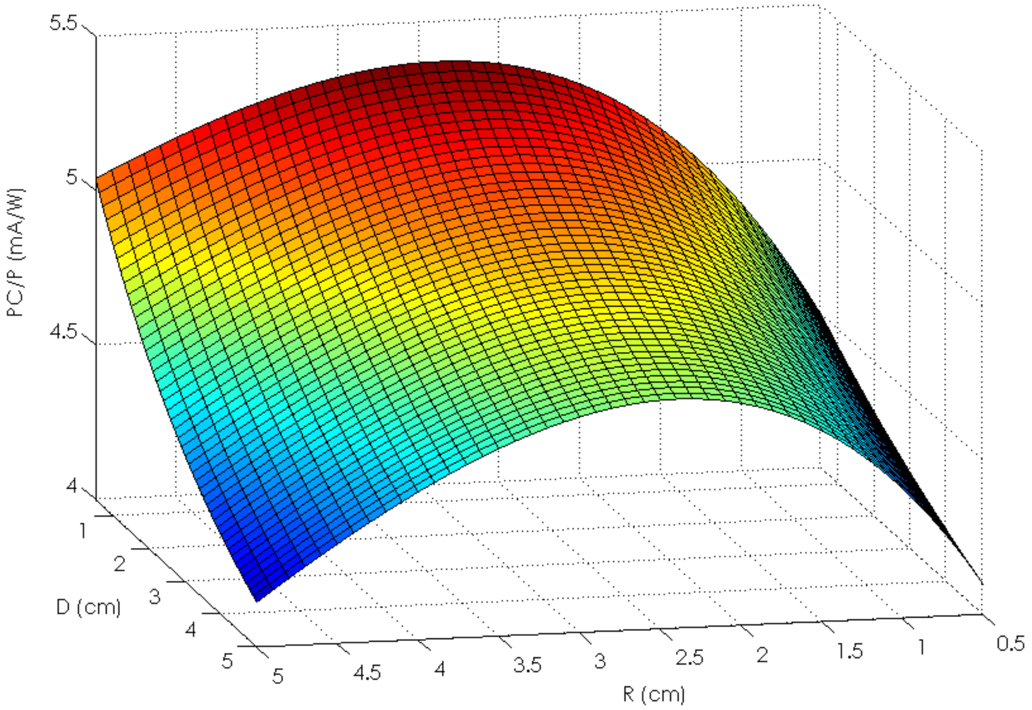

(b)

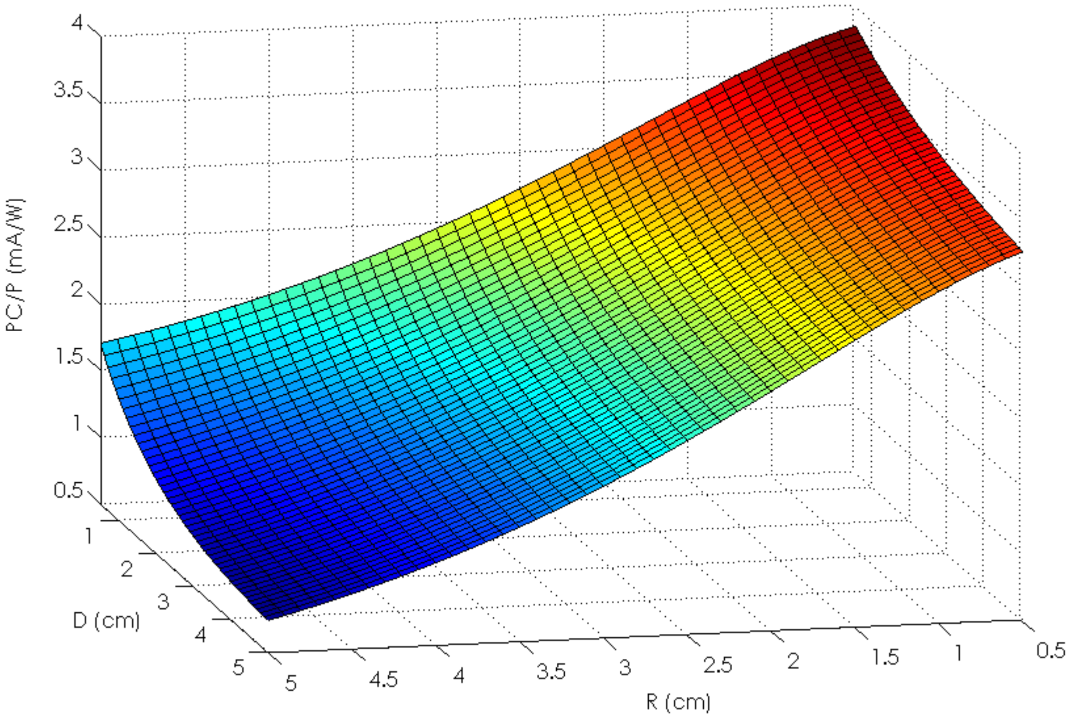

(c)

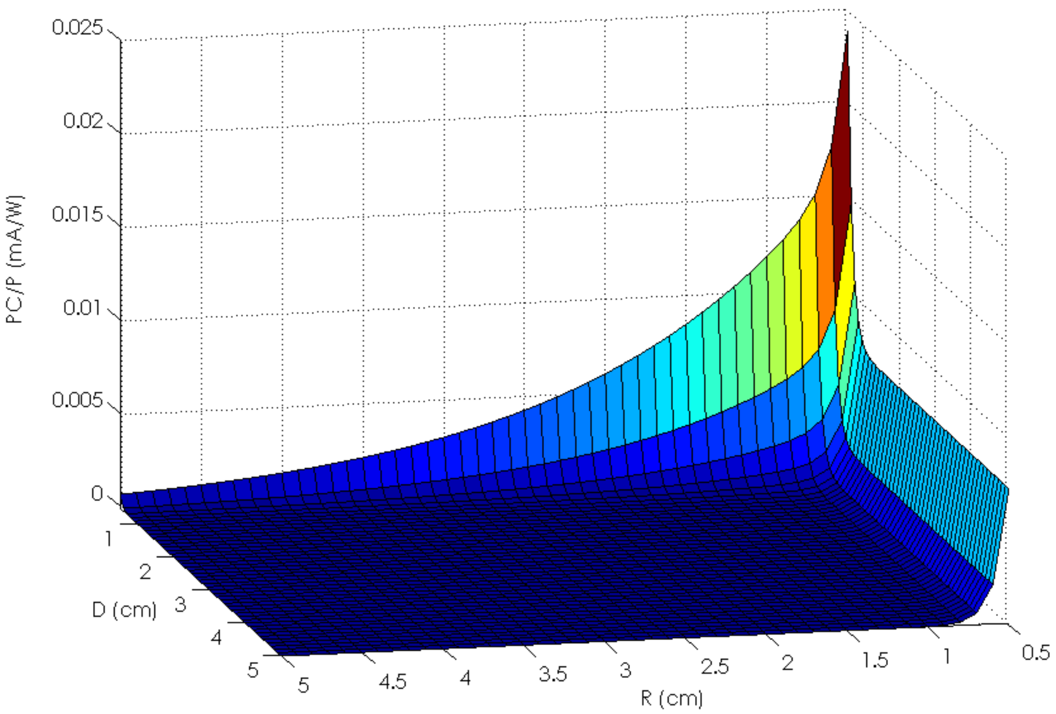

Figure SI7.5 PC/P values as a function of cylinder radius (R) and external irradiation distance (D) in triangular base unit configuration at three solution transmittance values: (a) 100%, (b) 60%, (c) 10%.

SI7.8 Electrophotocatalytic reactor scale-up

(a)

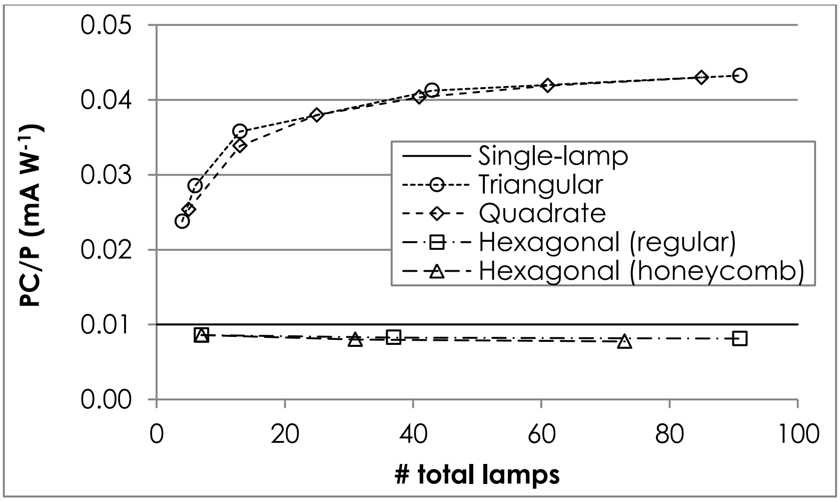

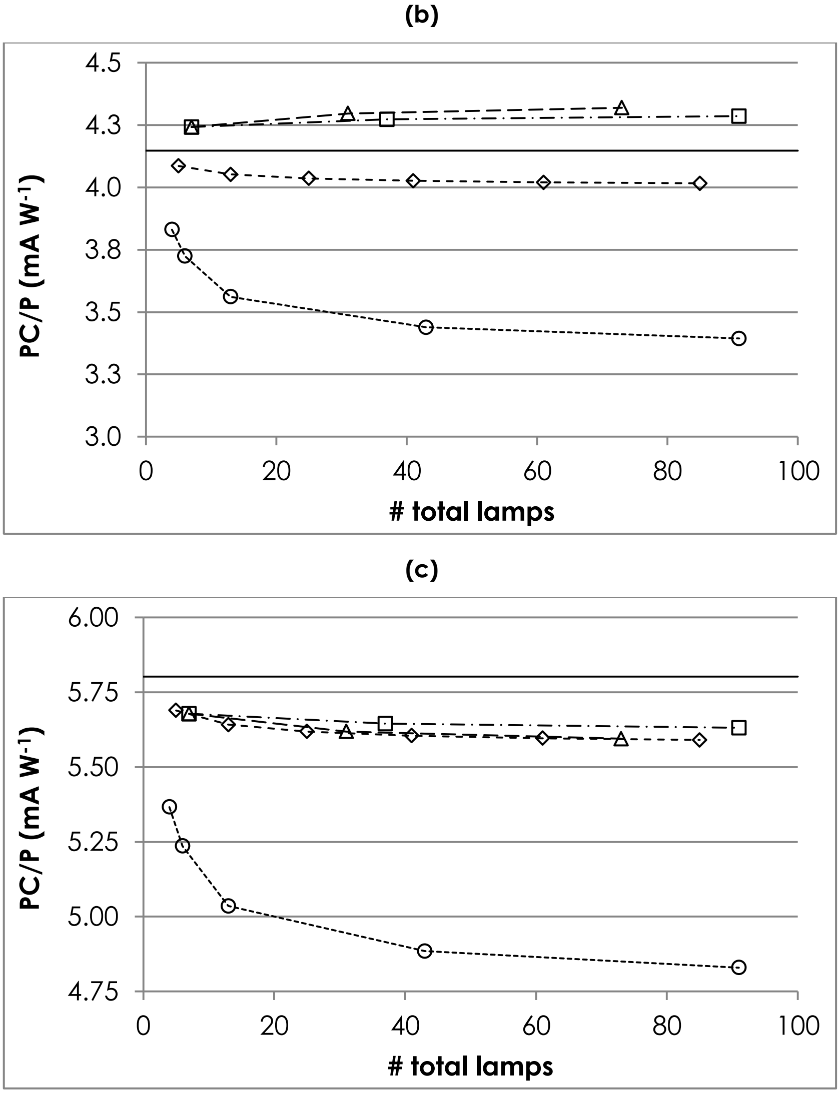

Figure SI7.6 PC/P vs. # total lamps as a function of modular configuration for reactor scale-up and solution transmittance: (a) 100%, (b) 60%, (c) 10%.

APPENDIX

CFD MODELLING OF RADIATION TRANSFER AND FLUID DYNAMICS IN AN UNBAFFLED STIRRED TANK REACTOR FOR TiO_2 NANOPARTICLE PHOTOCATALYSIS

ABSTRACT

In the present research work radiation transfer and fluid dynamics involved in titanium dioxide (TiO_2) photocatalysis have been modelled by a general-purpose computational fluid dynamics (CFD) software, i.e. ANSYS Fluent. The experimental setup was constituted by an unbaffled stirred tank reactor, in which TiO_2 nanoparticles were dispersed, and irradiated by UV-A radiation emitted by a lamp located horizontally over the reactor. CFD simulations of radiation transfer and fluid dynamics were performed in different configurations, as a function of UV lamp distance from the liquid surface, reactor and magnetic stirring bar size, as well as TiO_2 concentration. As for fluid dynamics, the effectiveness of the CFD code was assessed and the more adequate turbulence models for solving RANS equations in the experimental setup were selected by reproducing a previous work in which velocity fields were measured in a similar reactor setup. In detail, k-ε RNG and k-kl-ω models resulted as the most effective in predicting the flow velocity field. CFD simulations of fluid dynamics in the experimental setups evidenced the scarce efficiency of the stirrer in mixing the reactor volume and suggested the best conditions for maximizing the mixing extent. Concerning radiation transfer, CFD model was calibrated by radiometric measures and resulted effective in describing the radiation field, allowing for the determination of radiation intensity and local volumetric rate of photon adsorption throughout reactor volume as a function of TiO_2 concentration.

The research work described in the present chapter was carried out with the valuable support of
Paolo Vicario, MSc student, Politecnico di Milano, Italy
Gianandrea Messa, Research fellow, Politecnico di Milano, Italy
Stefano Malavasi, Associate professor, Politecnico di Milano, Italy

The research work was partially carried out in collaboration with the Hydraulic Section of the Department of Civil and Environmental Engineering (DICA) of Politecnico di Milano.

The present chapter, after the integration of CFD model with process chemistry, will lead to the preparation of a paper intended for publication in an international peer-reviewed scientific journal, being ‘Chemical Engineering Science’ journal a possible candidate.

A.1 INTRODUCTION

Computational fluid dynamics (CFD) codes are powerful modelling tools, capable of solving the governing equations for chemical-physical phenomena in a selected geometrical domain [1]. The valuable contribution of these tools has already been pointed out in previously published research works, *inter alia* [2,3], for water and wastewater treatment including TiO_2 photocatalysis [4].Concerning TiO_2 photocatalysis, the main benefits of CFD codes consist in (i) modelling irradiation phenomena throughout reactor volume, for which the solution of radiative transfer equation (RTE) is required, and (ii) predicting the local values of process-descriptive parameters, which are strongly affected by fluid dynamics, since the extent of mixing throughout reactor volume strongly impacts on the development of kinetic equations.

As for irradiation phenomena, the solution of radiative transfer equation is a computational-intensive issue in case of TiO_2 nanoparticle suspensions, since radiation scattering is not negligible. Several numerical and stochastic methods have been proposed in the past for RTE solution [5], including the discrete ordinate (DO) model, which is typically implemented in CFD codes [6]. On the other hand, the use of empirical techniques, as the six-flux model [7], resulted as the best alternative in case of simple geometries, as annular reactors [8] or thin film slurry reactors [9].

Concerning fluid dynamics, modelling is based on the Navier-Stokes equations, but the accurate prediction of turbulence at all scales is a challenging task, usually unsuitable in engineering applications for the huge demand of computational resources. Therefore, usually-adopted turbulence models are based on the Reynolds-averaged Navier-Stokes (RANS) equations, in which averaged velocity fields are used and the concept of eddy viscosity is introduced [1]. In most of published works on TiO_2 photocatalysis fluid dynamics is neglected by assuming the good mixing of reactor volume or it is analytically described for laminar systems, while only few works used CFD codes for dealing with turbulence, *inter alia* [10,11]. In fact, simplified methods are generally preferred even if they are not able to successfully describe complex systems or to ensure high accuracy in reactor simulation. Conversely, CFD codes can provide a detailed and reliable description of a multi-physics system, potentially representing a key step in the future for the optimization and the scale-up of photocatalytic technologies.

In the present work radiation transfer and fluid dynamics involved in TiO_2 photocatalysis have been modelled by a general-purpose CFD software, i.e. ANSYS Fluent. In particular, a stirred tank reactor was considered, in which TiO_2 nanoparticles were dispersed and vertically irradiated under UV-A monochromatic radiation (365 nm). Radiation transfer and fluid dynamics were simulated as a function of TiO_2 concentration and geometrical characteristics of the experimental setup, considering various conditions for UV lamp positioning as well as reactor and magnetic stirring bar size. Radiation transfer was calibrated by radiometric measures. Fluid dynamics was validated by reproducing a previous work in which velocity fields in a similar reactor setup were measured [12].

A.2 MATERIAL AND METHODS

A.2.1 Experimental setup

Experiments were performed on P25 Aeroxide TiO_2 nanopowder (Evonik, Germany) suspended in deionized water (DI). TiO_2 nanoparticles were dispersed at 40 and 100 mg L^{-1}, respectively by adding 4 and 10 mg of P25 TiO_2 to 100 mL of deionized water and mixing on a magnetic stirrer for 2 minutes (120 RPM). TiO_2 suspension was poured into a small beaker (Flint glass), continuously mixed on a magnetic stirrer (220 RPM) and irradiated.

Experiments were carried out in a UV box equipped with a 15 W fluorescent UV lamp (Helios Italquartz, Italy), emitting at 365±10 nm (mean±st.dev.) and thermostated at room temperature (22±1°C). The UV lamp was housed in a cylindrical quartz sleeve (Ø=3.4cm), which was hold horizontally over the reaction beaker. A black cardboard cylinder (Ø=6 cm), assumed as a perfectly absorbing surface, was vertically positioned around the beaker to limit the experimental domain. A sketch of the experimental setup is shown in figure A.1a.

Two configurations were tested (R1 and R2), differing for the beaker and the cylindrical stirring bar sizes, as well as for the rotation speed, as summarized in table A.1. UV lamp positioning was also modified during experiments by changing the distance between the bottom of the setup and the lowest point of the lamp from 2.5 to 12 cm (0.5 cm step). Radiation intensity was monitored at the bottom and in the centre of the reactor beaker by a radiometer (HD9021, Delta Ohm, Italy), for any UV lamp positioning in both configurations R1 and R2. Measures were performed both in the presence and absence of the black cardboard cylinder. When it was present, it hindered the penetration of the radiation emitted by UV lamp sections external to experimental domain.

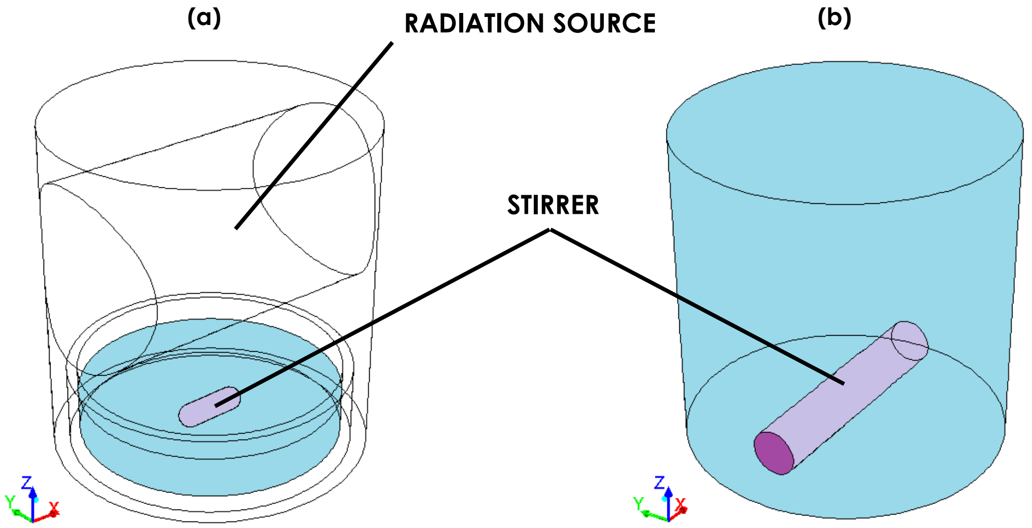

Figure A.1 Reactor configuration schemes: (a) experimental setup (the configuration here sketched has a 2.5 cm distance between the bottom of the setup and the lowest point of the lamp), (b) validation case.

A.2.2 CFD models for radiation transfer and fluid dynamics

CFD simulations were performed using ANSYS Fluent 15.0, using a desktop computer equipped with an Intel i7-4770 processor at 3.40 GHz and 16 GB RAM memory. Two geometrical domains were modelled, respectively referring to the experimental setup and the validation case.

As for the experimental setup, the geometry was constituted by the air domain, the TiO_2 suspension domain and the glass domain. Computational details for fluid dynamics and radiation transfer simulations are described in paragraph A.2.3.1 and A.2.3.2, respectively.

As for the validation case, only fluid dynamics was assessed. The geometry, whose scheme is reported in figure A.1b, was constituted as described by [12]. Reactor configuration and computational details are summarized in paragraph A.2.3.3.

Table A.1 Geometric characteristics of reactor configurations.

Configuration	R1	R2
Reactor volume (mL)	10	15
Reactor internal diameter (mm)	57.0	50.0
Reactor external diameter (mm)	59.6	54.0
Liquid layer thickness (mm)	3.9	8.0
Stirrer length (mm)	10.0	14.0
Stirrer diameter (mm)	3.0	4.4
Rotation speed (RPM)	400	220

A.2.2.1 Fluid dynamics

Since fluid dynamics involves only the TiO_2 solution volume, only this one has been assumed as computational domain for fluid dynamic modelling. The flow in the unbaffled reactor was modelled by a rotating reference frame, as reported in some previously published works for similar problems, *inter alia* [13,14]. In detail, a rotational speed was imposed to the stirrer bar, while the reactor walls were kept stationary. As a consequence, the stirrer bar was raised from reactor bottom of 0.5 mm, to avoid the contact. This distance value was selected for allowing the generation of non-degenerated element meshes, having skewness lower than 0.75, in the zone between the stirrer and the bottom of the reactor. The turbulent flow was solved by two models, namely k-ε RNG (swirl dominated flow) and k-kl-ω, using the 'SIMPLE' algorithm for pressure-velocity coupling and second-order upwind discretization. The 'PRESTO!' algorithm was set for spatial discretization and the under-relaxation factor for momentum was imposed at 0.3. Unstructured meshes were prepared to discretize the geometrical domain, constituted by elements regularly growing from the stirrer boundary, being here required a bigger accuracy, to the reactor external wall. The solution convergence was determined by assessing the stability of residual values and by monitoring the tangential velocity in several points throughout the computational domain.

First, the two experimental configurations R1 and R2 were reproduced in a two-dimensional domain, resulting from the intersection of the experimental setup three-dimensional geometry with the horizontal plane containing the stirring bar axis. Three unstructured meshes were prepared, constituted by triangular elements, ranging between 0.0001 and 0.005 m in size. The largest number of elements was obtained in the finest mesh for configuration R2 (~ 64,000), and the lowest in the coarser mesh for configuration R1 (~ 8,000). As for turbulent flow, the no-slip velocity condition was applied to the walls. About 50,000 iterations were needed to get convergence in a few hours.
Secondly, configuration R2 was modelled as a three-dimensional domain. Three unstructured meshes were prepared, composed by tetrahedral elements. The number of elements in the three meshes varied from about 210,000 to 595,000 elements. The no-slip velocity condition was applied to the solid surfaces, except for the upper boundary, in which the zero-shear boundary condition was assigned. Converged solutions were achieved in about 100,000 iterations after about 24 h computational time.

A.2.2.2 Radiation transfer

The experimental setup in configuration R2 was reproduced in a three-dimensional domain. Two conditions were simulated, respectively characterized by a distance between the bottom of the experimental setup and the lowest point of the lamp of 2.5 and 7 cm.
The radiation source was approximated to an emitting cylindrical surface having the radius of the quartz sleeve, as described in [15], considering the coaxial characteristics of radiation field within the external wall of the quartz sleeve. It was then modelled as a Lambertian monochromatic emitter at 365 nm using the DO model with second order upwind scheme for solving the RTE in the computational domain. A composite mesh was prepared, consisting of tetrahedral elements, having different sizes: (i) the finest three-dimensional mesh introduced in paragraph A.2.2.1 was adopted for water, counting 595,000 elements, (ii) an uniform mesh of about 285,000 elements (size 0.0006 m) was used for glass, (iii) an adaptive mesh was used for air, counting about 681,000 and 1,306,000 elements (0.001 m) respectively for the two simulated conditions. The meshes were designed in order to ensure a matching arrangement of elements belonging to different domains at the point of convergence. The parameters for the DO model were increased for angular discretization both on Phi and Theta to 12 in case of division terms and to 8 in case of pixelation terms. This adaptation was necessary for obtaining a fully-developed solution for radiation transfer. As for the boundary conditions, all walls were assumed to be opaque, the glass surfaces were set as semi-transparent having diffuse fraction equal to zero and the radiation source was modeled as a semi-transparent wall emitting diffuse radiation. The optical properties for the various domains are reported in table A.2. The values for TiO_2 suspension were derived from chapter 3, assuming the Henyey-Greenstein function as the scattering phase function; the optical properties of Flint glass were obtained from supplier datasheets.

Table A. 2 Optical properties of TiO_2 suspensions and Flint glass referred to 365 nm wavelength. Absorption (κ) and scattering (σ) coefficients, asymmetry factor for the Henyey-Greenstein scattering phase function (g) and refractive index (RI) are reported.

Material	κ (m^{-1})	σ (m^{-1})	g	RI
TiO_2 suspension (40 mg L^{-1})	15	60	0.870	1.349
TiO_2 suspension (100 mg L^{-1})	25	135	0.543	1.349
Flint glass	10	0	-	1.61

A.2.2.3 Validation case

The three-dimensional computational domain was constituted by a cylindrical reactor (H=15 cm, Ø=15 cm) filled with water, in which the cylindrical stirrer bar (H=11.3, Ø=2.16 cm) was positioned at 3 mm over the reactor bottom, as already discussed in paragraph A.2.2.1. A rotational speed of 150 RPM was imposed to the stirrer. Three mesh were prepared to discretize the geometrical domain, constituted by uniform tetrahedral elements, respectively characterized by different size of elements (S) and overall number of elements (#): (i) V1: S=0.004 m, #=308,000, (ii) V2: S=0.003 m, #=662,500 and (iii) V3: S=0.0025, #=1,168,000. The same boundary conditions already described for three-dimensional case in paragraph A.2.2.2 were applied. Four turbulence models were tested, namely k-ε RNG (swirl dominated flow), k-kl-ω, k-ω SST and RST. About 100,000 iterations were needed to get the convergence in any configuration, resulting in a calculation of some days.

A.3 RESULTS AND DISCUSSION

Considering the TiO_2 nanoparticle concentration and assuming a TiO_2 density equal to 3.8 g/cm^3, the volume occupied by TiO_2 aggregates is very low (<0.003%) in both configurations R1 and R2. As a consequence, the fluid flow field is not influenced by TiO_2 aggregates in suspension. As a matter of fact, when the particle volume is lower than 0.1%, namely when TiO_2 concentration is lower than 3.8 g/L, the problem can be considered as a decoupled multi-phase system, in which the water flow field can be solved independently [16]. Besides, depending on the Stokes number, which is extremely low (~10^{-5}) also in case of large TiO_2 aggregates (~1.5 μm), it can be supposed that TiO_2 aggregate inertia is negligible in determining a deviation in the water flow field. In addition, TiO_2 suspensions are basically stable in the order of hours. In fact, the terminal settling velocity (v_s) of TiO_2 aggregates can be estimated by the Stokes' law, whose formulation for laminar flow is:

$$v_s = \frac{g(\rho_{TiO_2} - \rho_{H_2O})d^2}{18\mu} \qquad \text{(eA.1)}$$

where g is the acceleration due to gravity, ρ is the mass density, d is TiO_2 aggregate diameter and μ is the dynamic viscosity. Assuming the size distribution reported in chapter 3 and 4 for TiO_2 aggregates in deionized water (number weighted median diameter of 114±0.5 nm), terminal settling velocity is lower than 0.1 mm/h. Therefore, TiO_2 nanoparticles in deionized water can be assumed as a scalar tracer with no inertia in CFD simulations, in which only equations describing the water flow have to be solved.

A.3.1 Fluid dynamics

The CFD analysis of an unbaffled tank reactor mixed by a magnetic stirrer is a complex problem, which has been scarcely faced in the past, unlike baffled tank reactors mixed by impellers, which represent the most common agitated vessel for carrying out chemical reactions at industrial scale, *inter alia* [17,18]. Mahmud et al. [12] studied the water velocity field in a swirl dominated flow, using an unbaffled cylindrical reactor mixed with a magnetic stirrer. Experimental data collected by [12] were here used to validate several turbulence models implemented by CFD codes, in order to select the most effective models to be used for the description of flow fields in the present experimental setup. In particular, given the focus of the present work, a relatively slow mixing condition (rotation speed 150 RPM) was selected among the configurations reported by [12], having the free water surface almost flat and a limited vortex formation on the axis. In fact, in the present case the reactor geometry was considered as a rigid cylindrical domain, since the bending of free water surface and the formation of a vortex are detrimental for radiation transfer from air to water. Moreover, it should be mentioned that the computational cost is high for simulating free water surface, involving a multi-phase approach for explicitly modelling the gas–liquid interface. CFD simulations were considered satisfactory when led to residual values lower than 10^{-8} for every component in any configuration.

Experimental data from [12] and CFD simulation results are shown in figure A.2, where tangential velocity profiles are plotted against reactor radius in x direction at two reactor heights, namely 0.06 and 0.133 m. The grid-independence among the three tested meshes was observed for all turbulence models. A fairly good prediction of experimental data trend was provided by CFD simulations, although a slight underestimation in the tangential velocity was observed for any turbulence model irrespectively of reactor height. The best fitting was achieved by k-ε RNG and RST models, despite the simplifications with respect to [12]. In fact, our CFD simulations do not consider the influence of the free water surface bending, notwithstanding the formation of a small vortex was experimentally observed by [12]. On the other hand, RST model, involving the solution of 7 governing equations for the flow field, determined much longer computational times with respect to other models. Therefore, this model is discarded, while in the following k-ε RNG and k-kl-ω are used, by which good results were achieved. Vectors for velocity magnitude obtained in CFD simulation by k-ε RNG model are reported in figure A.3, where the swirling water flow induced by stirrer rotation is clearly evidenced. Tangential velocity is null on reactor axis and on the reactor outer wall, as imposed by boundary conditions, while it is maximum at about half of the radius.

(a)

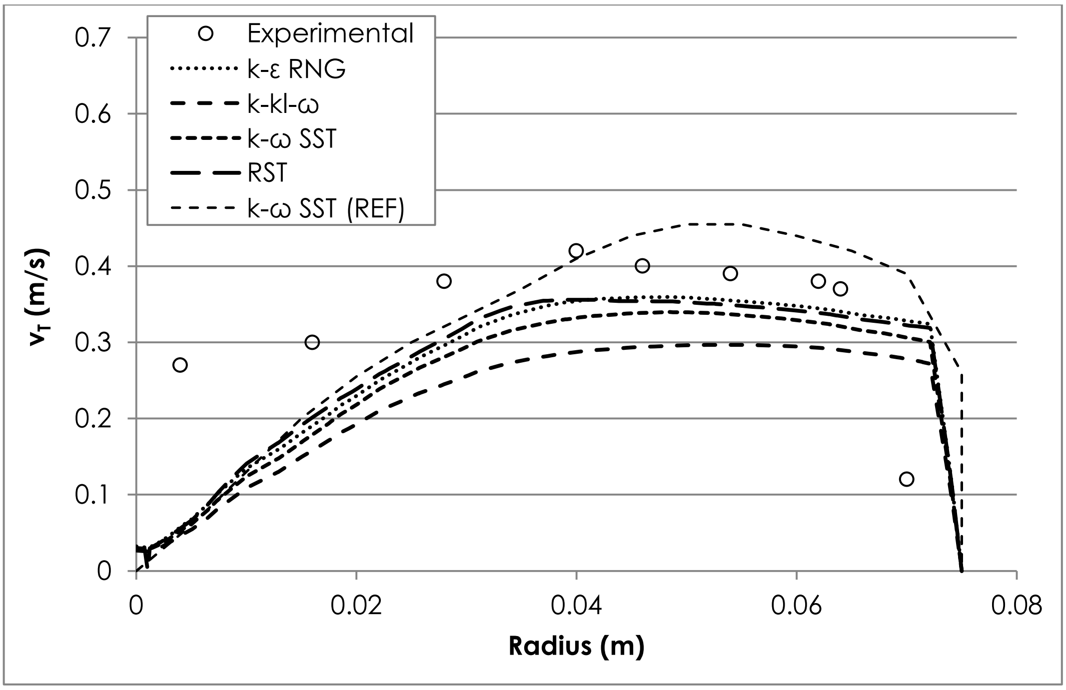

(b)

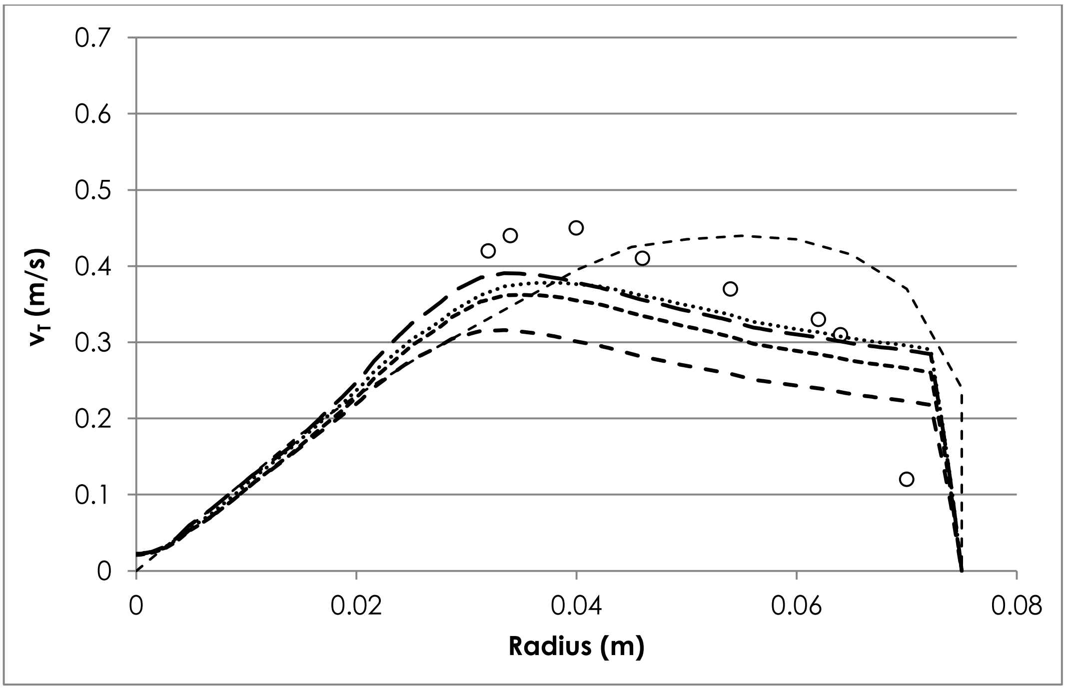

Figure A.2 Tangential velocity vs. reactor radius in x direction at two reactor heights, namely 0.06 and 0.133 m. Experimental data from [12] and CFD simulation results, obtained both in the present work and from the reference work (REF) are shown. As for the present work, CFD simulation results are referred to the solution of mesh V2 by various turbulence models.

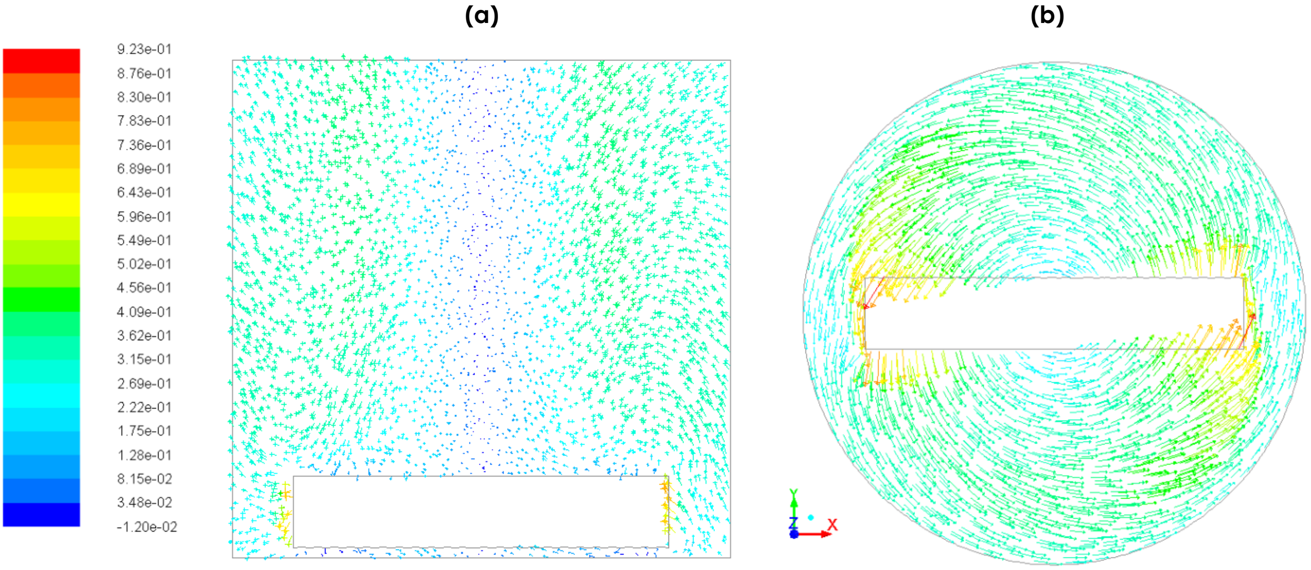

Figure A.3 Vectors for velocity magnitude (m s^{-1}) obtained in CFD simulation on mesh V2 by k-ε RNG model: (a) axial vertical plane oriented in x direction, (b) horizontal plane including the stirring bar axis.

In conclusion, despite the introduced simplifications, the good effectiveness of CFD simulation in flow field modelling was observed and k-ε RNG and k-kl-ω models were applied for modelling fluid dynamics in the experimental setup. Actually, considering the importance of the shape of free water surface and of the formation of the vortex in determining velocity fields over the whole water volume, in both configurations R1 and R2 the rotational speed was experimentally determined in order to maximize the turbulence without the occurrence of free water surface bending. The maximum acceptable rotational speed was set at 400 and 220 RPM in configurations R1 and R2, respectively. The higher value required for observing surface bending in configuration R1 was probably due to the smaller size of the stirring bar, resulting in a smaller perturbation of the liquid volume at the same speed.

First, fluid dynamics were modelled in a two-dimensional domain in order to achieve a preliminary assessment of the reactor behaviour within short computational times. The results of CFD simulations implementing the two turbulence models are reported in figure A.4, in which tangential velocity profiles are plotted against reactor radius in x and y directions for configurations R1 and R2. CFD simulation suggests that mixing in configuration R1 is scarce, being the influence of stirring bar on tangential velocity spatially limited, despite the higher rotational speed with respect to configuration R2. The substantial absence of mixing in configuration R1 is clearly visible in figure A.5, where vectors for velocity magnitude obtained are reported. Tangential velocity values at the lower radius correspond to the velocity at the stirrer boundary, being the size of the stirrer different in the two reactor configurations, and they can be easily estimated by the following relation:

$$v_T = \omega R \qquad \text{(eA.2)}$$

in which v_T is the tangential velocity, ω is the rotational speed and R is the radius.

A significant difference in the prediction of tangential velocity along reactor radius by the two models was also observed, probably due to the different approach in treating turbulence, being the theory behind turbulence models extensively discussed in [1] and the specific features of these two models presented in ANSYS Fluent manual.

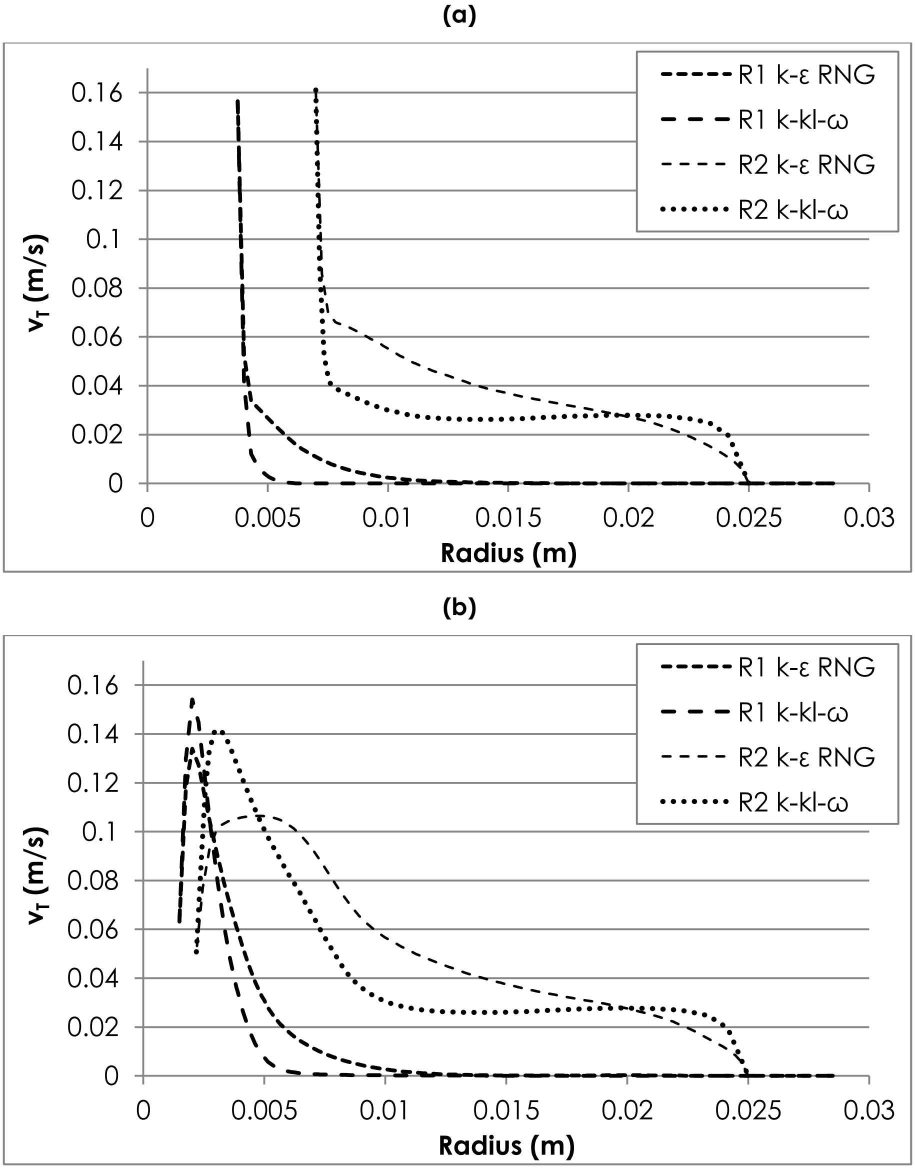

Figure A.4 Tangential velocity vs. reactor radius along x direction (a) and y direction (b) for R1 and R2 configurations in a two-dimensional domain, which was solved by k-ε RNG and k-kl-ω models. Results are representative of all the tested meshes, since the grid-independence was verified.

As a matter of fact, configuration R2 has to be preferred to configuration R1 for reactor mixing, so fluid dynamics was assessed only for configuration R2 in the three-dimensional domain by means of the two turbulence models k-ε RNG and k-kl-ω. In figure A.6 tangential velocity profiles are plotted against reactor radius passing through the central point of the stirrer on the x and y directions for the two turbulence models; vectors for velocity magnitude on the axial vertical plane oriented in x direction and on the horizontal plane including the stirring bar axis are reported in figure A.7. The observed behaviour is rather different from the validation case (figure A.2), mostly because in the present case the size of the stirrer in comparison to the reactor diameter is much smaller. Contrarily to the assumption made by Jassby at al. [19] with reference to an experimental setup similar to the present case, the magnetic stirrer does not provide a uniform and vigorous mixing throughout reactor volume. In fact, the presence of an intensively-mixed solution volume closed to the stirring bar was observed, but in the most of the reactor volume TiO_2 suspension flow is likely laminar.

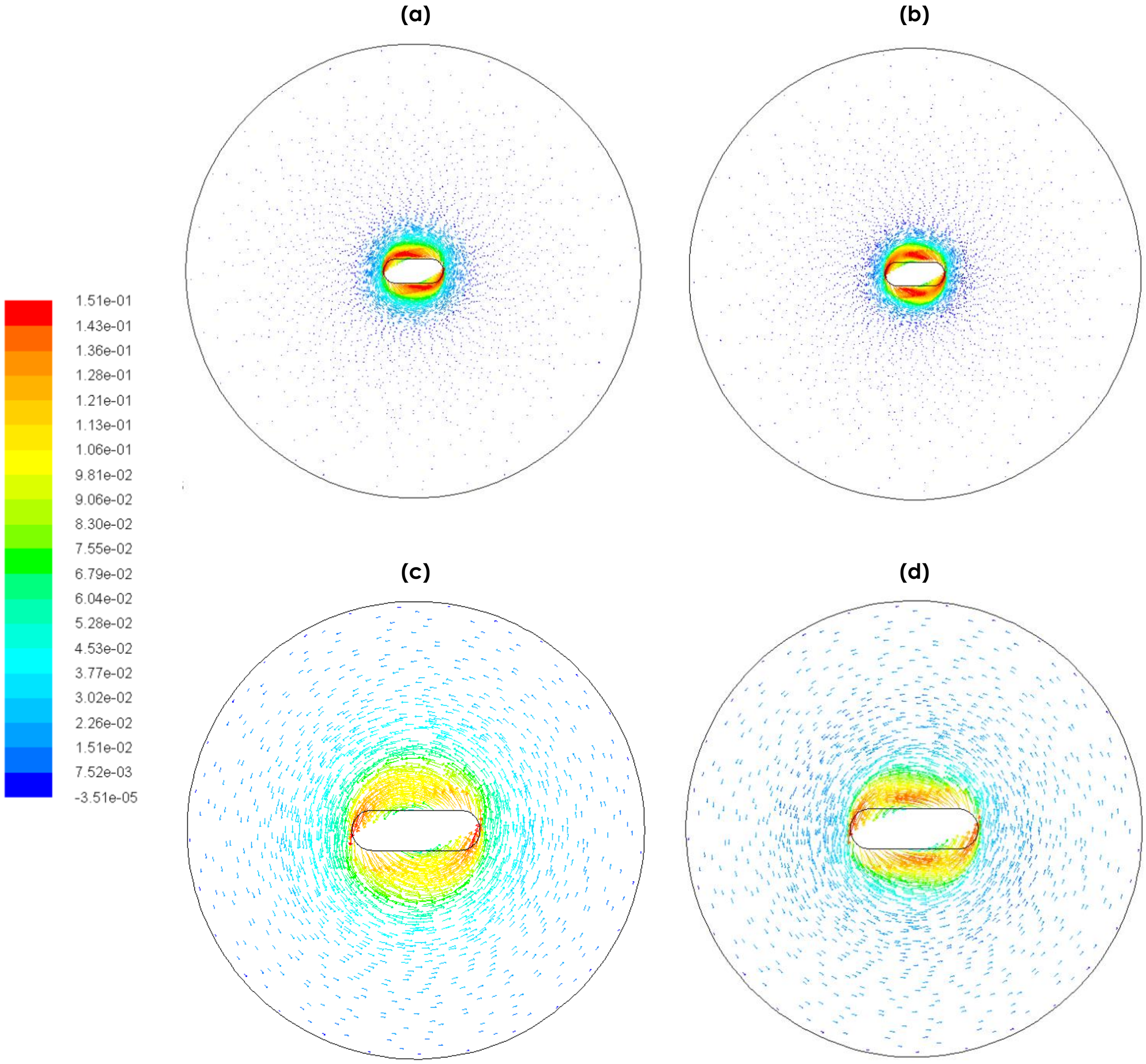

Figure A.5 Vectors for velocity magnitude (m s^{-1}) obtained in CFD simulations for configurations R1 and R2 in a two-dimensional domain, implementing two turbulence models: (a) R1 k-ε RNG, (b) R1 k-kl-ω, (c) R2 k-ε RNG, (d) R2 k-kl-ω.

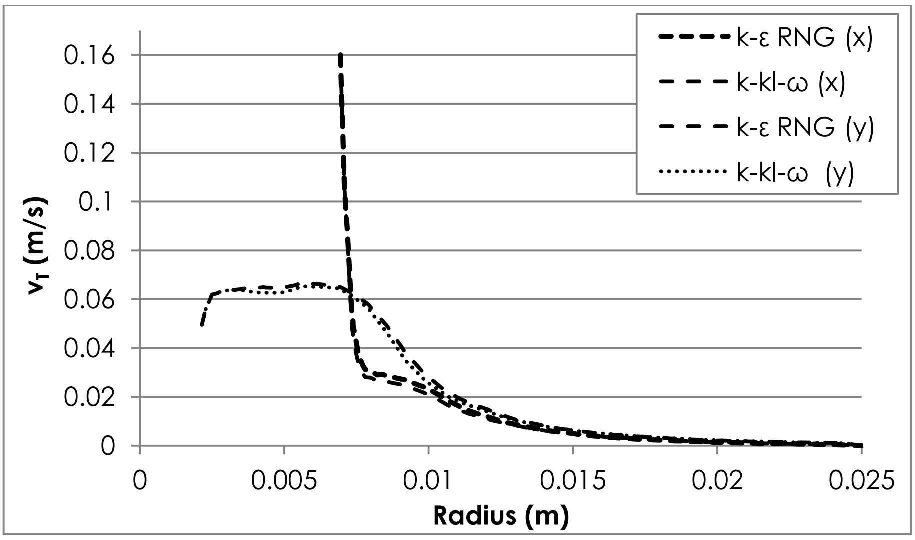

Figure A.6 Tangential velocity vs. reactor radius on the x and y directions for configuration R2 in a three-dimensional domain, which was solved by k-ε RNG and k-kl-ω models. Results are representative of all the tested meshes, since the grid-independence was verified.

It is interesting to note that the two turbulence models behave similarly in describing flow fields, indicating that the previous results for the two-dimensional domain were affected by the geometry simplification. Summarising, the assessment of the effectiveness of mixing with respect to the specific process and geometry is fundamental, considering the influence on the mass transport of chemical species, which is determined by the turbulent diffusion throughout reactor volume.

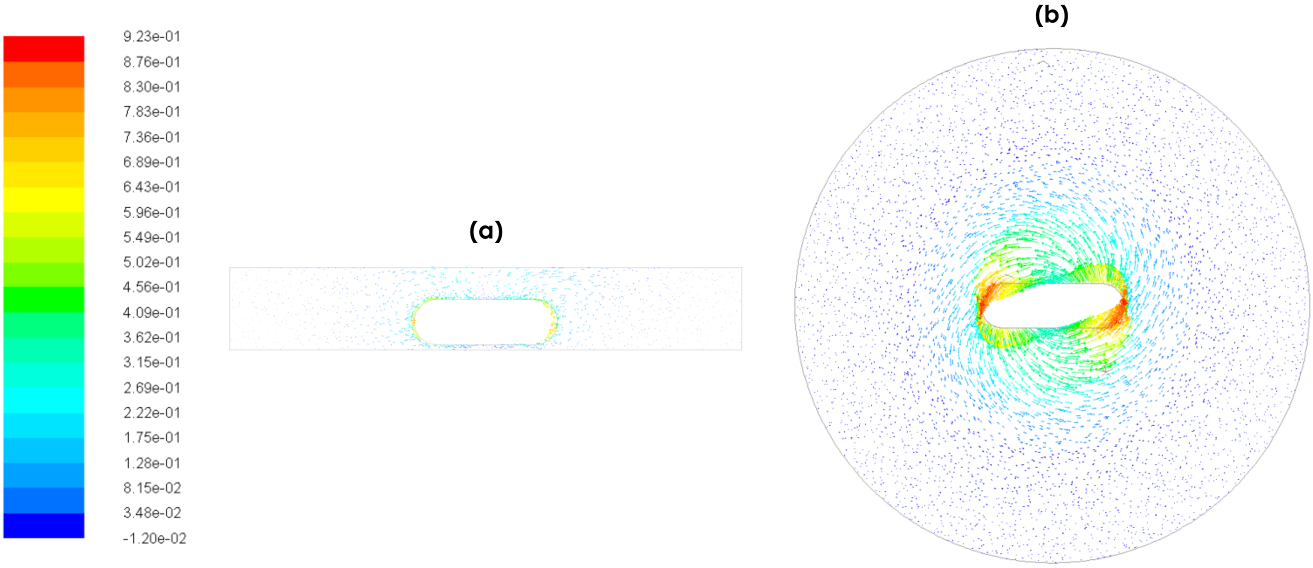

Figure A.7 Vectors for velocity magnitude (m s^{-1}) obtained in CFD simulations for configuration R2 in three-dimensional domain: (a) axial vertical plane oriented in x direction, (b) horizontal plane including stirrer axis.

A.3.2 Radiation transfer

Radiation transfer was assessed by means of three subsequent steps: (i) irradiation fields in the experimental setup were characterized by radiometric measurements, (ii) CFD modelling framework was defined and calibrated by experimental data, (iii) CFD simulations of irradiation fields in the experimental setup were performed for assessing the irradiation of TiO_2 suspensions.

A.3.2.1 Experimental measurements

Radiometric measurements were carried out to determine the radiation intensity (I) at the bottom of the experimental setup in central position at various distances from the lowest point of the lamp. Experimental values were increased by a factor of 1.169 for considering the spectral response of the sensor. In agreement with [9], the correction factor was estimated by equation eA.2:

$$I = I_{sensor} \frac{\int W_\lambda d\lambda}{\int W_\lambda P_\lambda d\lambda} \qquad \text{(eA.3)}$$

in which I_{sensor} is the incident radiation measured with the radiometer, P_λ is the relative spectral response of the sensor, W_λ is the radiant power of the UV lamp at wavelength λ. Integration limits are set by the emission spectrum of the UV lamp and by the TiO_2 photoactivation spectrum.

Radiation intensity measured at the bottom of the experimental setup in the centre of the reactor beaker is reported in figure A.8, both in presence and absence of the black cardboard cylinder externally limiting the experimental domain; the difference in radiation intensity measured in the two irradiation conditions is also reported.

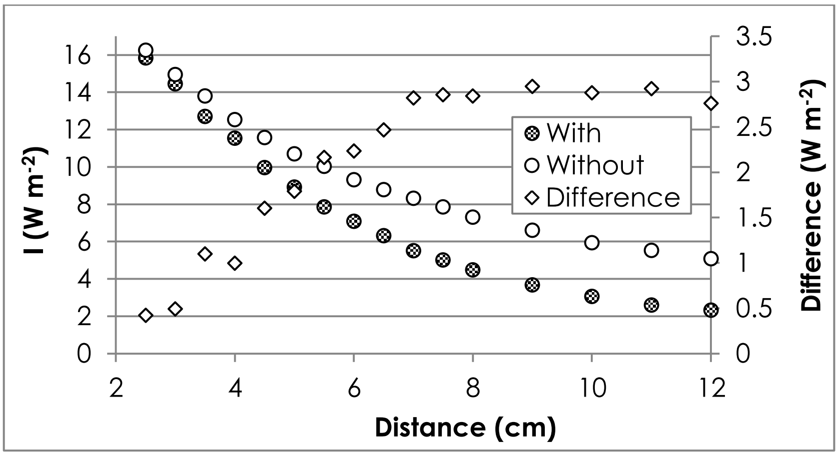

Figure A.8 Radiation intensity vs. distance between the bottom of the setup and the lowest point of the lamp in the presence (with) or in the absence (without) of the black cardboard cylinder. The difference in radiation intensity measured in the two conditions is reported.

As expected, a decrease in radiation intensity with increasing the distance of the radiation source was observed, as well as a reduction in radiation intensity in case of the application of the black cardboard cylinder. On the other hand, a changing behaviour can be noted as a function of the distance from the UV lamp: the radiation intensity gap between the two irradiation conditions increases almost linearly up to about 7 cm, then it maintains a constant value, around 2.5 W m^{-2}. Such phenomenon could be related to the effect operated by the black cardboard cylinder on the incoming radiation through the domain boundaries, or to the detection angle of the sensor. Therefore, with the aim of obtaining a general assessment of radiation transfer phenomena, both the irradiation conditions were selected for CFD simulations.

A.3.2.2 CFD simulations of radiation transfer

Preliminarily, the radiation source was calibrated in order to define the emitting power of radiation source in CFD simulations. Such procedure was conducted by iteratively changing the emitting power until matching the radiation intensity value that was measured in central position at the bottom of the experimental setup positioning the UV lamp at 2.5 cm distance, namely 15.8 W m^{-2}. An emitting power of 40.9 W m^{-2} at radiation source surface was evidenced as appropriate and validated by repeating the same procedure in case of 7 cm distance between the lowest point of the UV lamp and the bottom of the experimental setup. In fact, the same emitting power resulted in a radiation intensity close to the measured value (5.5 W m^{-2}).

The emitting power of the radiation source in the computational domain was estimated as the product of the emitting power and the radiation source surface (about 0.006 m^2), obtaining a value of about 0.24 W. Such value, corresponding to the emitting power of a short portion of the lamp and not accounting for the small absorption due to the presence of the quartz sleeve, is in agreement with the indications provided by the manufacturer about the UV lamp performance.

In figure A.9 the CFD simulated radiation intensity for the experimental setup with 2.5 cm distance between the lowest point of the lamp and the bottom of the experimental setup is reported for various TiO_2 concentrations. The local volumetric rate of photon absorption (LVRPA) has been subsequently estimated by the equation eA.4:

$$LVRPA = \int_{\lambda} I_{\lambda} \kappa_{\lambda} \, d\lambda \qquad \text{(eA.4)}$$

in which κ_λ is the absorption coefficient. LVRPA is also shown in figure A.9.

In agreement with CFD simulation results presented in [10], the irradiation of the upper liquid surface is far from uniformity; the absorption of incident radiation decreases progressively with the optical path through the liquid volume. CFD simulation of the radiation transfer indicates the presence of several side optical phenomena in the domain, determined by the presence of elements participating in the radiation transfer, such as the beaker or the stirring bar. Moreover, given the presence of the rotating frame, the occurrence of a change in radiation fields due to the motion of the magnetic stirrer should be considered.

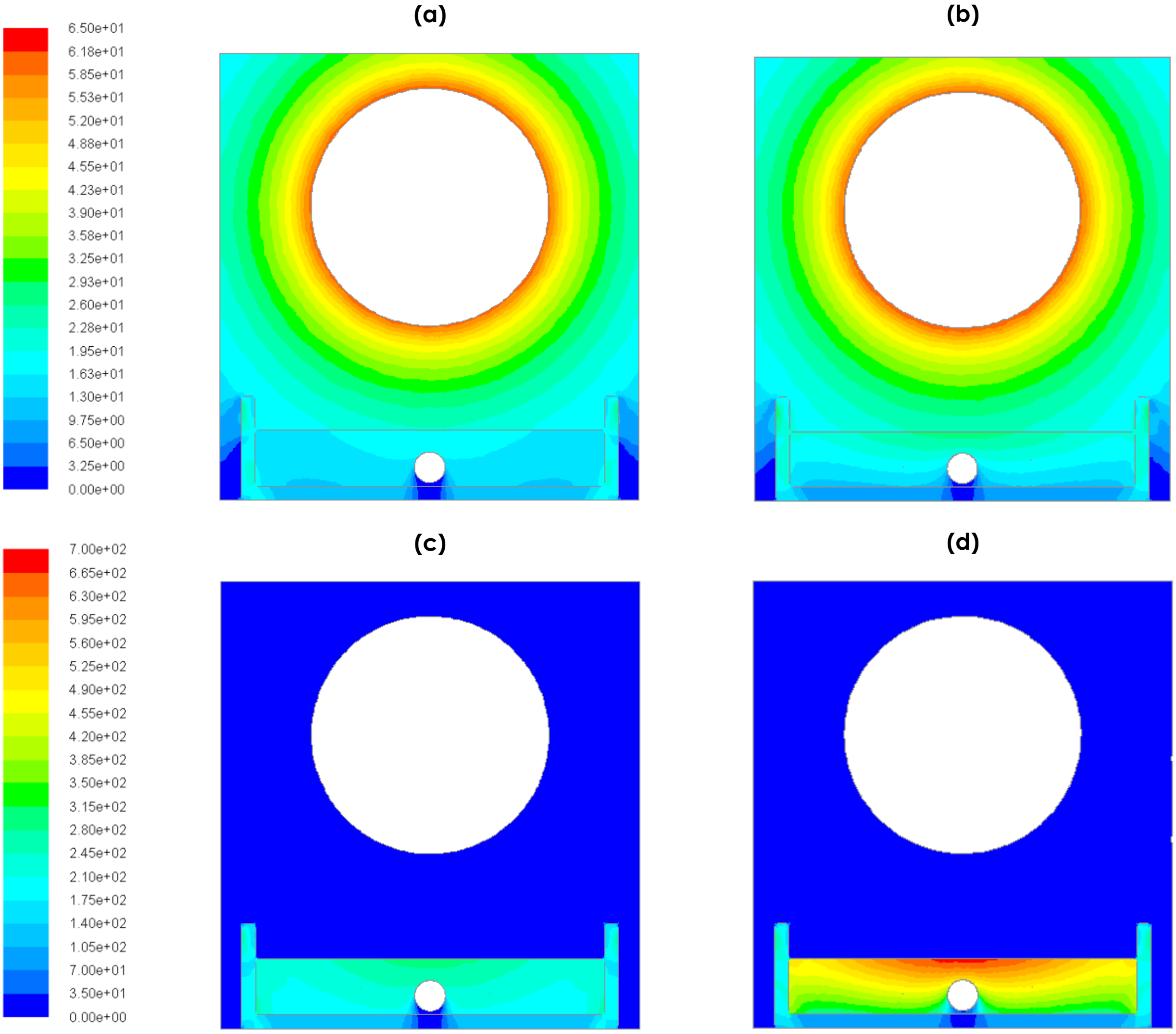

Figure A.9 CFD simulation of radiation intensity as W m^{-2} (a,b) and LVRPA as W m^{-3} (c,d) in the experimental setup with 2.5 cm distance between the lowest point of the lamp and the bottom for various TiO_2 concentrations, on the axial vertical plane oriented in y direction: 40 mg L^{-1} (a,c) and 100 mg L^{-1} (b,d).

The energy balance was calculated for the two irradiation conditions. Results are reported in table A.3. It interesting to note that in the experimental setup the overall emitted radiation is almost completely lost through domain boundaries, and only a small percentage is absorbed by the liquid volume, consistently with the absorption coefficient of TiO_2 suspension. It should be noticed that the amount of radiation lost by the bottom boundary of the experimental setup is higher for 40 mg L^{-1} TiO_2 concentration. Roughly speaking, at 40 mg/L TiO_2 concentration, about 70% of the radiation entering the volume from the top is transmitted through the bottom, but this percentage is reduced to 50% at 100 mg L^{-1} TiO_2 concentration. This difference accounts for the greater radiation fraction of emitted radiation that is absorbed by TiO_2 aggregates. Finally, it can be observed that the extent of radiation absorption increases in the liquid volume closest to the radiation source with increasing TiO_2 concentration (figure A.9c, d). Therefore, being LVRPA the driving-force of the photocatalytic process, it can be stated that TiO_2 photoactivation and, thus, the related chemical reaction are progressively favoured in proximity of the liquid surface. Such behaviour should be accounted in the view of reactor optimization for defining liquid thickness.

Table A.3 Energy balance in the experimental setup with 2.5 cm distance between the lowest point of the lamp and the bottom, for various TiO_2 concentrations. Results are given in terms of absorbed Watts and as percentage over total emitted energy.

[TiO_2] (mg L^{-1})	40		100	
Liquide volume	0.0040	1.7%	0.0080	3.4%
Reaction beaker	0.0016	0.7%	0.0016	0.7%
External loss (side+top)	0.1721	72.1%	0.2050	85.9%
External loss (bottom)	0.0603	25.5%	0.0229	9.6%

A.4 CONCLUSIONS

The modelling of radiation transfer and fluid dynamics in an unbaffled stirred tank reactor for TiO_2 nanoparticle photocatalysis by a general-purpose CFD code was conducted. The efficiency of the CFD code in modelling fluid dynamics was proved by reproducing a validation case, also indicating k-ε RNG and k-kl-ω models as the most effective in predicting the flow field. CFD simulations of fluid dynamics in the experimental setup evidenced the scarce efficiency of the rotating stirrer in agitating reactor volume and indicated the best alternative for maximizing the extent of mixing. Concerning radiation transfer, CFD model was calibrated by radiometric measures and allowed the determination of radiation intensity and local volumetric rate of photon adsorption throughout reactor volume as a function of TiO_2 photocatalyst concentration. Future developments will concern the integration of these physics with chemical reactions in order to provide a comprehensive description of the photocatalytic process, requiring the implementation of scalar sources for defining the presence of chemical species and the coding of a kinetic model.

A.5 REFERENCES

[1] H.K. Versteeg, W. Malalaskekera, An introduction to computational fluid dynamics: the finite volume method, Prentice Hall, 2007.

[2] B. Wols, Computational fluid dynamics in drinking water treatment, IWA Publishing, 2011.

[3] J. Zhang, A.E. Tejada-Martínez, Q. Zhang, Developments in computational fluid dynamics-based modeling for disinfection technologies over the last two decades: a review, Environ. Model. Softw. 58 (2014) 71–85.

[4] Y. Boyjoo, M. Ang, V. Pareek, Some aspects of photocatalytic reactor modeling using computational fluid dynamics, Chem. Eng. Sci. 101 (2013) 764–784.

[5] V. Pareek, S. Chong, Light intensity distribution in heterogenous photocatalytic reactors, Asia-Pac. J. Chem. Eng. 3 (2008) 171–201.

[6] V.K. Pareek, A.A. Adesina, Light intensity distribution in a photocatalytic reactor using finite volume, AIChE J. 50 (2004) 1273–1288.

[7] G. Li Puma, A. Brucato, Dimensionless analysis of slurry photocatalytic reactors using two-flux and six-flux radiation absorption-scattering models, Catal. Today. 122 (2007) 78–90.

[8] B. Toepfer, A. Gora, G. Li Puma, Photocatalytic oxidation of multicomponent solutions of herbicides: reaction kinetics analysis with explicit photon absorption effects, Appl. Catal. B Environ. 68 (2006) 171–180.

[9] I. Grčić, G. Li Puma, Photocatalytic degradation of water contaminants in multiple photoreactors and evaluation of reaction kinetic constants independent of photon absorption, irradiance, reactor geometry, and hydrodynamics, Environ. Sci. Technol. 47 (2013) 13702–13711.

[10] F.J. Trujillo, T. Safinski, A.A. Adesina, Oxidative photomineralization of dichloroacetic acid in an externally-irradiated rectangular bubble tank reactor: computational fluid dynamics modeling and experimental verification studies, Ind. Eng. Chem. Res. 49 (2010) 6722–6734.

[11] J.E. Duran, M. Mohseni, F. Taghipour, Computational fluid dynamics modeling of immobilized photocatalytic reactors for water treatment, AIChE J. 57 (2011) 1860–1872.

[12] T. Mahmud, J.N. Haque, K.J. Roberts, D. Rhodes, D. Wilkinson, Measurements and modelling of free-surface turbulent flows induced by a magnetic stirrer in an unbaffled stirred tank reactor, Chem. Eng. Sci. 64 (2009) 4197–4209.

[13] J.N. Haque, T. Mahmud, K.J. Roberts, D. Rhodes, Modeling turbulent flows with free-surface in unbaffled agitated vessels, Ind. Eng. Chem. Res. 45 (2006) 2881–2891.

[14] N. Lamarque, B. Zoppé, O. Lebaigue, Y. Dolias, M. Bertrand, F. Ducros, Large-eddy simulation of the turbulent free-surface flow in an unbaffled stirred tank reactor, Chem. Eng. Sci. 65 (2010) 4307–4322.

[15] United States of America Environmental Protection Agency, Ultraviolet disinfection guidance manual for the final long term 2 enhanced surface water treatment rule, 2006.

[16] G.A. Messa, Two fluid model for solid liquid flows in pipeline systems, PhD thesis, Politecnico di Milano, 2013.

[17] G.M.C. Glover, J.J. Fitzpatrick, Modelling vortex formation in an unbaffled stirred tank reactors, Chem. Eng. J. 127 (2007) 11–22.

[18] G.R. Kasat, A.R. Khopkar, V.V. Ranade, A.B. Pandit, CFD simulation of liquid-phase mixing in solid–liquid stirred reactor, Chem. Eng. Sci. 63 (2008) 3877–3885.

[19] D. Jassby, J.F. Budarz, M. Wiesner, Impact of aggregate size and structure on the photocatalytic properties of TiO_2 and ZnO nanoparticles, Environ. Sci. Technol. 46 (2012) 6934-6941.